

**Land seismic data acquisition and preprocessing  
an operator solution to the near-surface problem**



# Land seismic data acquisition and preprocessing an operator solution to the near-surface problem

Proefschrift

ter verkrijging van de graad van doctor  
aan de Technische Universiteit Delft,  
op gezag van de Rector Magnificus, prof. dr. ir. J.T. Fokkema,  
voorzitter van het College voor Promoties,  
in het openbaar te verdedigen

op maandag 18 juni 2007 om 10:00 uur

door

**Mustafa Naser AL-ALI**

Master of Science in Geology,  
King Fahd University of Petroleum & Minerals, Dhahran

geboren te Al Ahsa, Saoedi Arabie

*Dit proefschrift is goedgekeurd door de promotor:*

Prof. dr. ir. A.J. Berkhout

*Samenstelling promotiecommissie*

Rector Magnificus, voorzitter

Prof. dr. ir. A.J. Berkhout

Prof. dr. ir. A. Gisolf

Prof. dr. D.G. Simons

Prof. T.A. Alkhalifah

Technische Universiteit Delft, promotor

Technische Universiteit Delft

Technische Universiteit Delft

King Abdulaziz City for Science and Technology,  
Riyadh, Saudi Arabia

Dr. ir. G. Blacquièrè

TNO Defensie en Veiligheid, Den Haag

Dr. ir. D.J. Verschuur

Technische Universiteit Delft

Dr. P. G. Kelamis

Saudi Aramco, Saudi Arabia

ISBN: 978-90-9022011-6

Copyright © 2007 by M. N. Al-Ali, Delft University of Technology, Delft, The Netherlands.

All rights reserved. No part of the material protected by this copyright notice may be reproduced or utilized in any form or by any means, electronic or mechanical, including photocopying, recording or by any information storage and retrieval system, without written permission of the author.

#### SUPPORT

The research of this thesis was financially supported by Saudi Aramco and by the DELPHI consortium.

Printed in the Netherlands by Gildeprint Drukkerijen, Enschede.

*This thesis is dedicated to my  
father, mother, and wife.*



# Contents

---

<b>1</b>	<b>Introduction .....</b>	<b>1</b>
1.1	The seismic method .....	1
1.2	Seismic data acquisition .....	3
1.3	3D seismic survey design .....	3
1.4	Land survey design as an integrated approach .....	6
1.5	Thesis objectives .....	10
1.6	Thesis outline .....	12
<b>2</b>	<b>3D land acquisition geometries .....</b>	<b>15</b>
2.1	3D data matrix .....	15
2.2	Basic 3D geometry building blocks .....	18
2.3	Initial 3D geometry design .....	20
2.4	Temporal and spatial sampling .....	22
2.4.1	Source and receiver arrays .....	24
2.4.2	A strategy for signal and noise spatial sampling .....	26
2.5	Source generated noise .....	28
2.6	Concluding remarks .....	31
<b>3</b>	<b>Theory of model-based land geometry design .....</b>	<b>33</b>
3.1	Introduction .....	33
3.2	The seismic experiment .....	34
3.2.1	Notation convention .....	38
3.3	Imaging by double focusing.....	38
3.3.1	Confocal imaging .....	39
3.3.2	Bifocal imaging .....	42
3.4	Acquisition geometry assessment .....	44

---

3.4.1	Focal beams .....	44
3.4.2	Focal functions .....	46
<b>3.5</b>	<b>Seismic noise .....</b>	<b>52</b>
3.5.1	Rayleigh waves .....	53
3.5.2	Scattered Rayleigh waves .....	54
3.5.3	Incoherent noise .....	57
<b>3.6</b>	<b>Concluding remarks .....</b>	<b>58</b>
<b>4</b>	<b>Computational aspects and numerical examples .....</b>	<b>59</b>
<b>4.1</b>	<b>Introduction .....</b>	<b>59</b>
<b>4.2</b>	<b>Focal beams and focal functions computational aspects .....</b>	<b>61</b>
4.2.1	1D subsurface model.....	62
4.2.2	Seismic noise .....	62
4.2.3	1D subsurface model overlain by a complex near-surface .....	63
<b>4.3</b>	<b>Interpretation of focal beams and focal functions .....</b>	<b>65</b>
<b>4.4</b>	<b>Influence of subsurface complexity on energy distribution .....</b>	<b>66</b>
<b>4.5</b>	<b>Numerical examples.....</b>	<b>71</b>
4.5.1	1D velocity model.....	72
4.5.2	1D model with scattered Rayleigh waves .....	78
4.5.3	Effects of field arrays on signal bandwidth.....	86
4.5.4	1D model overlain by a low-velocity near-surface anomaly .....	90
4.5.5	1D model overlain by a high-velocity near-surface anomaly .....	94
4.5.6	1D model overlain by a complex near-surface with topography ..	97
4.5.7	Fundamental problems of applying statics to correct for near-surface variations .....	103
<b>4.6</b>	<b>Model retrieval ability from data .....</b>	<b>106</b>
<b>4.7</b>	<b>Concluding remarks .....</b>	<b>108</b>
<b>5</b>	<b>An operator-based approach for solving the near-surface problem .....</b>	<b>109</b>
<b>5.1</b>	<b>Introduction .....</b>	<b>109</b>
<b>5.2</b>	<b>Theoretical review of the CFP method .....</b>	<b>111</b>
<b>5.3</b>	<b>Initial operators and updating.....</b>	<b>116</b>
<b>5.4</b>	<b>The integrated method and velocity model building .....</b>	<b>120</b>
<b>5.5</b>	<b>Field data example (2D) .....</b>	<b>121</b>

---

<b>5.6</b>	Operator estimation for 3D data .....	130
5.6.1	Introduction .....	130
5.6.2	Methodology .....	131
5.6.3	3D focusing operator updating using cross-spreads .....	133
5.6.4	Synthetic data example (3D) .....	136
5.6.5	Field data example (3D) .....	138
<b>5.7</b>	Concluding remarks .....	141
<b>6</b>	<b>Estimation of one-way focusing operators from two-way traveltimes .....</b>	<b>143</b>
<b>6.1</b>	Introduction .....	143
<b>6.2</b>	Starting with two-way traveltimes .....	144
<b>6.3</b>	Theory .....	147
<b>6.4</b>	Validation and/or refinement of the estimated focusing operators .....	148
<b>6.5</b>	Synthetic data example redatuming .....	150
<b>6.6</b>	Field data example redatuming .....	155
<b>6.7</b>	Concluding remarks .....	158
<b>7</b>	<b>Conclusions and recommendations .....</b>	<b>159</b>
<b>7.1</b>	Introduction .....	159
<b>7.2</b>	Seismic acquisition .....	160
7.2.1	Summary of methodology .....	160
7.2.2	Conclusions .....	160
7.2.3	Recommendations for future research .....	162
<b>7.3</b>	Preprocessing .....	164
7.3.1	Summary of methodology .....	164
7.3.2	Conclusions .....	164
7.3.3	Recommendations for future research .....	165
<b>A.</b>	<b>Focal source and detector beams .....</b>	<b>167</b>
<b>B.</b>	<b>Comparison between TWT and OWT tomography: a case study .....</b>	<b>173</b>

<b>Bibliography .....</b>	<b>187</b>
<b>Summary .....</b>	<b>193</b>
<b>Samenvatting .....</b>	<b>195</b>
<b>Curriculum vitae .....</b>	<b>197</b>
<b>Acknowledgments .....</b>	<b>199</b>

# Introduction

## 1.1 The seismic method

The seismic method manifests itself as the most important indirect method for collecting information about the Earth's geological structures and rock properties. It can be used inland, offshore, and in transition zones. The details of the seismic method are complex; however, the principle is relatively simple. Seismic sources at or just below the surface generate elastic waves that propagate in different directions through the subsurface. Variations in the physical properties of the geological layers cause the seismic signals to reflect, refract at the boundaries of these layers. The reflected waves head back towards the surface where detectors have been placed to record these waves. The recorded signals are subsequently processed to generate images of the subsurface, and to estimate physical properties such as wave velocity.

In the marine case, the seismic signals are generated either by an impulsive source, known as the airgun, or by a controlled vibratory source that generates a coded signal. The returning signals are detected by piezoelectric pressure sensors called hydrophones which are connected in streamers (measurement cables) towed by a boat. An alternative is that velocity and acceleration sensors are placed on the sea floor to detect the returning signals, so called ocean bottom cable (OBC) surveys. In the land case, seismic signals are generated by dynamite sources or by mechanical impulsive sources or by coded vibratory sources. The returning signals are detected by either velocity or acceleration sensors referred to as geophones. Figure 1.1 shows the principle of land seismic data acquisition.

The seismic method has been significantly improved since its start in the early twentieth century. Two-dimensional (2D) seismic data were primarily used for exploration as well as interpolation between wells during the production phase until the introduction of three-dimensional (3D) seismic data in the 1980's. Results revealed that 3D seismic data provide significantly better images, enabling the detection of small-scale reservoir features like channels and small faults or fractures. Currently, 3D seismic data are not only used during the development phase, but also during the exploration phase which is supported by

significant reduction in acquisition cost. Currently, there is a major attention to wide-azimuth marine 3D data which assist in improving complex subsurface imaging (see for example Moldoveanu and Egan, 2006 and Long, 2006). Wide-azimuth land 3D seismic data has aided in improving imaging in areas with complex near-surface (Hastings-James et al., 2000). In addition, four-dimensional (4D) seismic data or time-lapse data proved to be very useful in monitoring reservoir fluid movements with time in particular for the marine case. The use of multicomponent (i.e. compressional and shear waves) seismic recording has opened new opportunities for more accurate estimation of the rock properties.

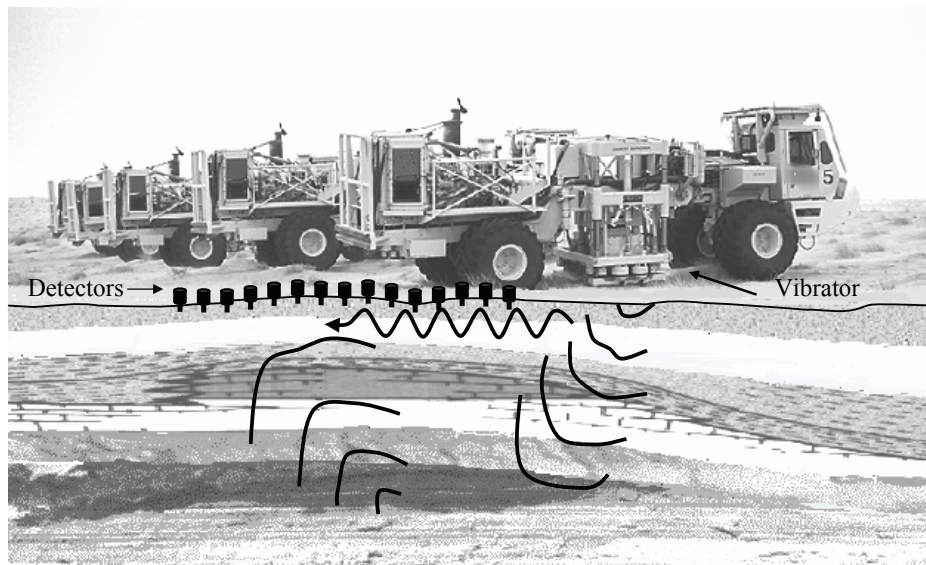


**Fig. 1.1** A picture of land seismic data acquisition. The propagation of seismic waves through the subsurface is represented schematically.

The increasing demands for oil and gas will nourish further developments of the seismic method. More information is sought from the seismic data, particularly when dealing with complex reservoir systems and the increasing quest for improving hydrocarbon recovery. We may expect seismic data being continuously recorded during the production phase and applied as an important tool to improve recovery. Then, the seismic data will be used not only to monitor the fluids movements but also to monitor changes in their movements. Seismic data are also used for mineral exploration and in civil engineering projects. The extended applications of the seismic method require continuous improvements in the theory and practice of acquiring, processing, and characterizing seismic data. This thesis focuses on the design of land 3D: acquisition geometries in combination with the capability of pre-processing.

## 1.2 Seismic data acquisition

Seismic data acquisition, being the first step in the seismic method, aims at measuring data of high quality to achieve the upstream business objectives. More specific, the objectives are high resolution images and accurate rock properties at minimum cost. Resolution is governed by temporal and spatial bandwidths of the reflected energy (signal). Besides, the acquired data has to contain low coherent and incoherent noise and preserve the signal fidelity.

Data acquisition geometries should reserve the signal and reduce the noise. These two requirements may conflict with each other because noise can be reduced in acquisition by using source and receiver arrays which also reduce the temporal and spatial bandwidth of the signal. Therefore, the acquisition parameters have to be tuned so that signal fidelity is preserved while providing data that allows effective noise suppression in processing. There are two approaches for determining the acquisition parameters or survey design: one that does not include a specific subsurface model while the other requires such a model in the design process. Both approaches are further explained in the next section.

## 1.3 3D seismic survey design

Design of acquisition geometries aims at selecting the acquisition parameters that meet the upstream information needs while minimizing the cost. Conventional 2D and 3D survey designs are still largely oriented towards common-mid-point (CMP) processing that assumes a more or less 1D depth model that allows a traveltime description with stacking velocity. The 2D stack-array design method developed by Anstey (1986), is widely accepted for 2D survey design. Ongkiehong and Askin (1988) provide more insight into the stack-array concept and they show how to further improve seismic data acquisition with this concept. Extension of the stack-array to 3D leads to the full-fold geometry (Marschall, 1997), which is conceptually straightforward (Figure 1.2). However, this extension is economically, and often operationally, not feasible especially when designing for deep targets (i.e. several thousands of meters deep). Consequently, smart design methods are required so that objectives are met within the constraints of the available of the resources. The solution is contained in the selection of a compromise-geometry from the 3D full-fold geometry (Figure 1.3). Cordsen et al. (2000) give a comprehensive description of the conventional seismic survey design.

Traditionally, the designer estimates sampling parameters based on a 1D depth model for the target reflectors. These parameters include source and receiver group spacing, source and receiver line spacing and the maximum inline and cross-line offset. There are different standard geometries that can encapsulate these parameters like areal, orthogonal, zig-zag, brick-wall, and others. Vermeer (2002) describes these geometries and their properties. The selection of an acquisition geometry is normally based on regularity of CMP attributes like fold, offset and azimuth (Galbraith, 1994) as well as operational feasibility. If the macro

subsurface model significantly deviates from the 1D model, seismic wavefields will be drastically different and the required layout of sources and detectors may be very different.

Model-based survey design can be performed by forward modeling of seismic data, using a certain subsurface model and acquisition geometry, and then process and characterize the resulting data. Modeling as well as assessment of the results have evolved since the start of model-based survey design. Initially, ray-tracing was used to compute design attributes at target reflectors. Slawson et al. (1994) and Campbell et al. (2002) describe generation of illumination maps using this method. Illumination maps assist in highlighting shadow zones, benefits of undershooting and optimum orientation of the survey. Sassolas et al. (1999) extend the illumination maps to predict pre-stack imaging results, showing the acquisition geometry footprint. Chang et al. (2001) use the CRP stack approach and estimate amplitudes on the target and the surface to optimize the acquisition geometry. All these explicit methods use a data modeling processing approach. In addition, global optimization is used since target reflectors instead of target points are considered (Laurain et al., 2004).

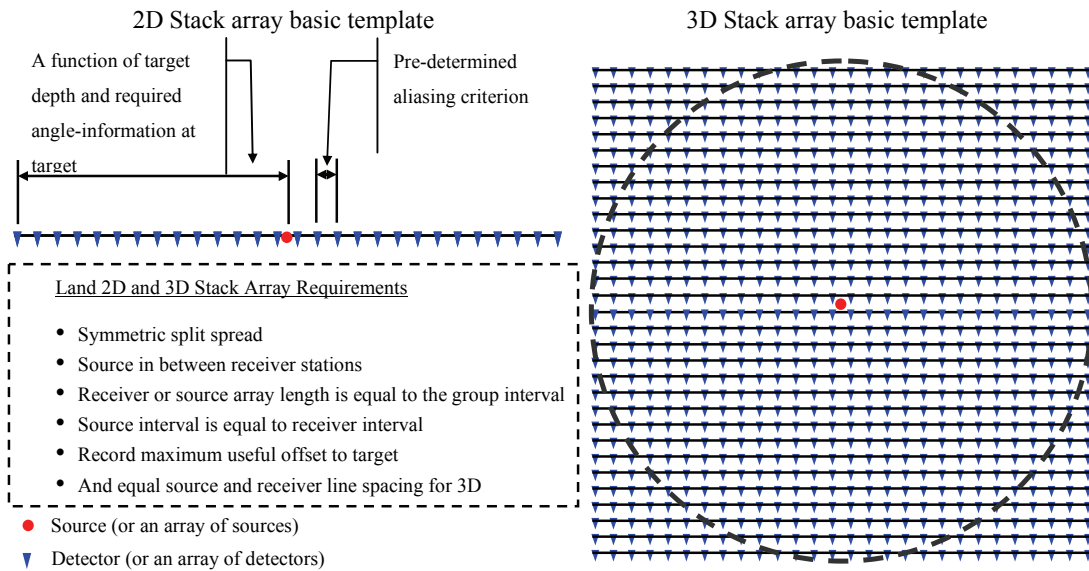


**Fig. 1.2** 2D and 3D stack array guidelines and basic template.

Implicit methods, i.e. those that do not rely on explicit forward modeling and processing of seismic data, exist that allow predicting pre-stack imaging results for a given acquisition geometry and subsurface model. Beylkin (1985) introduced a method to calculate the spatial resolution of a point diffractor at the target by a Fourier transformation of the wavenumbers

at the target as sampled by the acquisition geometry for homogeneous subsurface. Vermeer (2002) used Beylkin's method to calculate the spatial resolution of different 3D geometry building blocks. Beylkin's method was extended to an arbitrary subsurface model using ray-tracing to determine the wavenumbers at the target point by Gibson and Tzimeas (2002), Gelius et al., (2002) and Lecomte (2006). Wave-equation propagators can also be used with this method (Toxopeus et al., 2003). Beylkin's method *combines* the sources and detectors of a particular geometry. This is principally different from the focal beam approach introduced by Berkhout et al. (2001), Volker et al. (2001), and Volker (2002). The focal beam approach calculates the resolution of a point diffractor and the angle-versus-rayparameter (AVP) information at the target. This concept can accommodate ray-tracing as well as wave-equation modeling. It provides insight into the quality of each of the two seismic survey components namely: source and detector; of course while taking the subsurface into consideration. This assists in determining which geometry needs updating. Furthermore, the focal beam method does not rely on explicit forward modeling of seismic data. Van Veldhuizen (2006) illustrated the importance of including the inhomogeneous subsurface using wave-equation based propagators for calculating the focal beams. Her conclusions were that most marine acquisition geometries in practice lead to poor azimuthal information at the target.

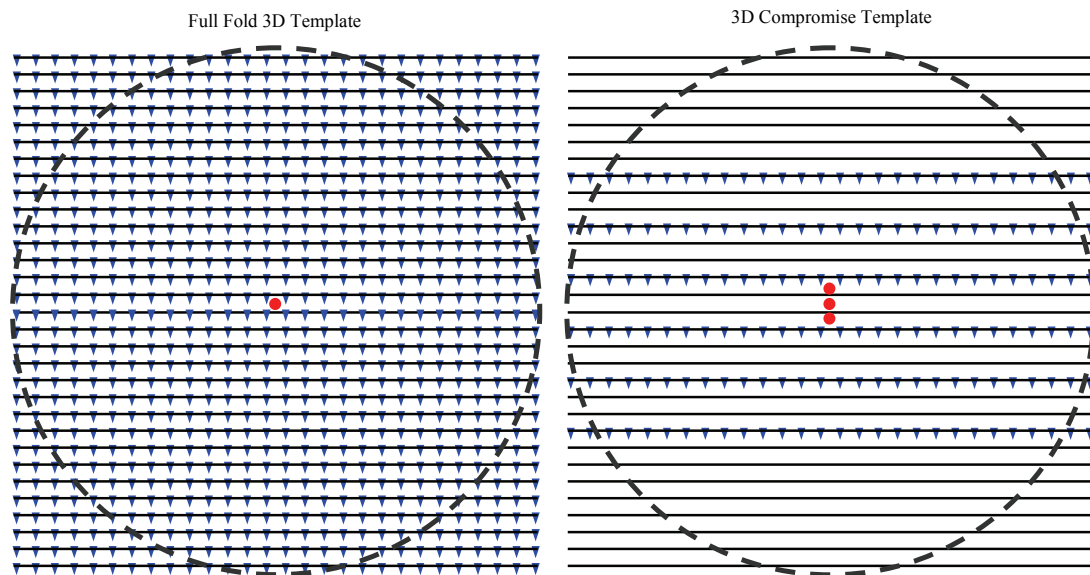


**Fig. 1.3** Selection of Compromise 3D basic design template.

This research extends the model-based survey design to the case of land data with a complex near-surface. The method of focal beams along with wave-equation based propagators will be used. The complex near-surface imposes many technical and operational constraints on

the survey design. Previous model-based survey design approaches take into account the signal requirements with little attention paid to the noise. This research will consider signal (distorted by the near-surface) as well as noise (generated in the near-surface).

#### 1.4 Land survey design as an integrated approach

Survey design should be an integrated process that relates acquisition, processing and characterization in a cyclic manner as conceptualized by the seismic value chain (SVC) Figure 1.4 (Berkhout, 2005). The SVC is not a one-way chain of sequential commands but has double paths, feedforward and feedbackward that connect the three principal nodes of the seismic method. This means that improvements at one node may not necessarily result in improvements in the second or the third node. But, developments at a particular node may open opportunities at the other nodes. In addition, the SVC should be a guiding concept throughout the life of a field which should develop as more knowledge of the problem becomes available from direct well measurements or indirect estimates from seismic data. Thus, seismic surveys at different times ( $t = T_1, T_2, \dots$ ) become more focused on revealing further information and on overcoming challenges.

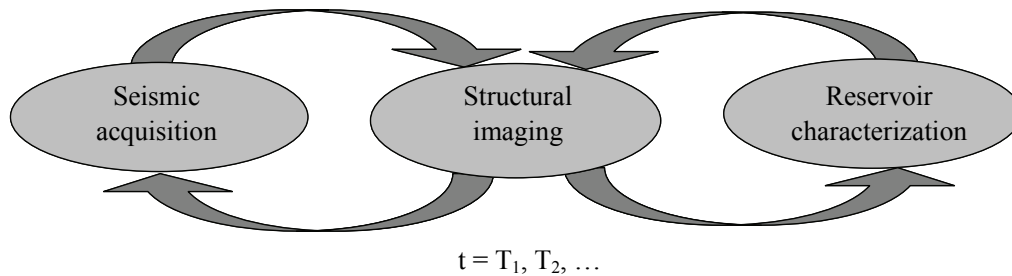
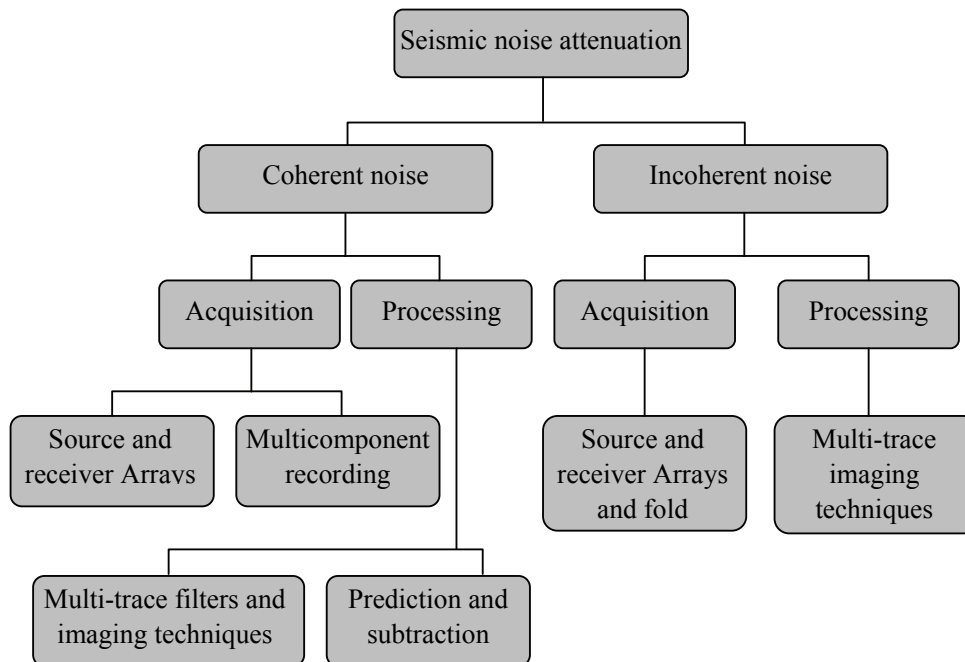


*Fig. 1.4 Cyclic interaction in the seismic value chain (Berkhout, 2005).*

The concept of the SVC will be utilized in the survey design approach outlined in this thesis. The best survey design parameters will be those that strike a balance between what can be done in acquisition on the one hand and processing on the other, to meet what is required by characterization. Depending on the prevailing needs of a particular project and the required fidelity, coherent and incoherent noise attenuation will be managed by splitting this task between acquisition and processing. Figure 1.5 shows a classification of how noise of different natures can be managed at the first two nodes of the SVC. If noise can be effectively attenuated at the acquisition phase without sacrificing the signal content, then most of the emphasis on attenuation should be put at this phase. Otherwise, the survey design

should focus on providing sufficiently sampled data to the processing so that effective noise attenuation can be performed in that stage.

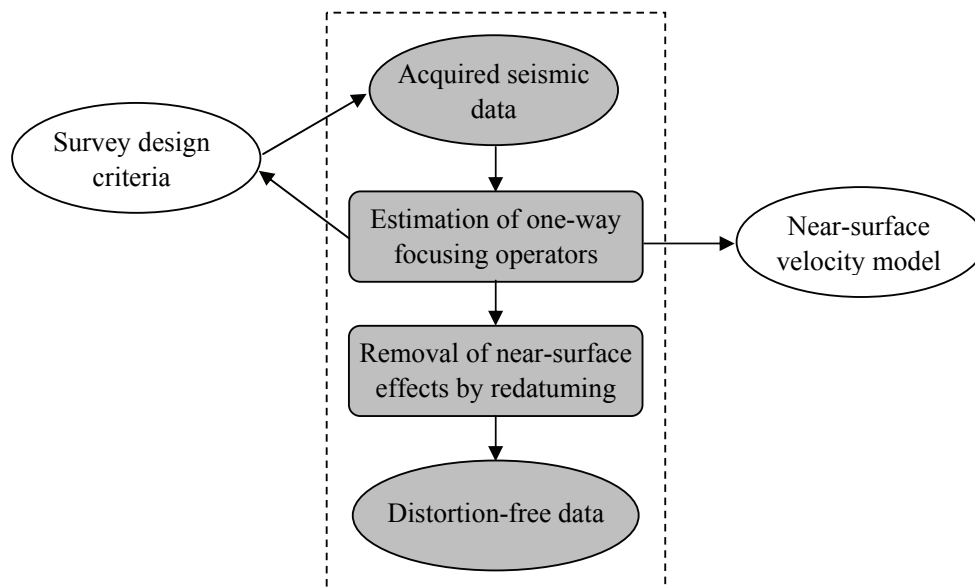
On the other hand, the distortions occurring to the body waves while passing through the complex near-surface have to be dealt with at the processing phase. The solution technique should consider the distortions as an imaging problem rather than as time-shifts or statics. In 1987, the Near Surface Effects Workshop, sponsored by the SEG's Research Committee, was held in Hyannis, Massachusetts. An interesting statement was made at this workshop by Chuck Edwards regarding the statics. "It has always bothered me that statics was something we dreamed up to make our jobs easier," he said. "But the situation is not static; it is dynamic, I think this is being accepted throughout the profession and the time will come when we do not do statics at all," (Clark 1987). It is now about twenty years later, and we are still trying to resolve the near-surface effects while carrying the dynamic nature of the problem. Most of the attempts to solve the near-surface problem in a dynamic solution were focused on estimating the near-surface model. This may not be the right direction to go.



**Fig. 1.5** Classification of noise attenuation methods in acquisition and processing.

The method of removing signal distortions, as proposed in this thesis, is based on redatuming (Berryhill, 1979). It uses one-way focusing operators (Berkhout, 1997) being estimated

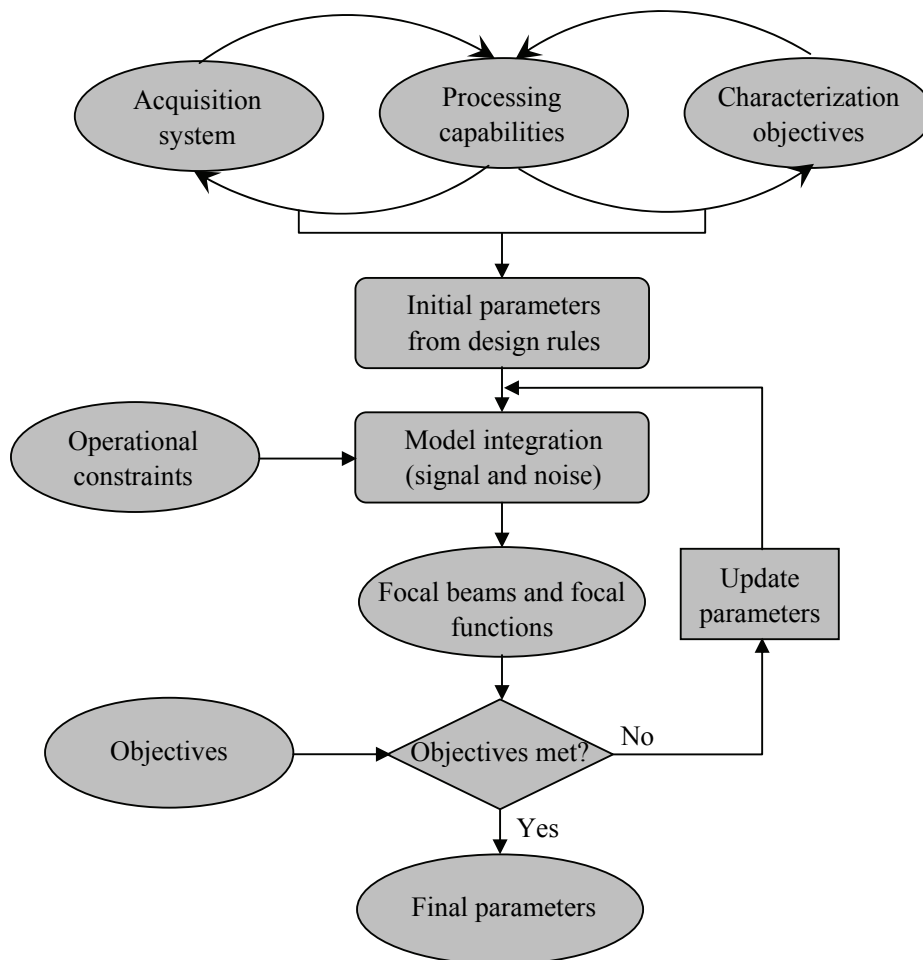
without knowledge of the underlying macro-model. This velocity-independent method is investigated for the 2D case using adequately sampled common source or adequately sampled common receiver gathers. However, extension to the 3D case requires either adequately sampled 3D common source or receiver gathers. This geometry is rarely available in standard 3D acquisition. To circumvent this limitation, this thesis will introduce the estimation of the one-way focusing operators using cross-spreads. The acquired seismic data must permit estimating the focusing operators, yielding a criterion imposed on the survey design process. The pre-processing flow of this approach is depicted in Figure 1.6. In this thesis, velocity-independent redatuming through the complex near-surface will be described in detail. The proposed theory will be supported by synthetic and real data examples for both the 2D and 3D cases.



**Fig. 1.6** Processing flow of removing the complex near-surface effects on body waves by redatuming. Note that the ability to estimate the one-way focusing operators from the acquired data is part of the design criteria. Therefore, it has to be taken into account during the design phase.

To summarize, the integrated model-based survey design process proposed here, is exhibited by Figure 1.7. Acquisition and processing capabilities and the characterization objectives are considered in a cyclic way (SVC) to estimate initial acquisition parameters. The survey design process comprising these parameters is integrated with a subsurface model to predict quantitative pre-stack imaging results using the focal beams. These results include two focal

functions: the resolution function and the AVP-imprint function (Berkhout et al., 2001). It should be noted that these results are target point oriented i.e. they are determined per selected target point. Furthermore, amplitude variations (acquisition footprint) at different target locations can be obtained from the pertaining AVP-imprint functions. Note that the geometry constraints such as obstacles can be incorporated. Furthermore, variable source and receiver coupling and mis-positioning can also be included in the focal beam computation.



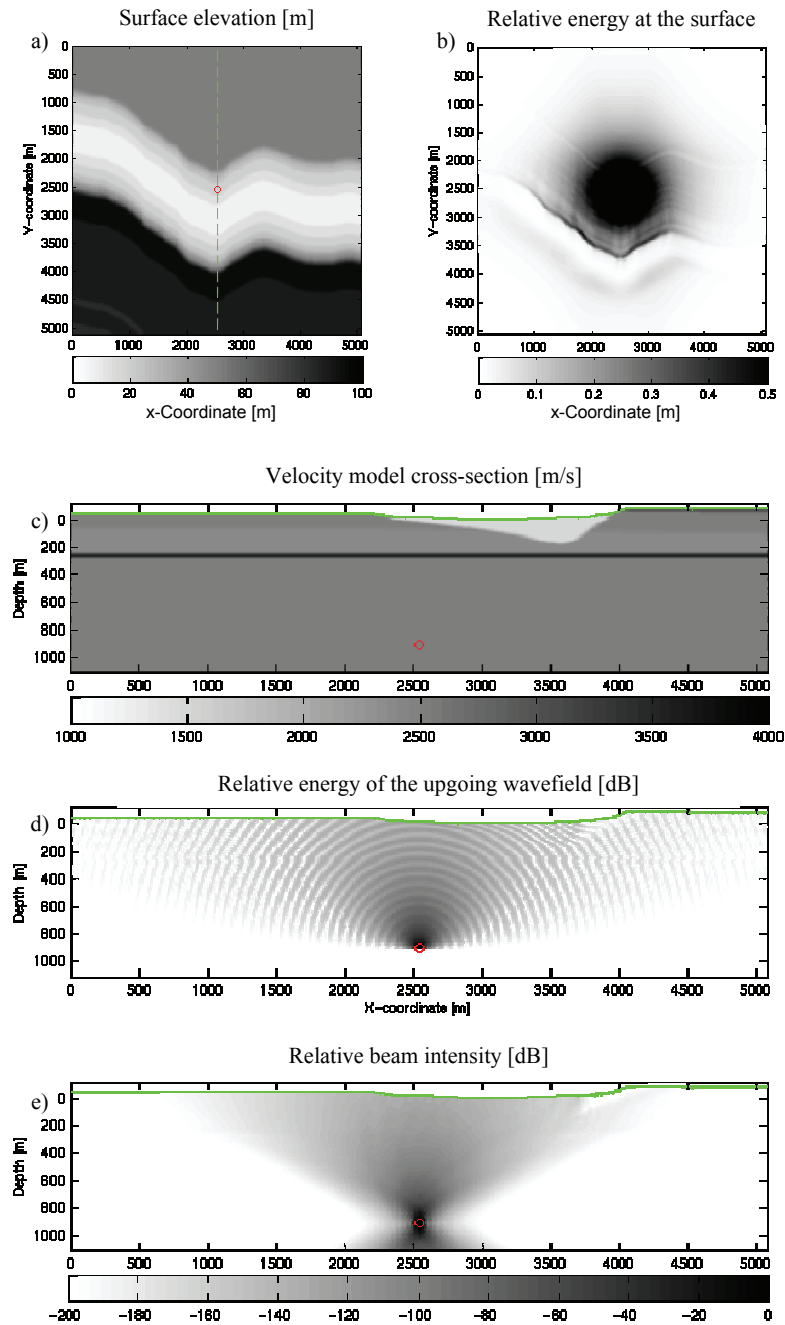
**Fig. 1.7** The process of survey design as an integrated approach. Note that the acquisition system includes instrumentation and geometry.

Figure 1.8 exhibits important properties of a typical land subsurface model and the behaviour of body waves in this model. Figure 1.8a shows the surface topography variation map exhibiting a valley-platue situation. The wavefield energy observed on the surface is shown in Figure 1.8b. This wavefield is originating from a point diffractor located in the center of the model at depth of 1000 m below the surface. A cross-section through the velocity model is shown in Figure 1.8c with a complex near-surface and a simple subsurface. It is clear from Figure 1.8b how the complex near-surface affects the energy distribution on the surface. Figure 1.8d shows a cross-section of the snap shot volume, clearly marking the distortions occurring to the body waves as they approach the complex near-surface. A focal beam can be generated by performing an inverse recursive depth extrapolation of the point diffractor response, being measured at the surface. Next, energy is calculated at each depth level as a function of spatial coordinates. Figure 1.8e presents a cross-section of the beam volume, showing how the energy is focused back to its origin. The sharpness of this focus point is greatly dependent on how we sample the wavefield on the surface and how accurately we can estimate the underlying velocity model from the acquired data. Of course, the sparser the surface sampling and the less accurate the underlying model, the poorer the focusing will be. The focal beams and the focal functions will be discussed thoroughly in the subsequent chapters and demonstrated with examples.

## 1.5 Thesis objectives

The primary objective of this thesis is to establish an integrated approach for improving land seismic images in areas characterized by a complex near-surface. This is one of the most challenging problems that have not been solved yet. The integration should include interaction between acquisition, processing, and characterization with the properties of the underlying subsurface model. This thesis will focus on the following goals:

- 1 Establish general land survey design rules that are compatible with the current advances in seismic data processing and characterization, and inline with our acquisition capabilities and limitations.
- 2 Incorporate the complex near-surface effects into the focal beam and focal function calculations. In addition, use the focal beams to investigate the ability of retrieving the underlying macro velocity model from the focusing operators.
- 3 Include surface waves and scattered surface waves in the design process.
- 4 Extend the model-independent estimation of one-way focusing operators method to work with cross-spreads, the basic building block of the preferred orthogonal geometry on land.



**Fig. 1.8** a) Surface topography variation, b) relative energy of wavefield originating from a point diffractor at depth of 1000 m below the surface in the center of the model (red circle) as observed on the surface, c) cross-section through the velocity model along the green-dotted line of (a), d) cross-section of subsegment snapshots of the wavefield, and e) cross-section through the beam volume. Note that scale for c, d, and e is the same. The green line in c, d, and e marks the surface topography along this cross-section.

## 1.6 Thesis outline

This thesis adds the following techniques to the existing toolbox:

- provides an integrated scheme for acquisition design and preprocessing;
- extends the focal beam concept for the complex near-surface, including signal and noise;
- extracts different design metric attributes from the focal beams;
- adds the concept of assessing the ability to retrieve the velocity model from the focal beams;
- solves the problem of estimating 3D focusing operators for sparse land geometries by using properly sampled cross-spreads as geometrical building blocks;
- introduces an approach for directly estimating the focusing operators in one-step from tracked two-way reflection times.

**Chapter 2** describes the 2D and 3D data matrices and how they can be formed using the basic building blocks of standard 3D geometries. Next, general land 3D survey design rules are presented. In addition, alias free spatial sampling requirements and source and receiver arrays are discussed.

**Chapter 3** describes the theory of imaging by double focusing (Berkhout, 1980), showing how to compute focal beams and focal functions at a target point. The focal beams and focal functions will be extended to accommodate coherent and incoherent noise. Besides, the focal beam concept is developed to validate the ability of retrieving the underlying model the focusing operators.

**Chapter 4** discusses the computational aspects of focal beams. Different examples to demonstrate the use the focal beams method for design optimization are presented. These examples include signal and noise. Furthermore, examples of using the focal beams to validate the ability of estimating the underlying macro-model from the acquired data are presented.

**Chapter 5** describes the operator-based (i.e. velocity independent) approach for removing distortion effects of the complex near-surface by redatuming. The latter is performed using one-way focusing operators estimated directly from the data. The problem of coarse sampling in the land 3D case is solved by extending the operator estimation technique that uses properly sampled common source or common receiver gathers to properly sampled cross-spreads. Synthetic and real data examples are shown.

**Chapter 6** introduces a method for calculating one-way-time (OWT) focusing operators from tracked two-way-time (TWT) data. Advantages are discussed. This method is demonstrated on synthetic and field data.

**Chapter 7** contains conclusions and recommendations of this research.

---

**Appendix A** describes the physical meaning of focal beams, and **Appendix B** presents a case study that compares TWT-and OWT-tomography.



## 3D land acquisition geometries

*This chapter starts with an overview of how seismic data can be arranged in matrices that can be used to facilitate subsequent data processes. The 3D data matrix includes submatrices, where each submatrix is considered to be a building block of the entire 3D data. Furthermore, initial land 3D survey design rules are introduced similar to the known stack-array and symmetric-sampling approaches. These initial design rules should be carried out before introducing the interaction between the subsurface model and the design process. The proposed rules advocate that the best design building block for economical land geometries is the cross-spread, being suitable for source generated noise attenuation and pre-stack imaging. We elaborate on spatial sampling particularly with respect to the source and receiver arrays. Furthermore, we discuss the characteristics of source generated noise within the realm of the proposed design rules.*

### 2.1 3D data matrix

Berkhout (1985) shows that any configuration of seismic surface measurements (2D and 3D) can be arranged in the so called data matrix. In the forward space, this data matrix is a result of multiplying five complex-valued matrices in space per monochromatic seismic experiment (i.e. single frequency sources) as formulated by the so called **WRW** model (Berkhout, 1980). This model will be summarized in Chapter 3. In the 2D case (Figure 2.1) the rows and the columns of the data matrix show common receiver and source gathers, respectively. Figure 2.1 represents a typical moving-spread acquisition. As an extension of this representation to 3D, the data matrix will consist of a matrix that contains submatrices. In Berkhout (1997) and Volker (2002) the submatrices have the sources and receivers  $x$  coordinates varying in the inner rows and columns, respectively. The  $y$  coordinates of the sources and receivers vary in the outer rows and columns of the complete matrix (Figure 2.2). In this representation, the data matrix will generally have many empty positions because of sparse sampling and limited aperture. Berkhout (2006) presented different representations of the 3D data matrix for line geometries including parallel and orthogonal. He shows that these different presentations determine the integration order in mathematical operations (first in  $x$  then in  $y$ , or the other way around). Note that these representations are compatible with the mathematical formulations that will be presented in Chapter 3.

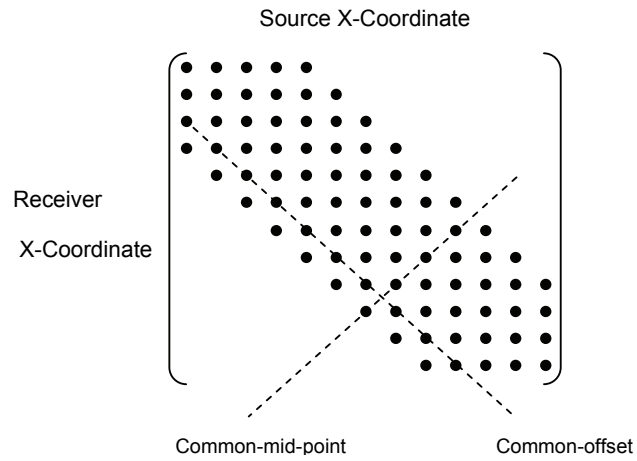


**Fig. 2.1** 2D data matrix where each dot represents a complex-value for monochromatic signals. Note that in time domain each dot represents a seismic trace.

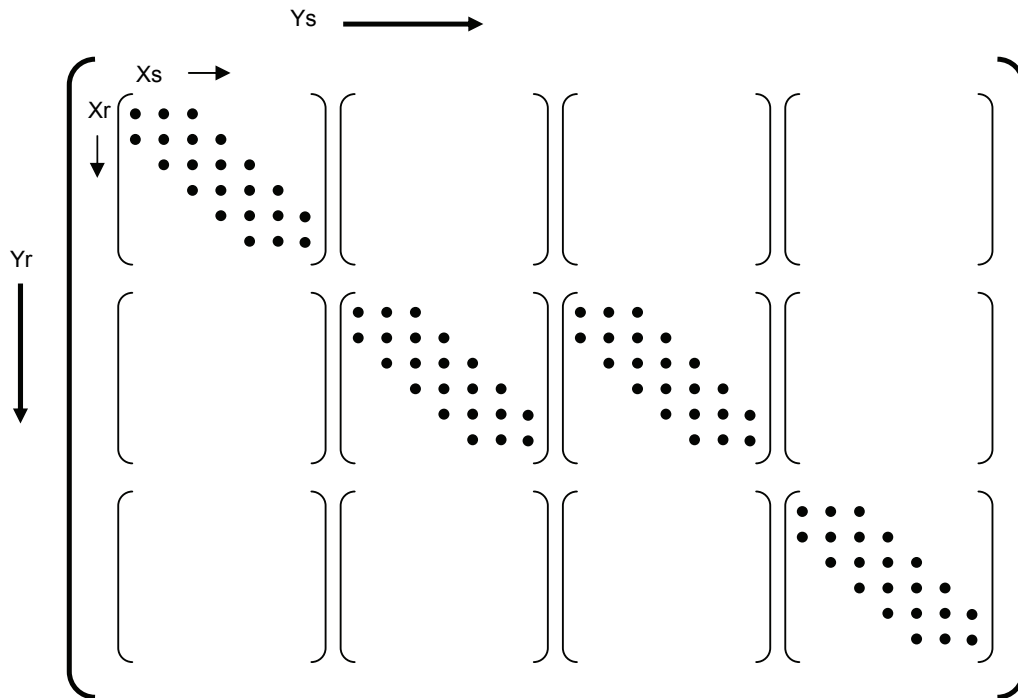


**Fig. 2.2** 3D data matrix Berkhout (1997),  $X_s$  refers to source x-coordinate,  $Y_s$  refers to source y-coordinate,  $X_r$  refers to receiver x-coordinate, and  $Y_r$  refers to receiver y-coordinate.

In this section the representation followed will have source and receiver stations and lines indices as shown in Figure 2.3. In other words, instead of having  $x$  and  $y$  coordinates, we will use station and line numbers in order to accommodate irregularities taking place in practice. This representation also accommodates slanted and irregular line geometries. Figure 2.4 shows the spatial distributions of sources and receivers represented in the submatrices. Obviously, each submatrix represents common source and common receiver lines. For regularly sampled parallel geometries the representation of Figure 2.3 is the same as given in Berkhout (1997) and Volker (2002).

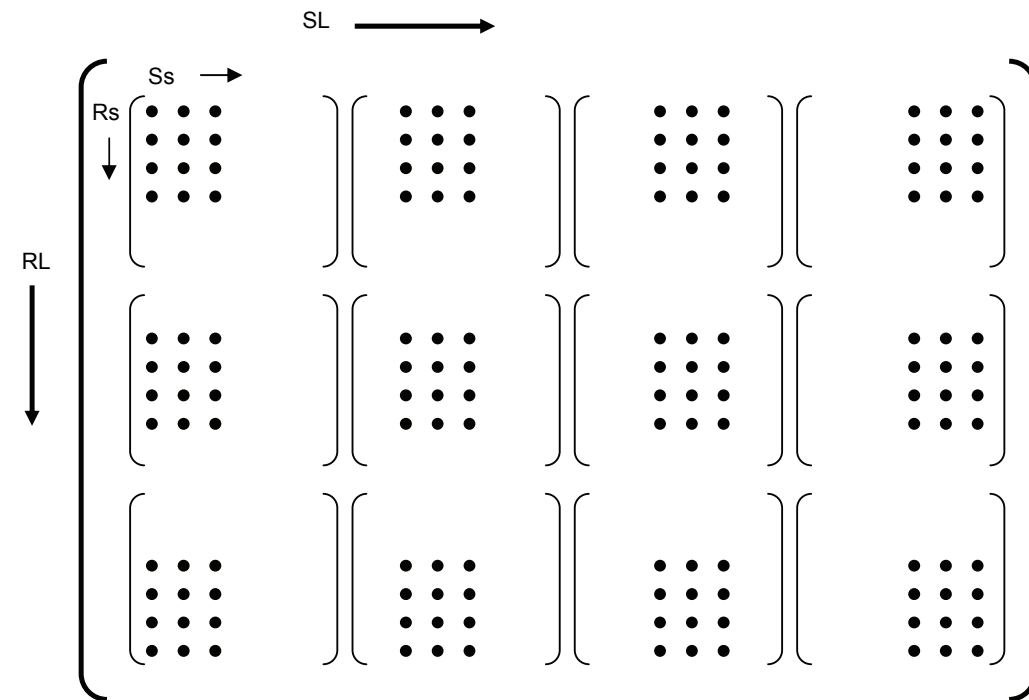


**Fig. 2.3** 3D data matrix, *Ss* refers to source station, *SL* refers to source line, *Rs* refers to receiver station, and *RL* refers to receiver line.

For orthogonal geometries each submatrix represents cross-spreads (single fold) while for parallel geometries each submatrix represents a common-mid-point (CMP) line i.e. multiple fold. Therefore, the latter does not have 2D spatial extent as the submatrix obtained from the crossed-array geometries. The submatrices constructed for the slanted geometries have 2D spatial extent, depending on the angle between the source and receiver lines. It should be noted that for zigzag geometries two 3D matrices have to be constructed. A final note for the new representation is that the exact spatial coordinates are assumed to be stored in a separate matrix or, more practically, in the seismic trace headers.

In summary, there are different representations of the 3D data matrix. Both the representations of Figure 2.2 and 2.3 are suitable for direct formulation of statistical and wave-theory numerical implementations in seismic processing. However, for land geometries, the representation of Figure 2.3 is more suitable for noise attenuation and estimating focusing operators as will be discussed in section 2.2 and Chapter 5 respectively.

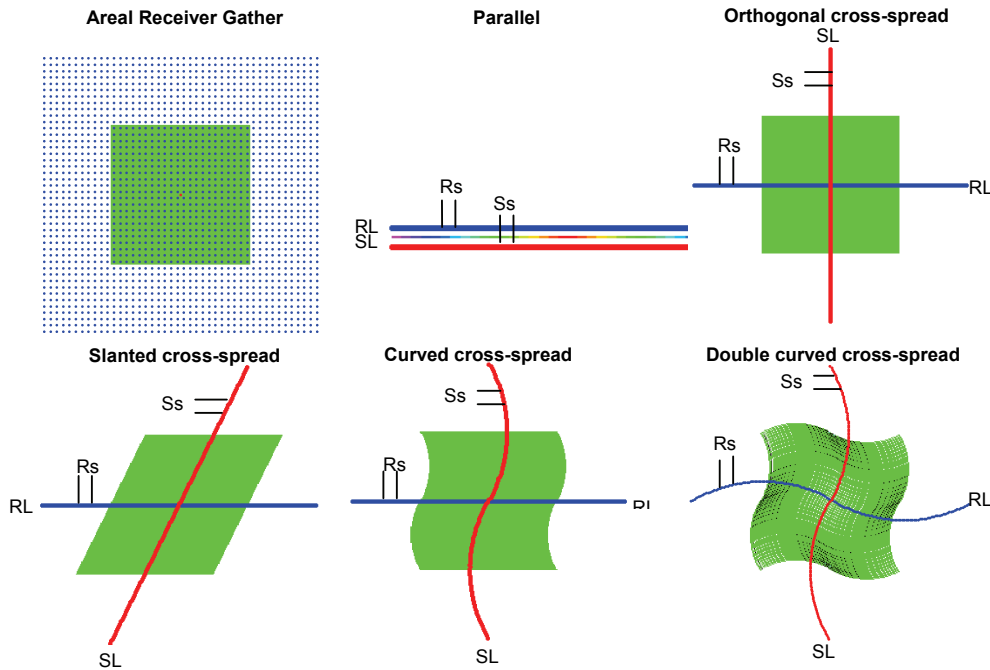


**Fig. 2.4** Spatial geometry layout in submatrices,  $S_s$  refers to source station,  $SL$  refers to source line (red),  $R_s$  refers to receiver station, and  $RL$  refers to receiver line (blue). The green color back ground indicates the CMP area and unit fold while the variable colors in the parallel case indicates variable CMP fold.

## 2.2 Basic 3D geometry building blocks

Seismic data, 2D and 3D, can be sorted into different subsets. These subsets can be seen as the building blocks of the acquisition geometry. Each data sort or subset is suitable for performing certain processing depending on how well the wavefield is sampled by the subset. Various authors have considered basic building blocks in their respective works, e.g. Bleistein (1987) and Schleicher et al. (1993). Yet, the first explicit elaboration of this matter was introduced by Padhi and Holley (1997). They introduced the terminology of minimal data sets (MDSs) and their general application for imaging. They define an MDS as ‘a

single-fold data set that can be used by DMO (or migration) to effectively image a reflector'. For example, 2D and 3D common source and receiver gathers are minimal data sets. For 3D imaging, MDSs require sampling of two crossed-space coordinates out of the four geometry space coordinates. Although 3D source and receiver gathers are rarely acquired, other MDSs can be constructed from commonly used 3D survey geometries. These MDSs include cross-spreads for orthogonal geometries (land type) and common-offset-azimuth (COA) gathers for parallel geometries (marine type).

An extensive discussion of MDSs for various geometries and their construction and applications for imaging and other processes is presented in Vermeer (2002). In analogy to the 2D common-offset gather, some authors provide guidelines for constructing approximate COA gathers for 3D. This is because most of marine and land 3D geometries do not allow construction of true COA gathers that extend over the entire survey area. For more details regarding this topic see Cary (1999), Vermeer (2002), and Gesbert (2002).

MDSs can be classified into two categories. One is the MDS that extends over a limited part of the survey area i.e. common source and receiver gathers, and cross-spreads. The second category is the MDS that extends over the entire survey, including true common-offset gathers or any approximations to them. The limited spatial extent of MDS of the first category causes edge effects in imaging. Although these effects exist in the image per single MDS but not in the final image, they degrade the quality of the underlying subsurface model that can be estimated from the data if not treated properly. This limitation is the driving force for the wide-spread use of MDSs of the second category. This is motivated by the extensive development of 2D model-driven common-offset Kirchhoff type imaging which can directly be extended to 3D. In this case, macro-model updates can be performed on the basis of time depth residuals observed after migrating a range of MDSs of the second category. Note that in the case of a stationary geometry, meaning that the wavefields of all sources are recorded by the same detectors, MDSs of the first category are better suited for imaging because in that case they have greater spatial extent than those of the second category. This is particularly true in medical imaging where a fixed array of detectors is used.

In true wave-theory based imaging, only MDSs of the first category can be used because they represent physical seismic experiments. These MDSs are also required for data-driven (operator-based) imaging techniques such as the common-focus-point (CFP). On land, the only MDS that can be generated from most practical geometries is the cross-spread. The idea of using the cross-spread as an ideal MDS for land was discussed by Vermeer (1994). Cross-spreads are the basic building blocks of orthogonal geometries, which does not mean that they have to be acquired in the field as such. All the templates shown in Figure 2.5 allow forming cross-spreads. As mentioned earlier, the latter combine two finely sampled crossed-coordinates of the four geometry coordinates to form a single fold 3D subset. This subset, if sampled adequately, is suitable for performing alias-free imaging of the illuminated part of the target. It is also good for source generated noise attenuation in processing. Therefore, the cross-spread can be considered as the 3D subset that needs to be adequately sampled to meet the signal and noise requirements. Note that a cross-spread could be considered to be a

collection of common source or common receiver gathers, which explains why they are well suited for wave-equation based processing.

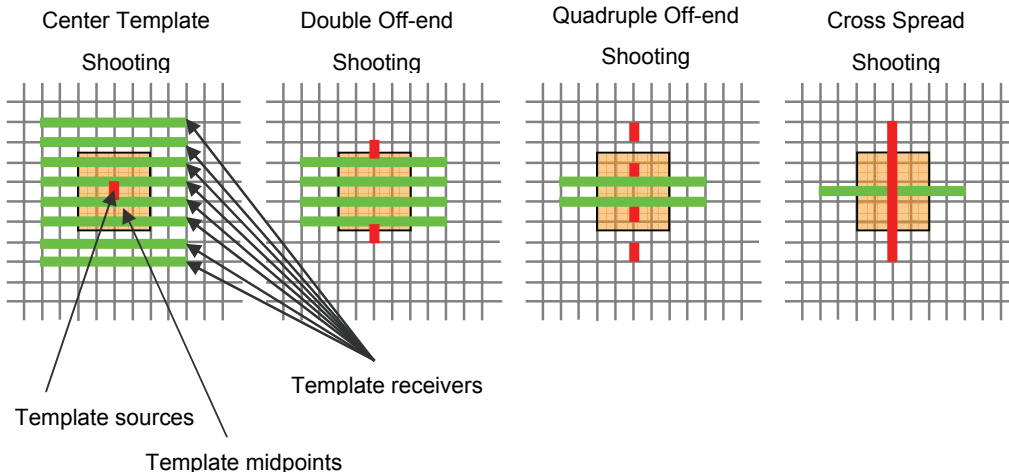


**Fig. 2.5** Equivalent orthogonal geometry templates. These templates can be organized into cross-spreads when one-receiver line is rolled at a time.

### 2.3 Initial 3D geometry design

The ultimate way of acquiring 3D seismic data is by equivalent sampling of all the four spatial coordinates while meeting pre-determined aliasing criteria, which leads to the full 3D geometry (uncommitted 3D survey design or the 3D stack-array). This approach produces redundant data that may not be required to meet the survey objectives. Besides, acquiring data in this way is currently very expensive and may be operationally not feasible. Therefore, data may be acquired by adequately sampling either the two source coordinates or the two receiver coordinates according to the pre-determined aliasing criterion while coarsely sampling the two other coordinates. This will lead into either adequately sampled common source or common receiver gathers, which will be suitable for pre-stack imaging and source generated noise attenuation, and thus, meet the target objectives. Although this approach can be considered as the second best after the full 3D sampling, it is not efficient for land acquisition because it creates an operational imbalance between source and receiver efforts.

Therefore, crossed-array geometries are preferred for land acquisition. They are operationally efficient because of the possible balance between source and receiver movements. In addition, these geometries permit constructing 3D single fold subsets which

represent cross-spreads. The data of these cross-spreads represent properly sampled submatrices in the data matrix. These submatrices are suitable for pre-stack imaging (Chapter 5) and source generated noise attenuation in processing (Section 2.5). Therefore, we advocate that the best compromise of the full 3D geometry for land is the crossed-array geometries with the best among them being the orthogonal with source lines perpendicular to the receiver lines. This leads us to our recommended design rules for initial land 3D survey design (Figure 2.6):

1. Start the design with a crossed-array geometry. This includes orthogonal and zigzag geometries, yet, the best choice would be the orthogonal geometry.
2. Sampling along the receiver and source lines (fine sampling within the 3D single fold subsets e.g. cross-spreads constructed from orthogonal geometries or slanted-spreads constructed from zigzag geometries) is based on anti-alias signal requirements while taking into account the effects of field arrays on high frequencies.
3. Receiver and source line intervals (coarse sampling) should be based on the minimum offset requirements of the shallowest reflector and the degree of complexity of the near-surface anomalies. Line intervals should be shorter than the anomalies. The minimum offset should allow for enough multiplicity of the shallowest reflector so that a high fidelity image can be obtained.
4. Maximum inline and cross-line offsets shall be determined by the maximum reflection angles required for the deepest target. For complex near-surface situations, the maximum inline and cross-line offsets should be equal at the datuming reflector below the complex near-surface (hanging horizon).
5. The minimum trace density or fold will be a result of the above criteria. Higher fold, if desired, should be obtained only by reducing source or receiver lines intervals or both.
6. The field execution method shall be determined based on operational efficiency and the available equipment.

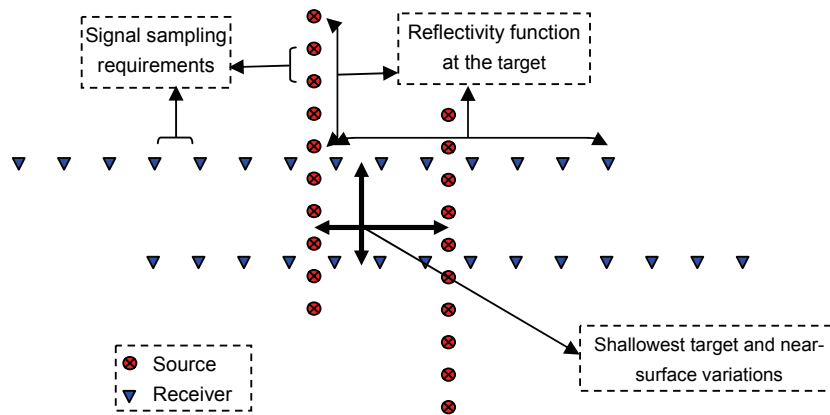


**Fig. 2.6** Schematic diagram showing the relation between the survey design parameters as proposed by the design rules.

Note that for increasing fold in rule number 5 we recommended that this should be obtained by decreasing source or receiver lines intervals or both. Of course, fold can also be increased by increasing the maximum offsets. Yet, this option is not preferred because a good design should propose the right maximum offsets as per rule number 4.

Our guidelines for the initial design are similar to the symmetric-sampling approach for orthogonal geometries (Vermeer, 2002), but they differ in two ways. First, we do not necessitate equal common source and common receiver gathers (squared cross-spreads). However, we necessitate squared cross-spreads at the datum reflector in case of complex near-surface. This will ensure proper redatuming below the complex near-surface if opted. In addition, it will allow estimating unbiased velocity models between the surface and the hanging horizon. Second, we explicitly relate the source and receiver line intervals to the near-surface complexity. This will be further discussed in Chapters 3 and 4.

## 2.4 Temporal and spatial sampling

The discussion of this section pertains primarily to the second rule of our initial survey design. In data acquisition seismic signals are discretized both in time and space. The discretization rates control the temporal and spatial bandwidths which in turn control the resolution (see Berkhout, 1984 for more details). The latter is also influenced by the discretization aperture. Bearing in mind that discrete signals have a periodic Fourier transform, it is important to minimize the overlap (aliasing) between frequencies or wave numbers located outside  $\pm 2\pi/2\Delta$  for signals sampled with a temporal or spatial interval  $\Delta$  Figure 2.7.

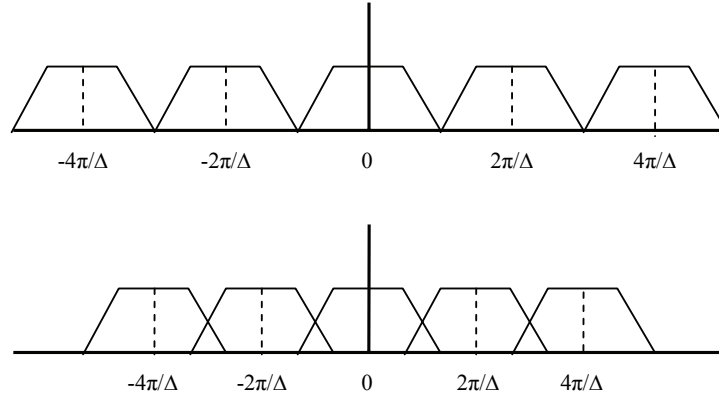


**Figure 2.7** Spectra of Fourier transform of discrete signals; a) sampling interval  $\Delta$  is well chosen for the available temporal or spatial bandwidth; and b) aliasing occurs indicating that  $\Delta$  is too large for the available bandwidth.

Temporal and spatial sampling criteria are similar. For signals with required maximum frequency  $f_{max}$ , the temporal sampling interval ( $\Delta t$ ) is given by:

$$f_{max} < \frac{1}{2\Delta t} = f_N, \quad 2.1$$

with  $f_N$  being the Nyquist frequency. Similarly, if  $k_{max}$  is the maximum wave number in the wavefield, the spatial sampling interval ( $\Delta x$ ) or the spacing between the detectors must be such that:

$$\Delta x < \frac{\pi}{k_{max}}. \quad 2.2$$

Given that  $k_{max} = \frac{2\pi f_{max}}{V_a}$  where  $V_a$  is the apparent velocity of the wave, then:

$$\Delta x < \frac{V_a}{2f_{max}} = \frac{V}{2f_{max} \sin \alpha}, \quad 2.3$$

where  $V$  is the velocity and  $\alpha$  is the angle of a plane wave with respect to the acquisition surface. Therefore, a stringent  $\Delta x$  would be calculated based on the minimum expected velocity ( $V$ ) and angle ( $\alpha$ ) of 90 degrees according to equation (2.3).

In a real land seismic shot record, apparent velocities range from the velocity of sound in air to infinity. Apart from air waves (airblast with a velocity of  $\sim 300$  m/s), low apparent velocities are always associated with surface waves which are considered to be noise, where high apparent velocities are associated with the signal including reflections and diffractions. Therefore, alias free sampling of both signal and noise is dictated by the minimum apparent velocity of surface waves and their maximum frequency assuming that air waves are reduced by sufficiently burying the detectors below the surface. However, alias free sampling would require very dense spatial sampling that may not be possible in most practical situations particularly for land 3D seismic data acquisition.

### 2.4.1 Source and receiver arrays

The elementary and traditional solution for defining sampling interval is based on signal properties. Coping with noise means resampling in the field by using source and receiver arrays rather than point sources and point receivers. Elaborate analysis of array design and performance is not intended in this thesis since it is widely covered in the literature. See for example Newman and Mahoney (1973) and Berni and Roeber (1989). Field arrays act as anti-alias filters by passing certain wavenumbers and rejecting others. High wavenumbers associated with the surface waves are rejected or reduced while low wavenumbers pertaining to the signal are passed depending on the array design.

The interaction between the array and the wavefield is best analyzed by computing the  $k$ - $f$  spectrum of the wavefield in a common source or a common receiver gather along with the array response as depicted in Figure 2.8. Here the  $k$ - $f$  spectrum schematically shows constant velocity lines where each point on any line represents a plane wave with temporal frequency  $f$  and spatial frequency  $k$  while the array response shows the reduction magnitude imposed by the array on these waves. The pass band of the array is bounded by the inverse of the spatial sampling interval i.e. in the wavenumber interval  $[-1/2\Delta x \ 1/2\Delta x]$ , where  $\Delta x$  is the effective length of the array. The fact that this passband is not flat imposes more constraints on the selection of  $\Delta x$ . The latter should be selected so that the signal is contained in the flatter part of this pass band. Care should also be taken when calculating  $\Delta x$  in the presence of high near-surface velocities which cause great ray bending of the signal in the far offsets which, in turn, lowers the apparent velocities of the signal as seen by the arrays. This causes attenuation of high frequencies of the signal.

All these arguments suggest that model-based analyses are important for optimizing the spatial sampling intervals since the interaction between signal, noise, arrays, and the subsurface model is not linear meaning that it can not be adequately predicted by equation (2.3). Yet, this equation acts as a starting point for selecting initial parameters for the optimization process. This will be further discussed in Chapters 3 and 4.

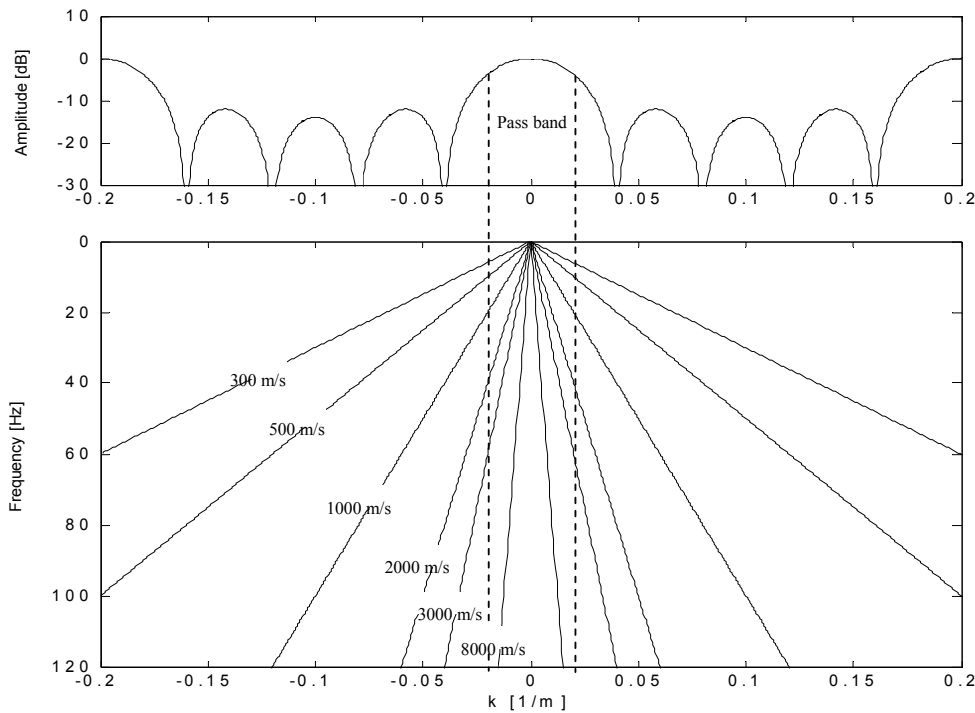


**Fig. 2.8** Schematic diagram of an  $k$ - $f$  spectrum (lower) and a five element array response calculated along the direction of its principle axis with an effective length of  $\Delta x=25$  m.

There are recent trends in the industry to move towards dense spatial sampling with results demonstrating great improvements (see for example Anderson et al. 2006). Single sensors are recorded which is advocated by Ongkiehong (1988). The dense spatial sampling is reduced in processing based on the signal sampling requirements after removing the noise. The problems with arrays as anti-alias filters or noise protection tools augment the philosophy of single sensor and single source recording. Intra-array statics, variable coupling, tilt, and positioning errors can be taken care of along with noise removal before array forming with any desired response in data processing. The effects of array problems are demonstrated by Blacchiere and Ongkiehong (2000). On land, single sensor recording seems to be feasible especially with the advent in the recording systems. During the 2006 SEG annual meeting in New Orleans, Sercel announced a system capable of recording up to one hundred thousand channels. However, there does not seem to be a clear vision around the source array since single vibrator recording, the preferred seismic source on land, causes too long survey turnaround times. Therefore, some of the advantages of single sensor recording are offset by the utilization of source arrays. There are some approaches to increase vibroseis acquisition productivity by simultaneous vibration in such a way that the signal of each involved vibrator can be separated to mimic single-vibrator recording. Paramount among these approaches is the high-fidelity-vibratory-system (HFVS) which can

be used with single-sensor recording (Krohn and Johnson, 2006). Yet, applicability and data quality uplift is still to be proven if such an approach is combined with single-sensor recording since each.

In single sensor recording, sensors are planted at a distance in the order of 5 meters which offers alias-free sampling of surface waves in most situations. On the other hand, conventional 3D spatial sampling intervals are in the order of 50-60 meters. Clearly, there is an order of magnitude reduction in spatial sampling in the case of single sensor recording. Vermeer (2004) suggests a spatial sampling in the range of 20-25 meters. This is demonstrated to be superior when compared with the conventional spatial sampling (i.e. 50-60 meters) as shown by Lansley (2004). The question is which way to go?

The simple answer for this is to compute the required spatial sampling based on the underlying model parameters including the near-surface and the deep subsurface based on equation (2.3). But, the answer to this question should take into account the big picture of the problem. Therefore, we need to consider the acquisition geometry design as a problem of two levels: macro and micro (Quigley, 2004). The macro level is the geometry type and the source and receiver spatial sampling intervals while the micro level lies in the details of source and receiver groups. Obviously, these two levels are dependent, but, attempt to improve should first focus on the macro level. For instance, if a choice has to be made between using the available resources to focus on resolving the array limitation issues or improving acquired data azimuthal distribution while using arrays, then the latter should be given a higher weight. Resolving the array deficiencies while keeping the 3D geometry sparseness, does not improve the final imaging results as would be achieved otherwise. Therefore, we believe that given a certain number of channels: the design should be optimized with respect to sampling, offset, and line spacing.

#### 2.4.2 A strategy for signal and noise spatial sampling

Alias-free sampling of all surface waves is not a necessary condition for noise free imaging. Surface waves can be sampled in such a way that the aliased part does not overlap with the wavenumbers associated with signal. This is referred to as the ‘adequate sampling’ by Baeten et al. (2000).

To put this in an equation form, assume that  $V_{mins}$  and  $V_{minn}$  are the minimum apparent velocities of respectively the signal and coherent noise. Also assume that  $f_{maxn}$  is the maximum frequency of noise. Then, the objective is to have the aliased wavenumbers of noise  $k_{aliasn}$  so that it does not overlap with signal maximum wavenumber  $k_{maxs}$  at  $f_{maxn}$  (Figure 2.9) such that:

$$k_{aliasn} - k_{maxs} > k_{maxn} - k_{aliasn} , \quad 2.4$$

where  $k_{maxn}$  is the maximum wavenumber of the noise, and  $k_{maxs}$  is defined as the signal wavenumber at  $f_{maxn}$ . Inequality 2.4 can be written as:

$$\frac{\pi}{\Delta x} - \frac{2\pi f_{maxn}}{V_{min s}} > \frac{2\pi f_{maxn}}{V_{min n}} - \frac{\pi}{\Delta x}, \quad 2.5$$

or

$$\Delta x < \frac{1}{\frac{f_{maxn}}{V_{min n}} + \frac{f_{maxn}}{V_{min s}}}. \quad 2.6$$

Inequality (2.6) is a sufficient condition for ensuring proper sampling of signal without being affected by the arrays. This means that arrays with effective dimensions equal to  $\Delta x$  can still be used to reduce the aliased noise at the acquisition phase. The arrays will also serve as quality assurance tools, because there is more than one detector feeding each channel; whereas if one or more fail, the rest will compensate. Then digital group forming with all its advantages including the possibility of solving intra-array statics and variable coupling can be pursued towards the signal required spatial sampling.

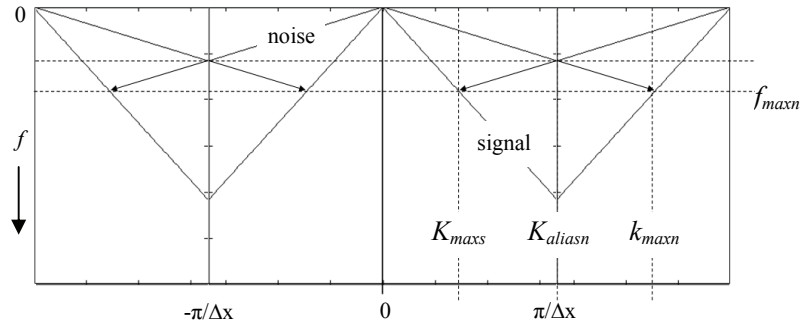


**Fig. 2.9** Schematic diagram of an  $k$ - $f$  spectrum the basis of inequality (2.6) which provides a criterion for sampling the signal in such a way that noise does not interfere with it even if noise is aliased.

## 2.5 Source generated noise

This section compares the geometry of source generated noise in both 3D common source or receiver gathers and in cross-spreads. Complexities in the onshore near-surface give rise to different modes of source generated noise due to waves that are trapped in the near-surface. These waves can be divided into two categories: radial Rayleigh waves (ground rolls that travel directly from sources to receivers) and scattered Rayleigh waves. Scattering of Rayleigh waves in the near-surface is one of the most difficult problems that have to be carefully taken into consideration during the design phase of a 3D survey. Scattering occurs because of near-surface heterogeneities such as escarpments or due to randomly distributed scatterers. Scattered Rayleigh waves have a great deal of effects on seismic imaging. Therefore, it is important to consider the near-surface complexities during the design phase of seismic data acquisition geometries. The required design is the one that aims at allowing high suppression of the source generated noise at the acquisition and processing phases.

Fully sampled common source or common receiver gathers are the best domain for attenuating source generated noise of both categories. Source generated noise, if adequately sampled, can be attenuated during processing using dip filters. This is due to the fact that both radial Rayleigh waves and scattered Rayleigh waves can be well separated from signal as they both map into their respective apparent velocities in the  $k_x, k_y, f$  domain. Figure 2.10a shows a common source geometry while Figure 2.10b shows a time slice of modelled radial Rayleigh waves assuming a homogeneous near-surface velocity model with Rayleigh wave velocity of 800 m/s and a frequency band of 5-40Hz. Figure 2.10d shows a frequency slice from the corresponding  $k_x, k_y, f$  volume. Three scatterers were distributed within the area of the common source gather as marked by the green circles in Figure 2.10a. Figure 2.10c shows a time slice of the modelled scattered Rayleigh waves. The modelling was performed in a non-interacting way (i.e. no interaction between the scatterers). The circular shapes are obtained because the scatterers act as new sources and get sampled in a similar way like the radial Rayleigh waves. This can easily be proven for a constant Rayleigh wave velocity. Figure 2.10e shows a frequency slice from the corresponding  $k_x, k_y, f$  volume. This clearly shows that scattered Rayleigh waves are mapped into the same wavenumbers as in the case of radial Rayleigh waves.

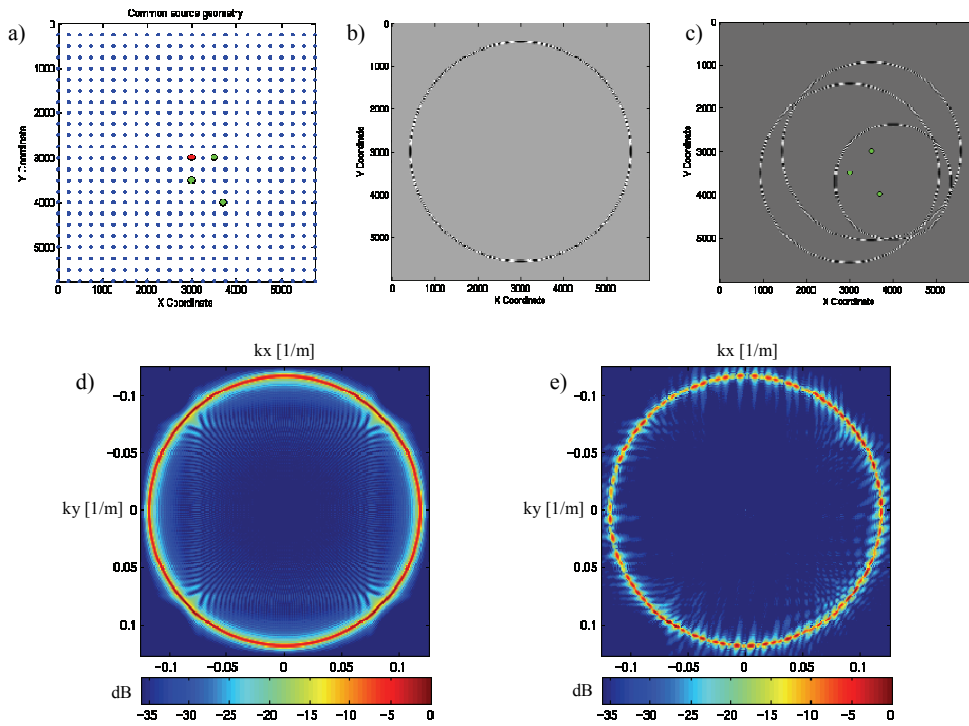


**Fig. 2.10** a) Common source geometry; b) A time slice from modelled Rayleigh waves using the common source geometry; c) a time slice from the modelled scattered Rayleigh waves using the common source geometry; d)  $k_x$ - $k_y$  slice at frequency of 15 Hz for Rayleigh waves; and e)  $k_x$ - $k_y$  slice at frequency of 15 Hz for the modelled scattered Rayleigh waves. The green dots in a and c indicate the locations of the scatterers.

Since fully sampled common source or common receiver gathers are rarely acquired in practice, because of either economical or operational constraints, the second best sampled 3D subsets are the cross-spreads. As mentioned before, cross-spreads combine the two finely sampled orthogonal coordinates in one 3D single fold subset. It leads to properly sampled submatrices of the data matrix. In the cross-spread domain, the radial Rayleigh waves can be attenuated at the processing phase using dip filters in a similar way as in the common source or common receiver gathers. This has been illustrated in the literature (see for example Meunier, 1999). Figure 2.11a shows the geometry of the cross-spread used to model radial Rayleigh waves. Figure 2.11b shows a time slice of the modelled radial Rayleigh waves. This slice is generated using similar parameters as in Figure 2.10b. Clearly, the radial Rayleigh waves have the same circular shape as in the case of the common 3D source gather. Note that the two shapes are the same only for constant near-surface velocity. Figure 2.11d shows  $k_x$ - $k_y$ - $f$  slice of the modelled cross-spread data indicating that 3D dip filters will effectively attenuate radial Rayleigh waves. Figure 2.11c shows a time slice of the modelled

scattered Rayleigh waves for the cross-spread while Figure 2.11e shows an  $k_x k_y$ - $f$  slice. It is clear that scattered Rayleigh waves are mapped almost to the entire  $k_x k_y$  region. This is because scattered Rayleigh waves have diffraction type travel times (hyperboloid in 3D) in the cross-spread domain, with their limbs having an apparent velocity equal to the velocity of Rayleigh waves. The limbs will separate in the  $k_x k_y$ - $f$  domain and can be attenuated by 3D dip filters. However, the flatter parts (apices) will not be attenuated because they have low apparent dips similar to the reflected signals. The flatter parts can adversely affect the signal particularly with the presence of high near surface velocities ( $> 1000$  m/s). Therefore, if not handled properly by areal arrays during the acquisition phase or by prediction and subtraction in the processing phase, they will leak into the final image.

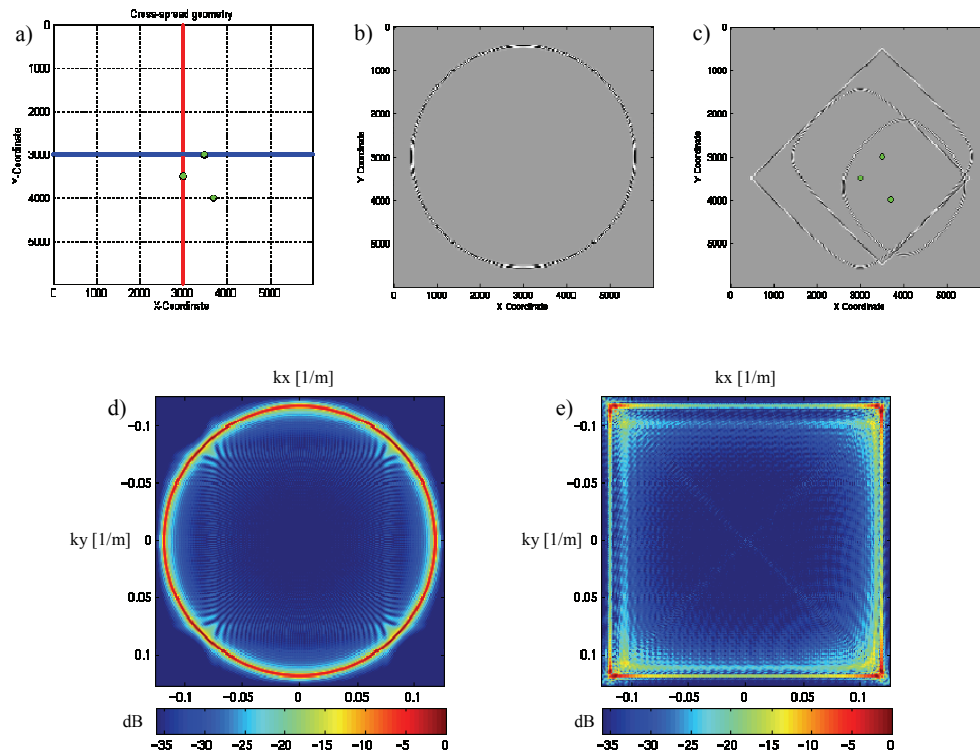


**Fig. 2.11** a) Cross-spread geometry; b) A time slice from modelled Rayleigh waves using cross-spread geometry; c) a time slice from the modelled scattered Rayleigh waves using the cross-spread geometry; d)  $k_x$ - $k_y$  slice at frequency of 15 Hz for Rayleigh waves; and e)  $k_x$ - $k_y$  slice at frequency of 15 Hz for the modelled scattered Rayleigh waves. The green dots in a and c indicate the locations of the scatterers.

---

Since we advocate that the signal and noise should be properly sampled in the cross-spread domain, then the flatter parts of the scattered Rayleigh waves can be dealt with as an imaging problem. We envisage a method of predicting such waves by an imaging process and then adaptively subtract them in a similar way as we deal with multiples.

## 2.6 Concluding remarks

We have defined in this chapter rules for the initial design of land 3D surveys. It shows great similarity with the stack-array and symmetric-sampling approaches. Large attention was paid to the spatial sampling. We advocated that the best geometries for land are the orthogonal geometries. This decision accounts for operational and technical requirements. Therefore, the cross-spread should be the most suitable building block as it is suitable for both pre-stack imaging and source generated noise attenuation. Using our sampling criteria, Radial Rayleigh waves can be well attenuated in the cross-spread domain using dip filters. The attenuation magnitude should be very similar to that achieved in the 3D common source gather if we assume constant near-surface Rayleigh wave velocities. However, scattered Rayleigh waves require well designed source and receiver arrays in the acquisition phase. An alternative is prediction followed by adaptive subtraction in the processing phase.

The initial design of the acquisition geometry is the starting point for a second design step, where specific information of the subsurface is included in the process. The theoretical framework of the subsurface model integration will be covered in Chapter 3. Computational aspects and various numerical examples will be presented in Chapter 4.



## Theory of model-based land geometry design

*This chapter presents a theoretical framework for integrating the acquisition geometry with the subsurface model. This integration is considered to be phase two of the survey design process described by this thesis.*

*First, the forward seismic experiment is formulated according to the WRW model. Then, the principles of structural imaging and reflectivity inversion are summarized and related to the concept of imaging by double focusing. Subsequently, focal beams are defined. These beams provide quantitative measures for the imaging capability of the two acquisition geometry components, being the sources and the receivers. The quantitative influence of the combined source-receiver geometry on structural imaging and reflectivity inversion is formulated based on the focal source and detector beams. Two focal functions, named resolution and AVP-imprint, are defined as two quantitative diagnostics to assess the suitability of a proposed acquisition geometry for imaging the subsurface under consideration. In addition, another diagnostic – called the DTS-gather – is derived from the focal beams. The DTS-gather indicates how well the velocity model can be retrieved from the acquired data. Since this research focuses on land acquisition aspects, special attention is given to the scattered surface-waves and ambient noise interference with the reflection signals. The focal functions are extended to take into consideration the different kinds of noise that may leak into the final image.*

### **3.1 Introduction**

The previous chapter presented general rules to define an initial acquisition geometry, being phase 1 of the design process. In the second phase the subsurface model is incorporated. The main objective of this design phase is to evaluate the interaction between the acquisition geometry and the subsurface model as an optimization process (see Figure 1.8). This evaluation is quantified by the quality of the imaging results. Obviously, it is important to know the limitations of the processing tools in order not to interpret processing deficiencies as being caused by the acquisition geometry. For instance, if the used imaging algorithm has dip limitation, then the final image will not contain information pertaining to high angles

even if they are contained in the acquired data. Hence, the interaction between the acquisition geometry and the processing algorithm is also included in this optimization process.

Therefore, it is important to establish an assessment methodology that can separate acquisition geometry effects on imaging results from other effects. The so called **WRW** model (Berkhout, 1980) is well suited for this task because the acquisition geometry is explicitly included in the forward model of the seismic experiment. The imaging technique (migration method) has to be fixed while evaluating different geometries. Similarly, we can evaluate the imaging techniques while keeping the acquisition geometry fixed. Furthermore, we can evaluate a preferred combination of acquisition geometry and imaging technique as well.

The concept of focal beams allows assessing the effects of an acquisition geometry on the image quality for a given subsurface macro-model, without going into explicit modelling of seismic data. This is achieved through the utilization of focal beams, and the focal functions resulting from them, according to the established theoretical framework by Berkhout et al. (2001) and Volker (2002).

### 3.2 The seismic experiment

The seismic experiment for reflections of different modes - including multiple scattering - can be described by the **WRW** model. In the subsequent formulations, the model will be limited to primary reflections. Besides, the formulations are expressed for the 2D situation; however, they can easily be extended to the 3D situation since the theory is general. A system representation of the entire monochromatic seismic experiment for multiple ( $M$ ) reflecting boundaries is expressed as:

$$\Delta \mathbf{P}(z_0, z_0) = \mathbf{D}(z_0) \sum_{m=1}^M \mathbf{W}(z_0, z_m) \mathbf{R}(z_m, z_m) \mathbf{W}(z_m, z_0) \mathbf{S}(z_0). \quad 3.1$$

In this discrete version of the **WRW** model, the matrix notation is used, where  $\Delta \mathbf{P}(z_0, z_0)$ <sup>1</sup> represents the pre-stack reflection data for all source positions at depth  $z=z_0$  and all receiver positions at depth  $z=z_0$  for one frequency component without multiple scattering. The capital delta sign ( $\Delta$ ) added to the symbol  $\mathbf{P}$  indicates that multiple reflections are not included. One column describes a monochromatic source gather and one row describes a monochromatic

---

<sup>1</sup> The symbol  $\mathbf{P}$  is not arbitrarily chosen. It means pressure for marine data and potential for land data assuming that decomposition has been applied to the multi-component velocity measurements.

receiver gather. Note that the earth is considered to be linear and time invariant, meaning that all operators refer to the same frequency component. In equation (3.1)  $\mathbf{S}(z_0)$  and  $\mathbf{D}(z_0)$  describe respectively the sources (including field arrays) and the detectors (including field arrays) at the acquisition surface  $z_0$ . In the case of point sources and point receivers (i.e. no arrays), they can be represented by scaled diagonal matrices, the scaling factor being the frequency dependent source signal and receiver instrument response respectively.  $\mathbf{W}(z_m, z_0)$  describes the downward wave propagation (by Green's functions) from the surface  $z_0$  to depth level  $z_m$ , while  $\mathbf{W}(z_0, z_m)$  describes the upward wave propagation from depth level  $z_m$  to the surface  $z_0$ . The transformation of the downgoing waves into upgoing waves is performed by the matrix  $\mathbf{R}(z_m, z_m)$ , which contains the angle-dependent reflection properties of the boundary. The recorded primary reflection data at the surface is contained in the data matrix  $\Delta\mathbf{P}(z_0, z_0)$ . According to equation (3.1), the seismic experiment is described by four spatial convolutions per frequency component. Figure 3.1 exhibits a schematic representation of equation (3.1) for one reflecting boundary, which is valid for stationary geometries where all source responses are detected by the same receivers. In the case of a moving spread, it is valid per stationary part. Note that according to equation (3.1) the only parameters that include traveltimes are the  $\mathbf{W}(z_m, z_0)$  and the  $\mathbf{W}(z_0, z_m)$ . This is the reason why we can perform subsurface imaging with seismic data as compared with potential methods (i.e. gravity and magnetic).

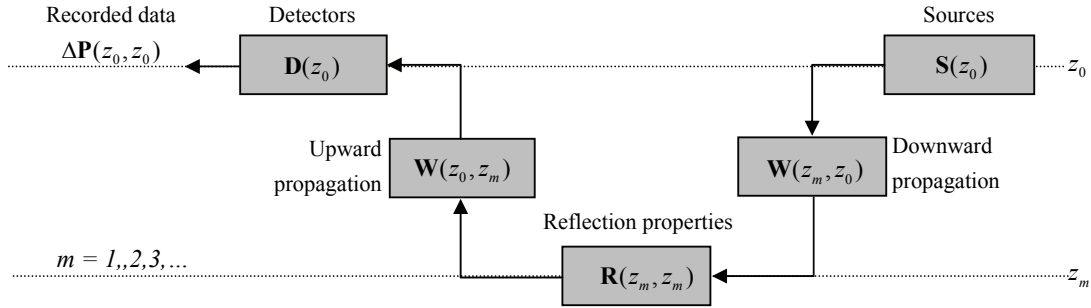


**Fig. 3.1** Schematic diagram of the forward seismic experiment for primary body waves. Note that  $W$ 's and  $R$  may include wave conversion i.e.  $P$ - $S$  or  $S$ - $P$ .

A seismic experiment for one source position can be written as:

$$\Delta\mathbf{P}_j(z_0, z_0) = \mathbf{D}(z_0) \sum_{m=1}^M \mathbf{W}(z_0, z_m) \mathbf{R}(z_m, z_m) \mathbf{W}_j(z_m, z_0) \mathbf{S}_j(z_0). \quad 3.2a$$

This equation represents a common source gather, being the  $j^{\text{th}}$  column of the data matrix  $\Delta\mathbf{P}(z_0, z_0)$ .

A common receiver gather can be written as:

$$\Delta\mathbf{P}_j^\dagger(z_0, z_0) = \mathbf{D}_j^\dagger(z_0) \sum_{m=1}^M \mathbf{W}_j^\dagger(z_0, z_m) \mathbf{R}(z_m, z_m) \mathbf{W}(z_m, z_0) \mathbf{S}(z_0). \quad 3.2b$$

This equation represents the  $j^{\text{th}}$  row of the data matrix  $\Delta\mathbf{P}(z_0, z_0)$ . Figure 3.2 exhibits a schematic representation of equations (3.1) and (3.2a,b) without field arrays and for one reflecting boundary.

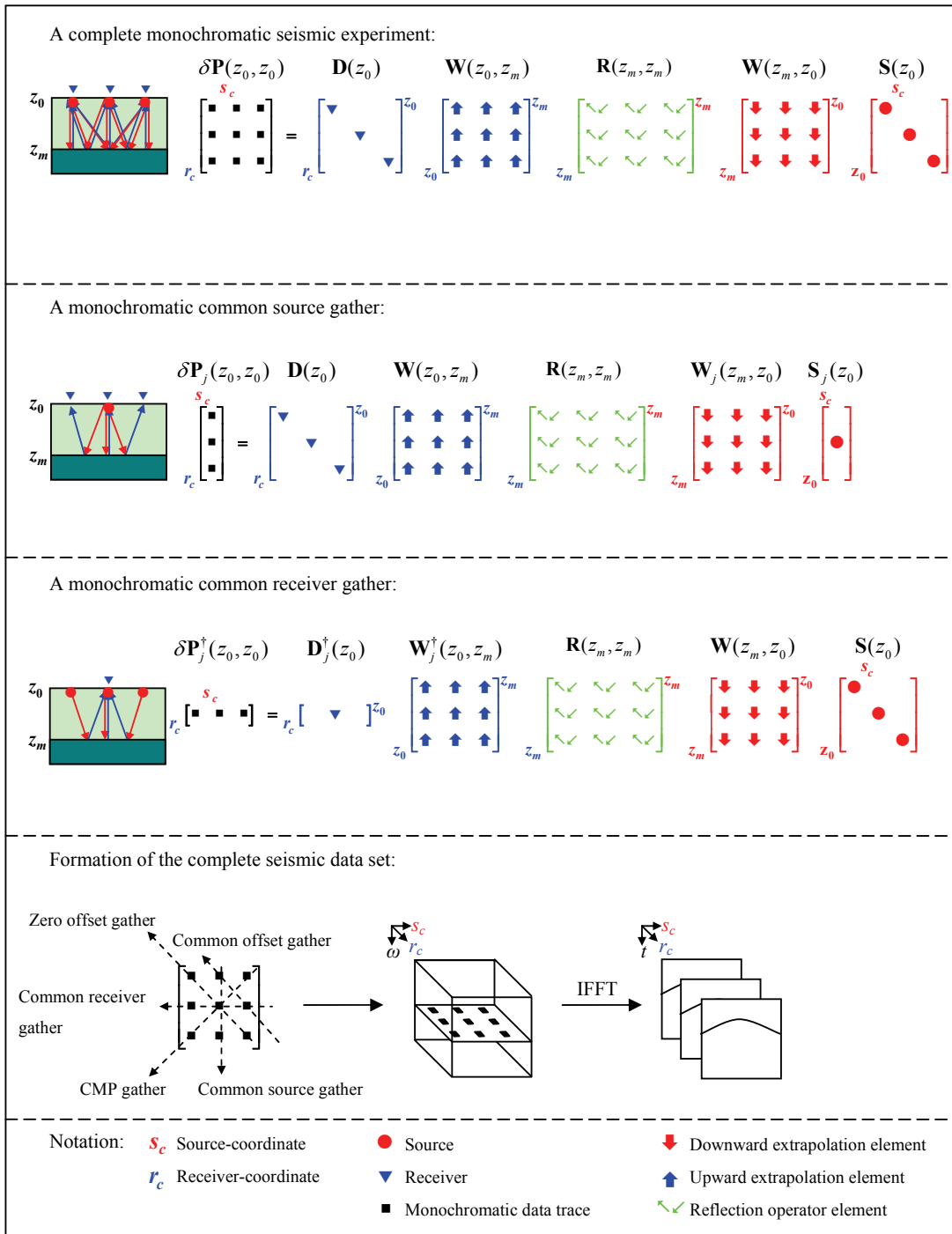


Fig. 3.2 Schematic representation of the *WRW* model for the stationary parts of a geometry. Note that IFFT means inverse fast Fourier transformation.

### 3.2.1 Notation convention

Throughout this thesis mathematical derivations will be represented by matrices and vectors. This is opted for because it is compatible with the temporal and spatial discretization process of the seismic wavefield in practice. In addition, it hides trivial mathematical procedures from the reader. The notation convention will be as follows:

- Matrices will be represented with capital bold abbreviations. For example,  $\Delta\mathbf{P}(z_0, z_0)$  represents primary reflection data with sources and detectors at  $z_0$ .
- Matrices, vectors, and elements are formulated per temporal frequency component  $\omega$ , but this symbol is omitted for convenience.
- The reference depth levels of a matrix or a vector are indicated between the parentheses that accompany the matrix. For instance,  $\mathbf{W}(z_0, z_m)$  describes the upward wave propagation from depth level  $z_m$  to the surface  $z_0$ .
- The seismic data are always indicated by the capital letter  $\mathbf{P}$ :
  - $\mathbf{P}(z_0, z_0)$  refers to reflection data and multiple scattering,
  - $\Delta\mathbf{P}(z_0, z_0)$  refers to reflection data for multiple boundaries,
  - $\delta\mathbf{P}(z_0, z_0)$  refers to reflection data from one boundary,
  - $\delta_j\mathbf{P}(z_0, z_0)$  refers to data for one point scatterer.
- A single letter subscript to a matrix indicates a column vector. For example,  $\mathbf{F}_j(z_0, z_m)$ . If the subscript letter is accompanied by the superscript dagger ( $\dagger$ ), then it indicates a row vector such as  $\mathbf{F}_j^\dagger(z_m, z_0)$ .
- A double letter subscript to a matrix indicates an element of a matrix. For example,  $\Delta\mathbf{P}_{jj}(z_m, z_m)$ .
- Letter superscripts are used to extend the definition of a matrix, vector or an element. For example,  $\Delta\mathbf{P}^N(z_0, z_0)$  refers to the combination of primary reflection data with noise.
- The index  $j$  is always fixed. The indices  $i$  and  $k$  are always running.
- Notations that do not fall under this convention will be defined when used.

### 3.3 Imaging by double focusing

In this thesis, imaging is defined as the process of mapping P-waves to their points of reflection in the subsurface. It reveals the position and strength of the subsurface reflectors. This process is referred to as structural imaging or confocal imaging. Furthermore, imaging

is also carried out to estimate the angle-dependent property of each reflection point. This extended process referred to as amplitude-versus-rayparameter (AVP) estimation or bifocal imaging. All imaging techniques being performed in the pre-stack domain carry out two weighted spatial summations of the recorded wavefield, even if not explicitly mentioned (see for example Berkhout, 1980, Claerbout, 1985, and Biondi, 2006). In post-stack imaging, the common-mid-point (CMP) stacking process can be considered as one of these two spatial summations while the other being the weighted summation along the zero-offset coordinates. In this thesis, the two spatial summations are performed sequentially along the source and the receiver coordinates. This physical-oriented process is referred to as imaging by double focusing (Berkhout, 1997). The two focusing steps are successively carried out: focusing in emission followed by focusing in detection or visa versa.

### 3.3.1 Confocal imaging

According to the **WRW** model (e.g. equation 3.1), it is obvious that in order to interpret seismic images,  $\mathbf{W}(z_m, z_0) \mathbf{S}(z_0)$  and  $\mathbf{D}(z_0) \mathbf{W}(z_0, z_m)$  have to be removed from the data. Therefore, the best definition of seismic imaging is to remove  $\mathbf{W}(z_m, z_0) \mathbf{S}(z_0)$  and  $\mathbf{D}(z_0) \mathbf{W}(z_0, z_m)$  from the data such that the undisturbed reflection properties (position and reflectivity) are obtained. This removal process means that detectors and sources are focused to the same subsurface point: *confocal imaging*.

First, *focusing in detection* is applied to the data where each common source gather is transformed into a single trace by the focusing-in-detection operator for the subsurface gridpoint under consideration (Fresnel stacking). Each trace is placed at the location of the involved source. This can be mathematically formulated as:

$$\begin{aligned} \mathbf{P}_j^\dagger(z_m, z_0) &= \mathbf{F}_j^\dagger(z_m, z_0) \mathbf{P}(z_0, z_0) \\ &= \mathbf{F}_j^\dagger(z_m, z_0) [\mathbf{D}(z_0) \mathbf{W}(z_0, z_m) \mathbf{R}(z_m) \mathbf{W}(z_m, z_0) \mathbf{S}(z_0)] \\ &= [\mathbf{F}_j^\dagger(z_m, z_0) \mathbf{D}(z_0) \mathbf{W}(z_0, z_m)] \mathbf{R}(z_m) \mathbf{W}(z_m, z_0) \mathbf{S}(z_0), \end{aligned} \quad 3.3$$

where row vector  $\mathbf{F}_j^\dagger(z_m, z_0)$  represents the focusing operator for the  $j^{\text{th}}$  subsurface gridpoint at depth level  $z_m$ . Theoretically:

$$\mathbf{F}_j^\dagger(z_m, z_0) \mathbf{D}(z_0) \mathbf{W}(z_0, z_m) = \mathbf{I}_j^\dagger(z_m), \quad 3.4$$

where  $\mathbf{I}_j^\dagger(z_m) = (0, 0, \dots, 0, 1, 0, \dots, 0)$ . This condition, meaning perfect detection by a unit point receiver (at the  $j^{\text{th}}$  subsurface gridpoint), is not obtainable because of theoretical and

practical constraints pertaining respectively to wave propagation, acquisition geometry and band limitation. However, the objective is to get as close as possible to this condition.

The result obtained after focusing in detection is referred to as the *common focus point* (CFP) gather. According to the *principle of equal traveltimes*, the travel times of the focus point response in this CFP gather will be the same as the time-reversed focusing operator if the used velocity model is correct (Berkhout, 1997).

The second focusing step (*focusing in emission*) is done by transforming the CFP gather into a seismic image trace after the application of the same focusing operator. This is given by:

$$\begin{aligned}
 \mathbf{P}_{jj}(z_m, z_m) &= \mathbf{P}_j^\dagger(z_m, z_0) \mathbf{F}_j(z_0, z_m) \\
 &\approx \mathbf{I}_j^\dagger(z_m, z_0) \mathbf{R}(z_m, z_m) \mathbf{I}_j(z_0, z_m) \\
 &\approx \mathbf{R}_{jj}(z_m, z_m).
 \end{aligned} \tag{3.5}$$

According to the imaging principle, the image is found in the image trace at  $t=0$ . The order of the two focusing steps can be interchanged. After the application of the two focusing steps at the  $j^{\text{th}}$  subsurface gridpoint, equation 3.5 shows that the  $j^{\text{th}}$  diagonal element of  $\mathbf{R}(z_m, z_m)$  is obtained, representing average angle-dependent reflectivity. Figure 3.3 gives a simplified representation of the confocal imaging process. In practice, this process is referred to as structural imaging once repeated for all subsurface gridpoints ( $j=1:N$ ) at all depth levels ( $m=1:M$ ).

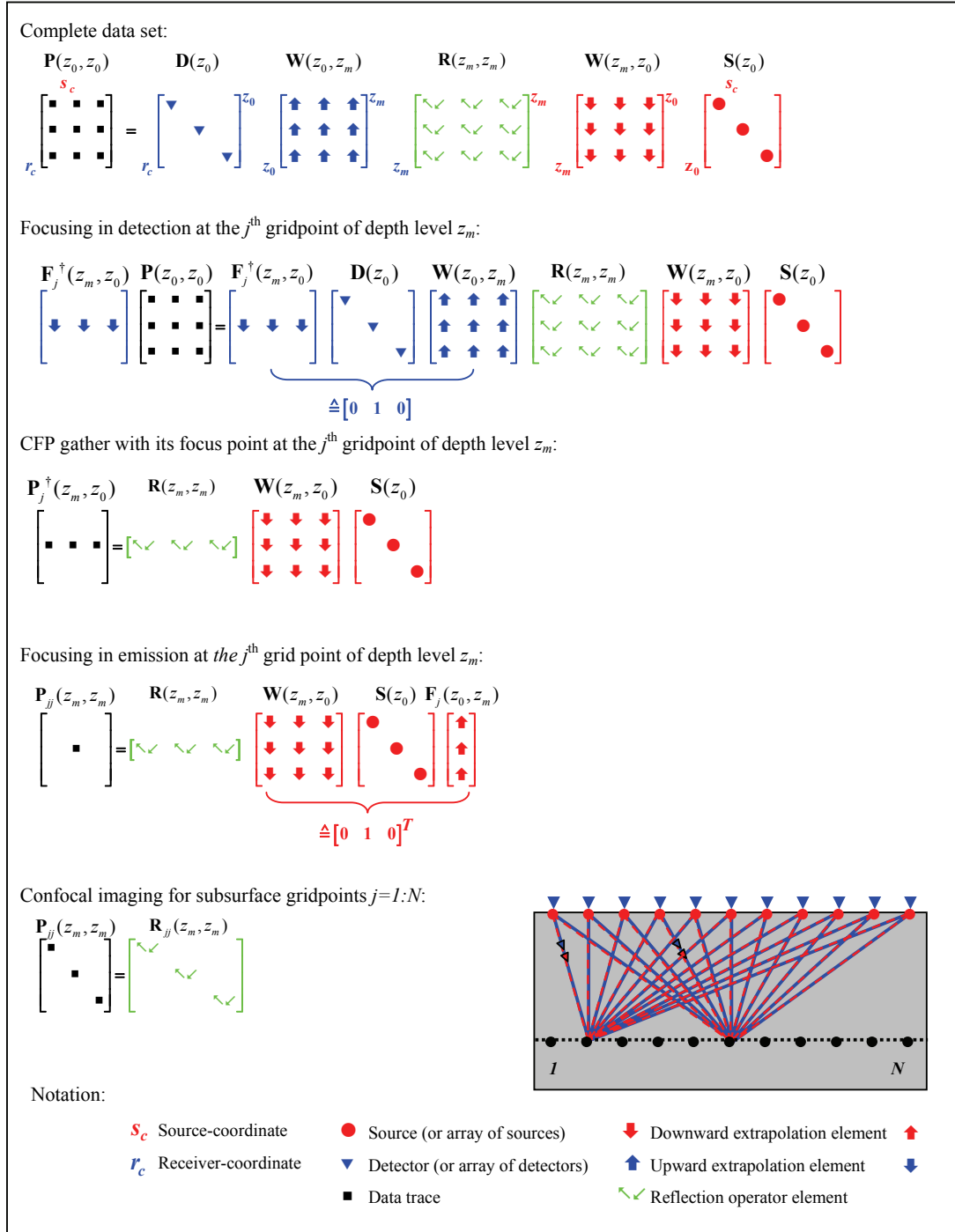


Fig. 3.3 Schematic representation of the confocal imaging process.

### 3.3.2 Bifocal imaging

*Bifocal imaging* aims at extracting angle-dependent reflectivity from seismic data. According to the **WRW** model, the angle-dependent reflection coefficients for gridpoint  $j$  at  $z_m$  are represented by either the  $j^{\text{th}}$  row or the  $j^{\text{th}}$  column of the reflection matrix  $\mathbf{R}(z_m, z_m)$ . Therefore, angle-dependent reflectivity can be extracted from the data using the focusing concept. First, focusing in detection or focusing in emission is applied for the  $j^{\text{th}}$  subsurface gridpoint. The second focusing step is applied in such a way that not only focusing to the  $i=j$  subsurface gridpoint is carried out, but also to the points around it ( $i \neq j$ ).

If focusing in detection at the  $j^{\text{th}}$  subsurface gridpoint is applied followed by focusing in emission at points  $i$  around  $j$ , this can be expressed mathematically as:

$$\begin{aligned} \mathbf{P}_{ji}(z_m, z_m) &= \mathbf{F}_j^\dagger(z_m, z_0) \mathbf{P}(z_0, z_0) \mathbf{F}_i(z_0, z_m) \\ &\approx \mathbf{R}_{ji}(z_m, z_m), \end{aligned} \quad 3.6$$

where  $j$  is fixed and  $i$  is varied and  $\mathbf{R}_{ji}(z_m, z_m)$  is a band limited version of the actual reflectivity function. Hence, each element of the reflection matrix is obtained by a double focusing process. The complete reflectivity information at one subsurface gridpoint is represented by the  $j^{\text{th}}$  row vector:

$$\begin{aligned} \mathbf{P}_j^\dagger(z_m, z_m) &= \mathbf{F}_j^\dagger(z_m, z_0) \mathbf{P}(z_0, z_0) \mathbf{F}(z_0, z_m) \\ \mathbf{P}_j^\dagger(z_m, z_m) &\approx \mathbf{R}_j^\dagger(z_m, z_m). \end{aligned} \quad 3.7$$

A schematic illustration of the *bifocal imaging* process according to the double focusing sequence of equation 3.7 is given by Figure 3.4.

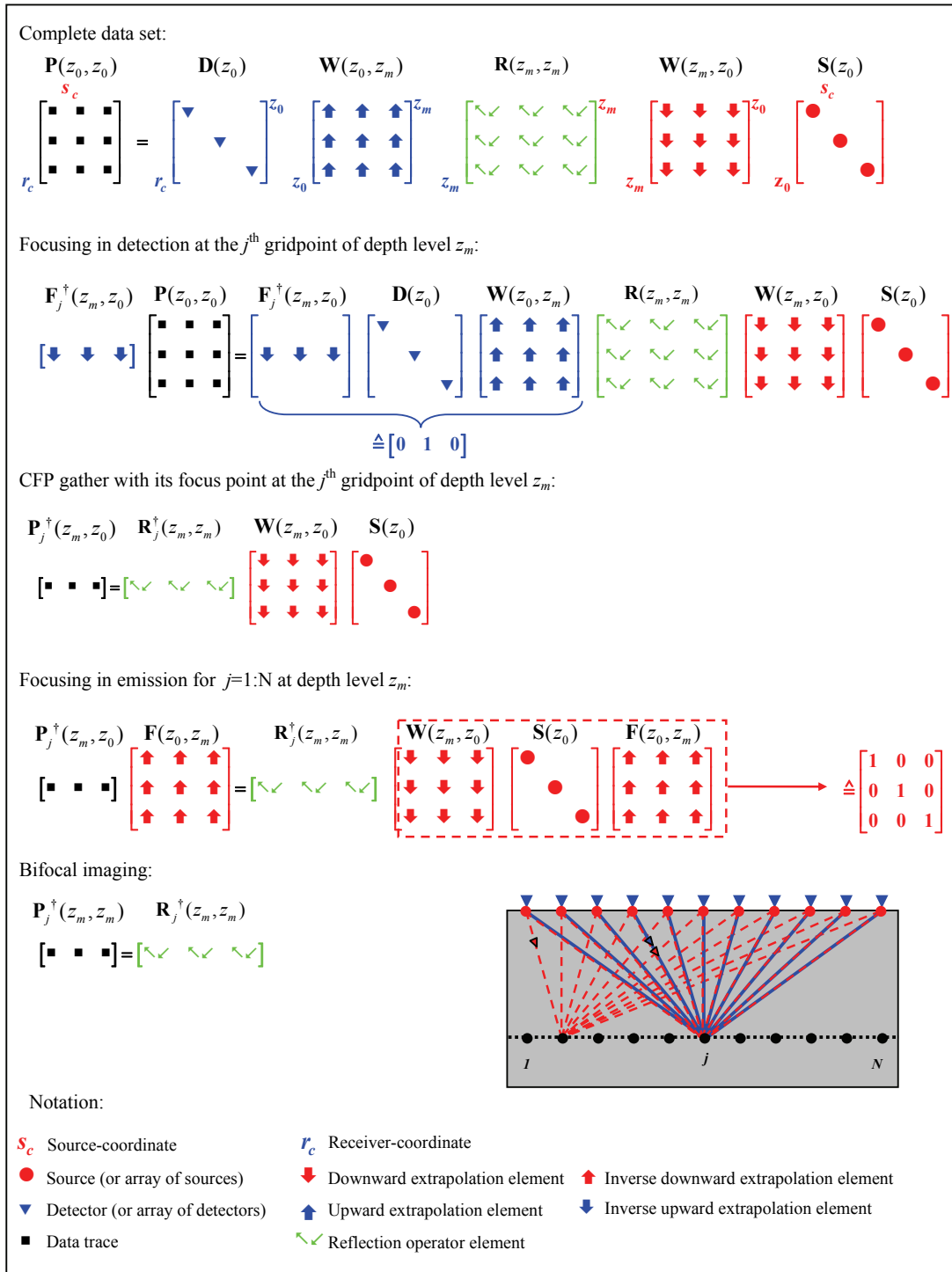


Fig. 3.4 Schematic representation of the bifocal imaging process starting with focusing in detection at one subsurface gridpoint followed by focusing in emission at and around that point.

Similarly, a column vector of  $\mathbf{R}(z_m, z_m)$  will be obtained if the sources are focused at the  $j^{\text{th}}$  subsurface gridpoint followed by focusing of the receivers at and around that point. This is expressed mathematically as:

$$\begin{aligned} \mathbf{P}_j(z_m, z_m) &= \mathbf{F}(z_m, z_0)\mathbf{P}(z_0, z_0)\mathbf{F}_j(z_0, z_m) \\ &\approx \mathbf{R}_j(z_m, z_m). \end{aligned} \quad 3.8$$

Row vector  $\mathbf{P}_j^\dagger(z_m, z_m)$  and column vector  $\mathbf{P}_j(z_m, z_m)$  in equations 3.7 and 3.8 are called the *gridpoint gathers* for the  $j^{\text{th}}$  subsurface gridpoint. The Radon transform of  $\mathbf{P}_j^\dagger(z_m, z_m)$  or  $\mathbf{P}_j(z_m, z_m)$  provides the angle-dependent reflection coefficients for the  $j^{\text{th}}$  reflection point on depth level  $z_m$  under the condition that the focusing operators are perfect. The coefficients will be located at the zero intercept time  $\tau = 0$ .

### 3.4 Acquisition geometry assessment

Model-based acquisition geometry assessment is a natural extension to the conventional approach. The objective is to provide an optimized acquisition geometry, using available subsurface information. The input to this optimization process will be the initial acquisition geometry and the macro-model of the subsurface. For example, if the objective is to provide a good structural image of the subsurface, then the geometry can be characterized by the quality of the *confocal image*. Similarly, if the objective is to extract rock properties from seismic data, then the geometry should be optimized based on the quality of the *bifocal image*. Note that confocal imaging is less demanding than bifocal imaging.

#### 3.4.1 Focal beams

The process of double focusing, focusing in emission and focusing in detection, involves the formation of two focal beams at the subsurface points towards which these beams are directed. The reader is referred to Appendix A for a detailed discussion of the physical meaning of focal beams and their computations. Furthermore, Figure 1.8e presents a beam calculated through a model characterized by a complex near-surface.

Using **WRW**, the double focusing process can be expressed for a stationary geometry as:

$$\mathbf{P}_{jj}(z_m, z_m) = [\mathbf{F}_j^\dagger(z_m, z_0)\mathbf{D}(z_0)\mathbf{W}(z_0, z_m)]\mathbf{R}(z_m, z_m)[\mathbf{W}(z_m, z_0)\mathbf{S}(z_0)\mathbf{F}_j(z_0, z_m)], \quad 3.9$$

where index  $j$  refers to the focus point corresponding to focussing in detection and to the focus point corresponding to focussing in emission. From this equation, the focal detector and source beams can be respectively identified as (Berkhout, et al., 2001):

$$\mathbf{D}_j^\dagger(z, z_m) = \mathbf{F}_j^\dagger(z, z_0) \mathbf{D}(z_0) \mathbf{W}(z_0, z_m), \quad 3.10$$

$$\mathbf{S}_j(z_m, z) = \mathbf{W}(z_m, z_0) \mathbf{S}(z_0) \mathbf{F}_j(z_0, z), \quad 3.11$$

where  $z$  is varying and  $z_m$  is the target depth level. The detector beam at  $z=z_m$  shows how well the  $j^{\text{th}}$  gridpoint in the subsurface (focus point) is listened to by the detector geometry  $\mathbf{D}(z_0)$  on the surface. Likewise, the focal source beam  $z=z_m$  shows how well the  $j^{\text{th}}$  subsurface gridpoint is illuminated by the source geometry  $\mathbf{S}(z_0)$  on the surface.

For non-stationary geometries the two focal beams can be calculated by summation over all sub-beams obtained from contributing templates for the subsurface gridpoint under consideration.

### **Focal beam matrices**

The physics of beam forming is well understood among scientists. However, the beams can be computed in two different ways which are discussed in Appendix A. Therefore, to assist in understanding the relation between the focal beams and the focal functions which will be discussed later, the focal detector beam matrix and focal source beam matrix are introduced for a stationary geometry which are respectively defined as:

$$\mathbf{D}(z, z_m) = \mathbf{F}(z, z_0) \mathbf{D}(z_0) \mathbf{W}(z_0, z_m). \quad 3.12$$

$$\mathbf{S}(z_m, z) = \mathbf{W}(z_m, z_0) \mathbf{S}(z_0) \mathbf{F}(z_0, z). \quad 3.13$$

The focal detector beam in equation 3.10 is the  $j^{\text{th}}$  row of equation 3.12. Similarly, equation 3.11 is the  $j^{\text{th}}$  column of the focal source beam matrix in equation 3.13 (see Figure 3.5).

It is proven in Appendix A that the rows and the columns in both the focal detector beam matrix and focal source beam matrix are complex conjugate of each other (i.e. each matrix is Hermitian). It follows that the main diagonal of each matrix is real which should be physically obvious from the focal beam forming process! That is because the main diagonal points represent the points for which the different focal arrays are tuned on the surface; thus, during the beam forming process the focal arrays are brought to their focus points.

Consequently, the phase at the diagonal points will be zero resulting in real valued numbers in the space-frequency domain.

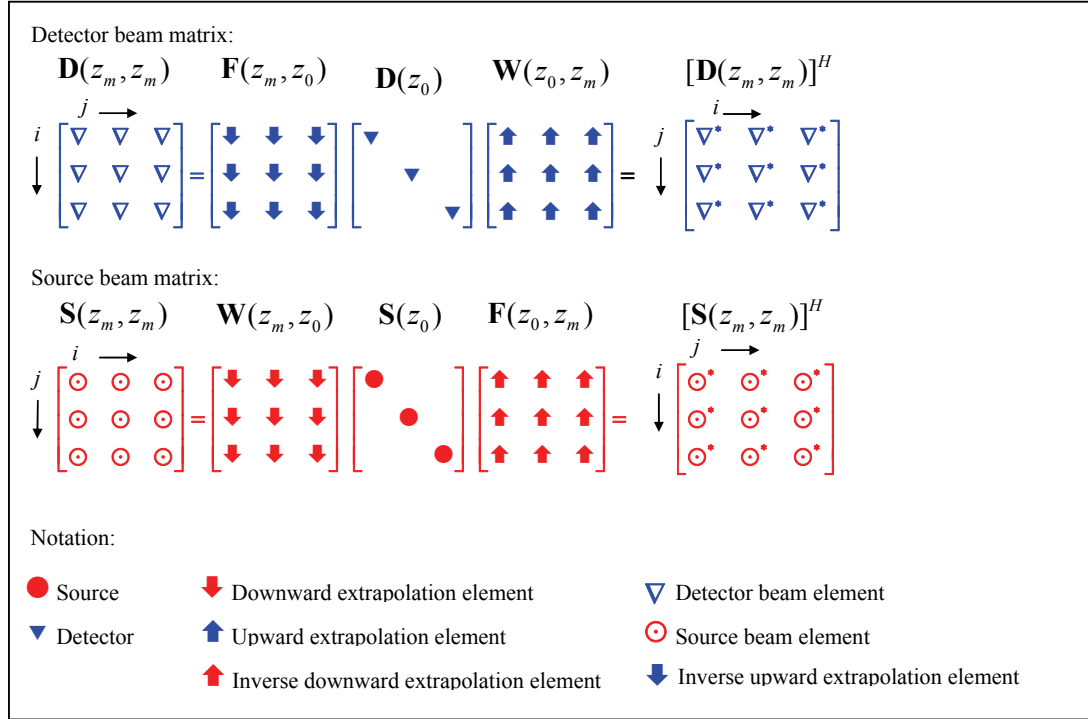


**Fig. 3.5** Schematic representation of the focal detector and focal source beam matrices.

### 3.4.2 Focal functions

It was stated earlier that acquisition geometries are optimized to meet certain objectives. Angle-averaged (structural) imaging and angle-dependent (AVP) imaging encapsulate the primary purposes of seismic imaging. For structural imaging, the resolution is important while for AVP imaging the range of reflection angles is important. Based on these two requirements, Berkhout, et al. (2001) identified two focal functions namely: the resolution function and the amplitude-versus-ray parameter (AVP) function.

#### **Resolution function**

Taking into account that the response of any reflector can be considered as the response of a distribution of point diffractors, the image resolution can be evaluated based on the resolution achieved from imaging a point diffractor. Of course, for a given acquisition

geometry, the seismic response of a point diffractor can be modelled, and then be imaged to evaluate the resolution. However, it will be shown in this section that the focal beams can be used to perform this task without going into explicit modelling of the data. Let us start with the forward model expression for a point diffractor located at the  $j^{\text{th}}$  subsurface gridpoint:

$$\Delta \mathbf{P}(z_0, z_0) = \sum_j \delta_j \mathbf{P}(z_0, z_0), \quad 3.14$$

with

$$\delta_j \mathbf{P}(z_0, z_0) = \mathbf{D}(z_0) [\mathbf{W}(z_0, z_m) \delta_j \mathbf{R}(z_m, z_m) \mathbf{W}(z_m, z_0)] \mathbf{S}(z_0), \quad 3.15$$

where  $\delta_j \mathbf{R}(z_m, z_m)$  is equal to unity at the diffractor location ( $j^{\text{th}}$  position at depth level  $z_m$ ) and zero elsewhere. Note that the data is indicated by delta ( $\delta$ ) to emphasize that it is for one point diffractor. The resolution can be evaluated by performing structural imaging (*confocal imaging*) where both detectors and sources are focused at and around the  $j^{\text{th}}$  subsurface gridpoint (for  $i$  varying around  $j$ ):

$$\delta_j \mathbf{P}_{ii}(z_m, z_m) = [\mathbf{F}_i^\dagger(z_m, z_0) \mathbf{D}(z_0) \mathbf{W}(z_0, z_m)] \delta_j \mathbf{R}(z_m, z_m) [\mathbf{W}(z_m, z_0) \mathbf{S}(z_0) \mathbf{F}_i(z_0, z_m)]. \quad 3.16$$

The two focal beams defined in equations 3.10 and 3.11 are identified in equation 3.16, but since  $\delta_j \mathbf{R}(z_m, z_m)$  has only one non-zero element at the  $j^{\text{th}}$  subsurface position being equal to unity, equation 3.16 gives:

$$\begin{aligned} \delta_j \mathbf{P}_{ii}(z_m, z_m) &= [\mathbf{F}_i^\dagger(z_m, z_0) \mathbf{D}(z_0) \mathbf{W}_j(z_0, z_m)] [\mathbf{W}_j^\dagger(z_m, z_0) \mathbf{S}(z_0) \mathbf{F}_i(z_0, z_m)] \\ &= \mathbf{D}_{ij}(z_m, z_m) \mathbf{S}_{ji}(z_m, z_m), \end{aligned} \quad 3.17$$

where  $i$  varies around the position of the point diffractor  $j$ .

Remember that our objective is to quantitatively evaluate how well the point diffractor at the  $j^{\text{th}}$  subsurface gridpoint is resolved (i.e. the diagonal of  $\delta_j \mathbf{P}(z_m, z_m)$ ). Hence, each  $i^{\text{th}}$  focal beam of the detector and the source has to be directed towards the *same* gridpoints in the subsurface.

Equation 3.16 shows that the resolution function can be obtained by space-frequency *element-by-element multiplication* of the focal detector and source beams defined in equations 3.10 and 3.11. Figure 3.6 provides a schematic representation of the resolution function construction. It clearly shows the importance of the focal beam matrices (equations 3.12 and 3.13) being Hermitian and their influence in reducing the computational efforts.

For non-stationary geometries the resolution function can be computed by summation over resolution sub-functions. Each sub-function will be the result of space-frequency element-by-element multiplication of sub-beams obtained from contributing stationary geometry parts for the subsurface gridpoint under consideration.

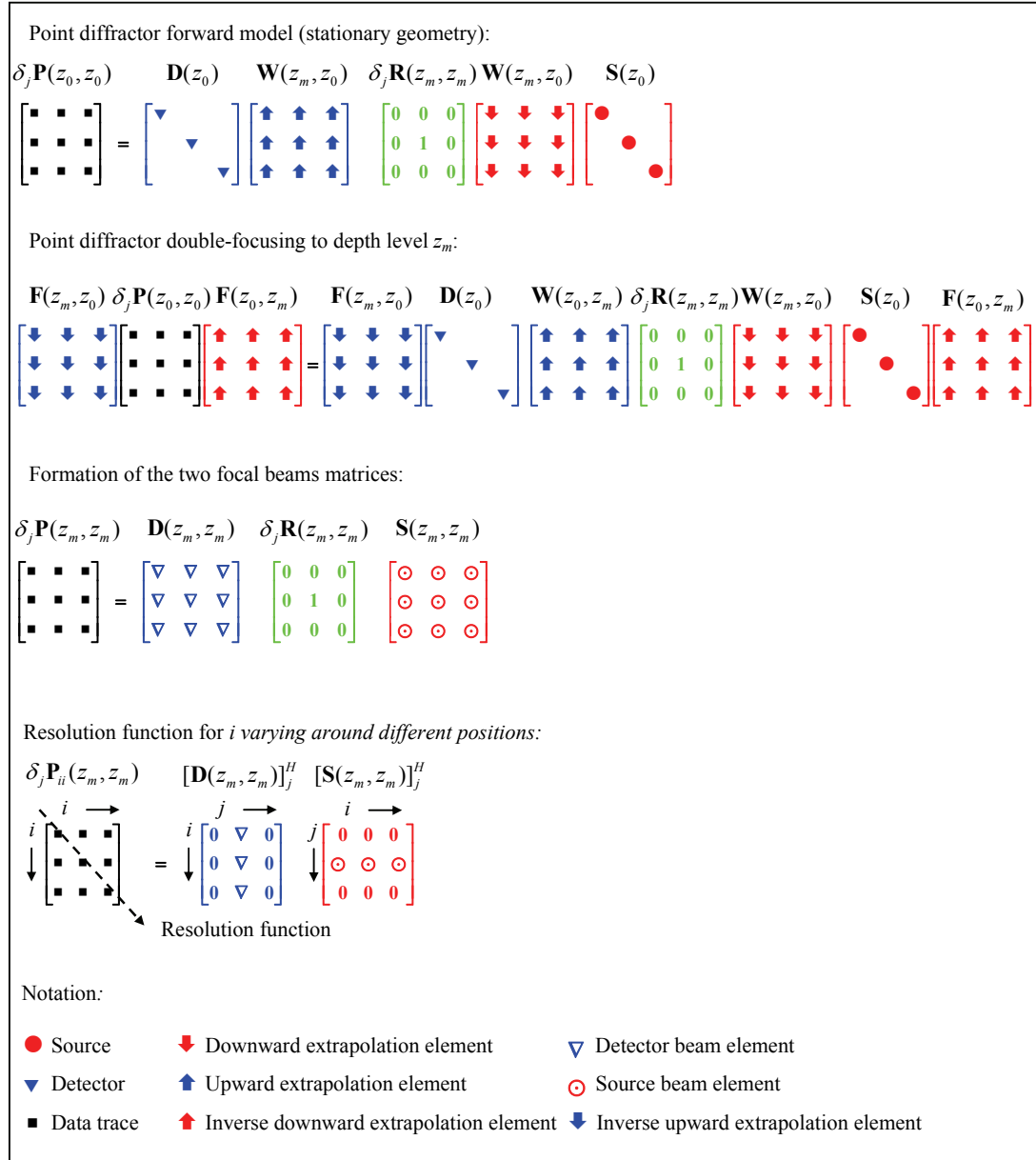


**Fig. 3.6** Schematic representation of the resolution function construction process for the stationary parts of a geometry.

### AVP-imprint function

The main objective of the AVP-imprint function is to quantitatively evaluate the effects of the acquisition geometry on the angle-dependent reflectivity contained in the acquired seismic data. Therefore, we will take an angle-independent reflector with zero dip — i.e.  $\mathbf{R}(z_m, z_m) = \mathbf{I}(z_m, z_m)$  with ones on the main diagonal and zeroes elsewhere — in order to separate the acquisition geometry effects from angle dependency variations. Therefore, the AVP-imprint function represents the imprint of the acquisition geometry on the unit sampling comb of the reflectivity function. Hence, the AVP-imprint will quantitatively show how the magnitude of this comb differs from unity. According to this assumption, the forward model of an angle-independent reflector can be written as:

$$\begin{aligned} \delta \mathbf{P}(z_0, z_0) &= [\mathbf{D}(z_0) \mathbf{W}(z_0, z_m)] \mathbf{R}(z_m, z_m) [\mathbf{W}(z_m, z_0) \mathbf{S}(z_0)] \\ &= [\mathbf{D}(z_0) \mathbf{W}(z_0, z_m)] \mathbf{I}(z_m, z_m) [\mathbf{W}(z_m, z_0) \mathbf{S}(z_0)] \\ &= [\mathbf{D}(z_0) \mathbf{W}(z_0, z_m)] [\mathbf{W}(z_m, z_0) \mathbf{S}(z_0)]. \end{aligned} \quad 3.18$$

The reflectivity information can be obtained by performing *bifocal imaging* (Berkhout, 1997) for the  $j^{\text{th}}$  subsurface gridpoint as:

$$\begin{aligned} \delta \mathbf{P}_j(z_m, z_m) &= [\mathbf{F}(z_m, z_0) \mathbf{D}(z_0) \mathbf{W}(z_0, z_m)] [\mathbf{W}(z_m, z_0) \mathbf{S}(z_0) \mathbf{F}_j(z_0, z_m)] \\ &= \mathbf{D}(z_m, z_m) \mathbf{S}_j(z_m, z_m). \end{aligned} \quad 3.19$$

It is obvious that *bifocal imaging* (i.e. the AVP-imprint function for depth level  $z_m$ ) in this case is obtained by multiplication of the focal detector beam matrix (equation 3.12) with the focal source beam for gridpoint  $j$  (equation 3.11). Therefore, equation 3.19 represents a space-variant convolution operation i.e. matrix-vector multiplication. If we assume that the focal detector beams do not laterally vary around gridpoint  $j$ , then equation 3.19 can be written as:

$$P(x, y, z_m; \omega) \approx D(x, y, z_m; \omega) * S(x, y, z_m; \omega), \quad 3.20$$

where the discrete version of  $D(x, y, z_m; \omega)$  is equal to  $\mathbf{D}_j^\dagger(z_m, z_m)$  of equation 3.10 and the discrete version of  $S(x, y, z_m; \omega)$  is equal to  $\mathbf{S}_j(z_m, z_m)$  of equation 3.11. This space invariant convolution of the focal detector and source beams can be written as a multiplication of two functions in the Radon domain such that:

$$\tilde{P}(p_x, p_y, z_m; \omega) = \tilde{D}(p_x, p_y, z_m; \omega) \tilde{S}(p_x, p_y, z_m; \omega), \quad 3.21$$

where the AVP-imprint function will be found at the zero intercept time  $\tau = 0$  of  $\tilde{P}(p_x, p_y, z_m; \omega)$ . From a computational viewpoint, the AVP-imprint is obtained by an element-by-element multiplication of the focal detector and source beams in the Radon domain.

Figure 3.7 exhibits a schematic representation of the AVP-imprint construction. For acquisition geometry optimization, the approximation embedded in equation 3.20 is of second order effects because the lateral variation of beams close to the target point is small. Finally, for non-stationary geometries the AVP-imprint function can be computed by summation over AVP-imprint sub-functions. Each sub-function will be the result of the Radon multiplication of sub-beams obtained from contributing templates for the subsurface gridpoint under consideration.

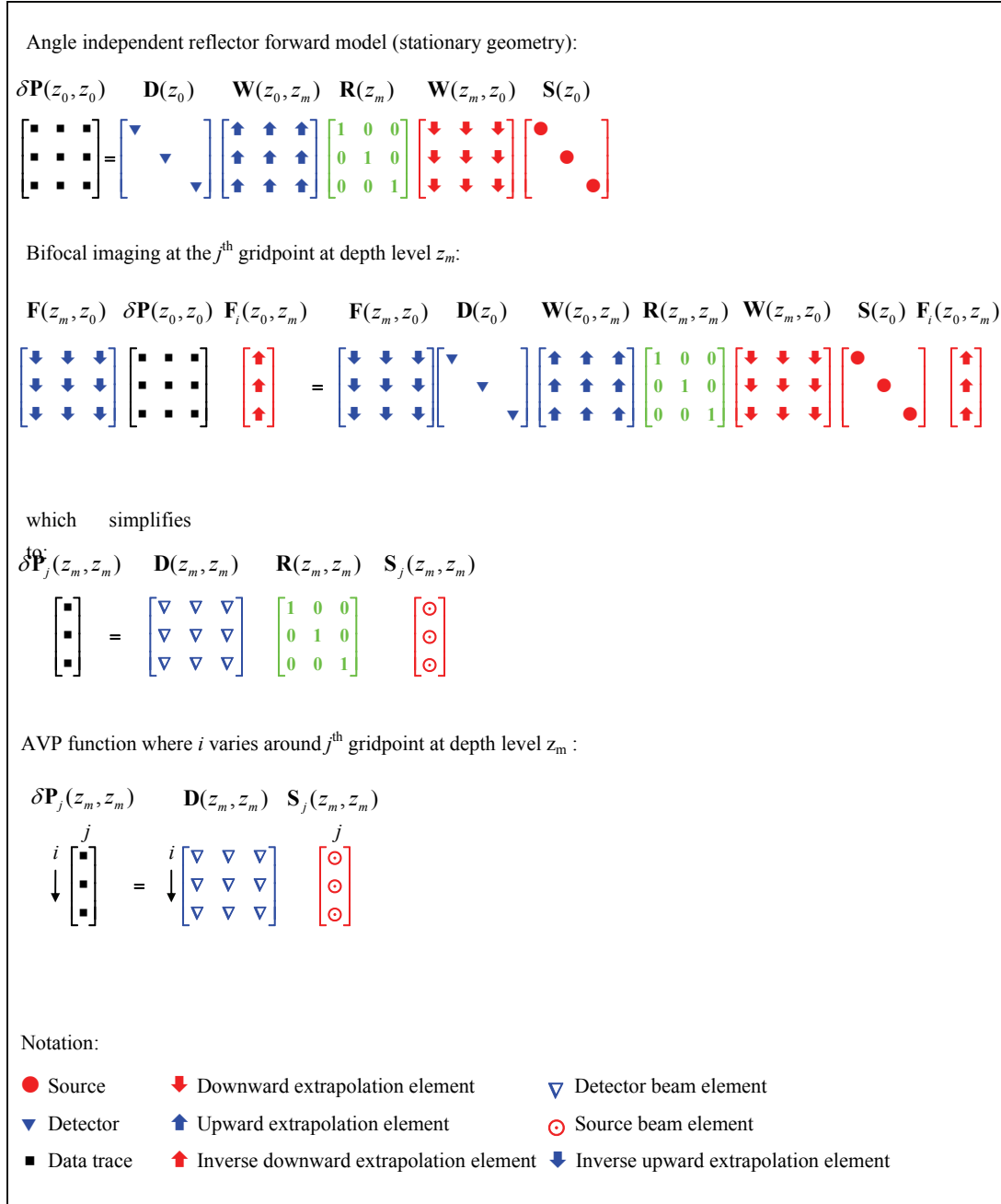


**Fig. 3.7** Schematic representation of the AVP-imprint function construction process the stationary parts of a geometry.

### 3.5 Seismic noise

Seismic noise can be divided into two categories: coherent noise and incoherent noise. Direct and scattered Rayleigh waves comprise primarily the coherent noise. The other category includes ambient noise, acquisition instrument noise, and noise resulting from operational aspects like coupling of sources and receivers and their positioning.

Surface and interbed multiples are not considered as noise. One reason for not including the multiples is the fact that they can be considered as signals and used to image the subsurface. See for example Berkhout and Verschuur (2006) for an elaborate description of this technique. In addition, scattering in the near-surface caused by upgoing body-waves (Campman, 2005) is not going to be considered in this research.

Therefore, only additive noise will be considered including Rayleigh waves, scattered Rayleigh waves and ambient noise. Following the previous formulation, the noise can be written as:

$$\mathbf{N}(z_0, z_0) = \mathbf{N}^R(z_0, z_0) + \mathbf{N}^{SR}(z_0, z_0) + \mathbf{N}^A(z_0, z_0), \quad 3.22$$

where matrix  $\mathbf{N}^R(z_0, z_0)$  contains the direct Rayleigh waves, matrix  $\mathbf{N}^{SR}(z_0, z_0)$  contains the scattered Rayleigh waves and matrix  $\mathbf{N}^A(z_0, z_0)$  contains ambient noise. The influence of each type of noise on the target image quality can be measured by the focal functions.

The resolution function with noise added can be expressed as:

$$\begin{aligned} \delta_j \mathbf{P}_{ii}^N(z_m, z_m) &= \delta_j \mathbf{P}_{ii}(z_m, z_m) + \mathbf{N}_{ii}(z_m, z_m) \\ &= \delta_j \mathbf{P}_{ii}(z_m, z_m) + \mathbf{N}_{ii}^R(z_m, z_m) + \mathbf{N}_{ii}^{SR}(z_m, z_m) + \mathbf{N}_{ii}^A(z_m, z_m), \end{aligned} \quad 3.23$$

where  $\delta_j \mathbf{P}_{ii}(z_m, z_m)$  is given by equation (3.17). The  $\mathbf{N}$  matrices will be discussed in the next section.

The AVP-imprint function with noise included is:

$$\begin{aligned} \delta \mathbf{P}_j^N(z_m, z_m) &= \delta \mathbf{P}_j(z_m, z_m) + \mathbf{N}_j(z_m, z_m) \\ &= \delta \mathbf{P}_j(z_m, z_m) + \mathbf{N}_j^R(z_m, z_m) + \mathbf{N}_j^{SR}(z_m, z_m) + \mathbf{N}_j^A(z_m, z_m), \end{aligned} \quad 3.24$$

where  $\delta \mathbf{P}_j(z_m, z_m)$  is given by equation (3.19).

In the following sections, the ‘cross resolution function’ noise components  $\mathbf{N}_{ii}^R(z_m, z_m)$ ,  $\mathbf{N}_{ii}^{SR}(z_m, z_m)$  and  $\mathbf{N}_{ii}^A(z_m, z_m)$  will be formulated. Note that the name ‘cross’ is added because these components represent the cross-image of noise with respect to the signal (i.e. using the focusing operators of the signal). Besides, the ‘cross AVP-imprint function’  $\mathbf{N}_j^R(z_m, z_m)$ ,  $\mathbf{N}_j^{SR}(z_m, z_m)$  and  $\mathbf{N}_j^A(z_m, z_m)$  will be formulated.

### 3.5.1 Rayleigh waves

Rayleigh waves comprise a considerable part of the elastic wavefield recorded in the seismic experiment. They are referred to as ground roll. Rayleigh waves travel along the surface with combined longitudinal and transverse motion. They travel directly from the source to the receiver with a velocity that is slightly less than the velocity of shear waves ( $0.92 V_s$ , where  $V_s$  is the shear-wave velocity). Their amplitude is much higher than the signal amplitude because Rayleigh waves diminish as  $r^{-0.5}$  where  $r$  is the distance from the source, compared to the body waves that diminish more rapidly as  $r^{-1}$  (Telford et al. 1990). Rayleigh waves are not dispersive in nature, but they show dispersive behaviour due to the variations of the near-surface velocity. Figure 3.8 shows a schematic diagram of the **WRW** model with Rayleigh waves included. Rayleigh waves can be modelled separately and then added to the modelled body-waves.

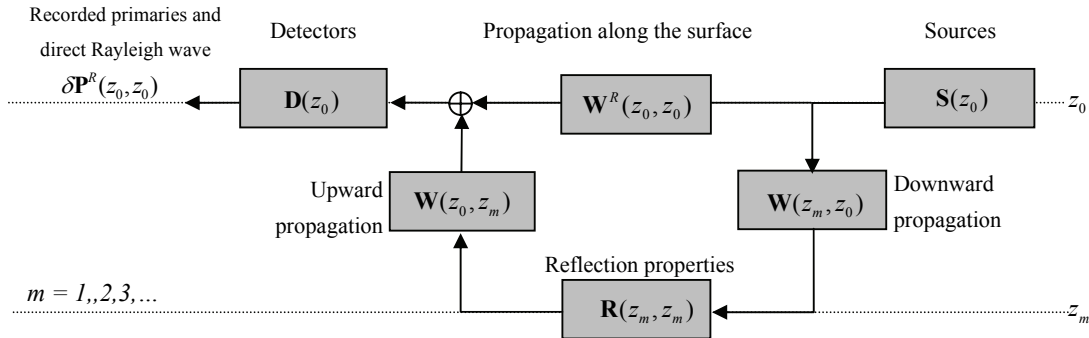


**Fig. 3.8** Forward seismic model of primary reflections with Rayleigh waves added.

#### Cross resolution function for Rayleigh waves

The forward model for Rayleigh waves can be written as:

$$\mathbf{N}^R(z_0, z_0) = \mathbf{D}(z_0)\mathbf{W}^R(z_0, z_0)\mathbf{S}(z_0), \quad 3.25$$

where matrix  $\mathbf{N}^R(z_0, z_0)$  describes the Rayleigh wave data and  $\mathbf{W}^R(z_0, z_0)$  describes the Green's functions of the Rayleigh waves from sources to receivers.

The cross resolution function of Rayleigh waves with the signal at the  $j^{\text{th}}$  target point is the output of the *confocal imaging* process of Rayleigh waves:

$$\begin{aligned}\mathbf{N}_{ii}^R(z_m, z_m) &= \mathbf{F}_i^\dagger(z_m, z_0)\mathbf{N}^R(z_0, z_0)\mathbf{F}_i(z_0, z_m) \\ &= \mathbf{F}_i^\dagger(z_m, z_0)\mathbf{D}(z_0)\mathbf{W}^R(z_0, z_0)\mathbf{S}(z_0)\mathbf{F}_i(z_0, z_m),\end{aligned}\tag{3.26}$$

for  $i$  varying around  $j$  at depth level  $z_m$ . Note that  $\mathbf{F}_i^\dagger(z_m, z_0)$  and  $\mathbf{F}_i(z_0, z_m)$  are the same as those calculated for the signal as in equation 3.17.

Equation 3.26 shows that the *confocal 'cross image'* of Rayleigh waves can not be obtained by the multiplication of two beams. The cross resolution function of the Rayleigh waves can only be obtained by explicit modeling of  $\mathbf{N}^R(z_0, z_0)$ , and then perform the confocal imaging process on it.

### **Cross AVP-imprint function for Rayleigh waves**

The cross AVP-imprint function for Rayleigh waves is defined as the bifocal imaging of  $\mathbf{N}^R(z_0, z_0)$  as:

$$\begin{aligned}\mathbf{N}_{jj}^R(z_m, z_m) &= \mathbf{F}(z_m, z_0)\mathbf{N}^R(z_0, z_0)\mathbf{F}_j(z_0, z_m) \\ &= \mathbf{F}(z_m, z_0)\mathbf{D}(z_0)\mathbf{W}^R(z_0, z_0)\mathbf{S}(z_0)\mathbf{F}_j(z_0, z_m),\end{aligned}\tag{3.27}$$

for the  $j^{\text{th}}$  gridpoint at depth level  $z_m$ . Equation 3.27 shows that the cross AVP-imprint function of Rayleigh waves is the *bifocal 'cross imaged'* Rayleigh waves. This can be obtained by forward modeling of Rayleigh waves followed by performing bifocal imaging to the  $j^{\text{th}}$  gridpoint at depth level  $z_m$ . Again beams are not involved in this process.

## **3.5.2 Scattered Rayleigh waves**

Scattered Rayleigh waves are generated when Rayleigh waves encounter inhomogeneities in the near-surface during their propagation. These inhomogeneities act as new sources that transmit Rayleigh waves in all spatial directions. Since scattered Rayleigh waves do not travel directly from the source to the receiver as in the case of direct Rayleigh waves, we can

separate them into a source component and a receiver component as in the case of body waves. Assuming that the scatterers are randomly distributed in the near-surface (Volker, 2002), the scattered Rayleigh waves can be represented using the concept of the **WRW** model as:

$$\mathbf{N}^{SR}(z_0, z_0) = \mathbf{D}(z_0) \sum_{k=1}^N \mathbf{W}^{SR}(z_0, z_n) \delta_k \mathbf{R}(z_n, z_n) \mathbf{W}^{SS}(z_n, z_0) \mathbf{S}(z_0), \quad 3.28$$

where matrix  $\mathbf{N}^{SR}(z_0, z_0)$  contains the scattered Rayleigh waves,  $\mathbf{W}^{SS}(z_n, z_0)$  describes Green's functions of the scattered Rayleigh waves from the source at depth level  $z=z_0$  to the scatterer at depth level  $z=z_n$  and  $\mathbf{W}^{SR}(z_0, z_n)$  describes the Green's functions from the scatterer to the detectors. Matrix  $\delta_k \mathbf{R}(z_n, z_n)$  is equal to unity at the scatterer location ( $k^{\text{th}}$  position at depth level  $z_n$ ) and zero elsewhere.  $N$  is the number of surface gridpoints that may or may not contain a scatterer depending on the value of  $k$ . Figure 3.9 shows a schematic representation of the forward model of body-waves and scattered Rayleigh waves.

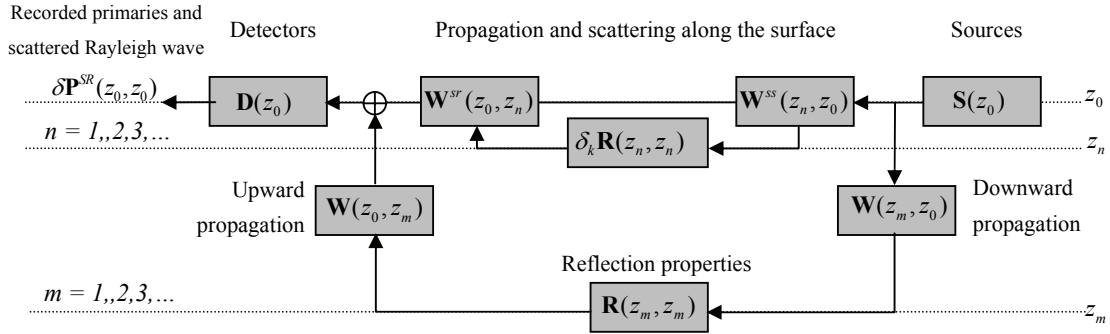


**Fig. 3.9** Forward seismic model of primary reflections with scattered Rayleigh waves added. Note that  $n < m$ .

### Cross resolution function of scattered Rayleigh waves

The objective of computing the cross resolution function of scattered Rayleigh waves is to assess their influence on the resolution of body waves at the target. Therefore, we need to perform a confocal imaging process to the scattered Rayleigh waves with respect to a target point at the  $j^{\text{th}}$  position on depth level  $z_m$ . This means that the focusing operators are tuned towards this depth level at  $j$  and around it. This can be formulated as:

$$\begin{aligned}
\mathbf{N}_{ii}^{SR}(z_m, z_m) &= \mathbf{F}_i^\dagger(z_m, z_0) \mathbf{D}(z_0) \sum_{k=1}^N \mathbf{W}^{SR}(z_0, z_n) \delta_k \mathbf{R}(z_n, z_n) \mathbf{W}^{SS}(z_n, z_0) \mathbf{S}(z_0) \mathbf{F}_i(z_0, z_m) \\
&= \sum_{k=1}^N \mathbf{F}_i^\dagger(z_m, z_0) \mathbf{D}(z_0) \mathbf{W}^{SR}(z_0, z_n) \delta_k \mathbf{R}(z_n, z_n) \mathbf{W}^{SS}(z_n, z_0) \mathbf{S}(z_0) \mathbf{F}_i(z_0, z_m) \\
&= \sum_{k=1}^N [\mathbf{F}_i^\dagger(z_m, z_0) \mathbf{D}(z_0) \mathbf{W}_k^{SR}(z_0, z_n)] [\mathbf{W}_k^{\dagger SS}(z_n, z_0) \mathbf{S}(z_0) \mathbf{F}_i(z_0, z_m)] \\
&= \sum_{k=1}^N \mathbf{D}_{ik}^{SR}(z_m, z_m) \mathbf{S}_{ki}^{SR}(z_m, z_m),
\end{aligned} \tag{3.29}$$

for  $i$  varying around the target point  $j$ .  $\mathbf{N}_{ii}^{SR}(z_m, z_m)$  is an element of the ‘cross resolution function’ of the scattered Rayleigh waves.  $\mathbf{S}_{ji}^{SR}(z_m, z_m)$  is a cross focal source beam element caused by the scattered Rayleigh waves due to surface scatterer at the  $k^{\text{th}}$  location at depth level  $z_n$  as observed at the  $j^{\text{th}}$  point diffractor of depth level  $z_m$ . Similarly,  $\mathbf{D}_{ij}^{SR}(z_m, z_m)$  is cross focal detector beam element of the scattered Rayleigh waves.

Equation 3.29 shows that the cross resolution function of scattered Rayleigh waves can be computed without explicit modeling of these waves.

### **Cross AVP-imprint function of scattered Rayleigh waves**

The cross AVP-imprint function can be defined as in section (3.4.2) but for scattered Rayleigh waves. The AVP-imprint function will be the bifocal imaging of  $\mathbf{N}^{SR}(z_0, z_0)$  for the  $j^{\text{th}}$  gridpoint at depth level  $z_m$ :

$$\begin{aligned}
\mathbf{N}_j^{SR}(z_m, z_m) &= \mathbf{F}(z_m, z_0) \mathbf{D}(z_0) \sum_{k=1}^N \mathbf{W}^{SR}(z_0, z_n) \delta_k \mathbf{R}(z_n, z_n) \mathbf{W}^{SS}(z_n, z_0) \mathbf{S}(z_0) \mathbf{F}_j(z_0, z_m) \\
&= \sum_{k=1}^N \mathbf{F}(z_m, z_0) \mathbf{D}(z_0) \mathbf{W}^{SR}(z_0, z_n) \delta_k \mathbf{R}(z_n, z_n) \mathbf{W}^{SS}(z_n, z_0) \mathbf{S}(z_0) \mathbf{F}_j(z_0, z_m) \\
&= \sum_{k=1}^N [\mathbf{F}(z_m, z_0) \mathbf{D}(z_0) \mathbf{W}_k^{SR}(z_0, z_n)] [\mathbf{W}_k^{\dagger SS}(z_n, z_0) \mathbf{S}(z_0) \mathbf{F}_j(z_0, z_m)] \\
&= \sum_{k=1}^N \mathbf{D}_k^{SR}(z_m, z_m) \mathbf{S}_{kj}^{SR}(z_m, z_m).
\end{aligned} \tag{3.30}$$

Equation 3.30 shows that the bifocal cross imaging of the scattered Rayleigh waves with respect to the  $j^{\text{th}}$  subsurface grid point can be obtained by multiplication of one cross focal beam and a specific element of another cross focal beam. The latter is the calculated element at the  $j^{\text{th}}$  subsurface grid point.

### 3.5.3 Incoherent noise

Incoherent noise is caused by many factors and it is random in such a way that it does not follow a known physical model. Ambient noise varies from one area to another. For instance, ambient noise may overcome the signal in cultural areas. Open areas, on the other hand, like deserts have smaller ambient noise intensity. However, the only obvious way to assess the influence of ambient noise on image quality is by onsite measurements of this noise through noise records. Seismic data if available can also be used to measure the intensity of ambient noise from the pre-firstbreaks data, particularly in the far offsets. The availability of ambient noise data would allow including it in the focal functions computations. This data will be referred to as  $\mathbf{N}^A$  in the subsequent derivations.

As stated earlier, there are other factors that contribute to the incoherent noise. These include intra-array statics, source and receiver coupling, positioning errors, tilt, and instrument distortions. According to Muyzert and Vermeer (2004) the latter is the least significant and the specifications of current instrument are more than adequate. Yet, the most significant are the intra-array statics and the coupling issues. Tilt and positioning errors may become significant in rugged terrains if not properly taken care of. It should be emphasized that it is the data acquisition goal to strive for reducing these sources of noise, which is indeed one of the driving elements for single-sensor and single-source acquisition. The effects of these noise elements can be incorporated into the focal beam and focal function analyses. This is possible because the sources and receivers including their properties and positions are explicitly defined in the formulations. Any distributions of coupling variations (amplitude weights) and statics (time shifts) can be included within the source and receiver matrices.

#### **Cross resolution function for ambient noise**

The cross resolution function of ambient noise ( $\mathbf{N}^A$ ) at the  $j^{\text{th}}$  subsurface gridpoint on depth level  $z_m$  is defined as the confocal imaging of  $\mathbf{N}^A$  (for  $i$  ranging around  $j$ ) as:

$$\delta \mathbf{N}_{ii}^A(z_m, z_m) = \mathbf{F}_i^\dagger(z_m, z_0) \mathbf{N}^A \mathbf{F}_i(z_0, z_m). \quad 3.31$$

#### **Cross AVP-imprint function for ambient noise**

The cross AVP-imprint function will be the bifocal imaging of  $\mathbf{N}^A(z_0, z_0)$  for the  $j^{\text{th}}$  subsurface gridpoint at depth level  $z_m$ :

$$\mathbf{N}_j^A(z_m, z_m) = \mathbf{F}(z_m, z_0) \mathbf{N}^A \mathbf{F}_j(z_0, z_m), \quad 3.32$$

Assessing the influence of ambient noise on the target image quality requires onsite measurement of such noise.

### 3.6 Concluding remarks

The previous sections establish a theoretical framework for integrating the acquisition geometry with the subsurface model, which is phase two of the survey design. The focal beams are utilized to compute two diagnostics: resolution function and AVP-imprint function. These diagnostics provide measures for the suitability of a proposed acquisition geometry using image quality (confocal and bifocal). The diagnostics are constructed without the need for explicit modeling of seismic reflection data. Rayleigh waves and ambient noise have to be modeled and measured respectively. In the formulation of the AVP-imprint function, a flat target reflector was assumed. A dipping reflector, however, can also be accounted for, see Volker (2002).

In summary, an acquisition geometry can be assessed using the focal beams and diagnostics calculated from them, where:

- The focal detector and focal source beams are used to separately assess the geometry of detectors and sources respectively.
- The focal resolution function is used to measure the spatial resolution at the target and to reveal whether spatial aliasing exists.
- The focal AVP-imprint function is used to show how the angle-dependent reflectivity function is sampled at the target. The AVP-imprint function gives the sampling function and its deviations from unity.
- The noise leaking into the final image is measured.

Computational aspects and various numerical examples will be presented in Chapter 4. More insight into the focal beams and the focal functions and how to interpret them will be gained from the numerical examples.

## Computational aspects and numerical examples

*This chapter presents numerical examples for the assessment of land 3D geometry designs, using focal beams and focal functions. Computational aspects of these beams and functions are discussed first. The selected computational methods are dictated by the subsurface model under consideration. For 1D subsurface models, wavefield extrapolation in the  $(k_x, k_y, \omega)$  domain is used because this method is fast. Wavefield extrapolation in the  $(x, y, \omega)$  domain is used in the case of a complex near-surface. The latter technique is also used in case of an acquisition surface with varying topography. Focal source and focal receiver beams are computed to assess the quality of respectively source and receiver geometries. The focal functions – resolution and AVP-imprint – are used to provide quantitative measures for image quality (resolution and amplitude accuracy). Focal beams and focal functions are presented for a simple 1D model to illustrate their properties. Two diagnostics are derived from the focal functions, being the image-fold and the effect of field arrays. Subsequently, the focal beams and focal functions are shown for a 1D model with scattered Rayleigh waves. The capability of field arrays to attenuate scattered Rayleigh waves is quantified. Three complex near-surface models are analyzed including one model with varying topography. Finally, differential-time-shift (DTS) gathers are generated to assess whether the underlying velocity model can be retrieved from the acquired data.*

### 4.1 Introduction

In the second phase of the design process, a model of the subsurface is included to optimize the initial geometry. Of course, this integration process of the initial design and the subsurface can be performed by explicitly modelling seismic data, computing an image by migration followed by characterizing this image. However, we will show that survey design can be better performed in an *implicit* way using the concept of focal beams as described in Chapter 3 of this thesis. The concept of focal beams allows design assessment by providing

separate quantitative metrics for the two focal beams (source and receiver), for the image amplitude, resolution, signal/noise and for the distortion in the angle-dependent reflectivity information (AVP-imprint). This chapter discusses the computational aspects of focal beams and focal functions. Furthermore, various numerical examples are presented to demonstrate how the focal beams and focal functions are used to answer specific questions related to geometry design. In addition, differential-time-shift (DTS) gathers, being constructed from the focal beams, are used to assess the ability of retrieving the underlying velocity model from the data.

As formulated in Chapter 3, focal beams and focal functions are functions of four variables. These variables are space-coordinates  $(x,y,z)$  and temporal frequency  $(\omega)$  or time. The advantage of using temporal frequency is that computations can be independently done per frequency component, which is the efficiency aspect of the method. The calculations performed in this chapter are carried out for a range of frequencies. The focal beams are calculated for a target area of  $1km$ -by- $1km$  – with the target point being in the center – and are visualized in the space-coordinates at image time  $(t=0)$ . In addition, the focal beams are visualized in the Radon domain at the zero intercept-time  $(\tau=0)$ . The resolution function is visualized along the space-coordinates, both at and around  $t=0$ . The AVP-imprint function is displayed in the Radon domain at  $\tau=0$ .

Throughout this chapter, the following display scaling convention is used:

- The focal beams are presented in both the spatial and the Radon domains. The spatial domain is displayed on a dB scale normalized to unity (0 dB) with respect to the maximum amplitude. The Radon domain is displayed as a function of the horizontal ray parameters  $p_x$  and  $p_y$  on a linear scale from zero-to-one also normalized with respect to the maximum amplitude. Exception to this convention is the presentation of the focal beams for noise in the Radon domain where they are displayed on a dB scale.
- The resolution function at the image time  $(t=0)$  is presented in the spatial domain on a dB scale normalized to unity. In addition, the display of the resolution function around image time is shown as 2D cross-sections along the x-coordinate and the y-coordinate using wiggle traces normalized to unity with respect to the maximum amplitude.
- The AVP-imprint function is presented in the Radon domain on a linear scale, and on a dB scale for the noise.
- The 3D DTS-gather is displayed as a 2D panel using wiggle traces normalized to unity with respect to the maximum amplitude of the gather.

## 4.2 Focal beams and focal functions

### computational aspects

In Chapter 3 a theoretical framework was presented for the assessment of acquisition geometries using focal beams. These beams are calculated assuming a user specified subsurface model and an initial acquisition geometry. A beam computation involves three steps as shown in Figure 4.1. The first step includes *forward* extrapolation of the wave field generated by a point source located at the target and measured by a fine grid at the acquisition surface. The second step involves *resampling* this finely sampled impulse response according to the acquisition geometry. The third step is *inverse* extrapolation of the resampled wavefield from the acquisition surface to a subsurface area around the target point. This step represents the actual focal beam computation. The inverse extrapolation algorithm of the migration software to be used in data processing can be incorporated in the third step. However, it should be noted that the forward modelling part ought to be made as accurate as possible as it represents the actual wavefield propagation in the Earth. Note that this is fundamentally different from Duquet et al. (1998), who recommend modelling seismic acquisition using the migration algorithm adjoint.

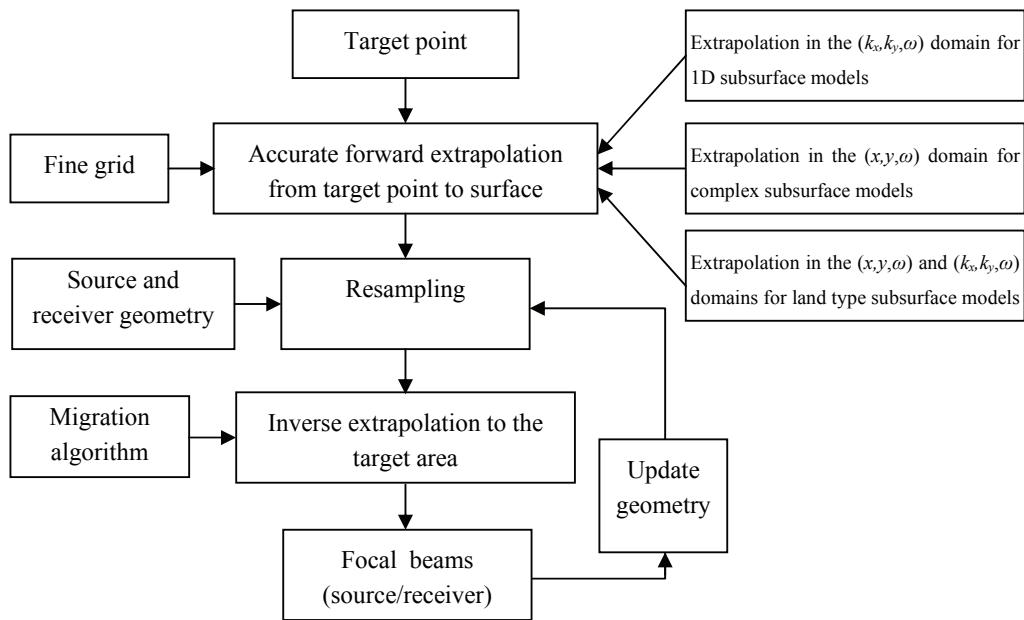


**Fig. 4.1** Steps involved in the computation of focal beams starting with a target point and ending with the source and receiver focal beams for that target point. The process can be efficiently repeated for different geometries. It is advised to do this in an interactive manner.

Subsequently, focal functions are calculated from the focal beams by multiplication in the space domain (resolution function) and wavenumber domain (AVP-imprint). The selection of the extrapolation algorithm is governed by the subsurface model under consideration and the required accuracies. Of course, the speed of the computational method is also of a concern. A general review of the most used methods in forward modelling of seismic data is given by Krebs (2004).

#### 4.2.1 1D subsurface model

1D subsurface models only vary with depth (see Figure 4.2a). For this simple case, the computation of the focal beams can be efficiently carried out in the  $(k_x, k_y, \omega)$  domain. The wavefield is extrapolated through the layers of the subsurface model by multiplication with the well-known phase-shift operator (Gazdag, 1978). Volker (2002) presented a method for computing the focal beams for a homogeneous subsurface based on Fourier transformation of the acquisition sampling function. Volker's method is very fast and can be easily extended to 1D subsurface models. However, because this method is based on a far-field assumption, it is less accurate than the extrapolation in the  $(k_x, k_y, \omega)$  domain. This particularly applies for targets that are relatively shallow compared to the offsets of the geometry design. In this thesis we choose accuracy, and therefore, the  $(k_x, k_y, \omega)$  extrapolation is used.

#### 4.2.2 Seismic noise

The effects of scattered Rayleigh waves can be directly included in the focal beam computation, as discussed in Chapter 3. Other types of seismic noise such as direct Rayleigh waves and incoherent noise can be incorporated in the focal functions. This is performed by using the same inverse extrapolation operators used in the computation of the focal to image modelled Rayleigh waves and incoherent noise as measured in the intended acquisition area. However, it is advocated that the acquisition design requirements for scattered Rayleigh waves should be sufficient to meet the requirements for direct Rayleigh waves. This is valid under the assumption that scatterers are randomly distributed in the near-surface. In this case, the predominant apparent velocity of the scattered Rayleigh waves is equal to the apparent velocity of the direct Rayleigh waves.

In the computation of the focal beams for scattered Rayleigh waves, the forward extrapolation from a scatterer close to the surface to all of the acquisition surface gridpoints can be approximated using the 2D Rayleigh II operator (Berkhout, 1980) defined for the  $(x, z, \omega)$  domain. Note that the 3D Rayleigh II operator defined for the  $(x, y, z, \omega)$  domain is equivalent to the phase shift operator we use to forward and inverse extrapolate the signal in the  $(k_x, k_y, \omega)$  domain. The choice of the 2D Rayleigh II operator is made because Rayleigh waves travel only along the surface and exhibit cylindrical spreading rather than spherical spreading. This modeling approach for calculating the Green's functions of scattered

Rayleigh waves is not as accurate as, for instance, elastic finite-difference methods. However, it should be accurate enough to highlight first-order effects that have to be taken into consideration during the acquisition design. The reader can refer to Aki and Richards (2002) for an elaborate coverage of Rayleigh waves. In this thesis, the scattered Rayleigh waves are computed assuming a random distribution of scatterers in a homogeneous near-surface layer.

### 4.2.3 1D subsurface model overlain by a complex near-surface

Focal beams can be computed with varying accuracies for complex subsurface models using different forward modelling methods such as ray-tracing, wavefield extrapolation in the frequency-space domain, and finite difference. Wavefield extrapolation has been used by van Veldhuizen and Blacqui re (2003) and Thorbecke et al. (2004) for forward and inverse extrapolation in complex subsurface. We also use this method for the computation of focal beams in the case of 1D subsurface models overlain by a complex near-surface as shown in Figure 4.2b. This type of subsurface models is typical for land areas in the Middle East. In the computation of the focal beams through such a model, a hybrid approach is used. In this approach forward and inverse wavefield extrapolation is performed using a phase-shift operator in the  $(k_x, k_y, \omega)$  domain for the simple 1D part of the subsurface model. Optimized short phase-shift operators defined in the  $(x, y, \omega)$  domain are used for forward and inverse wavefield extrapolation through the complex near-surface. This hybrid approach is used to optimize for accuracy and speed. Note that extrapolation in the  $(x, y, \omega)$  domain is a computationally intensive convolutional process while extrapolation in the  $(k_x, k_y, \omega)$  domain is an efficient multiplicative process. We also honor the rugged topography through an approach similar to migration with zero-velocity (Beasley and Lynn, 1992). Since we are performing wavefield extrapolation using short operators, we only zero the wavefield at the topography but not the velocity. Remember that Figure 1.8 of Chapter 1 exhibits some properties of a typical land subsurface model showing also the body waves in this model.

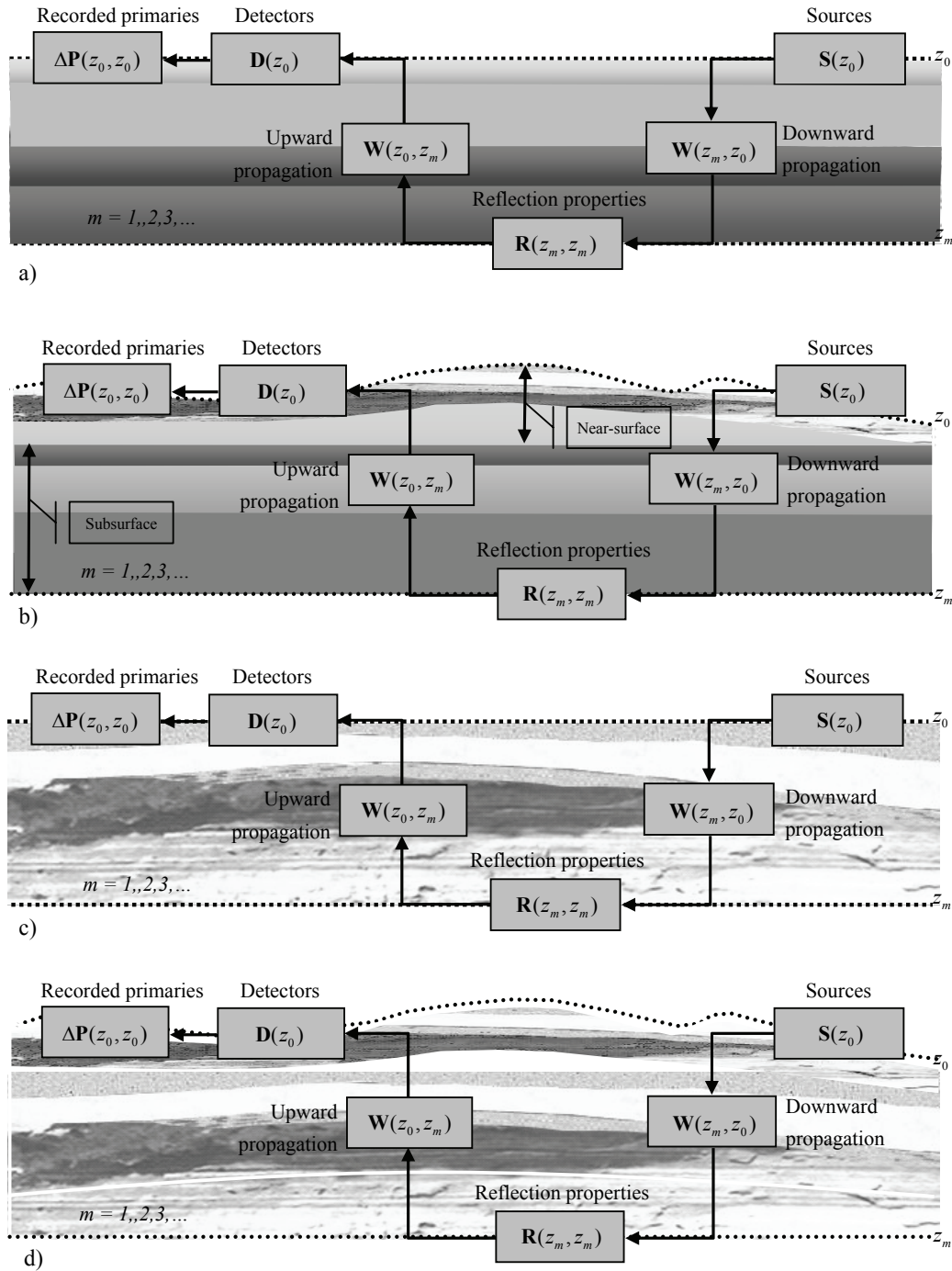


**Fig. 4.2** Subsurface models, a) 1D model; b) 1D model overlain by a complex near-surface; c) A complex subsurface model overlain by a simple near-surface; and d) A complex subsurface overlain by a complex near-surface model.

### 4.3 Interpretation of focal beams and focal functions

Seismic signals are generated and also detected at discrete locations on the acquisition surface over a limited area (aperture) on the upper boundary of the half-space. The detected wavefield is also discretized in time. Therefore, during acquisition of seismic data temporal and spatial discretization (sampling) of the wavefield occur. For the 3D case, the sampling is carried out along five coordinates being the time and four spatial coordinates, two for the source (i.e. source geometry) and two for the receiver (i.e. receiver geometry). All these sampling processes impose limitations on how well the subsurface layers can be resolved. The requirements for alias-free temporal sampling are manageable in practice because a time signal is measured in an analogue way and then it is band limited before digitization. On the other hand, space signals are never available in an analogue version. Therefore, the spatial sampling has to be carefully chosen. This choice can be assessed and optimized using the focal source and detector beams, and their combinations in the focal functions.

Bear in mind that the concept of focal beams enables a separate evaluation of the source and receiver geometries by analysing their respective beams in the space and wavenumber domains. Visualizing the focal beams in the spatial domain allows measurement of the resolving power of each beam. A high-quality beam is characterized by a narrow main-lobe and low-amplitude side-lobes. Note that the 3D beam response at the target point is a first-order cylindrical Bessel function (Berkhout, 1984). Aliasing is also measured by the focal beams. Aliasing in the beams can be allowed provided the aliased energy does not occur in the same area of both focal beams. For instance, a cross-spread geometry will produce aliasing in the source and detector focal beams in two orthogonal coordinates as observed in the spatial domain. This means that the aliasing will cancel if the two beams are combined to construct the resolution function. The detector beam of an adequately sampled common source gather must only exhibit the main-lobe and its adjacent side-lobes with no energy away from them. This is equally valid for common receiver gathers.

The resolution function shows how well a point diffractor at the subsurface gridpoint under consideration can be resolved. Several authors wrote about resolution estimation for acquisition geometries while considering homogeneous subsurface velocity models. See for example von Seggern (1994), and Vermeer (1999). All authors considered the main-lobe of the resolution while not paying attention to the importance of side-lobes (Volker, 2002). Most of the differences in resolving power of acquisition geometries are contained in the side-lobes. This is particularly true for 1D velocity models. In general, if aliasing criteria are taken into consideration, the main-lobe of the focal resolution function can be reduced by increasing the aperture. The side-lobes can be reduced by reducing the sampling intervals. The last two points assume the absence of major shadow zones i.e. illumination problems. For good resolution, it is sufficient to adequately sample two orthogonal coordinates out of the four spatial coordinates  $(x_s, y_s, x_r, y_r)$  of a 3D geometry.

However, the requirements of low amplitude variations between adjacent target points caused by the acquisition geometry (footprint) impose further constraints on the characteristics of the beams. For amplitude accuracy, both focal source and detector beams should exhibit a broad band and uniform amplitude when visualized in the Radon domain. The broad band is a function of the aperture while the amplitude uniformity is a function of source and receiver spatial sampling.

The AVP-imprint function shows for one target point the range of dip angles and their azimuths that will be present in the data i.e. the angles that have been illuminated and detected. The ideal AVP-imprint function should exhibit a uniform unit amplitude over all angles up to  $90^\circ$  (and possibly beyond) for all azimuths. Yet, this would require a very large acquisition aperture and very dense surface sampling for both source and receiver and a simple subsurface. Remember that the AVP-imprint exhibits how the reflectivity at the target is sampled. Therefore, the designer should know the range of angles that need to be adequately sampled at the target interfaces. This is a function of the elastic properties at these interfaces. The required angles should be at least those that would allow proper inversion for the elastic properties. This information should be provided by the third node of the seismic value chain that is reservoir characterization (see Figure 1.8). Having determined the range of angles that have to be present in the pre-stack data, the designer should seek a uniform unit amplitude AVP-imprint function over such range. If anisotropy is present, then the range should be uniform for all azimuths. Note that the bandwidth of the AVP-imprint function also affects the possibility of velocity estimation from the data. The broader the band the more accurate the inverted velocity model will be.

#### **4.4 Influence of subsurface complexity on energy distribution**

The image quality of any target point is determined by the acquisition geometry and the influence of the subsurface model on the energy registered at the acquisition surface. In this section we analyze how different subsurface complexities influence the energy distribution. Figure 4.2 shows four combinations of plausible subsurface models. This thesis focuses on common land subsurface models characterized by a simple subsurface and a complex near-surface (Figure 4.2b). Therefore, before we perform assessment of land geometries using the focal beams, it is prudent to analyze the energy distribution in some models.

Nine 3D subsurface models with varying complexity depth and velocity were considered. The background velocity of each model is 3000 m/s and the velocity was varied from 1000 to 4500 m/s. Forward extrapolation using these models was performed to calculate the energy distribution in each model. Figures 4.3 to 4.5 exhibit the results of these modelling exercises. The subsurface models that have the complexity away from the acquisition surface showed the most distortions to the energy distribution. The closer the complexity to the target the more distorted the wavefield becomes before it reaches the surface. On the other

hand, a more uniform energy distribution is obtained when the complexity is close to the acquisition surface as exhibited by Figures 4.3a, 4.4a, and 4.5a. These figures show some indications that acquisition grid points close to the cliff will not illuminate the target point. This is a function of the elevation difference – which is about 300 m in this case – and the near-surface velocity. Additional modelling revealed that the higher the velocity and the elevation in the near-surface the less the illumination will be by acquisition grid points close to the sharp topographic variations. But this only affects a limited portion of the wavefield, which in turn, does not impose a serious problem if handled properly in processing.

In short, the complex near-surface has to be carefully considered during the acquisition design. The acquisition design should aim at attenuating noise of different kinds or allow their attenuation in processing. Furthermore, the acquisition design should allow removing the distortions caused by the near-surface from the signal in processing. The energy distribution analyses illustrated that the complex near-surface does not impose fundamental challenges that are not manageable. In other words, there does not seem to exist significant illumination problems that can be attributed to the complex near-surface. This aspect will be further illustrated using the focal beams analyses in the subsequent examples where different near-surface complexities are considered.

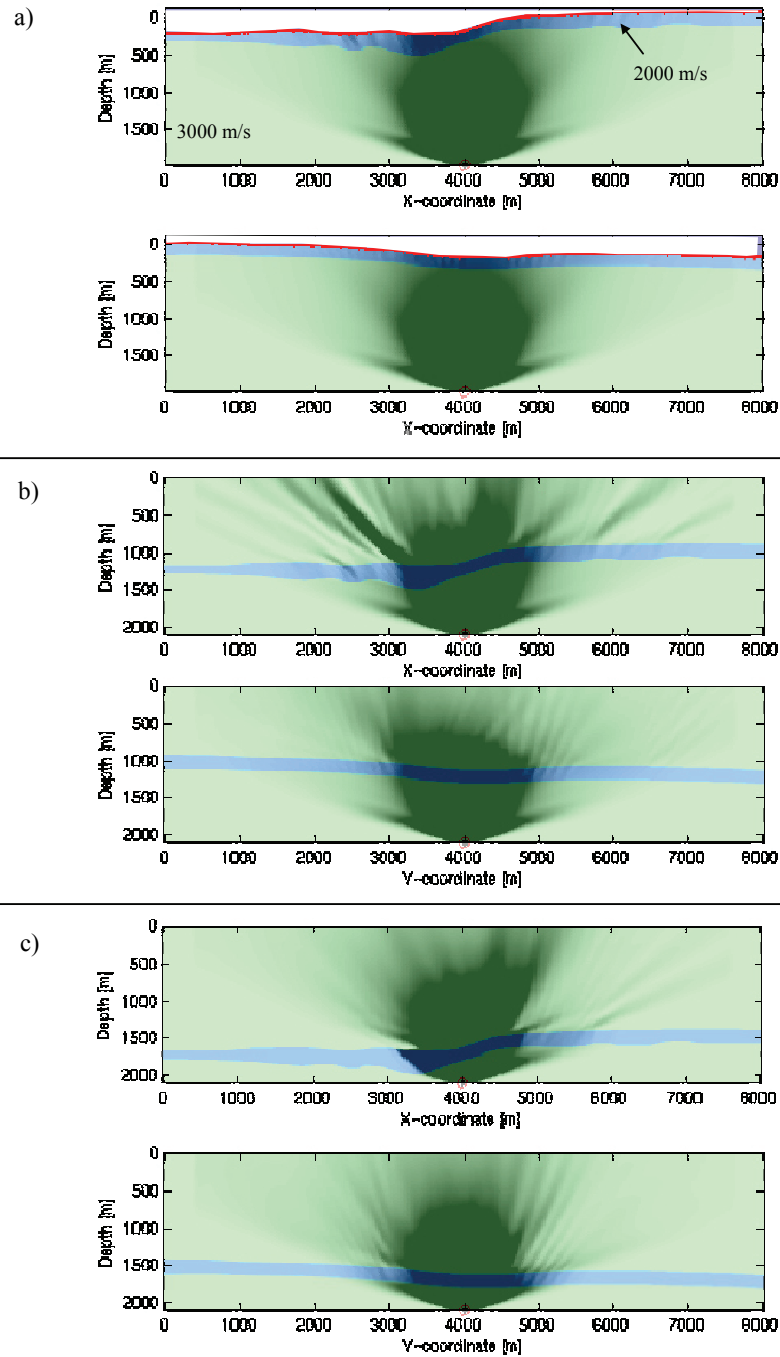


**Fig. 4.3** Two cross sections of the relative energy distribution in the subsurface along the  $x$ -direction (top) and along the  $y$ -direction (bottom) for subsurface models with a low-velocity-anomaly at different depths as shown by the background color, a) anomaly near the surface; b) anomaly at intermediate depth; c) anomaly close to the target point. The red line in (a) indicates the surface elevation.

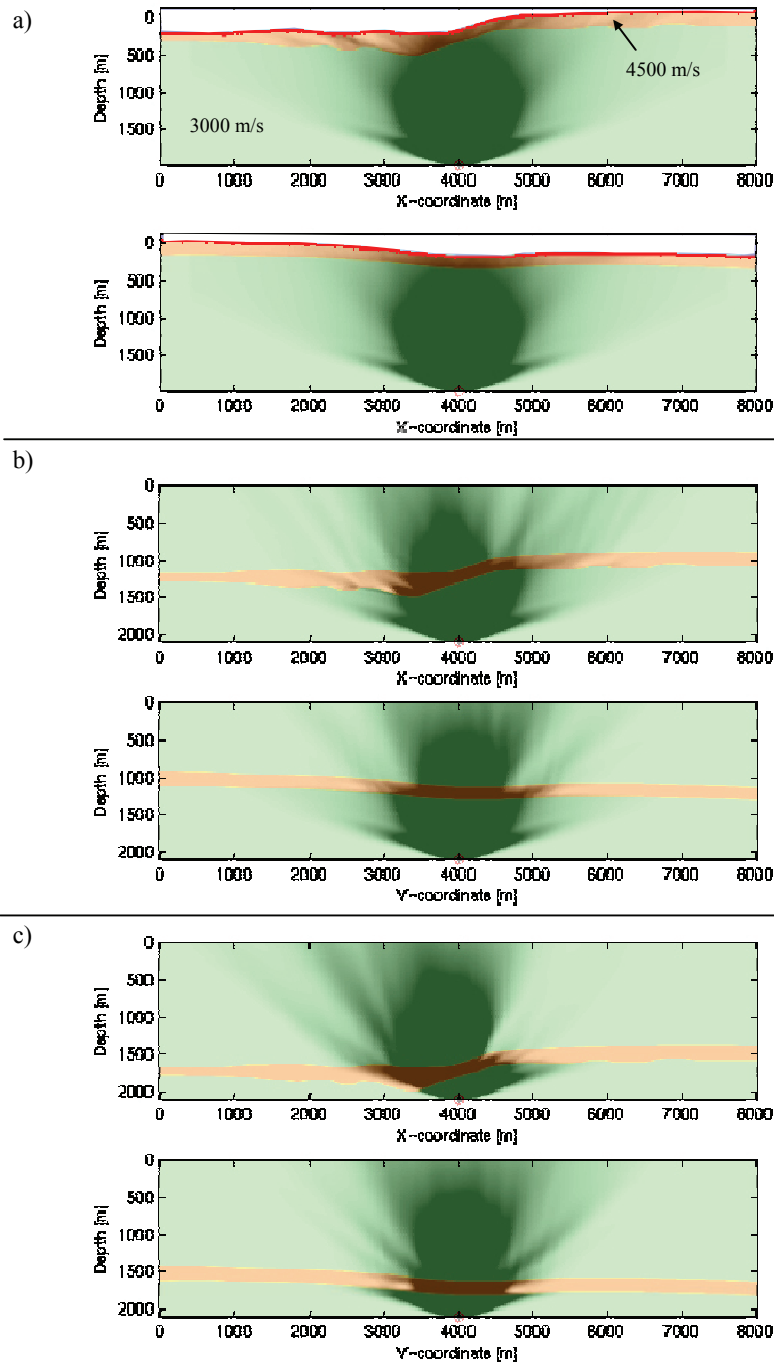


**Fig. 4.4** Two cross sections of the relative energy distribution in the subsurface along the  $x$ -direction (top) and along the  $y$ -direction (bottom) for subsurface models with a high-velocity-anomaly at different depths as shown by the background color, a) anomaly near the surface; b) anomaly at intermediate depth; c) anomaly close to the target point. The red line in (a) indicates the surface elevation.

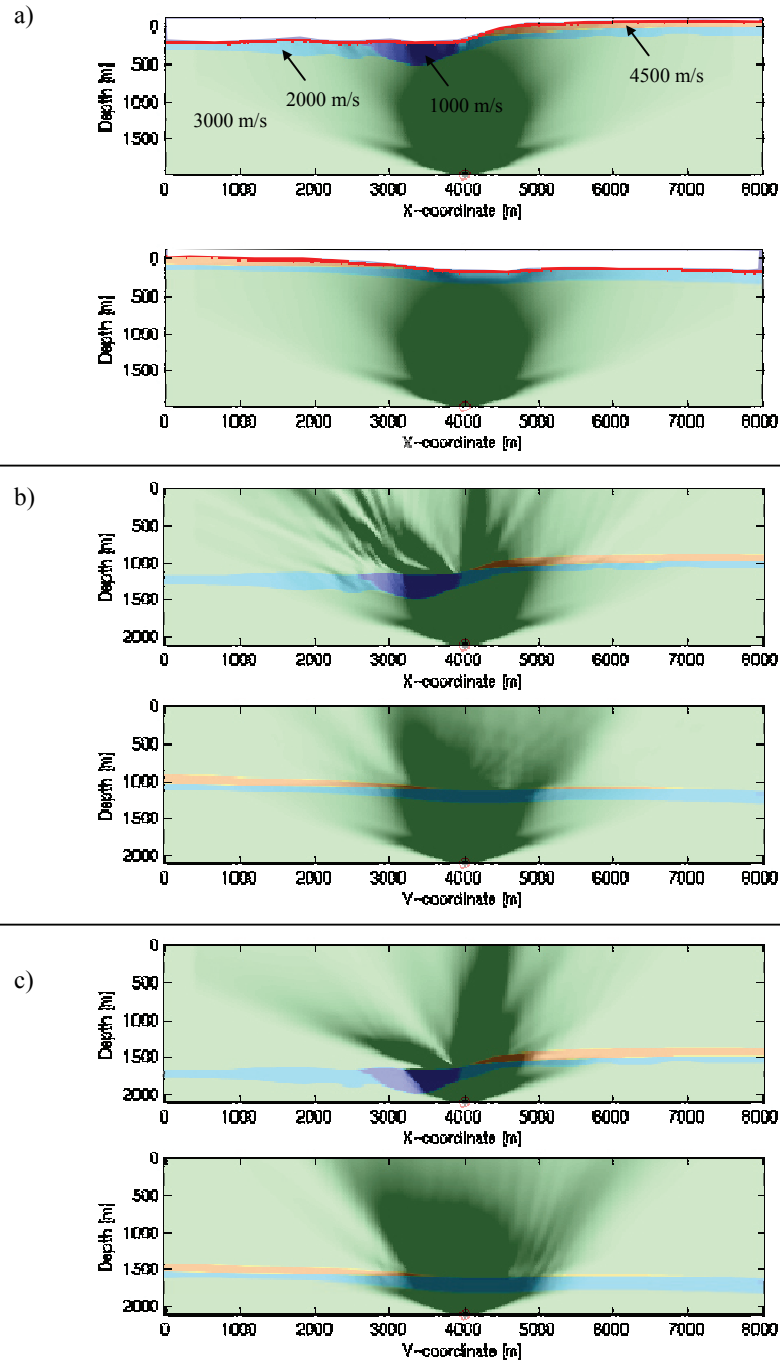


**Fig. 4.5** Two cross sections of the relative energy distribution in the subsurface along the  $x$ -direction (top) and along the  $y$ -direction (bottom) for subsurface models with a varying-velocity-anomaly at different depths as shown by the background color, a) anomaly near the surface; b) anomaly at intermediate depth; c) anomaly close to the target point. The red line in (a) indicates the surface elevation.

## 4.5 Numerical examples

This section presents examples to demonstrate the assessment of land geometries using the focal beams and the focal functions. These examples will use the same geometry design with a cross-spread template consisting of 144 sources and 144 receivers as shown in Figure 4.6a. The source station interval is 25 meters and the receiver station interval is also 25 meters. This template is rolled over a distance of 300 meters 7 times in both cross-line and inline directions resulting in 49 cross-spreads (Figure 4.6b). This geometry produces a CMP fold of 36. Exceptions to this geometry will be stated when used. The analyzed target point is located in the center of the area at depth of 2000 meters. The focal beams are computed for a frequency band of 10 to 50 Hz. The wavelet has a cosine-squared-shaped spectrum.

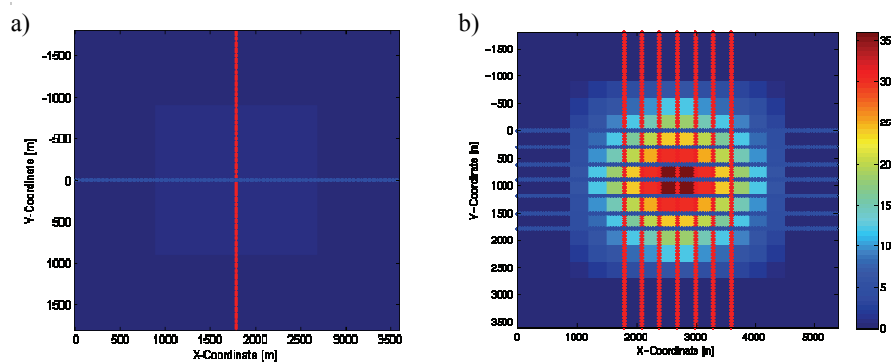


**Fig. 4.6** a) Design template, sources (red) and receivers (blue); and b) The entire design geometry. (The background color refers to the CMP fold)

The subsequent examples will address different design issues for different land-type subsurface models:

- Focal beams and focal functions for a 1D velocity model;
- Scattered Rayleigh waves and the effects of field arrays to attenuate them;
- The effects of field arrays on temporal frequencies;
- Low-velocity near-surface anomaly and the effects of applying statics;
- High-velocity near-surface anomaly;
- Narrow and wide geometries for a complex near-surface velocity model with topography;
- Fundamental problems with statics.

### 4.5.1 1D velocity model

The main objective of this example is to show the focal beams and focal functions characteristics for a simple velocity model before introducing complex models. More insight about the interpretation of the focal beams and focal functions can be gained from this example. In addition, some quantitative attributes that can be extracted from the focal beams analyses are discussed. These attributes include the differential-time-shifts (DTS) gather and the image-fold, and the wavelet spectrum at the target compared to the source wavelet.

The velocity model used in this section is very simple and consists of a flat layer-cake down to a depth of 2000 m where the target point is located in the spatial center of the model. Figures 4.7a and 4.7b show two cross-sections through the center of the model along the  $x$ -direction and the  $y$ -direction respectively. The surface topography is assumed to be flat for this model.

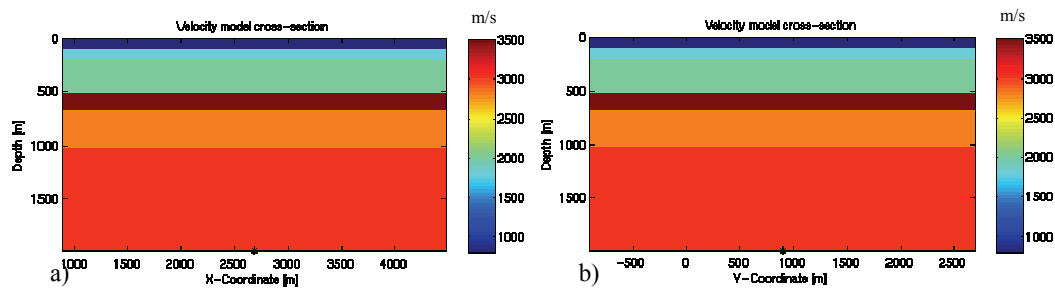


*Fig. 4.7 Two cross sections through the center of the velocity model with a simple near-surface, a) along the  $x$ -direction; and b) along the  $y$ -direction. Both figures are to scale.*

#### *Focal beams and focal functions*

The computed focal beams and focal functions are shown in Figure 4.8a to 4.8f for the full geometry. Note that the focal beams are obtained by summing the beams of every stationary geometry (template). Also the focal functions result from summing the functions of the different templates. In this example, the focal source and detector beams show the same characteristics because the subsurface model geometry is symmetric and also the source and detector geometries are similar. The focal detector beam exhibits a narrower main-lobe in the  $x$ -direction than in the  $y$ -direction. This is because the receiver sampling along the  $x$ -direction is finer than along the  $y$ -direction. These arguments are the same for the focal source beam in the reverse directions. Furthermore, the focal detector beam shows some aliasing effects in the  $y$ -direction while the focal source beam shows the aliasing effects in the  $x$ -direction.

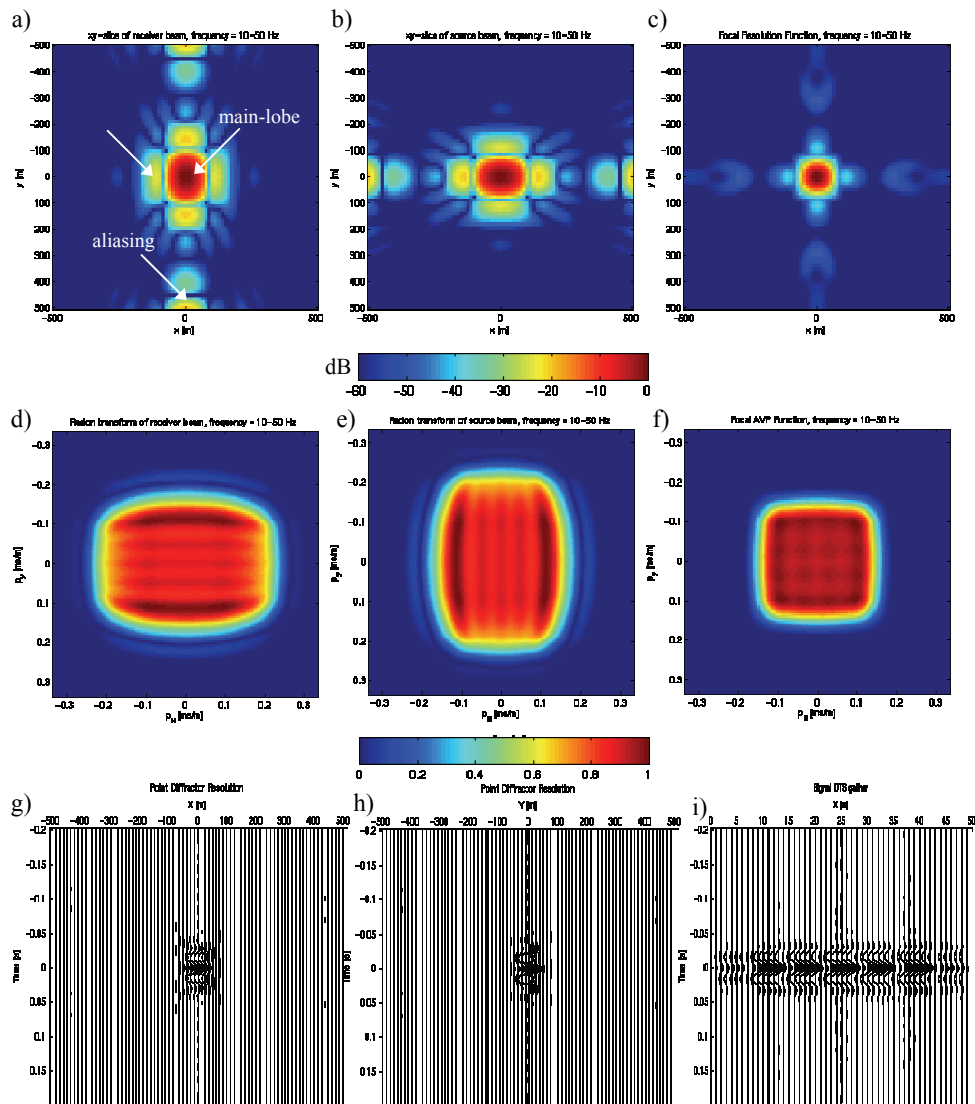


**Fig. 4.8** a) Focal detector beam in space at  $t=0$ ; b) Focal source beam in space at  $t=0$ ; c) Resolution function in space-time; d) Focal detector beam in the radon domain at  $\tau=0$ ; e) Focal source beam in the radon domain  $\tau=0$ ; f) AVP-imprint function; g) A cross-section through the center of the resolution function volume along the  $x$ -direction; h) A cross-section through the resolution function volume along the  $y$ -direction; and i) A 3D DTS gather displayed as a 2D panel. The scale of a, b, and c is in dB. The scale of d, e, and f is from 0-1. The scale of g, h, and i is linear with respect to the maximum of the display.

Fortunately, these aliasing effects occur in two orthogonal directions which means that they will cancel in the final image as illustrated by the focal resolution function (Figure 4.8c). This function shows a symmetric narrow main-lobe and low side-lobes without aliasing occurring away from the target point. The AVP-imprint function shows quite a uniform

sampling of the reflection angles. There are no obvious deficiencies of the used geometry for the analyzed frequency band and the applied wavelet with its cosine-squared-shaped amplitude spectrum. The bandwidth of the AVP-imprint function can be increased by increasing the maximum inline and/or cross-line offsets. Increasing these offsets will also result in reducing the width of the main-lobe of the focal resolution function. Note that the side-lobes of this function exhibit a low amplitude which suggests that reducing the source and receiver intervals will not further improve the resolution. Bear in mind that the primary objective of computing the focal beams and focal functions is to evaluate and optimize the initial geometry parameters. Clearly, we see that the focal beams and focal functions can direct the designer to the geometry parts that need updating: source or receiver, aperture or sampling, template or intra-template. This aspect will be more emphasized as the subsequent examples are discussed.

The AVP-imprint function exhibited by Figure 4.8f represents the AVP information at  $\tau=0$  i.e. the summation of all frequencies in the Radon domain after applying the wavelet weight. The geometry imprint on each frequency is different. High frequencies are more sensitive to the sparseness of the geometry. This information is available in our computational method. The AVP-imprint function calculated for different bandwidths using the model of Figure 4.7 is shown in Figure 4.9. It is clear from this figure that the receiver and source line intervals become more apparent as the frequency increases. This can be visualized by displaying the AVP-imprint as a function of  $p_x$ - $f$  or  $p_y$ - $f$  as shown in Figures 4.9e and 4.9f. These two cross-sections are displayed before applying the wavelet weights.

#### *Focal resolution function as a function of space and time*

The resolution function can be constructed as a volume in space-time domain since the modelling was performed for a range of frequencies. Figures 4.8g and 4.8h show two cross-sections through the resolution function volume along the  $x$ -direction and the  $y$ -direction respectively. These images give an indication of how diffractions and reflections from the target point under consideration will interfere with points within its vicinity since these time images are very similar to depth images. In addition, aliasing that might occur at different depth levels around the target can be revealed by these displays.

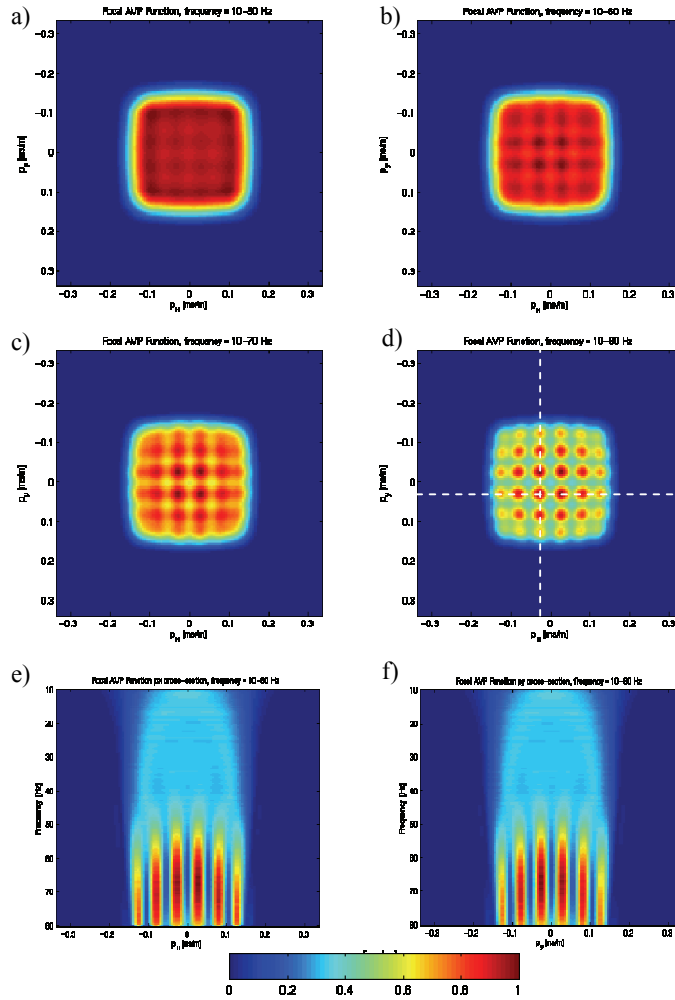


**Fig. 4.9** AVP-imprint functions for different frequency bands, a) 10-50 Hz; b) 10-60 Hz; c) 10-70 Hz; d) 10-80 Hz; e) A cross section through the AVP-imprint volume ( $p_x, p_y, f$ ) along the  $p_x$  axis along the horizontal white dashed-line on (d); and f) A cross section through the AVP-imprint volume along the  $p_y$  axis along the vertical white dashed-line on (d).

#### DTS gather and image fold

A 3D DTS gather can be constructed with each trace generated from a cross-spread as shown in Figure 4.8i. This DTS gather serves two purposes. First, it is used as a quality control tool to check the inverse extrapolation accuracy which is measured by the flatness of the gather.

Therefore, this can be used to check the accuracy of the migration technique. Second, the relative amplitudes of the individual traces show which cross-spread has a complete Fresnel stack, and hence, which cross-spread actually contributes to the final image. The CMP fold of the used geometry is 36, however, the number of traces in Figure 4.8i that are within a 6 dB range below the highest amplitude is 25 which can be considered as the image-fold in this case. Note that the choice of 6 dB range is a user defined parameter.

To provide more insight into the image-fold, reflection data for the deepest target boundary at depth of 2000 m of the model in Figure 4.7 were modelled. The modelling was performed for only one template (see Figure 4.6a) since the subsurface velocity model is 1D.

Consider  $\delta\mathbf{P}(z_0, z_0)$  to be the modelled 3D seismic data.  $\delta\mathbf{P}(z_0, z_0)$  is a matrix consisting of sub-matrices (see Figure 2.3) and it included primary reflections from one boundary. Each submatrix contains data from one cross-spread. The subscripts in the following formulations use the same convention as described in Section 3.2.1, but they refer to the sub-matrices. The confocal imaging of this data – according to Section 3.3.1 – can be expressed as:

$$\delta\mathbf{P}_{ii}(z_m, z_m) = \mathbf{F}_i^\dagger(z_m, z_0) \delta\mathbf{P}(z_0, z_0) \mathbf{F}_i(z_0, z_m), \quad 4.1$$

where  $\mathbf{F}_i^\dagger(z_m, z_0)$  is a row vector representing the focusing operator in detection for the  $i^{\text{th}}$  subsurface gridpoint and  $\mathbf{F}_i(z_0, z_m)$  is a column vector representing the focusing operator in emission for the  $i^{\text{th}}$  subsurface gridpoint. One frequency component of the target image  $\delta\mathbf{P}_{ii}(z_m, z_m)$  is obtained after the application of the two focusing steps at the same subsurface gridpoint where each sub-matrix will reduce to one element. The complete image is obtained by summing all the elements of  $\delta\mathbf{P}_{ii}(z_m, z_m)$ .

The so called CFP matrix (Bolte, 2003) can be constructed by time correlation of the focusing operators with the reflection data  $\delta\mathbf{P}(z_0, z_0)$ . This correlation is trace-by-trace, which corresponds to an element-by-element multiplication in our matrix notation. First, the focusing operator in detection is correlated with  $\delta\mathbf{P}(z_0, z_0)$ :

$$\text{Receiver traveltimes removed: } \mathbf{F}_{ik}^\dagger(z_m, z_0) \delta\mathbf{P}_{kl}(z_0, z_0), \quad 4.2$$

for all  $k$ 's and  $l$ 's, and then, the focusing operator in emission is correlated with the result of 4.2:

$$\text{Source and receiver travel time removed: } \mathbf{F}_{ik}^\dagger(z_m, z_0) \delta\mathbf{P}_{kl}(z_0, z_0) \mathbf{F}_{li}(z_0, z_m), \quad 4.3$$

for all  $l$ 's and  $i$ 's. Performing this process on all available frequency components followed by a summation over all frequencies (i.e. selecting the image time  $t=0$ ), a matrix containing the image-samples is obtained. Each sub-matrix in this matrix represents the data that will be stacked (Fresnel stack) to obtain a single-fold image of the subsurface gridpoint due to one cross-spread. This matrix of the modelled  $\delta\mathbf{P}(z_0, z_0)$  is shown in Figure 4.10. Obviously, the results of the summation carried out over the sub-matrices will differ. Sub-matrices that include the complete Fresnel zone will produce high amplitude traces as shown in Figure 4.8i. Incomplete Fresnel zone stack will result in low amplitude traces. Therefore, there is a one to one relation between this matrix and the DTS gather, which means that the latter can be used to calculate the image fold.

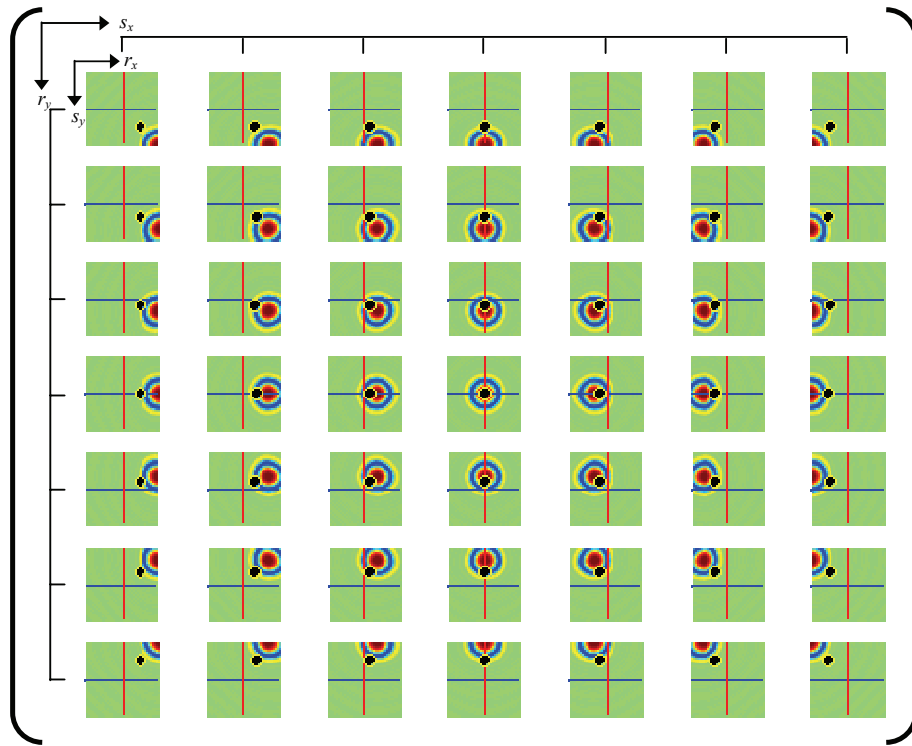


**Fig. 4.10** 2D representation of the 3D CFP-matrix where a time slice at  $t=0$  (image time) is shown for each cross-spread before summation. The red line indicates the source line while the blue line indicates the receiver line. The target point with respect to each cross-spread (template) is indicated by the black circle.

### Wavelet at the target

The focal beams can also be used to measure the effects of the geometry design on the temporal bandwidth at the target. The focal beam computation can be performed using a pre-defined wavelet (i.e. source wavelet). The resulting wavelet of a target point can be generated by summing its resolution function over the space coordinates to mimic a wavelet produced from reflecting waves. Figure 4.11a and 4.11b show the input source wavelet used in the focal beam computation and the resulting wavelet at the target. The resulting wavelet at the target does not seem to have been affected by the used geometry. Note that no frequency decay with depth has been applied in this analysis because we wanted to isolate the effects of the geometry from other effects. Any decay function can be applied after computing the beams. Computing the output wavelet at the target will highlight the effects of source and receiver arrays on the frequency bandwidth particularly in the case of using wide arrays and the presence of a high velocity near-surface that causes strong ray bending. This will be demonstrated in Section 4.5.3.

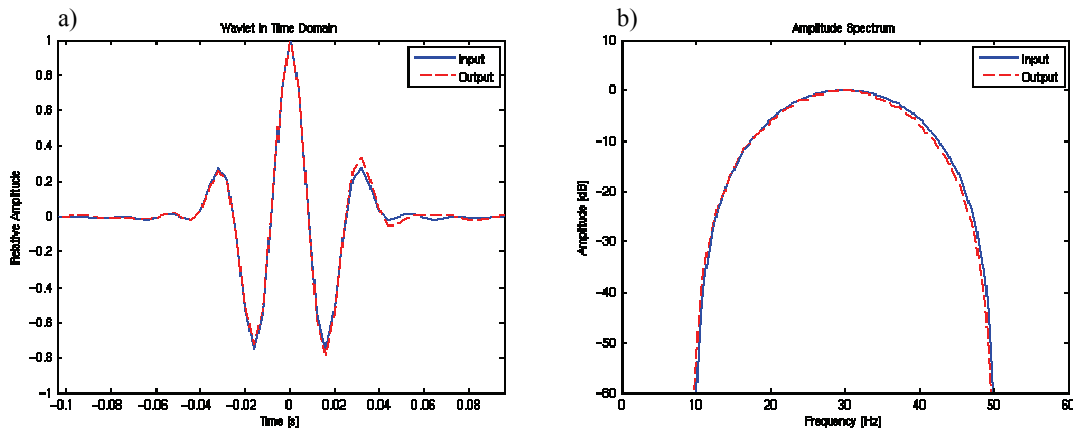


*Fig. 4.11 a) Input source wavelet and output target point wavelets in time; and b) Amplitude spectra of the input and output wavelets.*

### 4.5.2 1D model with scattered Rayleigh waves

The geometry used in this section is shown in Figure 4.12a and 4.12b; it is the same as the geometry used in the previous section. The velocity model that was used in the previous section is also used in this section as shown in Figure 4.12c and 4.12d. In addition, scattered Rayleigh waves are considered in the calculations of the focal beams and focal functions. The four scatterers indicated by the white circles in Figure 4.12b are irregularly distributed in the near-surface at depth of 100 m. The used Rayleigh wave velocity is 400 m/s (note that

the P-wave velocity in the near-surface of this model is 850 m/s). The used frequency bands are 10-50 Hz for the signal and 10-30 Hz for the scattered Rayleigh waves.

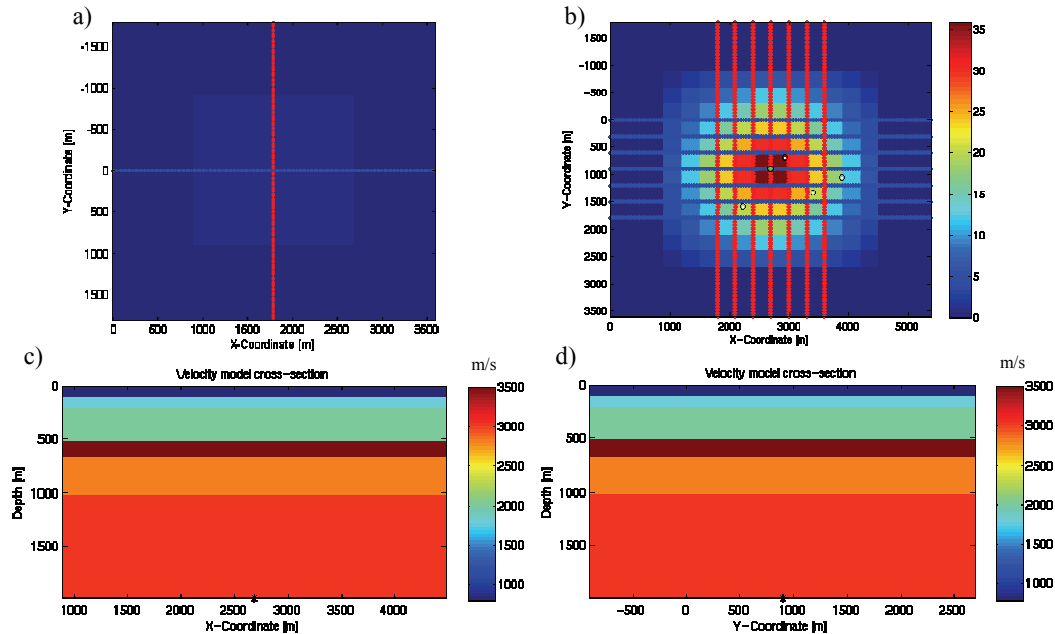


**Fig. 4.12** a) Design template, sources (red) and receivers (blue); and b) The entire design geometry; c) A cross section from the velocity model along the x-direction; and d) A velocity cross section along the y-direction. (The background color in (a) and (b) indicates CMP fold and white circles in (b) indicate the locations of the scatterers in the near-surface).

Since the seismic noise is considered to be an additive term according to the theoretical framework of Chapter 3, the focal beams and focal functions for the scattered Rayleigh waves can be modelled separately. Besides taking into account the cylindrical divergence of the Rayleigh waves compared to the spherical divergence of the body waves, the scattered Rayleigh waves have been magnified to 24 dB above the signal. It is observed in many areas with significant scattered Rayleigh waves that these waves have higher amplitudes than the reflection signals by 20-30 dB (Regone, 1998).

Figures 4.13a to 4.13f exhibit the focal beams and the focal functions for the scattered Rayleigh waves. Note that these focal beams and focal functions show the leakage of the Rayleigh waves into the target image (i.e. after migration). These displays are scaled relative

to the signal's displays of Figures 4.8a to 4.8f. In addition, the focal beams displayed in the Radon domain and the AVP-imprint function are shown on a dB scale. This is done to allow clear comparison between these displays and their counterparts when field arrays are introduced. The focal detector and source beams displayed in the space domain show different characteristics from the signal because of the locations of the scatterers with respect to the source and receiver geometries and, of course, the difference in velocity. The leakage in the resolution function is irregular and about 30 dB below the signal level. The irregularity is clearly visible in the space-time displays of the resolution function in Figures 4.13g and 4.13h. The AVP-imprint function (Figure 4.13f) shows the angles and azimuths that leak into the target image. These should guide the design of the field arrays.

The influence of the scattered Rayleigh waves on the image quality at the target is measured by the combined focal beams and focal functions for the signal and noise as shown in Figure 4.14. The relative amplitude of the target point can be quantified by summing the AVP-imprint function. The leakage of scattered Rayleigh waves will differ from one point to another in the image of the target. This can be inferred from the varying leakage in the resolution function. The designer should aim at reducing the amplitude variations caused by this leakage at the target points. Calculating the AVP-imprint function for different target points shall assist in determining this variation.

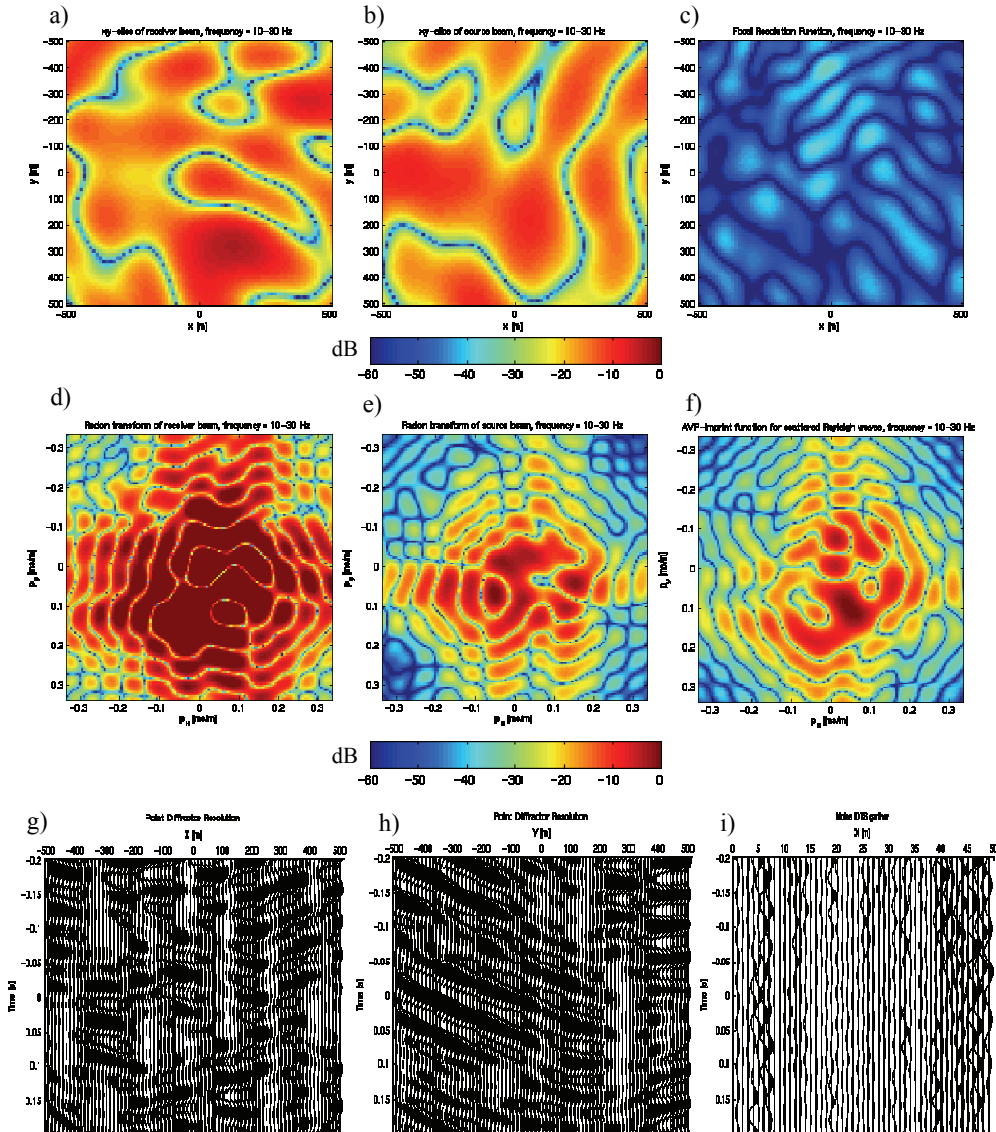


**Fig. 4.13** Scattered Rayleigh waves only, a) Focal detector beam in space at  $t=0$ ; b) Focal source beam in space at  $t=0$ ; c) Resolution function in space-time; d) Focal detector beam in the radon domain at  $\tau=0$ ; e) Focal source beam in the radon domain  $\tau=0$ ; f) AVP-imprint function for scattered Rayleigh waves, frequency = 10–30 Hz; g) A cross-section through the center of the resolution function volume along the  $x$ -direction; h) A cross-section through the resolution function volume along the  $y$ -direction; and i) A 3D DTS gather displayed as a 2D panel. The scale of a, b, c, d, e, and f is in dB. The scale of g, h, and i is linear with respect to the maximum of the display.

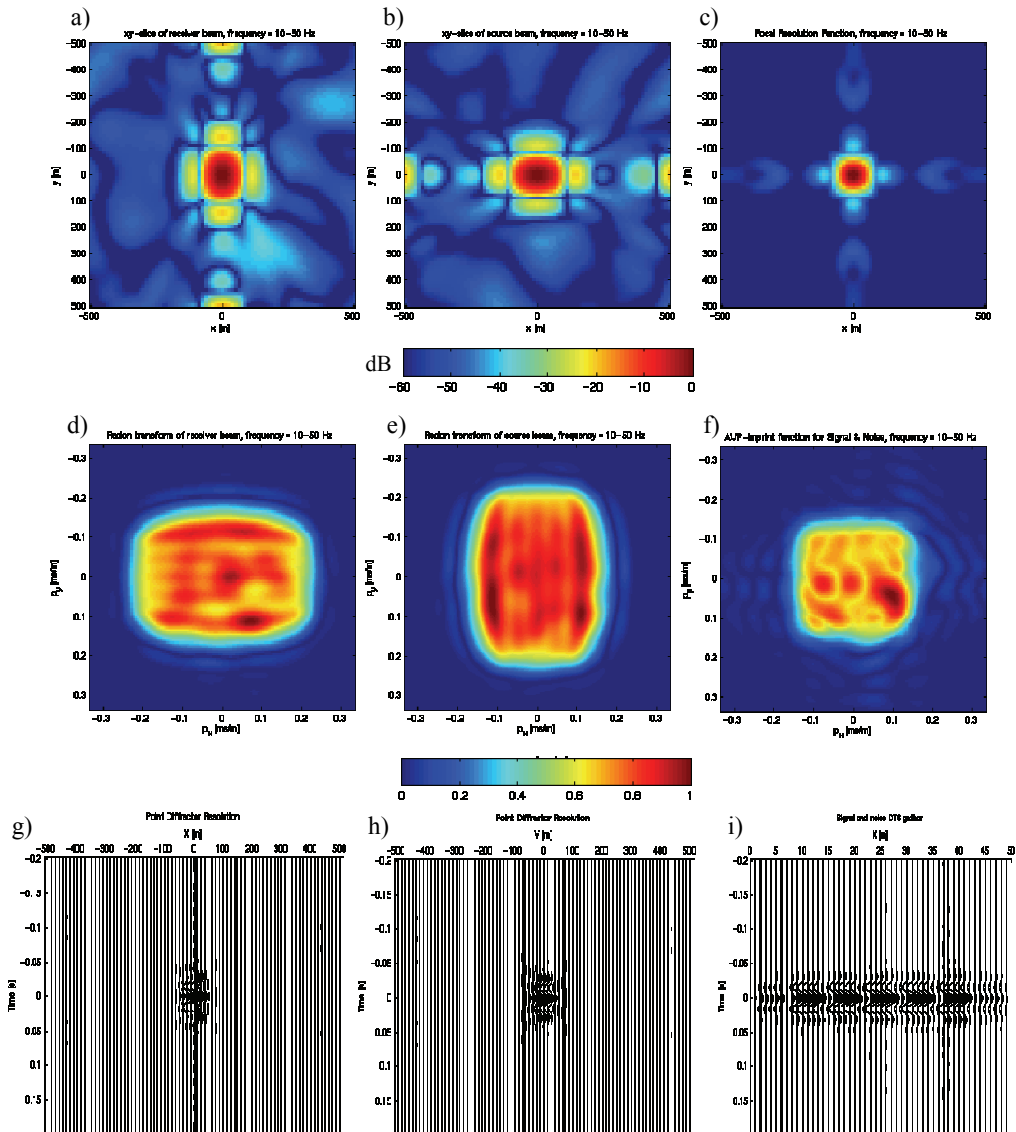


**Fig. 4.14** Signal plus scattered Rayleigh waves, a) Focal detector beam in space at  $t=0$ ; b) Focal source beam in space at  $t=0$ ; c) Resolution function in space-time; d) Focal detector beam in the radon domain at  $\tau=0$ ; e) Focal source beam in the radon domain  $\tau=0$ ; f) AVP-imprint function; g) A cross-section through the center of the resolution function volume along the  $x$ -direction; h) A cross-section through the resolution function volume along the  $y$ -direction; and i) A 3D DTS gather displayed as a 2D panel. The scale of a, b, and c is in dB. The scale of d, e, and f is from 0-1. The scale of g, h, and i is linear with respect to the maximum of the display. Compare with Figure 4.8.

### *Influence of field arrays*

Subsequently, the modeling was performed using the field arrays shown in Figure 4.15. The source array is linear consisting of five elements, while the receiver array is areal consisting of 25 elements. These configurations are often used in practical situations but with different number of elements per array. In the calculation of the beams, the first step (i.e. forward modeling) was carried out to all surface grid points that include the array elements. Next, summation over the array elements was carried out before performing the second step (i.e. imaging). This is done to mimic the real situation.

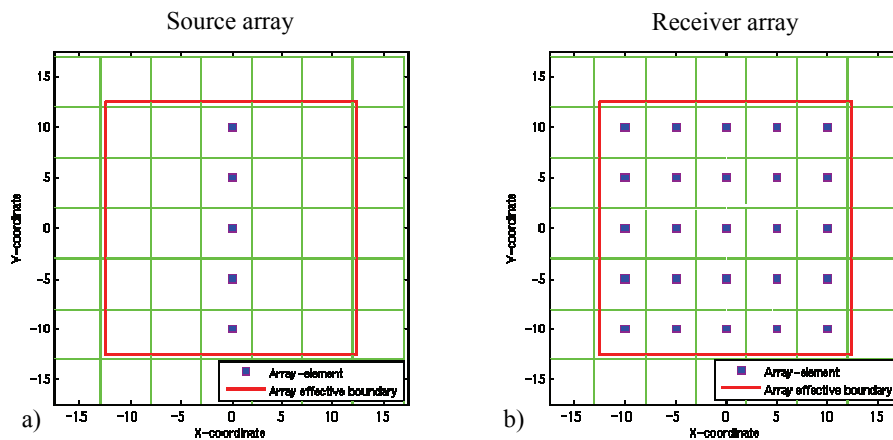


**Fig. 4.15** Field arrays, a) Linear source array consisting of five elements; and b) Areal receiver array consisting of 25 elements.

The focal beams and focal functions of the scattered Rayleigh waves after applying the field arrays are shown in Figure 4.16. The reduction of Rayleigh waves can be quantified by comparing the figure with Figure 4.13. The focal detector beam (Figure 4.16a) shows more reduction than the focal source beam because of the areal array applied. The highest leakage in the AVP-imprint function is about 24 dB below the signal. The combination of signal focal beams and focal functions with those of the scattered Rayleigh waves is shown in Figure 4.17. This figure shows that the field arrays have been effective in attenuating the scattered Rayleigh waves in this case. It should be noted that the higher the velocity of the Rayleigh waves the more they leak into the target image. In that case, the dimensions of the field arrays can be increased to an extent that they do not affect the signal bandwidth. The designer can circumvent this problem by laying out some receiver lines adjacent to each other to protect against the leakage of scattered Rayleigh waves.

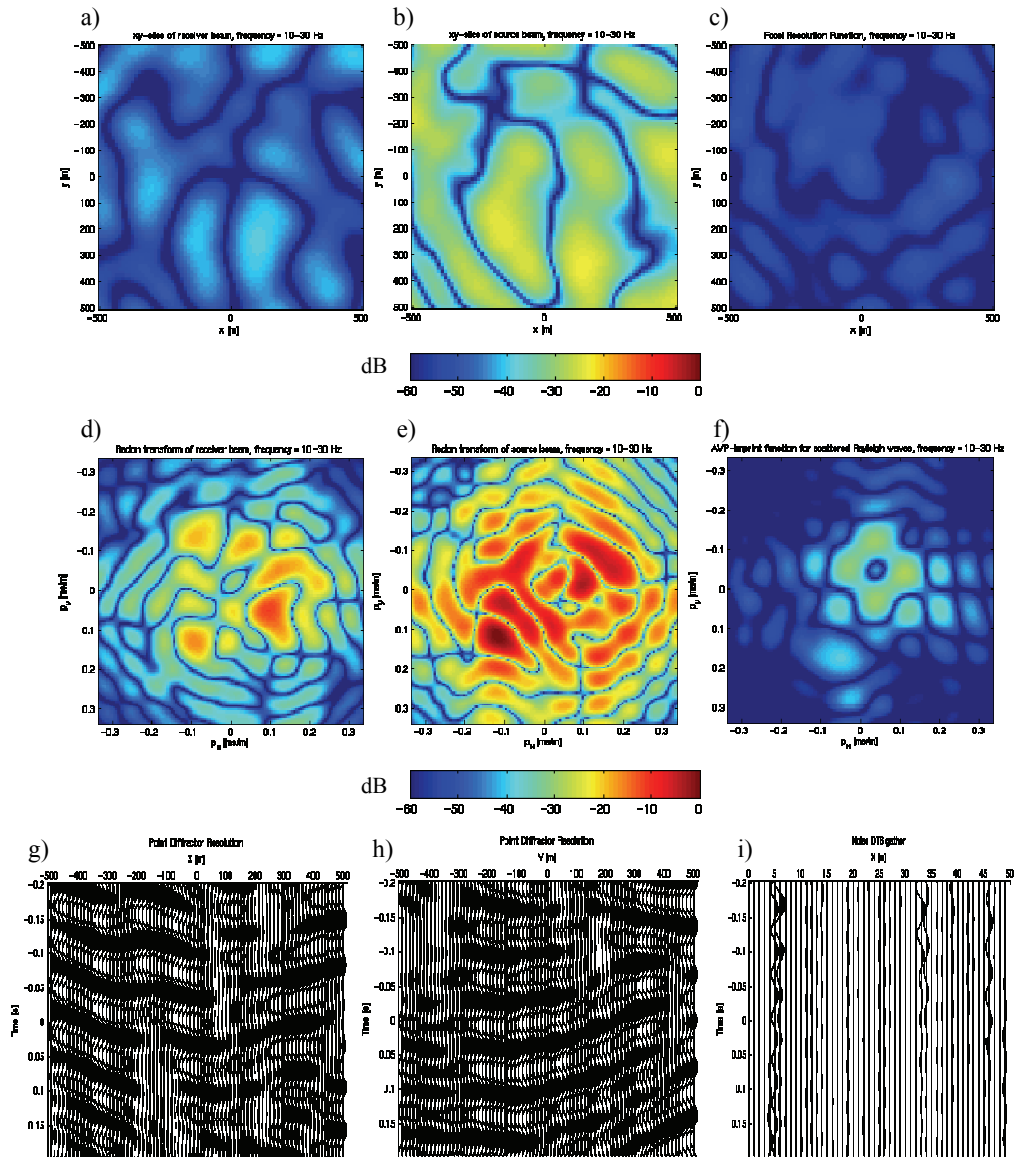


**Fig. 4.16** Scattered Rayleigh waves and influence of field arrays, a) Focal detector beam in space at  $t=0$ ; b) Focal source beam in space at  $t=0$ ; c) Resolution function in space-time; d) Focal detector beam in the radon domain at  $\tau=0$ ; e) Focal source beam in the radon domain  $\tau=0$ ; f) AVP-imprint function; g) A cross-section through the center of the resolution function volume along the  $x$ -direction; h) A cross-section through the resolution function volume along the  $y$ -direction; and i) A 3D DTS gather displayed as a 2D panel. The scale of a, b, c, d, e, and f is in dB. The scale of g, h, and i is linear with respect to the maximum of the display. Compare with Figure 4.13.

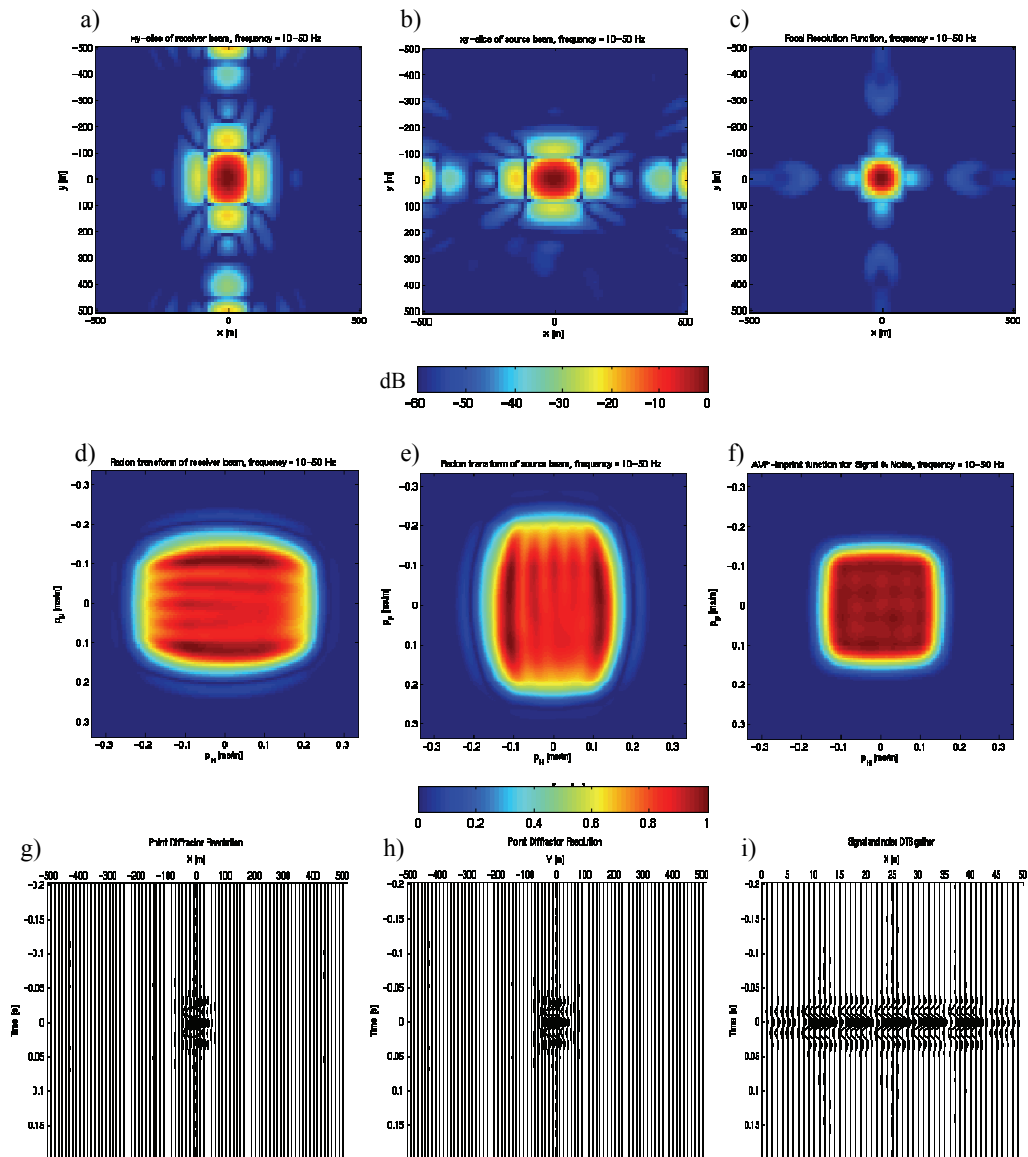


**Fig. 4.17** Signal and scattered Rayleigh waves with influence of field arrays, a) Focal detector beam in space at  $t=0$ ; b) Focal source beam in space at  $t=0$ ; c) Resolution function in space-time; d) Focal detector beam in the radon domain at  $\tau=0$ ; e) Focal source beam in the radon domain  $\tau=0$ ; f) AVP-imprint function; g) A cross-section through the center of the resolution function volume along the  $x$ -direction; h) A cross-section through the resolution function volume along the  $y$ -direction; and i) A 3D DTS gather displayed as a 2D panel. The scale of a, b, and c is in dB. The scale of d, e, and f is from 0-1. The scale of g, h, and i is linear with respect to the maximum of the display. Compare with Figures 4.8 and 4.14.

### 4.5.3 Effects of field arrays on signal bandwidth

The main objective of this example is to show the effects of source and receiver arrays on the signal frequency band at the target. It is stated in Chapter 2 that field arrays attenuate high frequencies particularly in case there are high velocity layers in the near-surface. Five numerical examples with different surface sampling intervals along the source and receiver lines of the geometry exhibited by Figure 4.18a and 4.18b are considered in this section. The subsurface model used in these examples is shown in Figure 4.18c and 4.18d but the first layer (indicated by the black/white stripes) velocity was varied. Two values are used: 800 m/s referred to as low-velocity-layer (LVL) and 3400 m/s referred to as high-velocity-layer (HVL). All the examples use a frequency band of 10-80 Hz. Table 4.1 summarizes the parameters used in the five examples.

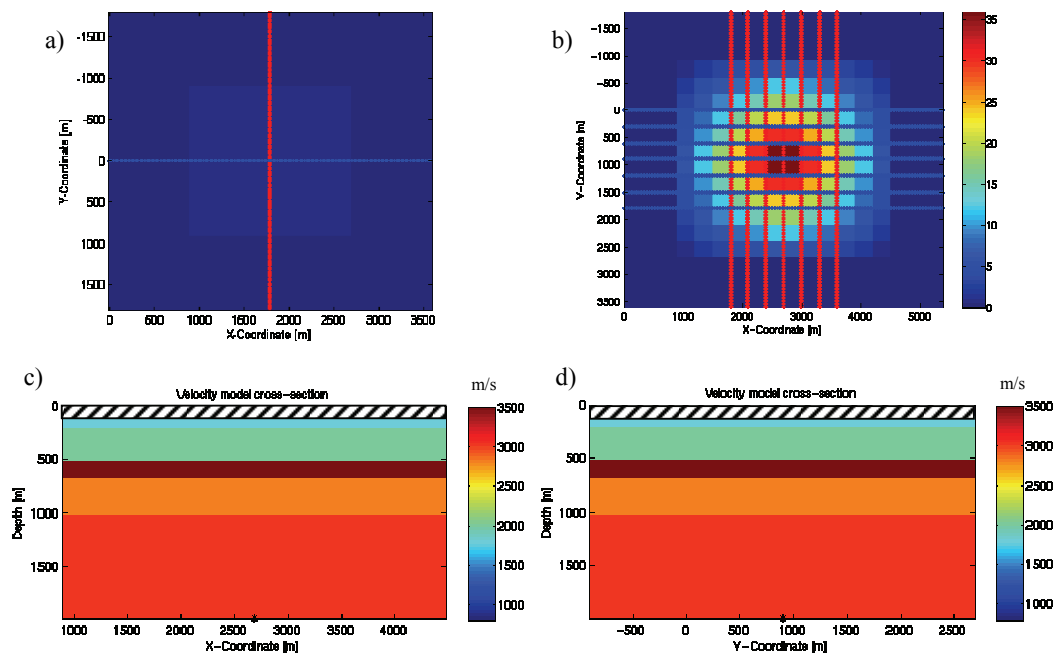


**Fig. 4.18** a) Design template, sources (red) and receivers (blue); and b) The entire design geometry; c) A cross section from the velocity model along the x-direction; and d) A velocity cross section along the y-direction. (The background color in (a) and (b) indicates CMP fold. The black/white stripes in (c) and (d) indicate that the velocity of this layer was varied in the examples.

Example	Surface sampling [m]	Near-surface velocity [m/s]	Varying coupling and intra-array statics	Reference name
1	25	800	Yes	25m-LVL-coupl
2	25	3400	No	25m-HVL
3	25	3400	Yes	25m-HVL-coupl
4	50	800	Yes	50m-LVL-coupl
5	50	3400	No	50m-HVL

**Table 4.1** A summary of the parameters used in the five examples presented in Section 4.5.3.

The used source and receiver arrays are the same as those shown in Figure 4.15a and Figure 4.15b respectively. The arrays effective dimensions are equal to the source and receiver intervals i.e. 25x25 m and 50x50 m while keeping the same number of elements. In addition, variable coupling conditions were used for the sources and receivers as stated in Table 4.1. The varying coupling conditions were applied as randomly distributed amplitude weights as exhibited by Figure 4.19a. These values are obtained from half (one side) of a normal distribution with a mean of one and a standard deviation of 0.1. The intra-arrays statics values used for the source and receiver arrays elements are shown in Figure 4.19b. The distribution of the statics values is half normal distribution with a mean of 0 ms and a standard deviation of .75 ms (i.e. a standard deviation of 0.6 m in the elevation for the 800 m/s near surface velocity and 2.6 m for the 3500 m/s near-surface velocity).

The effects of the arrays on the signal frequency bandwidth at the target can be quantified by comparing the input and the output amplitude spectra. Figure 4.20a shows the input and the output spectra for the five described examples. Generally, all the examples exhibit a reduction of the amplitude spectra above 50 Hz and an increase between 20-30 Hz. The 50m-HVL example shows a reduction of 2 dB above 50 Hz. The other examples show a reduction of 1 dB above 50 Hz. Therefore, the reduction of the amplitude spectrum at the target increases with increasing array size and near-surface velocity. The depth of the target is another factor to be considered where the size of the arrays and the near-surface velocity will have more influence on high reflection angles. In general, array effect is more serious for shallow targets. Figure 4.20b shows the resolution functions along the  $x$ -direction for the five examples. The 50 m sampling examples show wider resolution function than the 25 m sampling.

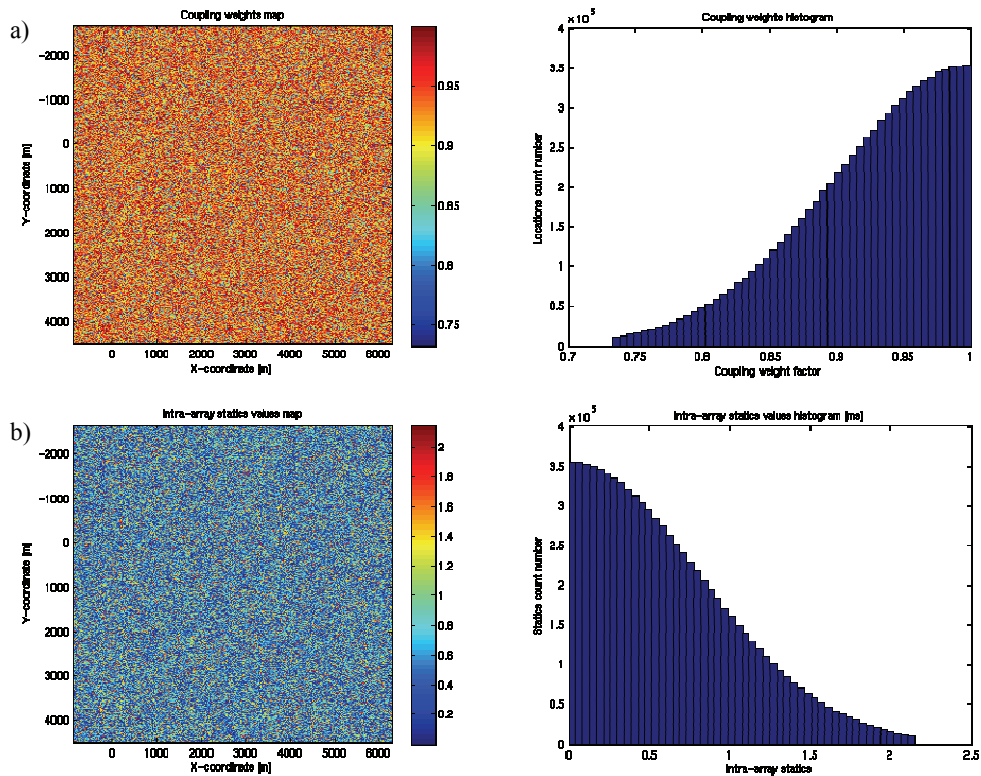


**Fig. 4.19** a) Varying coupling conditions in the survey area constructed using a random distribution with a mean of one and a standard deviation of .1 displayed in a map view (left) and a histogram (right); and b) Varying intra-arrays statics randomly generated with a mean of zero ms and a standard deviation of .75 ms displayed in a map view (left) and a histogram (right).

It is observed that the chosen variable coupling and intra-array statics did not result in more distortion to the amplitude spectra. This is attributed to the stringent standard deviations used in the modelling. The 25m-HVL-coupl example was repeated using the same coupling distribution as in Figure 4.19a and the same intra-array statics distribution as in Figure 4.19b but with a standard deviation of 8.0 ms. This amounts to a standard deviation in elevation of 28.0 m, which is relatively high. Figure 4.21a shows the obtained wavelets at the target using different intra-array statics standard deviations and compares them to the input source wavelet. The high intra-array statics distribution values (i.e.  $\sigma = 8.0$  ms) did not greatly affect the target amplitude spectrum compared to the case of  $\sigma = 0.75$  ms (Figure 4.21b). The influence of the intra-array statics is more obvious on the wavelets computed at the target. We see that the ( $\sigma = 8.0$  ms) resulted in a shift of 4.0 ms in the image time. Therefore, we can conclude that the higher the intra-array statics the more the fidelity of the seismic images will be affected.

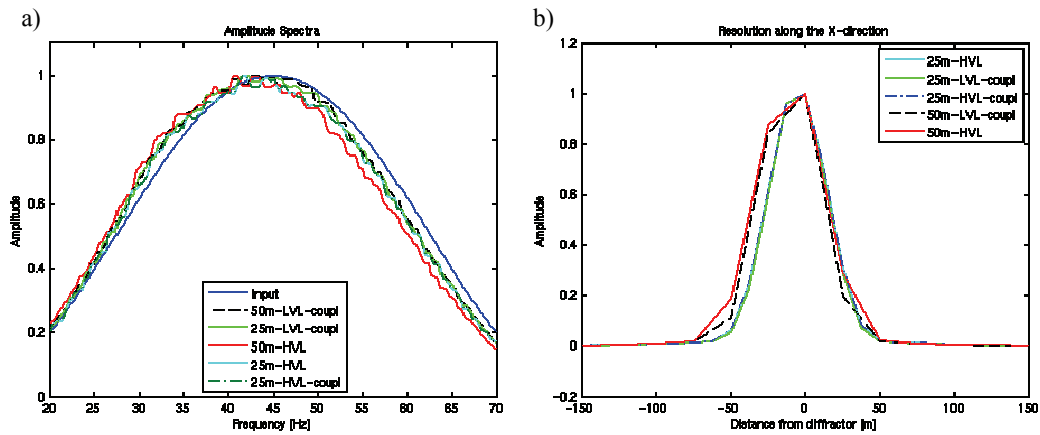


*Fig. 4.20* a) Amplitude spectra for the five examples summarized in Table 4.1 displayed in a linear scale; and b) The resolution functions along the  $x$ -direction at the target.

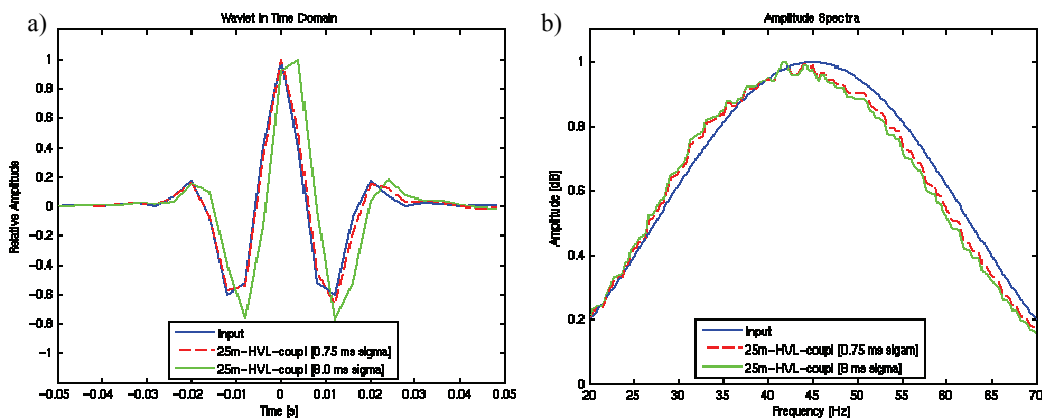


*Fig. 4.21* a) Wavelets at target obtained using different intra-array statics distributions ( $\sigma=0.75$  ms and  $\sigma=8.0$  ms); and b) The corresponding amplitude spectra of the wavelets in (a) displayed in linear scale.

In summary, there are three factors concerning the effects of arrays on signal temporal bandwidth. These are high-temporal frequency attenuation, intra-array statics, and variable coupling conditions. The importance of these factors differs depending on the near-surface velocities. High signal frequency attenuation increases with increasing near-surface velocity. Coupling problems may also increase in a high-velocity acquisition surface (for instance hard limestone), but it may be less of a problem in relatively soft soils. The intra-array statics are caused by near-surface velocity variation within the area covered by the array and by the

intra-array elevation differences. Assuming that the near-surface velocity does not vary considerably within the area covered by the array, then the intra-array statics will be primarily caused by elevation differences. Therefore, the lower the near-surface velocity the larger the intra-array statics will be. Table 4.2 highlights the areas where the factors concerning the arrays are more serious.

Near-surface velocity	Temporal frequency attenuation	Variable coupling	Intra-array statics
Low < 1500 m/s	✗ (small)	✗	✓
High > 1500 m/s	✓ (strong)	✓	✗

**Table 4.2** Problems associated with the field arrays where each problem is given marks based on its influencing magnitude with respect to the near-surface velocity.

#### 4.5.4 1D model overlain by a low-velocity near-surface anomaly

The main objective of this example is to evaluate the effects of low-velocity near-surface anomalies on the quality of the target image. The acquisition geometry used in this example is shown in Figure 4.22a and 4.22b. The subsurface velocity model used in this section consists of two parts. The upper part includes a variable near-surface down to a depth of 300 m with a lake-type 1000 m/s velocity anomaly with a diameter of 600 m (i.e. double the source and receiver line intervals) in the second layer. The velocity of the first layer has a gradient increasing with depth and ranging from 1000 m/s to 1500 m/s. The velocity of the second layer is 2000 m/s. The lower part of the velocity model consists of a flat layer-cake down to a depth of 2000 m where the target point is located in the spatial center of the model. Figures 4.22c and 4.22d show two cross-sections through the center of the model along the  $x$ -direction and the  $y$ -direction respectively. The surface topography is flat for this model.

The focal beams were computed through this model for the target point using the hybrid approach described in Section 4.2.2 for a frequency band of 10-50 Hz. Recursive depth extrapolation through the near-surface (upper 300 m of the model) was carried out using optimized operators in the space-frequency domain. Each operator includes 25 points in the  $x$ -direction and 25 points in the  $y$ -direction. This gives a spatial area of each operator of 312.5 m by 312.5 m since the grid increment that contains the sources and receivers is 12.5 m in both directions. These operators are optimized using a weighted least-squares method

(Thorbecke and Rietveld, 1994) for a maximum angle of 75 degrees and a depth increment of 12.5 m. These computational parameters will also be used in Sections 4.5.5 to 4.5.7, and 4.6.

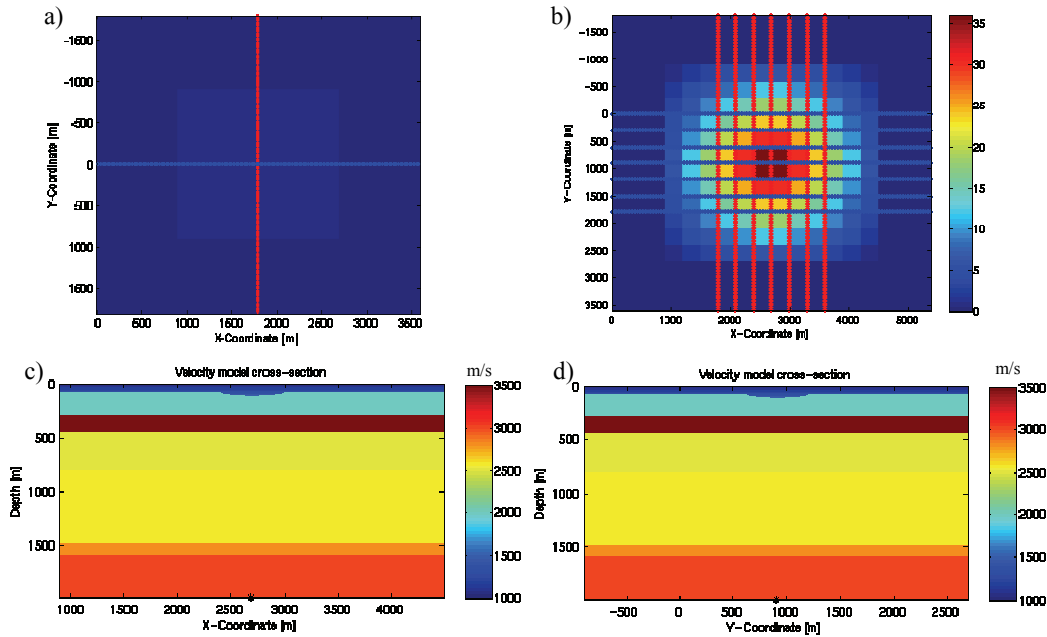


**Fig. 4.22** a) Design template, sources (red) and receivers (blue); and b) The entire design geometry; c) A cross section from the velocity model along the x-direction; and d) A velocity cross section along the y-direction. (The background color in (a) and (b) indicates CMP fold and white circles in (b) indicate the locations of the scatterers in the near-surface). Note that the acquisition geometry is the same as the one used in Sections 4.5.1 to 4.5.3.

The resulting focal beams and focal functions are shown in Figure 4.23a to 4.23f for the entire geometry. The focal source and detector beams show the same characteristics because the subsurface model geometry is symmetric and also the source and detector geometries are similar. The resulting focal functions do not highlight any deficiencies of the used geometry for the modelled frequency band. The focal resolution function shows a narrow main lobe with a high amplitude without aliasing occurring away from the target point. The AVP-imprint function shows a quite uniform sampling of the reflection angles.

Figures 4.23g and 4.23h show two cross-sections through the resolution function volume respectively along the  $x$ -direction and the  $y$ -direction. There are no indications of interference of energy from the target point under consideration with points within its vicinity. In addition, Figure 4.23i shows the DTS gather where each trace is constructed from a cross-spread. This gather shows that modelling was carried out correctly as confirmed by the horizontal alignment at  $\delta t=0$ . The image-fold – count of the number of traces with amplitudes that are 6 dB below the maximum – in this case is 25 compared to the CMP fold of the used geometry that is 36.

Figures 4.23j and 4.23k show two cross sections of the AVP-imprint function. These two figures show at which frequency the influence of the coarse sampling starts to appear. In this case the sampling effects start at a frequency of 40 Hz. Six angles are identified along the  $p_x$  and  $p_y$  directions which is in agreement with the CMP fold of the applied geometry of 36 (6 x 6). We can say that the acquisition footprint caused by this geometry will disappear at depth levels where the frequency content becomes less than 40 Hz. Of course, amplitude variations due to the near-surface will remain.

Comparing the results of this section with the results of Section 4.5.1, we can conclude that the presence of the low-velocity anomaly in the near-surface did not require further updating to the used geometry. An important aspect that we should notice is that the low-velocity layer did not diverge the wavefield away from the geometry on the surface. This is clear from the AVP-imprint function where there are no angles absent. This is in agreement with the conclusions drawn in Section 4.4 on basis of analyses of energy distributions.

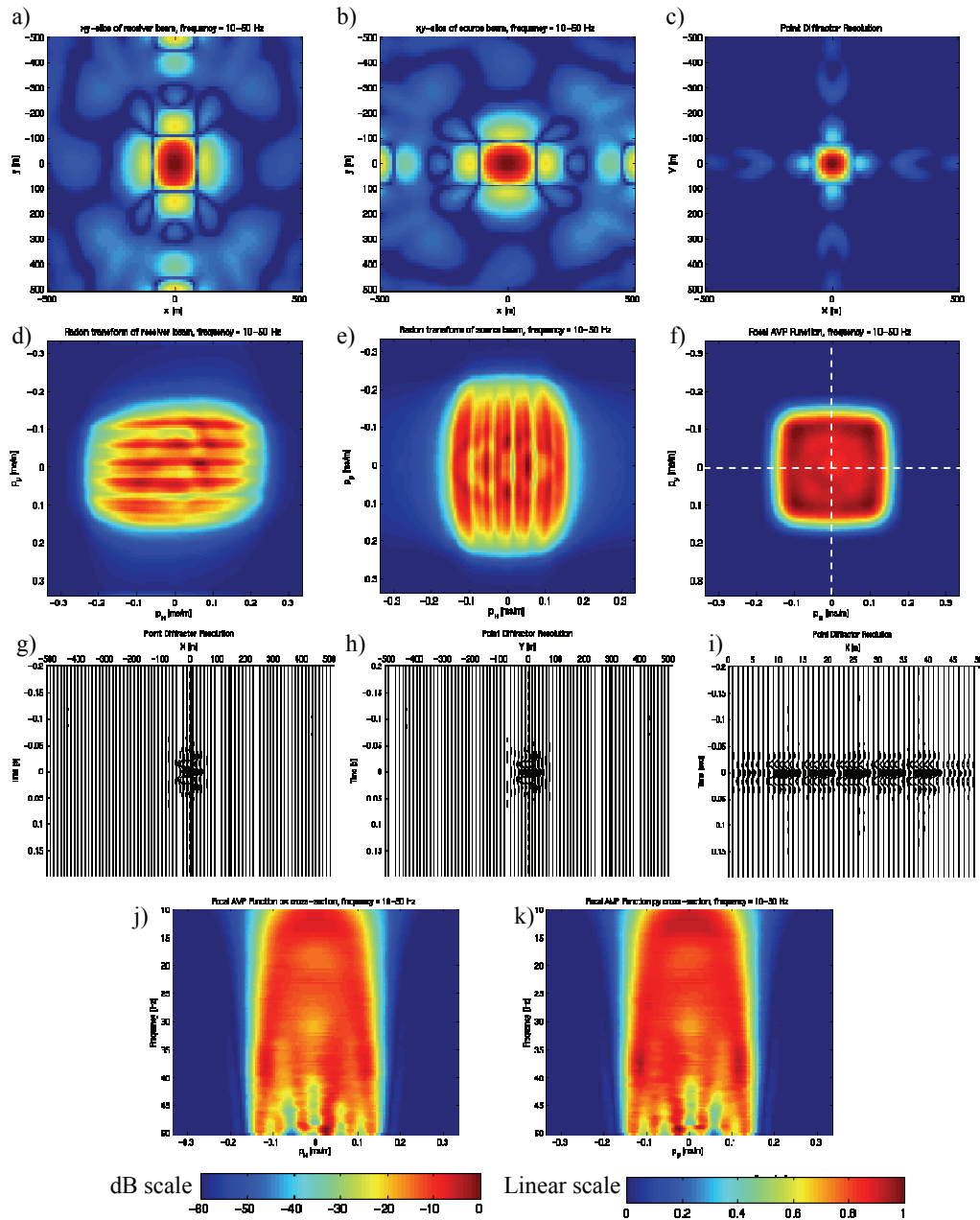


**Fig. 4.23** A low-velocity near-surface anomaly, a) Focal detector beam in space at  $t=0$ ; b) Focal source beam in space at  $t=0$ ; c) Resolution function in space-time at  $t=0$ ; d) Focal detector beam in the radon domain at  $\tau=0$ ; e) Focal source beam in the radon domain  $\tau=0$ ; f) AVP-imprint function; g) A cross-section through the center of the resolution function volume along the  $x$ -direction; h) A cross-section through the resolution function volume along the  $y$ -direction; i) A 3D DTS gather displayed as a 2D panel; j) AVP-imprint cross-section along the  $p_x$  axis indicated by the white horizontal dashed line in (f); and k) AVP cross section along the  $p_y$  axis indicated by the vertical white dashed line in (f). The scale of a, b, and c is in dB. The scale of d, e, f, j, and k is from 0-1. The scale of g, h, and i is linear with respect to the maximum of the display.

### 4.5.5 1D model overlain by a high-velocity near-surface anomaly

The main objective from this example is to evaluate the effects of high-velocity near-surface anomalies on the quality of the target image. The acquisition geometry used in this section is shown in Figures 4.24a and 4.24b. Similar to the previous section, the subsurface velocity model used in this section consists of two parts. The upper part includes a variable near-surface down to a depth of 300 meters consisting of two layers. The first layer has a velocity gradient of 1000 m/s to 2000 m/s. The lower layer has a constant velocity of 3500 m/s with a dome-type high velocity anomaly. The anomaly has a diameter of 600 m which is double the source and receiver line intervals. The second part of the velocity model consists of a flat layer-cake down to a depth of 2000 meters where the target point is located in the spatial center of the model. Figures 4.24c and 4.24d show two cross-sections through the center of the model along the  $x$ -direction and the  $y$ -direction respectively. The surface topography is flat for this model.

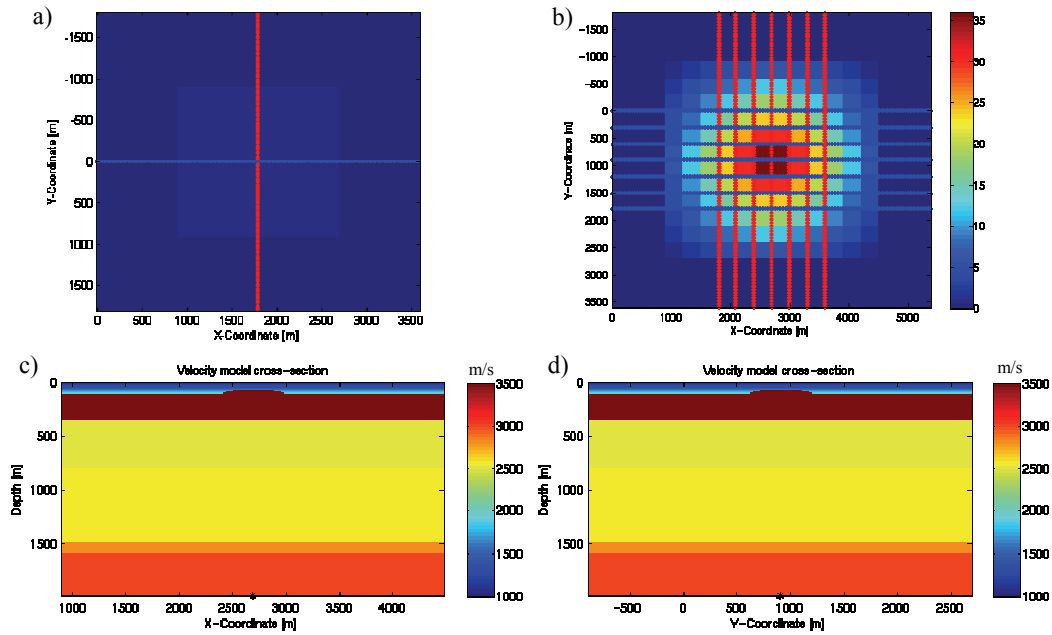


**Fig. 4.24** a) Design template, sources (red) and receivers (blue); and b) The entire design geometry; c) A cross section from the velocity model along the  $x$ -direction; and d) A velocity cross section along the  $y$ -direction. (The background color in (a) and (b) indicates CMP fold. Note that the acquisition geometry is the same as the one used in Sections 4.5.1 to 4.5.4.

The computed focal beams and focal functions are shown in Figure 4.25. The presence of the high-velocity anomaly produced some variations in the AVP-imprint function (Figure 4.25f), but no angles are absent. The variations in the AVP-imprint function can better be seen in the AVP-imprint function cross-sections along the  $p_x$  and  $p_y$  axis as a function of frequency ( $f$ ). The effects of the coarse sampling (source and receiver line intervals) start to appear at a frequency of about 45 Hz. The image-fold indicated by Figure 4.25i is the same as in the previous example that is 25 compared to the geometry CMP-fold of 36. Increasing the maximum inline and cross-line offsets of the used geometry will increase the image fold because then the Fresnel stack will be complete for the outer cross-spreads. We can conclude from Figure 4.25 that the presence of the high near-surface velocity anomaly did not result to losing any reflection angles from the target. This conclusion is also in agreement with our findings in Section 4.4.

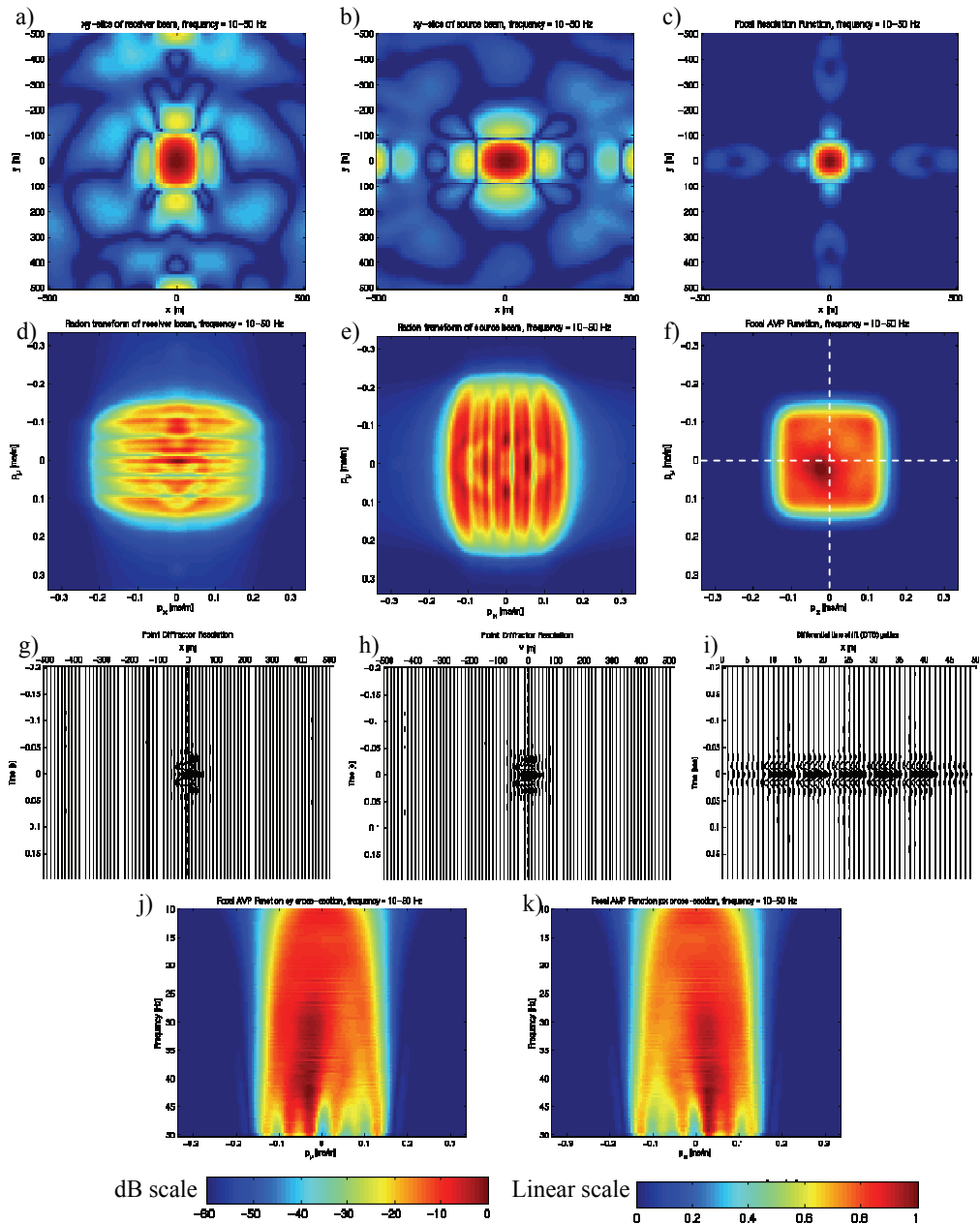


**Fig. 4.25** A high-velocity near-surface anomaly, a) Focal detector beam in space at  $t=0$ ; b) Focal source beam in space at  $t=0$ ; c) Resolution function in space-time at  $t=0$ ; d) Focal detector beam in the radon domain at  $\tau=0$ ; e) Focal source beam in the radon domain  $\tau=0$ ; f) AVP-imprint function; g) A cross-section through the center of the resolution function volume along the  $x$ -direction; h) A cross-section through the resolution function volume along the  $y$ -direction; i) A 3D DTS gather displayed as a 2D panel; j) AVP-imprint cross-section along the  $p_x$  axis indicated by the white horizontal dashed line in (f); and k) AVP cross section along the  $p_y$  axis indicated by the vertical white dashed line in (f). The scale of a, b, and c is in dB. The scale of d, e, f, j, and k is from 0-1. The scale of g, h, and i is linear with respect to the maximum of the display.

### 4.5.6 1D model overlain by a complex near-surface with topography

In this section a more representative land subsurface velocity model with varying topography is treated. Two cross-sections through the center of this model are shown in Figures 4.26a and 4.26b, exhibiting some features of complex near-surface geology. Figure 4.26c exhibits a top view of the acquisition surface elevation of this model. This model was constructed to mimic a real situation in an area in Saudi Arabia known for its poor seismic data quality because of the near-surface complexity. The velocity values were taken from borehole measurements in that area. The focal beams are calculated for a subsurface gridpoint at a depth of 2000 m in the center of the model for a frequency band of 10-50 Hz.

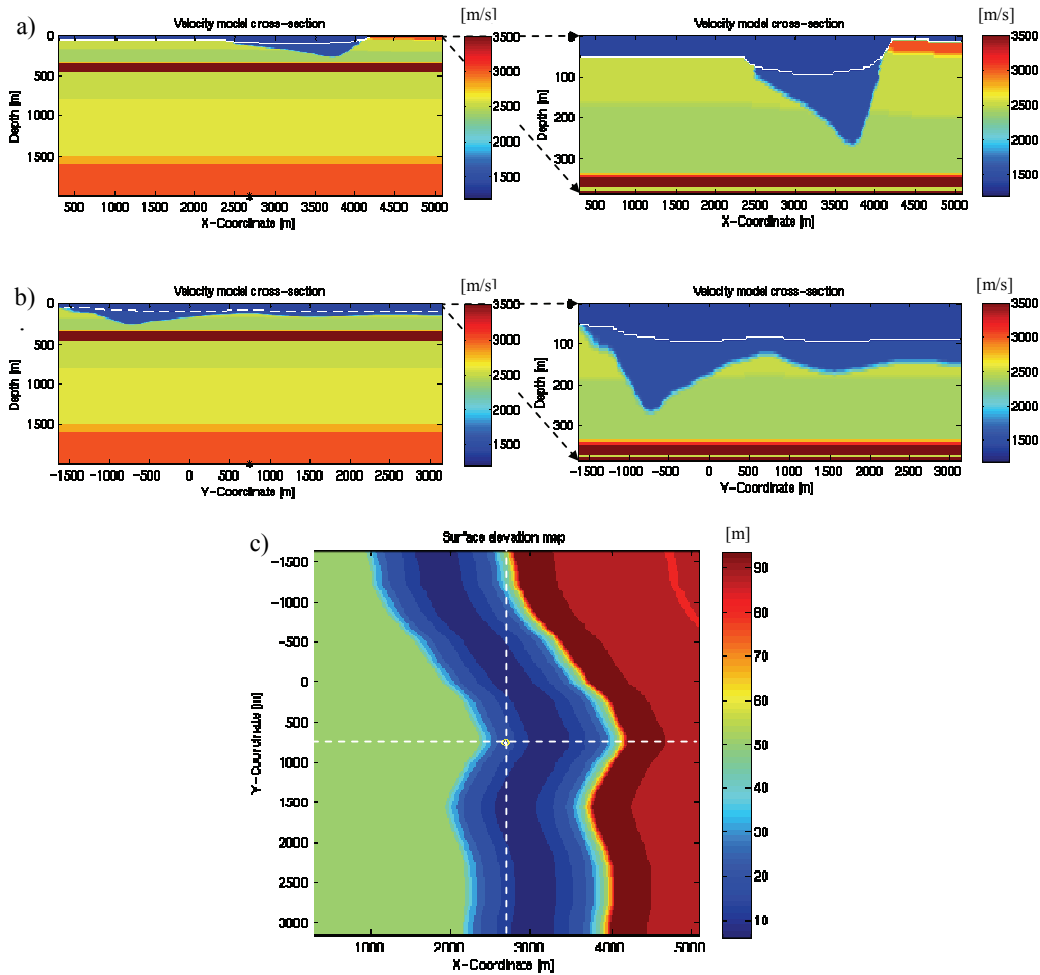


**Fig. 4.26** a) A cross section through the center of the velocity model with a complex near-surface: complete depth column (left) and zoom of the near-surface (right) along the x-direction; b) same as (a) along the y-direction; and c) map view of the surface elevation. The left figures of (a) and (b) are to scale and the dashed white lines indicate the surface topography.

Two acquisition geometries as described in Table 4.3 will be considered in this section. The two geometries produce equal CMP fold, but, they differ in the aspect ratio (i.e. cross-line-offset/inline-offset). Figure 4.27a shows the template of the first geometry with an aspect ratio of 0.44 that shall be referred to as narrow geometry. The template used for the second geometry is shown in Figure 4.27b and has an aspect ratio of 1.0. It shall be referred to as wide geometry. Note that narrow and wide here refer to the aspect ratio.

Geometry	Receiver geometry	Source geometry	CMP Fold
Narrow Orthogonal Aspect ratio (0.44)	$R_s = 25$ m RL=300 m Number of $R_s=216$ Number of RL=1	$S_s = 25$ m SL=300 m Number of $S_s=96$ Number of SL = 1	36 (9x4)
Wide Orthogonal Aspect ratio (1.0)	$R_s = 25$ m RL=300 m Number of $R_s=144$ Number of RL=1	$S_s = 25$ m SL=300 m Number of $S_s = 144$ Number of SL = 1	36 (6x6)

**Table 4.3** A summary of the parameters used for the two examples presented in Section 4.4.6.  $S_s$ -source station,  $SL$ -source line interval,  $R_s$ -receiver station, and  $RL$ -receiver line interval.

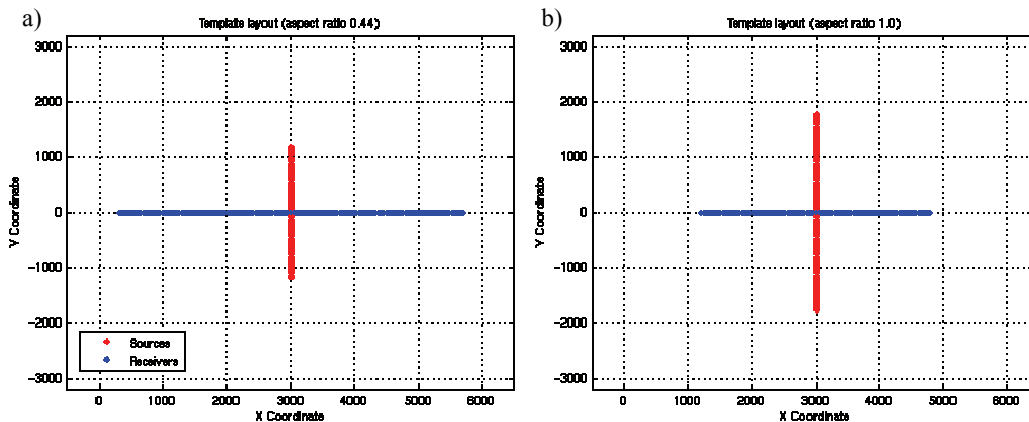


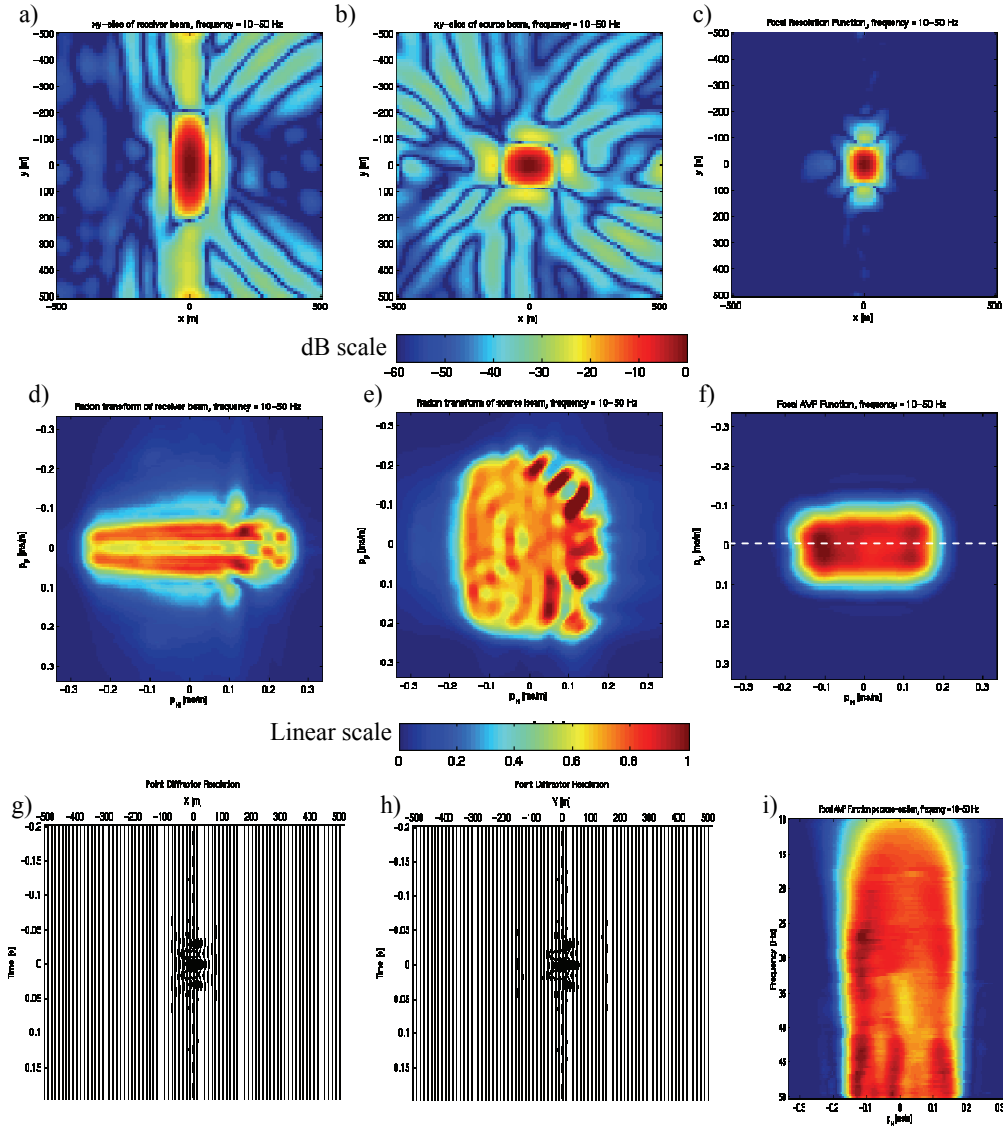
**Fig. 4.27** a) Narrow template; b) Wide template.

Figures 4.28a to 4.28f show the focal beams and the focal functions for the narrow geometry. The focal source and detector beams are not symmetric in this example because the underlying model is not symmetric and the source and receiver geometries are different as well. Although it shows more symmetry, the focal source beam shows less focusing than the focal detector beam as exhibited by the relatively higher energy away from the main lobe. The focal detector beam has more focusing in the  $x$ -direction than in the  $y$ -direction because of the coarse sampling and the narrow aperture in the  $y$ -direction. The resolution exhibits the best of each of the two focal beams with a relatively narrower main-lobe in the  $x$ -direction because the aperture is wider in this direction. The focal AVP-imprint shows a relatively stable amplitude radon-band with no gaps indicating that specular reflections have not been affected by the complex near-surface. The AVP-imprint cross-section of Figure 4.28i does not show systematic behaviour as shown in the case of the previous two examples. It shows that different plane-waves respond to the complex near-surface in different ways. Notice the continuity of the amplitude variations in the  $p_x$ - $f$  cross-section, these variations can be attributed to the structure of the near-surface velocity and how different plane-waves interact with this structure.

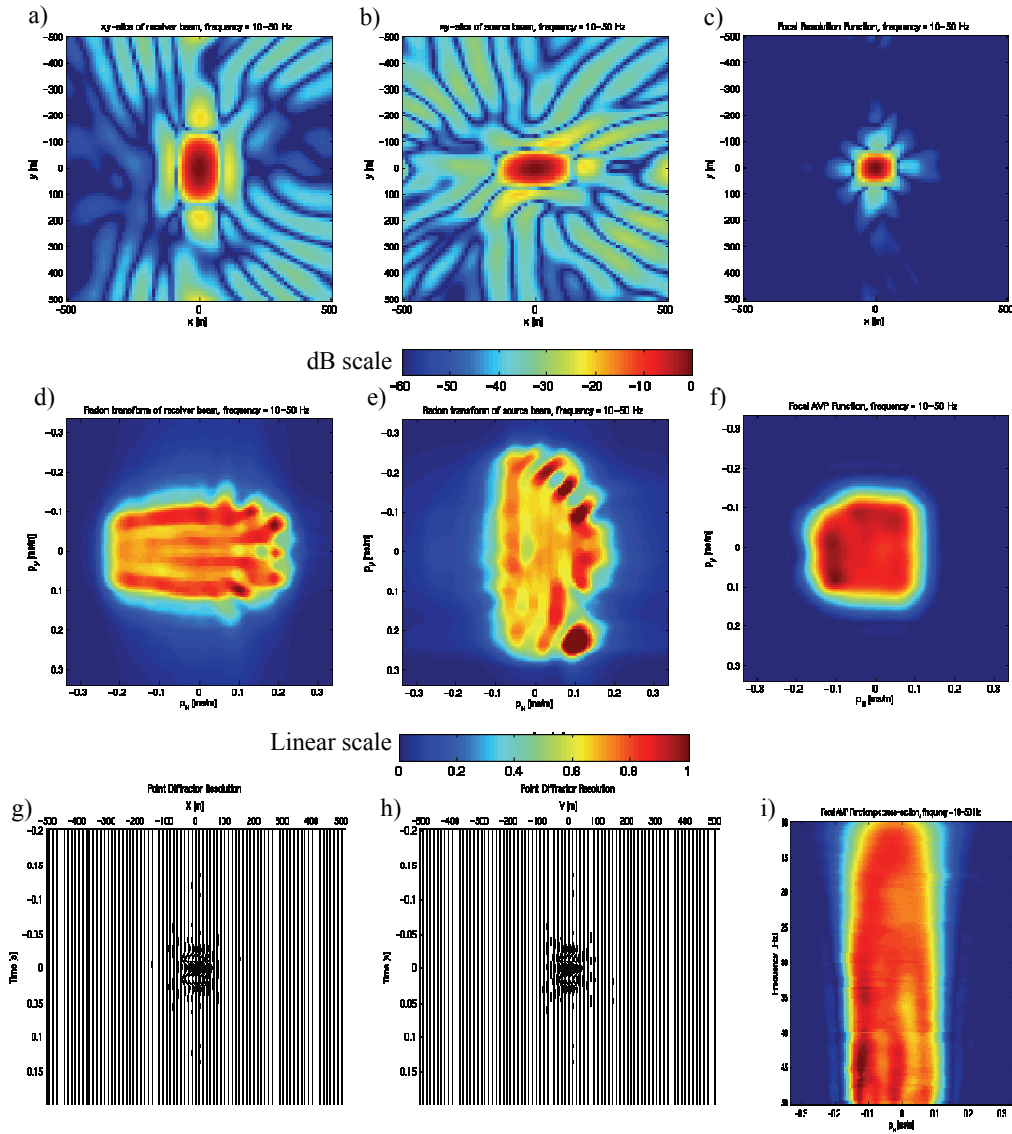
Figures 4.29a to 4.29f present the focal beams and the focal functions for the wide geometry. The resolution function (Figure 4.29c) exhibits more symmetry compared to the one of Figure 4.28c because in this case the geometry is more symmetric. Furthermore, the AVP-imprint is more symmetric but with a smaller range of sampled reflection angles along the  $p_x$  axis. This is because the narrow geometry had a wider aperture in the  $x$ -direction (longer inline offset).

The above two geometries have used equivalent source/receiver efforts but with different configurations. The narrow geometry puts more receivers in the  $x$ -direction and less number of receiver lines which lead to a longer inline offset of 2700 m compared to an inline offset of 1800 m of the wide geometry. The cross-line offset of the narrow geometry is 1200m as opposed to 1800 m of the wide geometry. The question that can be asked is, which one of the two geometries shall be used? The logical answer to this question would be by designing a geometry that combines the best of the two. The wider aperture in the  $x$ -direction of the narrow geometry has higher weights in its favour than the symmetry possessed by the wide geometry. Velocity analysis and multiple attenuation will benefit a great deal by the longer offsets or the high reflection angles. The best geometry choice will be using a geometry with maximum inline and cross-line offsets of 2700 m. However, in cases where limited resources are available, the right design approach should be to first fulfil the maximum required offset at the target in one direction. Increasing the source/receiver line intervals to maintain the symmetry will affect shallow reflectors and increases the acquisition footprint. Remember that limited resources cannot justify acquiring data that will not meet the objectives of the survey. In areas with a subsurface macro-model characterized by a high anisotropy the designer should strive to have the geometry as symmetric as possible while fulfilling all the

design basic parameters. Therefore, the wide geometry will be a better choice in this situation.



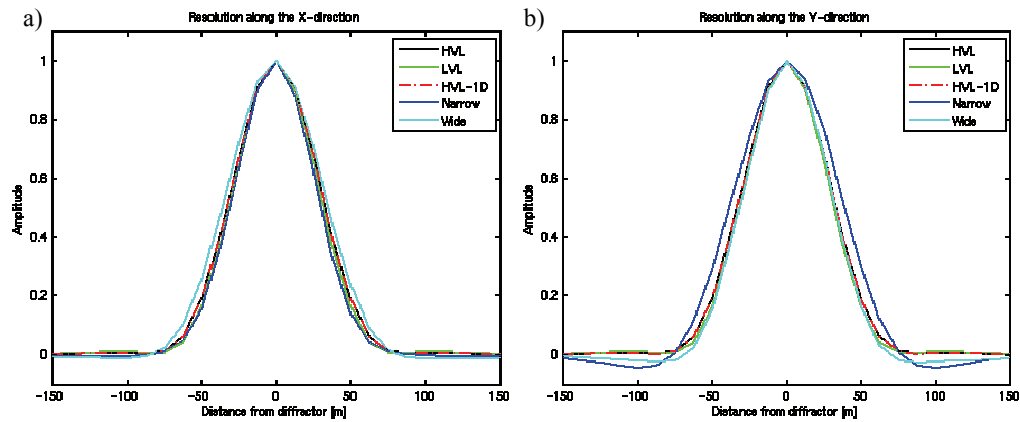
**Fig. 4.28** *Narrow geometry diagnostic plots, a) Focal detector beam in space at  $t=0$ ; b) Focal source beam in space at  $t=0$ ; c) Resolution function in space-time at  $t=0$ ; d) Focal detector beam in the radon domain at  $\tau=0$ ; e) Focal source beam in the radon domain  $\tau=0$ ; and f) AVP-imprint function; g) A cross-section through the center of the resolution function volume along the  $x$ -direction; h) A cross-section through the resolution function volume along the  $y$ -direction; and i) AVP-imprint cross-section along the  $p_x$  axis indicated by the white horizontal dashed line in (f). The scale of a, b, and c is in dB. The scale of d, e, f, and i is linear from 0-1. The scale of g and h is linear with respect to the maximum of the display.*



**Fig. 4.29** Wide geometry diagnostic plots, a) Focal detector beam in space at  $t=0$ ; b) Focal source beam in space at  $t=0$ ; c) Resolution function in space-time at  $t=0$ ; d) Focal detector beam in the radon domain at  $\tau=0$ ; e) Focal source beam in the radon domain  $\tau=0$ ; and f) AVP-imprint function; g) A cross-section through the center of the resolution function volume along the  $x$ -direction; h) A cross-section through the resolution function volume along the  $y$ -direction; and i) AVP-imprint cross-section along the  $p_x$  axis indicated by the white horizontal dashed line in (f). The scale of a, b, and c is in dB. The scale of d, e, f, and i is linear from 0-1. The scale of g and h is linear with respect to the maximum of the display.

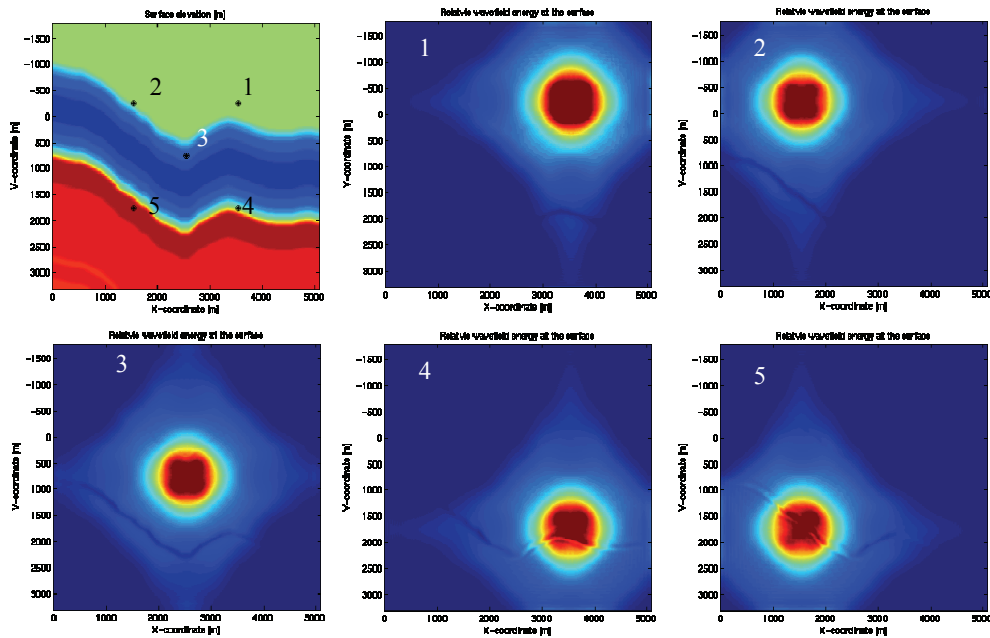
### Comparisons and concluding remarks from the examples

Figure 4.30 shows composite plots of the resolution functions of Sections 4.5.4 to 4.5.6 and the resolution function of the 25m-HVL example of Section 4.5.3. This figure shows that the resolution functions of all the analyzed examples do not significantly vary. This means that, at least theoretically the complex near-surface did not influence the target resolution. Note that these results are obtained because we know the underlying velocity model and also because we have used a high-quality inverse wavefield extrapolation technique. Figure 4.30b shows that the narrow geometry of Section 4.5.6 has the highest deviation in the  $y$ -direction compared to the rest of the examples.



**Fig. 4.30** Composite plots for the resolution functions Sections 4.5.4, 4.5.5, and 4.5.6 and the resolution function of the 25m-HVL example of Section 4.5.3, a) along the  $x$ -direction; and b) along the  $y$ -direction. Note that the target point is at the center of the  $x/y$ -axis.

The numerical examples analyzed in the previous three sections demonstrated that the near-surface anomalies cause the wavefield energy to vary at the acquisition surface. However, they do not cause major shadow zones at the surface as those observed when the anomalies are close to the target as in the case of sub-salt imaging (see for example van Veldhuizen, 2006). All the examples considered only one target point in a particular place. Therefore, the question is how other target points are influenced by the near-surface complexity. To answer this question the model shown in Figure 4.26 was used to calculate the energy at the surface due to different target points. Figure 4.31 shows the relative energy at the surface resulting from the different target points. These energy plots show how each target point is going to be illuminated or detected by respectively a source or a receiver located on the surface. Clearly, the energy varies but there are no significant shadow zones.



*Fig. 4.31* Relative wavefield energy distribution on the surface due to a source located at different points in the subsurface at a depth of 2000 m. The location of these points is indicated in the top-left plot.

The results obtained from the examples of Sections 4.5.4 to 4.5.6 gave a consistent message that the complex near-surface does not impose fundamental challenges that are not manageable. In other words, there does not seem to exist significant illumination problems that can be attributed to the complex near-surface. Therefore, it is concluded that *processing* must to remove the signal distortions caused by the near-surface. Of course, the acquisition rule is to provide the data that allows doing so. In addition, the acquired data should attenuate the noise or should be sampled adequately to allow noise attenuation in processing.

#### 4.5.7 Fundamental problems of applying statics to correct for near-surface variations

The main objective of this example is to show the limitations implied in the approach of solving the propagation effects through the near-surface using the statics assumption. The acquisition geometry and subsurface model used in this section are shown in Figure 4.32. As mentioned before, the forward modelling of the focal beams should be performed using an accurate technique. However, the inverse of this modelling shall be performed using the technique that is available in processing. Statics is a conventional processing technique to

remove the near-surface effects. Therefore, the accuracy of this technique can be measured by the focal functions and their attributes.

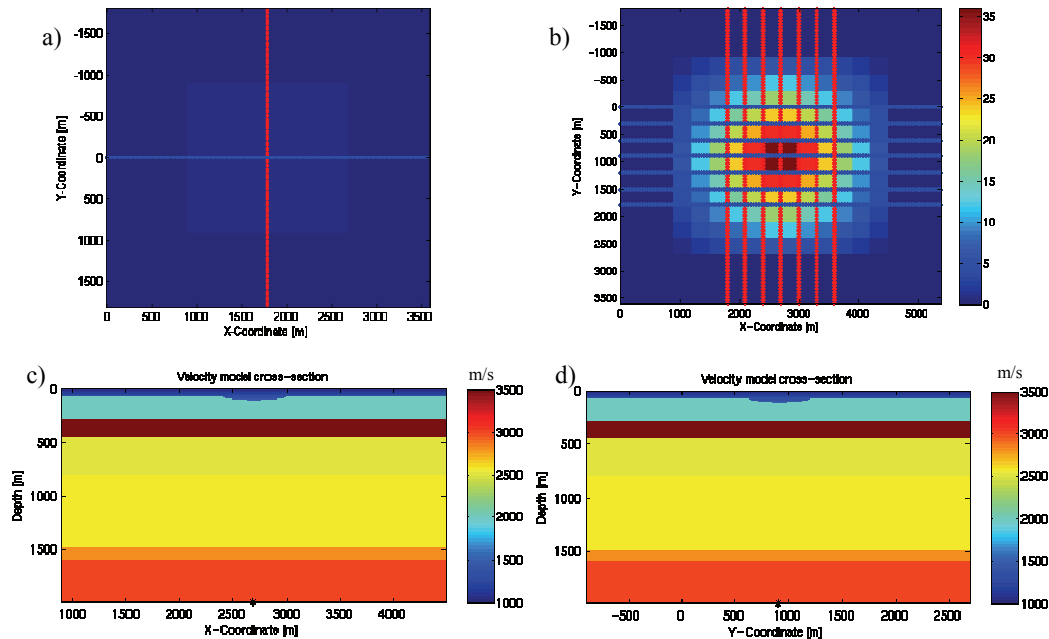


**Fig. 4.32** a) Design geometry template, sources (red) and receivers (blue); and b) The entire design geometry; c) A cross section from the velocity model along the x-direction; and d) A velocity cross section along the y-direction. (The background color in (a) and (b) indicates CMP fold. Note that the acquisition geometry is the same as the one used in Sections 4.5.1 to 4.5.5.

In this example the forward modelling was performed assuming the model of Figure 4.32c and 4.32d. But the inverse was carried out by applying statics to account for propagation through the near-surface. The applied statics values range from 91 to 102 ms and are shown in Figure 4.33a. Next, the inverse extrapolation was performed through the 1D model. The resulting resolution and AVP-imprint functions are shown in Figures 4.33b and 4.33c respectively. The effect of statics is clear from the resolution function wider main-lobe compared to Figure 4.23c. This can be better observed in Figures 4.33d and 4.33e which are two cross-sections from the resolution function volume.

Figure 4.33f shows the resulting DTS-gather with all the traces, in general, at  $\delta t=0$  but exhibiting some curvature. This is the most important aspect that needs further attention about the effects of statics and the fact that the near-surface problem is indeed dynamic rather than of a static nature. In this example we know the velocity model, and thus, we have calculated the correct statics values (i.e. vertical time shifts). After the application of the

statics we also used the correct velocity model from the new datum to the target. But because we used an inadequate solution to account for propagation effects through the near-surface which does not place the wavefield in the right physical perspective, the correct velocity model below the new datum is no longer valid. Therefore, what happens when we apply statics to the data and then estimate the velocity model, we replace the errors embedded in the statics approach by errors in the estimated velocity model (Beasley and Lynn, 1992).

In summary, even in simple cases the statics solution to the near-surface effects is not accurate. Note that in this example the near-surface velocity is 800 m/s which is relatively low, and therefore, the statics assumption is supposed to be close to the right solution. The problem of statics should be considered as dynamic and should be solved based on a wave-theoretical approach. This will be the subject of the next chapter.

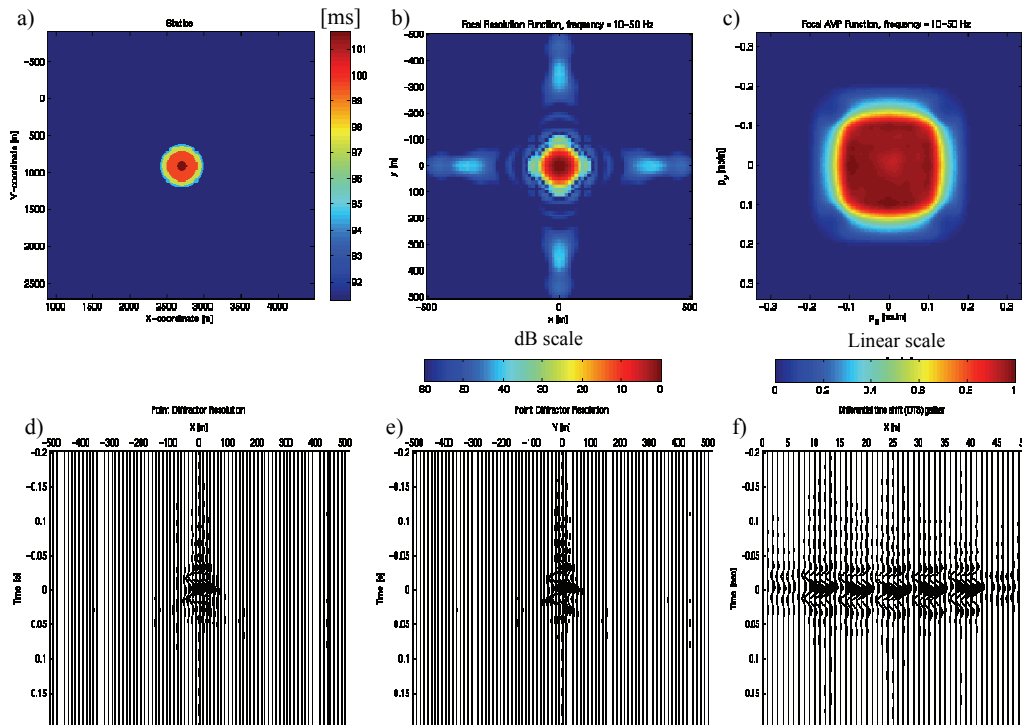


**Fig. 4.33** a) Statics values map; b) Resolution function in space-time; c) AVP-imprint function; d) A cross-section through the center of the resolution function volume along the  $x$ -direction; e) A cross-section through the resolution function volume along the  $y$ -direction; f) A 3D DTS gather displayed as a 2D panel. The scale of d, e, and f is linear with respect to the maximum of the display.

## 4.6 Model retrieval ability from data

The subsurface imaging results that can be achieved from a particular acquisition geometry while assuming a certain velocity model can be quantified by the focal functions shown in the previous section. However, these functions are calculated assuming knowledge of the underlying model. Therefore, the missing piece is that given an acquisition geometry, how well the model can be retrieved from the data acquired using this geometry. This is a very crucial requirement from model-based survey design. It is considered to be as phase 3 of our proposed survey design scheme. In this section, we will present some initial results to demonstrate if the used geometry will lead into accurate velocity model estimation. Comprehensive coverage of this topic is beyond the scope of this research.

All velocity model estimation techniques are based on alignment of imaged data subsets. A comprehensive review of such techniques can be found in Robein (2003). The differential-time-shifts (DTS) gather can be used to validate and update the underlying velocity model through focusing operators. This gather can be generated using the focal beams i.e. without going into explicit modeling of data.

DTS gathers can be constructed by performing forward extrapolation using a certain velocity model followed by performing the inverse extrapolation with another velocity model while computing the focal beams. Our primary goal from computing the DTS gather with different forward and inverse velocity models is to evaluate whether the deviations from the correct model are captured by the DTS gather. If this is the case, then such gather will allow updating the incorrect model. Otherwise, the spatial distance between the geometry subsets has to be reduced until the variations of the correct model are adequately captured. This brings us to step number 3 in our 3D survey design rules stated in Chapter 2, Section 2.3. The spatial distances between geometry subsets are indeed the source and receiver line intervals. Therefore, if the variations of the underlying velocity model are not captured in the DTS gathers obtained using the incorrect velocity model, then the line intervals have to be reduced.

The following two numerical examples use an orthogonal geometry with a basic template being a cross-spread consisting of 120 sources and 120 receivers. The source station interval ( $S_s$ ) is 25 meters and the receiver station interval ( $R_s$ ) is also 25 meters. This template is rolled over a distance of 100 meters, 10 times in both cross-line and inline directions resulting in 100 cross-spreads. The subsurface model used in this example consisted of two parts: a complex near-surface and a homogenous subsurface. In the first example, the width of the complex near-surface anomaly was set to 200 meters and to 100 meters in the second example. Figures 4.34a and 4.34d respectively show two cross-sections corresponding to these two near-surface models. Note that these cross-sections exhibit only the near-surface part of the models along one direction, but the anomaly is the same along the other direction. The deeper parts consist of a homogenous layer with a constant velocity of 3000 m/s. The

target point is located in the center of the model at a depth of 1000 m.

The focal beams computation was performed using these complex near-surface models for the forward extrapolation step and a homogenous model with a constant velocity of 3000 m/s for the inverse extrapolation step. The resulting DTS gathers corresponding to the two models are respectively shown in Figures 4.34b and 4.34e displayed as 2D panels. Note that the amplitudes are normalized for every trace. It is clear from these figures that the velocity used to generate these two DTS gathers is higher than the true velocity since all events are below ( $\delta t = 0$ ). Nevertheless, the most important aspect that we are looking for in these DTS gathers is whether the near-surface variations are captured in these gathers or not. It is clear from Figure 4.34b that near-surface variations are detected by the DTS gather which is the case where the source and receiver line intervals (100 meters) are smaller than the anomaly size (200 meters). Figure 4.34c shows the time picks of the DTS gather of Figure 4.34b in a map view with respect to their 3D subsets surface locations.

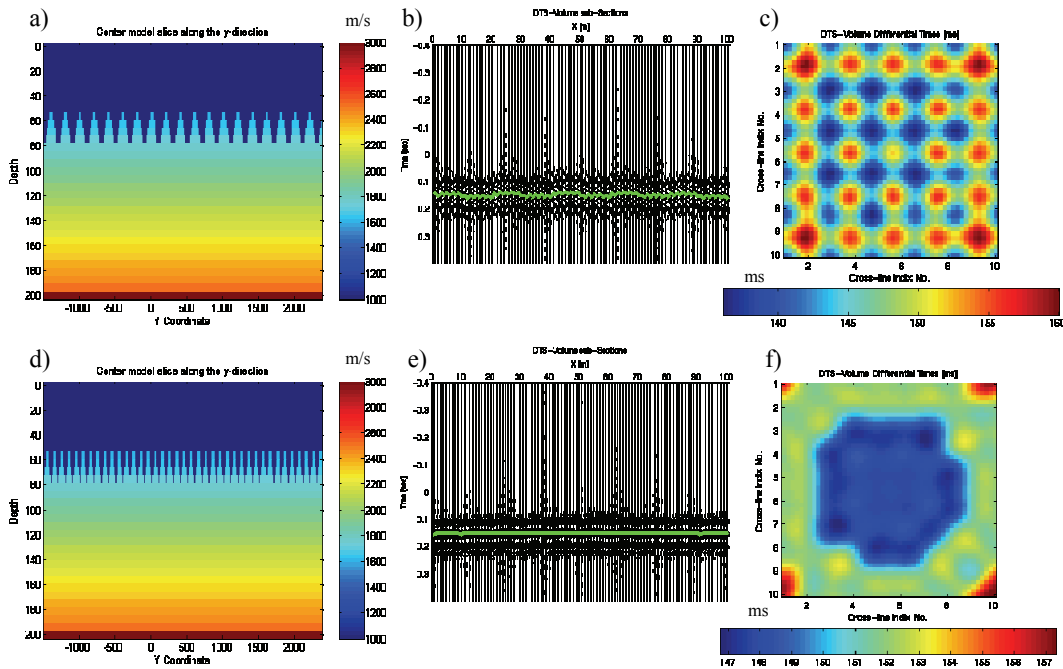


**Fig. 4.34** a) A cross-section through a near-surface velocity model with anomaly length of 200 meters; b) A 3D DTS gather displayed as a 2D panel for the model in a; c) A map view of the DTS time-picks in b with respect to their originating subsets surface locations; d) A cross-section through a near-surface velocity model with anomaly length of 100 meters; e) A 3D DTS gather displayed as a 2D panel for the model in d; and f) A map view of the DTS time-picks in e with respect to their originating subsets surface locations.

On the other hand, when the anomaly size is the same as the source and receiver line intervals the DTS gather (Figure 4.34e) did not detect the anomaly. This gather exhibited some sort of a bulk shift indicating that another constant velocity might align the DTS gather at  $\delta t=0$ . Figure 4.34f shows the time picks of the DTS gather of Figure 4.34e in a map view with respect to their 3D subsets surface locations.

Remember that our main goal for performing this DTS gather analysis is to assess whether the acquired data will lead to a sufficiently accurate estimated velocity model. Although not shown here, the analyses above were repeated for different combinations of near-surface anomalies and source and receiver line intervals. The observation made in those analyses was that in order to predict the near-surface velocity model variations, the source and receiver line intervals have to be shorter than the wavelength of the variations.

#### **4.7 Concluding remarks**

In the foregoing, we have discussed the computational aspects of focal beams for land-type subsurface models. Numerical examples were provided to demonstrate the geometry design assessment using the focal beams. Signal and noise can be analyzed with the focal beams. The rule/effects of the field arrays are quantified through the focal beams analyses. An important conclusion drawn from the analyzed examples is that the land near-surface problem does not cause illumination deficiency, however, the problem is a *processing* issue that has to be treated using a more effective technique than those commonly used in the industry. Therefore, it is the acquisition task to provide data to processing that allows noise attenuation from this data and removal of the near-surface distortions from the signal. Field arrays can be used to attenuate noise during the acquisition phase, otherwise, the data should be sampled alias-free— at least within the signal band – to allow digital array forming or other noise removal techniques.

Finally, we have described an approach of how to validate whether the acquired seismic data will lead to sufficiently accurate estimated subsurface velocity models. It is observed that the source and receiver line intervals have to be shorter than the length of the near-surface anomaly in order to be able to retrieve from the data a velocity that includes such variations. This approach warrants further research by linking it with a tomographic inversion technique which is beyond the scope of this thesis.

## An operator-based approach for solving the near surface problem

*This chapter describes the operator-based method for solving the complex near-surface problem in land seismic data. The solution is based on an operator approach without deriving a near-surface velocity model. We start with data-driven estimation of the focusing operators (one-way Green's functions) using the Common Focus Point technology. These operators describe the propagation between the acquisition surface and a chosen datum reflector. The conventional statics solutions are integrated in the initial estimates. The initial focusing operators are updated iteratively until the principle of equal travel time is fulfilled for each subsurface gridpoint of the datum reflector. Therefore, the measured reflection data is left intact without any application of time shifts. This makes the proposed method an uncommitted solution. For the 2D case, the estimation of the focusing operators is carried out in the common-source or common-receiver domain because it is assumed that one of these domains is properly sampled. For the 3D case, this type of acquisition is generally not valid and the CFP concept is extended to allow operator estimation in cross-spread geometries. The final focusing operators are directly used for wave-equation redatuming to the datum reflector (new datum). The underlying velocity model is obtained by applying tomographic inversion to the focusing operators, also including any hard prior information (e.g. shallow well information). This velocity model is used to calculate the depth of the new datum level. The full sequence is demonstrated on 2D field data acquired in the desert of Saudi Arabia. In addition, focusing operator estimation for the 3D situation is demonstrated using synthetic as well as field data also acquired in Saudi Arabia.*

*To accelerate application of the operator-driven near-surface solution, Chapter 5 is written in such a way that it is directly accessible for practical-oriented geophysicists who may not be interested in the theoretical details as described in Chapters 2-4.*

### 5.1 Introduction

Complexities of the near surface and varying acquisition-surface topography have degrading effects on land seismic images. These effects are caused by two factors: distortion of the

body waves (down and up) and high-level source-generated noise. In this chapter we describe a solution to problems arising from the first factor: distortion due to variable topography and heterogeneous sediments.

Conventional solutions that remove the near-surface effects from downgoing and upcoming waves mainly involve the assumption of vertical ray-paths through a relatively simple near-surface layer, imposing a static time shift on each seismic trace (Cox, 1999). However, the propagation of seismic waves through the unknown, often strongly inhomogeneous, near-surface layers is more dynamic than a simple time shift. Shtivelman and Canning (1988) provided ample insight into the imaging errors incurred when the near-surface problem is solved by static time shifts. Ideally, near-surface distortion must be addressed as an imaging problem. Already more than two decades ago, Berryhill (1979; 1984) introduced wave-equation datuming for respectively post-stack and pre-stack data as a solution to this problem. Since then, many authors have further studied the wave-equation datuming including Wiggins (1984), Yilmaz and Lucas (1986), Shtivelman and Canning (1988), Reshef (1991), Beasley and Lynn (1992), Bevc (1997), Yang et al. (1999) and Alkhalifah and Bagaini (2006). All of these authors have focused on either the accuracy or the efficiency of the involved datuming formulations. However, the crucial factor governing the success of wave-equation datuming is the *knowledge of the velocity model* between the acquisition surface and the new datum. In fact, if the near-surface velocity model is not known with sufficient accuracy, the conventional static solution may even be preferred (Salinas-Garnica and Larner, 1997).

Hindriks and Duijndam (1999) introduced a wave-equation approach for resolving the near-surface problem without the knowledge of the underlying velocity model. Their approach is based on the Common Focus Point (CFP) technology introduced by Berkhout (1997). The CFP technique is a velocity-independent (operator-based) imaging method that describes seismic migration by double focusing (Berkhout, 1980). The CFP technique is data-driven and aims at determining Green's functions (one-way focusing operators) that describe wave propagation between the surface locations and locations along the datum reflector via an iterative updating process, making use of the principle of equal travel time. This process occurs without updating the underlying velocity model. The resulting operators are used to perform downward extrapolation to the datum reflector below the complex near-surface. The near-surface velocity model that is consistent with the operator times ('effective velocity model') can be subsequently obtained by tomographic inversion of these focusing operators (Cox and Verschuur, 2001; Cox, 2004). The first results of near-surface distortion removal by the CFP-technology have already been demonstrated by a few authors (Hindriks and Verschuur, 2001, and Kelamis et al., 2002).

Representation of the near-surface by operators, together with the consequences for data acquisition design, are the topics of this thesis.

## 5.2 Theoretical review of the CFP method

Seismic reflections of any complexity, including mode conversion multiples, can be described by the so-called **WRW** model (Berkhout, 1980). In the subsequent review, we will limit the model to primary reflections. Besides, the following formulations are expressed for the 2D situation; however, they can easily be extended to the 3D situation since the theory is general. In this **WRW** model, the matrix notation is used, where  $\Delta\mathbf{P}(z_0, z_0)$  represents one frequency component of the pre-stack seismic data for all source positions at the acquisition surface  $z_0(x)$  and for all receiver positions at the acquisition surface  $z_0(x)$ . One column of  $\Delta\mathbf{P}(z_0, z_0)$  describes a monochromatic shot record. Therefore, a system representation of the entire monochromatic seismic experiment for multiple ( $M$ ) reflecting boundaries can be expressed as:

$$\Delta\mathbf{P}(z_0, z_0) = \mathbf{D}(z_0) \sum_{m=1}^M \mathbf{W}(z_0, z_m) \mathbf{R}(z_m, z_m) \mathbf{W}(z_m, z_0) \mathbf{S}(z_0), \quad 5.1$$

$\mathbf{S}(z_0)$  and  $\mathbf{D}(z_0)$  describing, respectively, the sources (including field arrays) and the detectors (including field arrays) at the acquisition surface  $z_0$ . Without field arrays, they can be represented by scaled diagonal matrices, the scaling factor being one frequency component of the source signal and receiver instrument response respectively. Matrix  $\mathbf{W}(z_m, z_0)$  describes the downward wave propagation (Green's functions) from the surface  $z_0$  to depth level  $z_m$ , while  $\mathbf{W}(z_0, z_m)$  describes the upward wave propagation from depth level  $z_m$  to the surface  $z_0$ . The transformation of the downgoing waves into upgoing waves is performed by the matrix  $\mathbf{R}(z_m, z_m)$ , which contains the angle-dependent reflection properties of boundary  $z_m(x)$ . The multi-record reflection measurements at the surface are contained in the data matrix  $\Delta\mathbf{P}(z_0, z_0)$ . Therefore, the seismic experiment according to equation (5.1) is represented by four spatial convolutions per frequency component for each reflecting boundary.

The imaging process aims at removing the influence of the field arrays and propagation effects in order to obtain  $\mathbf{R}(z_m, z_m)$ . This means removing for each depth level the matrices  $\mathbf{D}(z_0)\mathbf{W}(z_0, z_m)$  and  $\mathbf{W}(z_m, z_0)\mathbf{S}(z_0)$  from the data by matrix inversion. This matrix inversion process can be formulated in terms of two focusing steps: focusing in detection and focusing in emission where the detectors and sources are focused to the same subsurface gridpoint (see Berkhout, 1997).

Assuming proper sampling in the detector domain, *focusing in detection* is applied to the data first where each common source gather is transformed into a single trace by the focusing operator for the subsurface gridpoint under consideration (so-called Fresnel zone stacking). Each output trace is related to the location of the corresponding common source. If

we consider the response of one reflecting boundary,  $\delta\mathbf{P}(z_0, z_0)$ , this can be mathematically formulated as:

$$\begin{aligned}\delta\mathbf{P}_i^\dagger(z_m, z_0) &= \mathbf{F}_i^\dagger(z_m, z_0)\delta\mathbf{P}(z_0, z_0) \\ &= \mathbf{F}_i^\dagger(z_m, z_0)[\mathbf{D}(z_0)\mathbf{W}(z_0, z_m)\mathbf{R}(z_m, z_m)\mathbf{W}(z_m, z_0)\mathbf{S}(z_0)],\end{aligned}\tag{5.2}$$

where  $\mathbf{F}_i^\dagger(z_m, z_0)$  represents the focusing operator (the dagger  $\dagger$  indicates a row vector) for the  $i^{\text{th}}$  subsurface gridpoint at depth level  $z_m$ . Ideally, this operator has the property:

$$\mathbf{F}_i^\dagger(z_m, z_0)\mathbf{D}(z_0)\mathbf{W}(z_0, z_m) = \mathbf{I}_i^\dagger(z_m, z_m),\tag{5.3}$$

where  $\mathbf{I}_i^\dagger(z_m, z_m) = (0, 0, \dots, 0, 1, 0, \dots, 0)$ . This condition, meaning perfect unit detection at the  $i^{\text{th}}$  subsurface gridpoint, is not obtainable because of theoretical and practical constraints pertaining to wave propagation and acquisition geometry, respectively. However, the objective is to get as close as possible to this condition. The process of focusing in detection physically means simulating a seismic measurement such that the sources are still at the acquisition surface while one detector is considered that is located at the subsurface gridpoint under consideration (the focus point). In practice, the forward propagation operator is often approximated by  $\mathbf{F}_i^\dagger(z_m, z_0) = [\mathbf{W}_i(z_0, z_m)]^H$  (Claerbout, 1976; Berkhout, 1980). This means that focusing is carried out by correlation. Furthermore,  $\mathbf{D}(z_0)$  is often assumed to be a diagonal matrix.

The result obtained after focusing in detection is referred to as the *common focus point* (CFP) gather. Note that in a CFP gather, all reflection events are still present. According to the *principle of equal traveltimes*, the travel times of the target reflection event in each CFP gather will be the same as the time-reverse of the respective focusing operator if the kinematics of the operator are correct (Berkhout, 1997). The *principle of equal traveltimes* can be visualized on the data by time correlating the focusing operators – trace by trace – to their respective CFP gathers to generate the differential time shift (DTS) gathers:

$$\text{DTS-gather: } \quad \delta\mathbf{P}_{ik}(z_m, z_0)\mathbf{W}_{ik}^*(z_0, z_m) \quad \text{for all } k\text{'s}, \tag{5.4}$$

or in a function notation,

$$\text{DTS-gather: } \quad \delta P(x_i, z_m; x_k, z_0; \omega)\mathcal{W}^*(x_k, z_0; x_i, z_m; \omega) \quad \text{for all } k\text{'s}. \tag{5.5}$$

Figure 5.1 illustrates this focussing-correlation process on a synthetic response.

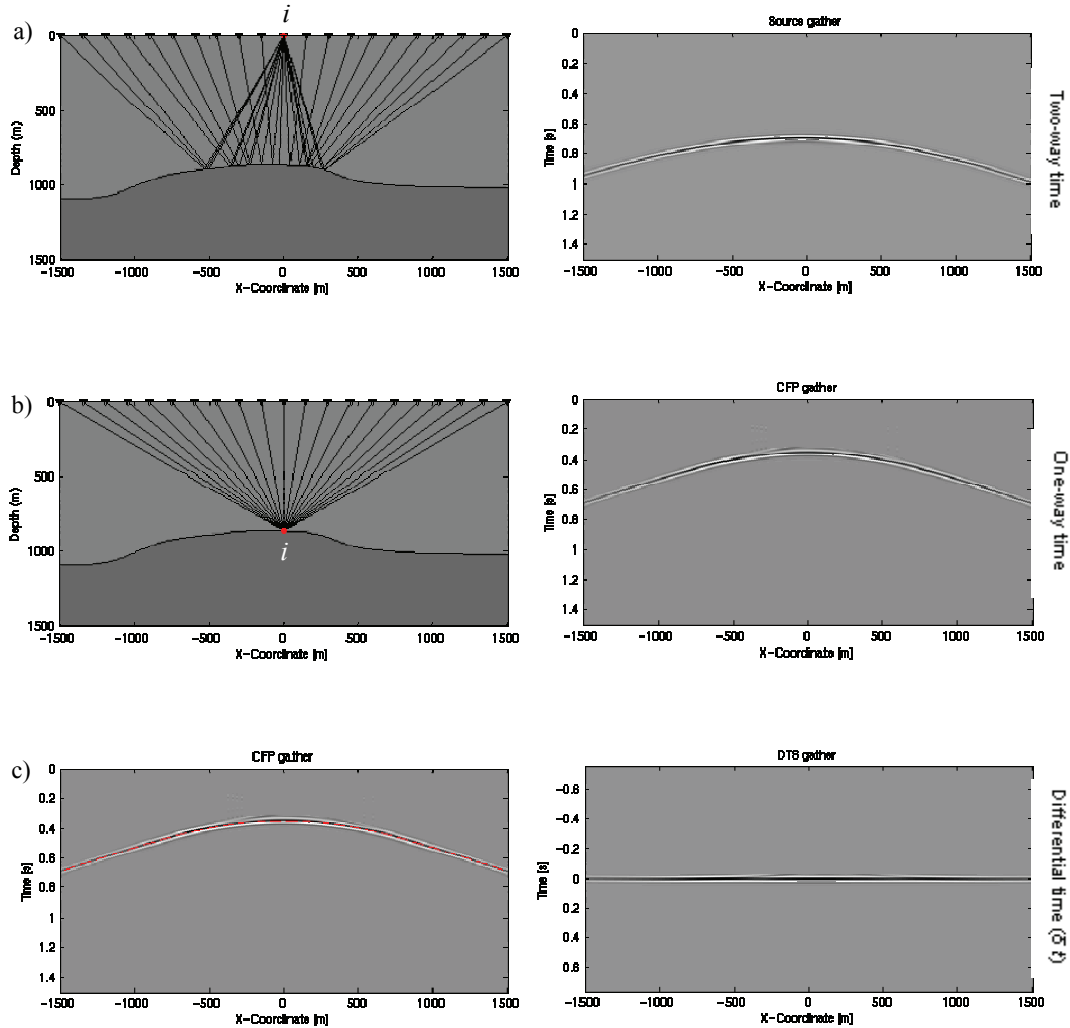


**Fig. 5.1** Synthetic illustration of the focussing-correlation process, a) Subsurface model (left) showing the reflection rays for one source point at the  $i^{\text{th}}$  surface position, and the corresponding synthetic source gather (right); b) CFP rays in the subsurface model (left) and the constructed CFP gather for the  $i^{\text{th}}$  subsurface grid point; c) The CFP gather overlain by the traveltimes curve (red) of the focusing operator (left), showing the principle of equal traveltimes, and the DTS gather constructed by – trace by trace – correlation of the focusing operator and the CFP gather.

The second imaging step (*focusing in emission*) is obtained by transforming the CFP gather into a single trace as follows:

$$\delta\mathbf{P}_{ii}(z_m, z_m) = \delta\mathbf{P}_i^\dagger(z_m, z_0)\mathbf{F}_i(z_0, z_m). \quad 5.6$$

Ideally, the operator  $\mathbf{F}_i(z_0, z_m)$  (being a column vector) has the property:

$$\mathbf{W}(z_0, z_0)\mathbf{S}(z_0)\mathbf{F}_i(z_0, z_m) = \mathbf{I}_i(z_m, z_m), \quad 5.7$$

where  $\mathbf{I}_i(z_m, z_m)$  is a column vector with only one non-zero, unit value at lateral position  $i$ .

If we combine 5.3 and 5.7, then we may write for the double focusing result:

$$\begin{aligned} \delta\mathbf{P}_{ii}(z_m, z_m) &= \mathbf{I}_i^\dagger(z_m, z_m)\mathbf{R}(z_m, z_m)\mathbf{I}_i(z_m, z_m) \\ &= \mathbf{R}_{ii}(z_m, z_m). \end{aligned} \quad 5.8$$

Figure 5.2 shows the second focusing process on the CFP gather in Figure 5.1.

Note the principle difference between a CFP gather and a downward extrapolated shot record. A CFP gather has a geometry with one detector in the subsurface and many sources at the surface. A downward extrapolated shot record has a geometry with one source at the surface and many detectors in the subsurface. This is illustrated in Figure 5.3. (Note that redatuming refers to the situation where both the sources and detectors are in the subsurface).

In terms of our matrix notation the CFP gather is given by;

$$\mathbf{P}_i^\dagger(z_m, z_0) = \mathbf{F}_i^\dagger(z_m, z_0)\mathbf{P}(z_0, z_0), \quad 5.9$$

where  $\mathbf{P}_i^\dagger(z_m, z_0)$  is a CFP gather for the  $i^{\text{th}}$  subsurface grid point. Similarly, a downward extrapolated shot record is given by:

$$\mathbf{P}_i(z_m, z_0) = \mathbf{F}(z_m, z_0)\mathbf{P}_i(z_0, z_0), \quad 5.10$$

where  $\mathbf{P}_i(z_m, z_0)$  is the downward extrapolated  $i^{\text{th}}$  surface shot record to depth level  $z_m$ . Equations 5.9 and 5.10 represent one row and one column of  $\mathbf{P}(z_m, z_0)$  respectively.

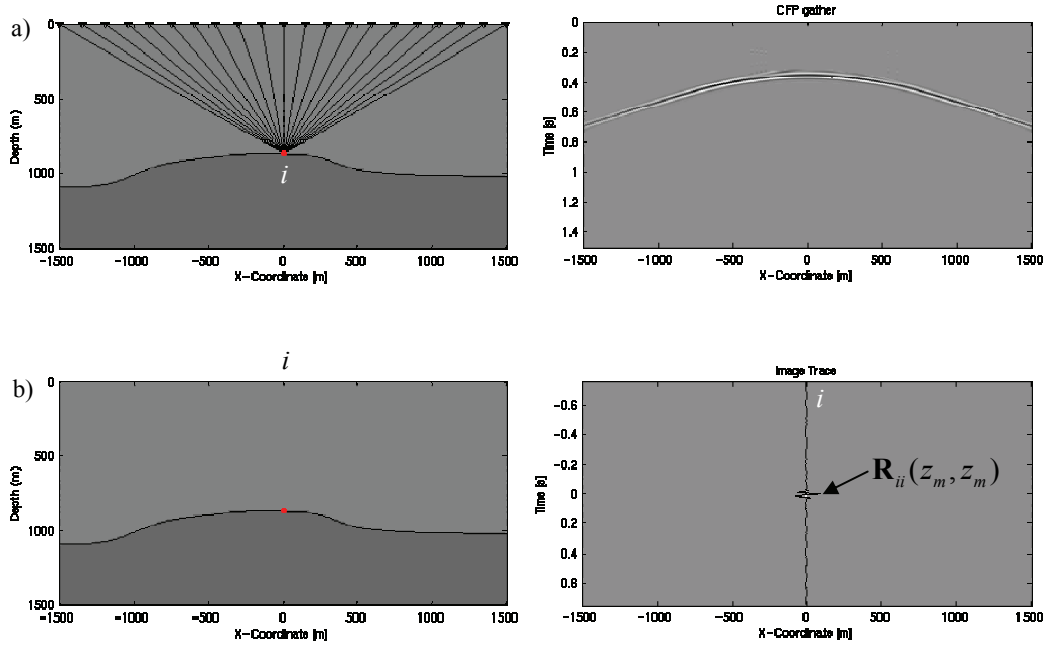


**Fig. 5.2** Illustration of the second focusing step on the CFP gather, a) CFP gather rays in the subsurface model (left) and the constructed CFP gather from the synthetic data; and b) the subsurface model indicating the target point (red) for which the image is constructed by focusing the CFP gather (right).

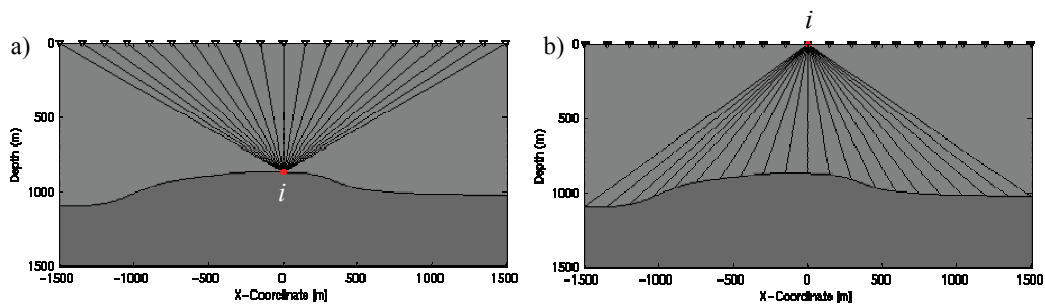


**Fig. 5.3** a) Illustration of the ray paths of a CFP gather; and b) illustration of the ray paths of a downward continued shot record.

### 5.3 Initial operators and updating

The previous section emphasized the importance of focusing operators (one-way Green's functions) for redatuming. Obviously, if the underlying velocity model is known, then the focusing operators can be directly calculated to any required degree of accuracy. In practice, however, we do not know this model in advance.

Fortunately, a velocity-independent determination of the focusing operators is possible through iterative updating of the initial focusing operators until the principle of equal traveltimes is fulfilled. The closer the resemblance of the initial operators to the true ones, the quicker the convergence of the updating process will be. In the following, we will focus on one reflecting boundary and consider only the kinematics of the focusing operators.

For relatively simple underlying velocity models, the initial focusing operators can be calculated using the rms velocity and the image-ray times of a certain reflector (see for example Bolte et al., 1999). Hindriks and Duijndam (1999) proposed building the initial operators by considering two propagation paths: propagation through the complex near-surface (conventional vertical ray paths) and propagation through the more homogeneous layers below the near-surface as depicted in Figure 5.4. This can be written according to our previous formulations as:

$$\mathbf{F}^{init}(z_2, z_0) = \mathbf{F}(z_2, z_1)\mathbf{F}(z_1, z_0), \quad 5.11$$

where  $\mathbf{F}^{init}(z_2, z_0)$  contains the initial operators,  $\mathbf{F}(z_2, z_1)$  represents the hyperbolic propagation in the more homogeneous part below the complex near-surface, and  $\mathbf{F}(z_1, z_0)$  is a diagonal matrix for the complex near-surface with its diagonal elements defined as  $\mathbf{F}_{ii}(z_1, z_0) = e^{i\omega\tau_{ii}}$ , where  $\tau_{ii}$  equals to the conventional surface consistent statics time shift for surface location  $i$ .

In this approach we have integrated the conventional statics concept into the initial operators but not into the data. Thus, CFP starts where the statics solution stops. This makes this approach an uncommitted solution since the seismic measurements are not changed and the operators will be updated during the iteration process.

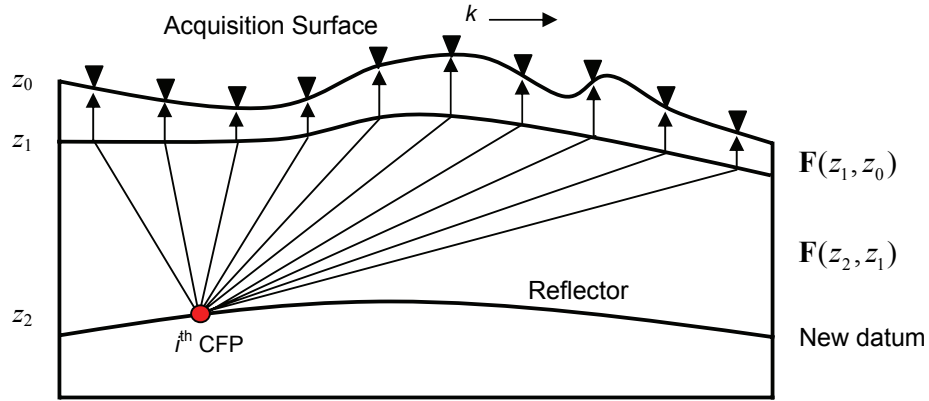


**Fig. 5.4** Schematic diagram of the initial focusing operator components. Here, the rays of one focusing operator are shown. This means that our operator-based solution starts where the statics solution ends

The initial operators can then be used to calculate the DTS gathers. Next, the DTS gathers are checked for horizontal alignment at  $\delta t=0$ , and if this condition is not fulfilled, they are tracked and their differential times are used to update the initial operators according to:

$$\mathbf{F}_{ik}^{\text{updated}}(z_m, z_0) = \mathbf{F}_{ik}^{\text{init}}(z_m, z_0) \Delta \mathbf{F}_{ik}(z_m, z_0) \quad \text{for all } k. \quad 5.12$$

In equation 5.12  $\Delta \mathbf{F}(z_m, z_0)$  has elements  $\Delta \mathbf{F}_{ik}(z_m, z_0) = e^{\frac{i\omega \delta \tau_{ik}}{2}}$  where  $\delta \tau_{ik}$  represents the differential traveltimes in one trace of the  $i^{\text{th}}$  DTS gather (deviation from  $\delta t=0$ ). Equation (5.12) is iterated until the DTS gathers contain a flat reflection event at zero differential time ( $\delta t=0$ ) for all subsurface gridpoints along the reflector under consideration. Through this iterative process the focusing operators capture as many details of the propagation through the complex near surface as possible within the limits of the surface spatial sampling of the data. Figure 5.5 shows a schematic diagram of the iterative updating flow. One-step updating is also possible as described by van de Rijzen (2006). This one-step updating approach requires only tracking the DTS gathers once. This is an important practical advantage.

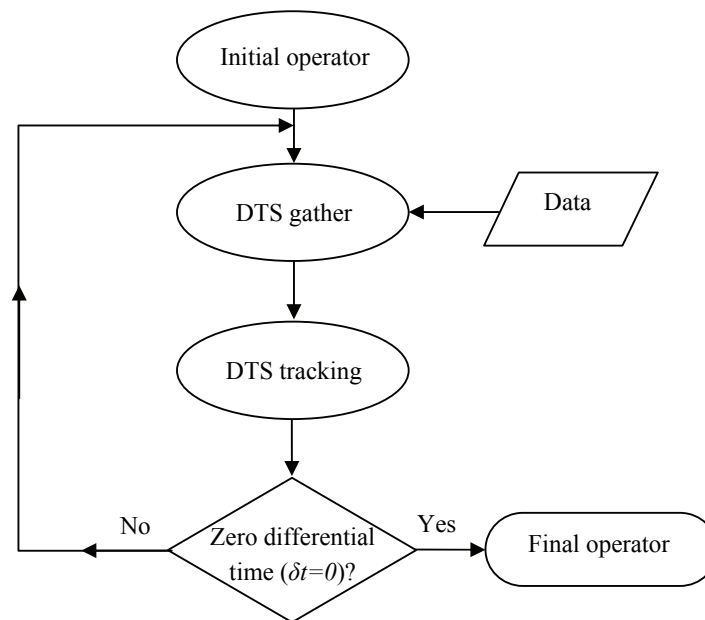


**Fig. 5.5** Schematic diagram showing iterative updating of focusing operators.

Figure 5.6a exhibits a CFP gather constructed from the synthetic data in Figure 5.1, but using an erroneous operator. The operator was altered by increasing the times of the true operator by 20 percent. Clearly, Figure 5.6a shows that the travel times of the focus point response in the CFP gather are not equal to the applied focusing operator. Therefore, we can conclude that the applied operator requires updating. To perform this, we construct the DTS gather and track it as shown in Figure 5.6b. The DTS values are all in the negative time indicating that the applied operator times are larger than the ones from the actual operator. The DTS times are applied to the initial operator according to equation 5.12. The updated operator is shown in Figure 5.6c (green curve) along with the applied erroneous operator (red curve) and the CFP response (black event). Note that the updated operator falls between the focus point response and the applied operator (see Berkhout, 1997, for more details). The operator updating was carried out for two iterations in order to arrive at a horizontally aligned DTS gather at  $\delta t=0$ , as shown Figure 5.6h. The estimated operator and the actual operator are shown in Figure 5.6i with an rms difference of 2.2 ms compared to a 4 ms temporal sampling used in the synthetic data.

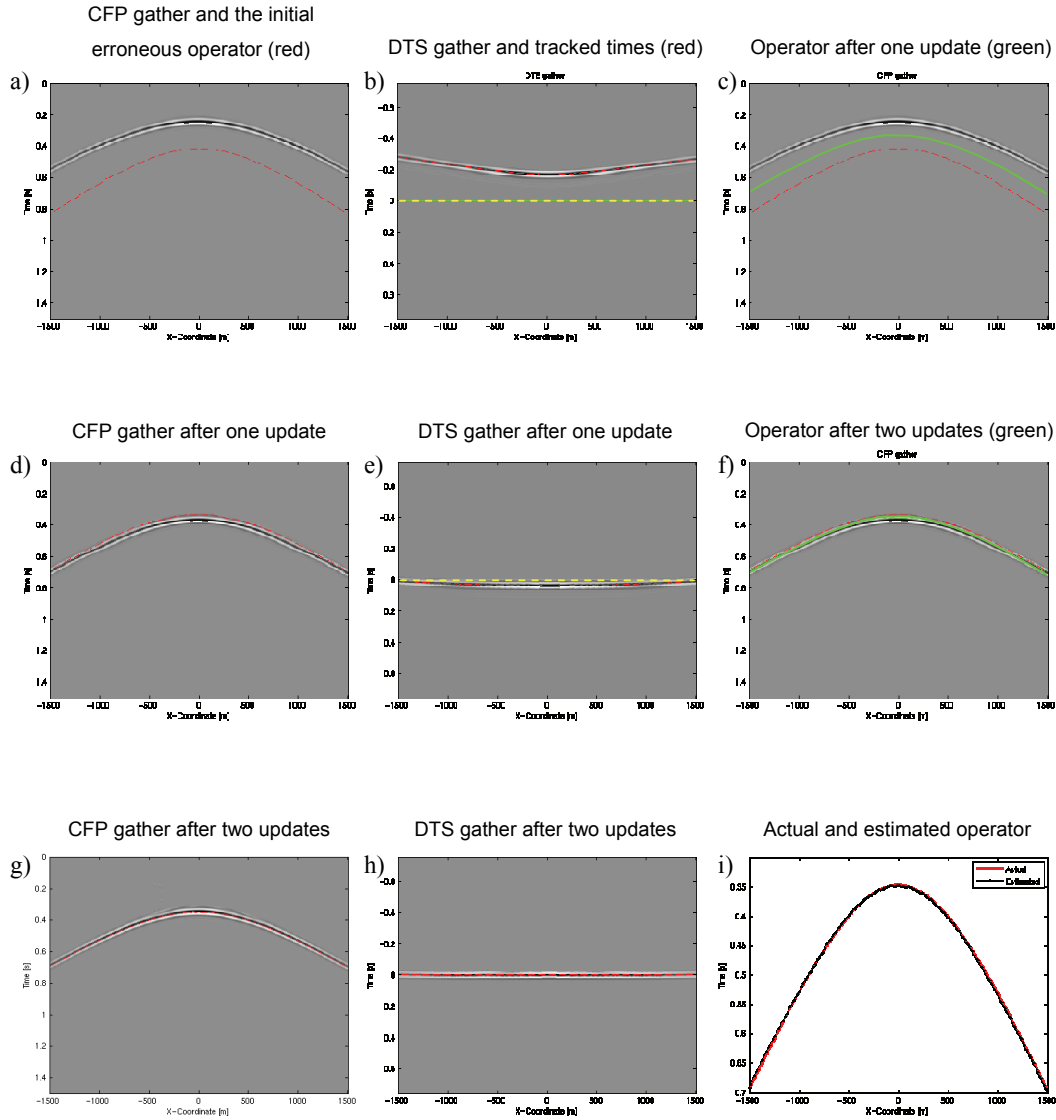


**Fig. 5.6** a) A CFP gather constructed by an erroneous initial operator (red); b) The resulting DTS gather showing non-alignment at  $\delta t=0$ ; c) The same CFP gather as in (a) with the updated operator (green); d) The CFP gather after one update together with the updated operator (red); e) The resulting DTS gather after one update of the initial operator; f) The CFP gather in (d) overlain by the second updated operator (green) and the single updated operator (red); g) The CFP gather obtained after two updates, showing the same travel times as the applied operator (red); h) The resulting DTS gather after two updates exhibiting horizontal alignment at  $\delta t=0$ ; and i) The actual (red) and the estimated (black) focusing operator. Note that the updated operator is in between the focus point response and the operator that created the CFP gather.

Tracking the DTS gathers is not an easy task in the case of a very complex near surface. Hindriks and Verschuur (2001) showed that tracking these gathers by sorting them into surface consistent locations is easier than if they are kept sub-surface consistent. Their approach makes use of the well-known wavefront-healing process. This means that operator and data are compared in the transposed domain.

We build on these findings by considering the DTS gathers as a 3-D volume with its two spatial coordinates as (surface and datum) and time as the third dimension. Therefore, tracking this volume can be considered as a 3-D interpretation problem. This makes tracking through low quality data zones easier by traversing them from different directions. In addition, the good quality data zones would require only a few guiding seeds for an auto tracker to perform the job. We should note that the signal quality of the DTS gathers is generally better than the signal quality of the raw data due to the summation involved in the formation of the CFP gathers (Fresnel zone stacking). This is beneficial for areas characterized with moderate near-surface complexity and low signal/noise ratio, providing a plus over the techniques that depend on tracking first breaks or reflections from the raw data. On the other hand, in areas characterized with good signal/noise ratio and complex near-surface, tracking the two-way reflection times may be easier than tracking DTS gathers based on initial operators that deviate significantly from the true ones. Chapter 6 describes these aspects in detail and introduces a new approach for estimating the focusing operators in *one-step* using tracked two-way-times. The one-step update is demonstrated on field data.

#### **5.4 The integrated method and velocity model building**

From the discussion in Section 5.3, we realize the integrated nature of the described method. Any a priori information of the near-surface velocity model can be included in the initial operators. A priori information can come from uphole data, refraction analyses, vibrator baseplate data (e.g. see Al-Ali et al., 2003), and other sources of information. Accordingly, the updated operators honor the available non-reflection data and the seismic data.

Once the focusing operators are obtained by the updating procedure, the underlying velocity model and the actual location of the focal point of each operator can be obtained by tomographic inversion of the updated focusing operators (Cox and Verschuur, 2001; Cox, 2004). Therefore, tomographic inversion of these operators offers a new way of integrating all a priori information in one final model. This inversion takes into account both the available hard and the soft data components:

- 1 Hard data coming from well measurements.
- 2 Soft data coming from statics solutions such as refraction analyses, gravity profiling, etc.

The final operators can directly be used to redatum to their corresponding reflector, provided the latter does not have conflicting dips. This can be applied to the entire data (2D and/or

3D) available in the survey area (i.e. per prospect). In this case, the reference of the data will be the new datum which has to be consistent among all the data.

In practice, interpreters require all seismic lines in the database to tie with each other so that interpretation can be extended easily from one prospect/field to another. In this case, an effective velocity-depth model has to be obtained by tomographic inversion of the final operator. Then, a new set of operators from pre-defined seismic-reference-datum (SRD) to the surface can be calculated by forward modelling in the velocity-depth model. Subsequently, wave-based redatuming can be performed using these new operators.

In addition, focusing operators from multiple reflectors can be inverted simultaneously to obtain the effective velocity-depth model. Appendix B shows a real data example where the focusing operators obtained for nine reflectors were used to estimate the velocity-depth model. The obtained model was subsequently used to perform pre-stack depth migration.

## 5.5 Field data example (2D)

The field data used in this section comprise a 30 km long 2D line acquired in Saudi Arabia in an area characterized by a complex near-surface geology. Each shot consists of 2880 traces acquired by using a symmetric split-spread with a 5 meter group interval – which is dense – for both sources and receivers leading to a maximum offset of about 7200 m. Figure 5.7a shows a raw shot record from this 2D line with a zoom of this display shown in Figure 5.7b (the location of this shot record is indicated by the red circle in Figure 5.10). Figure 5.7b shows how the reflected energy is just about masked by the Rayleigh waves. Figure 5.7c shows an  $k$ - $f$  plot of this shot record exhibiting the intensity of the Rayleigh waves with a dominant velocity around 600-700 m/s. This can be directly read by displaying the shot record in the linear Radon domain ( $\tau$ - $p$ ), as shown in Figure 5.7d. The Rayleigh waves maximum frequency is about 30 Hz as can be measured from Figure 5.7c. According to the spatial sampling criterion discussed in Chapter 2, the used 5 m sampling is more than adequate for the Rayleigh waves. This is clear from Figure 5.7c where the 5 m sampling has produced almost alias-free sampling of both signal and noise, with the exception of airblast ( $\sim$ 300 m/s) for frequencies above 30 Hz.

The minimum apparent velocity of shallow reflections is about 2500-4000 m/s (marked by the green lines in Figures 5.7a and 5.7b). Deeper reflections exhibit a higher apparent velocity. The 2500 m/s velocity belongs to a shallow reflector with variable thickness which obscures the reflections from deeper reflectors. It also causes an apparent structure. The 4000 m/s velocity pertains to a reflector that is known to be regionally flat. This reflector is always considered to be the ‘hanging-horizon’ where subsurface depth models are referenced to. Therefore, the acquisition geometry should allow removing the distortions occurring to the signal while travelling from the acquisition surface to the ‘hanging horizon’. According to Chapter 2, 25 m spatial sampling should be adequate to alias free sample reflections from surface to the ‘hanging horizon’ noting that the maximum signal frequency is about 60 Hz.

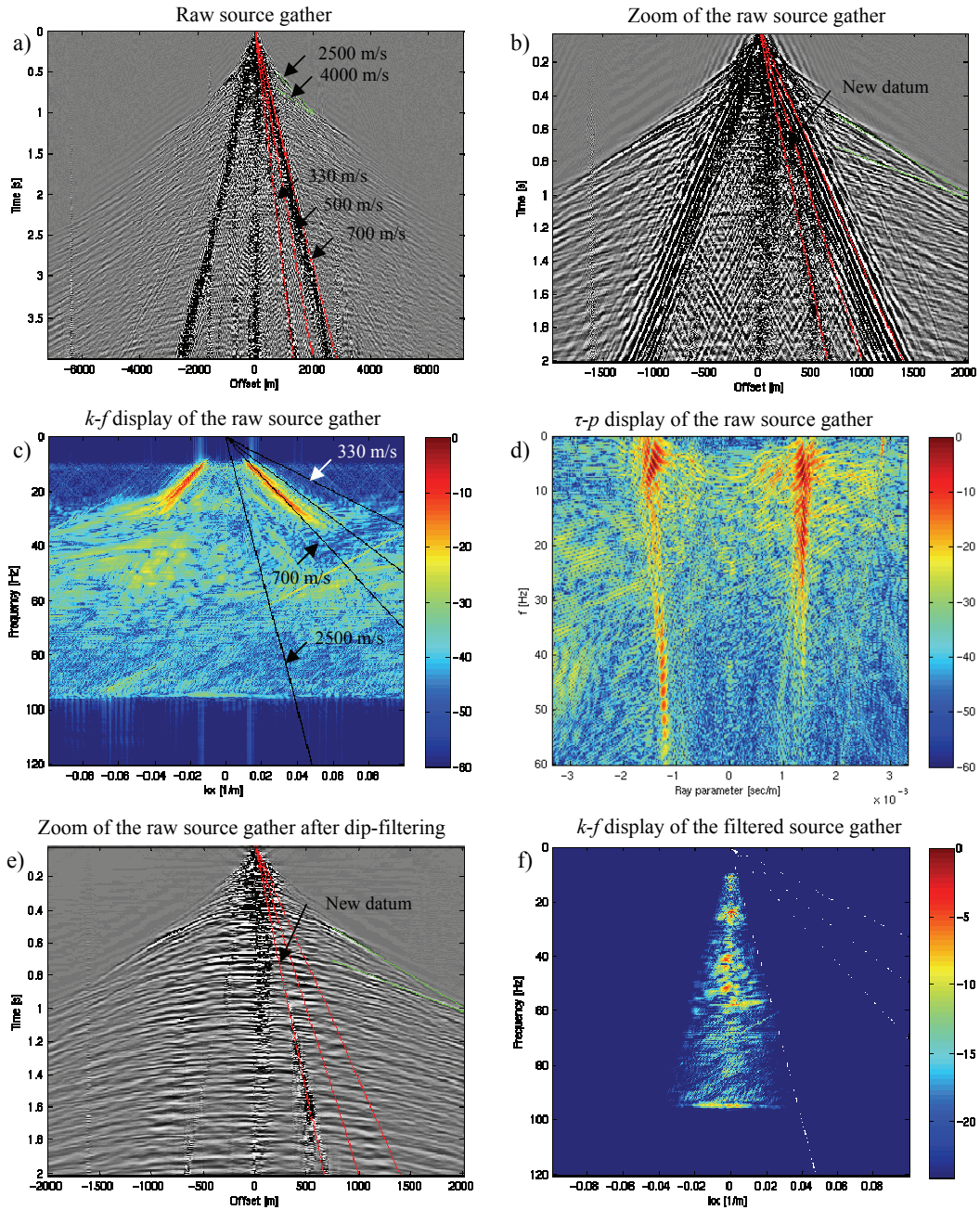


**Fig. 5.7** a) Raw shot record with 5 m spatial sampling; b) zoom of (a); c)  $k$ - $f$  spectrum of (a); d) Radon domain ( $\tau$ - $p$ ) of (a); e) the same as (b) after dip filtering of coherent noise; and f)  $k$ - $f$  spectrum of (e). (Courtesy of Saudi Aramco)

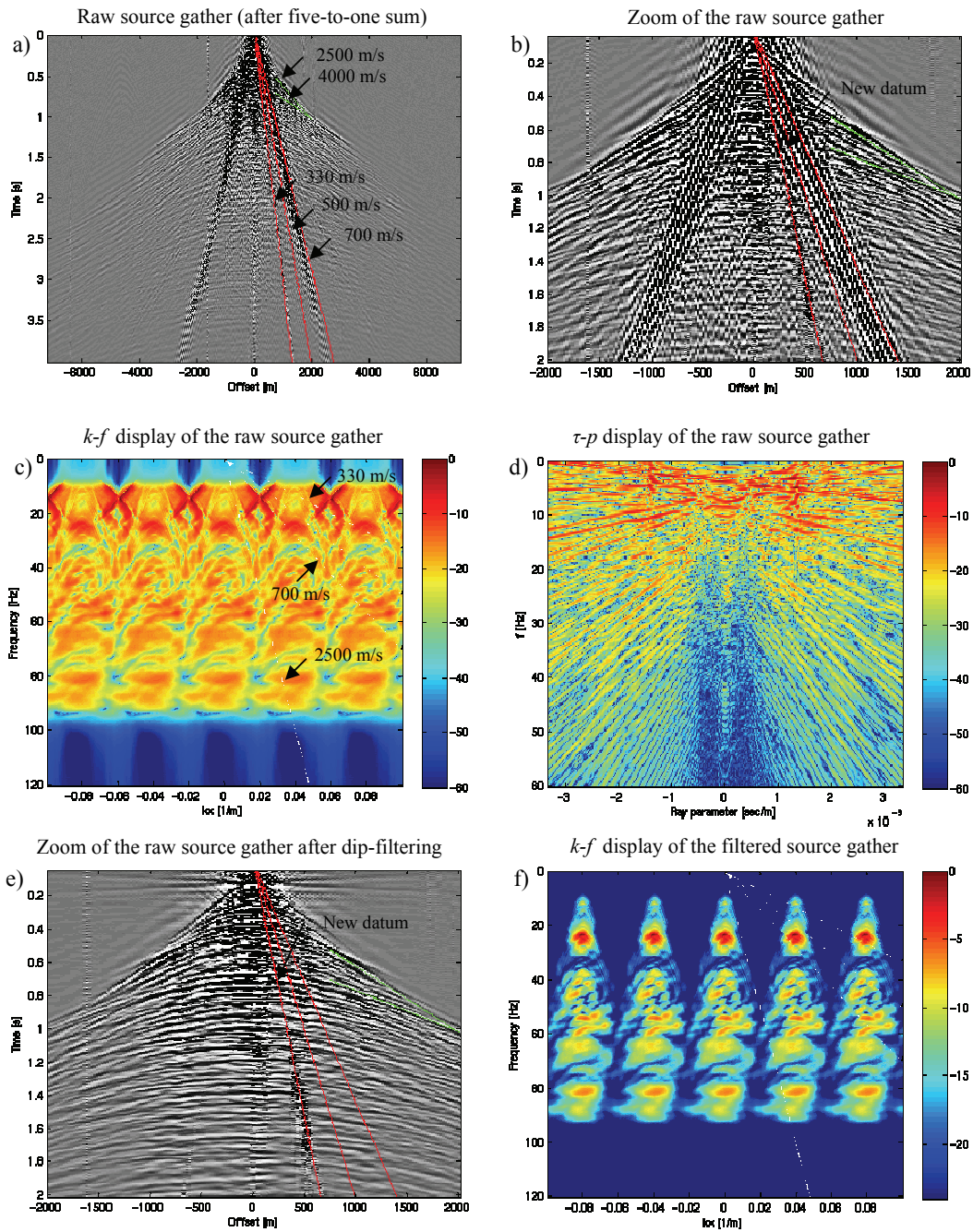
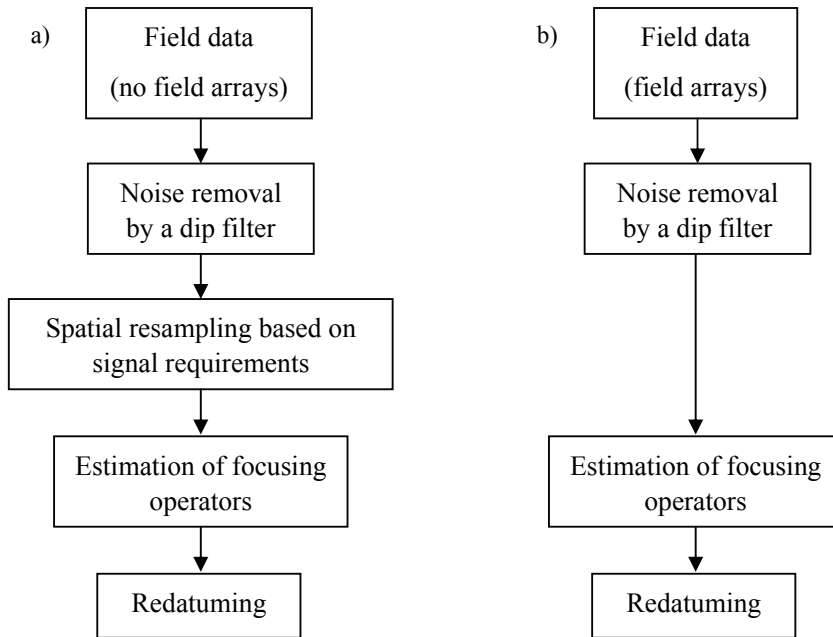


**Fig. 5.8** a) Raw shot record with 25 m spatial sampling obtained after five-to-one sum of the five gathers similar to the one in Figure 5.7a; b) zoom of (a); c)  $k$ - $f$  spectrum of (a); d) Radon domain ( $\tau$ - $p$ ) of (a); e) the same as (b) after dip filtering of coherent noise; and f)  $k$ - $f$  spectrum of (e).

The used 5 m spatial sampling allows removing the coherent noise in processing. Then, digital array forming can be performed to resample the data according to signal requirements. This is the approach for point-source point-receiver acquisition. Figure 5.7e shows the same shot record as in Figure 5.7b after removing the coherent noise by dip filtering, and Figure 5.7f shows the related  $f-k$  spectrum. It is clear that the coherent noise has been effectively removed. What remains of the proposed pre-processing scheme is the removal of the signal distortions due to the complex near-surface. This is done by an operator based approach. Figure 5.9a shows this acquisition and pre-processing flow.

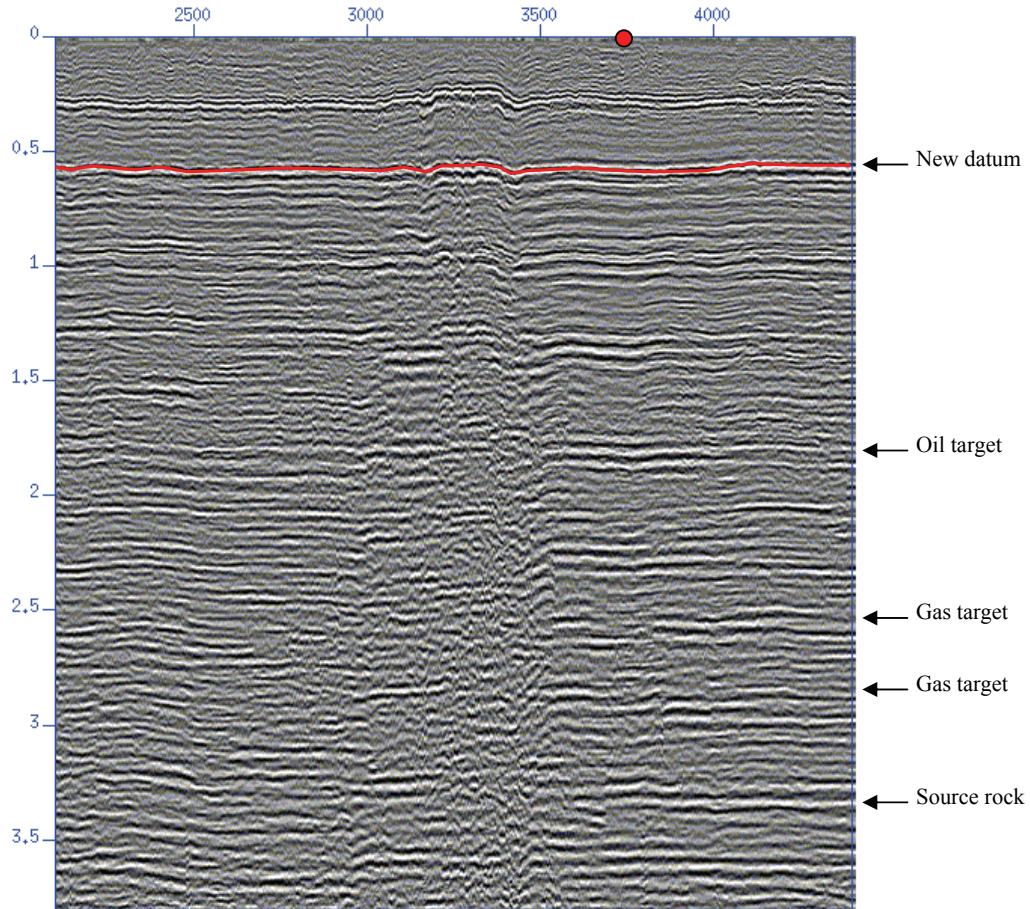
Another approach to acquire the data, as described in Chapter 2, is to sample the data in the field based on signal requirements while making sure that the aliased noise does not overlap with the signal band. In this case, field arrays are necessary to attenuate noise. This approach can be simulated using our field data set. We stated above that 25 m spatial sampling is adequate for the signal from different levels. Thus, a five-to-one summation was applied to the data that results in 576 traces per shot with a group interval of 25 meters for both source and receiver. Figure 5.8a shows the same shot record as in Figure 5.7a but after the five-to-one summation with a zoom of this display shown in Figure 5.8b. The latter exhibits less coherent noise than Figure 5.7b, which means that the field arrays have attenuated part of the noise but not completely. Figure 5.8c and 5.8d show the  $f-k$  and  $\tau-p$  displays of the shot in Figure 5.8a respectively. Figure 5.8c shows that coherent noise is aliased but it does not overlap with the signal band. Further attenuation of noise can be done using dip filtering as shown in Figure 5.8e with the  $f-k$  spectrum in Figure 5.8f. The complete acquisition and pre-processing flow using this approach is shown in Figure 5.9b. We will carry on with this processing flow to demonstrate the proposed operator-based approach to remove signal distortions.

Figure 5.10 shows a common-mid-point (CMP) stack which clearly shows a relatively deep near-surface anomaly around  $t=0.3$  s between CMP's 3000 to 3500 that obscures the deeper reflections. A reflector below the complex near-surface marked by a red line (Figure 5.10) was chosen to be the new datum. Subsequently, initial operators were calculated using the conventional statics, according to Section 5.3. Then, DTS gathers were generated using coherent noise free data to a maximum offset of 750 meters.



**Fig. 5.9** a) Acquisition and pre-processing flow for point-source point-receiver acquisition; and b) acquisition and pre-processing flow where field arrays are used.

Figure 5.11 shows the initial DTS stack around the new datum, using the initial operators. The result is obtained by stacking the traces of each DTS gather, which represents the double focusing result without imaging (i.e. double summation). It functions as a quality-control tool. The quality of the DTS stack shows that the operators do not describe the data sufficiently well. This is confirmed by Figure 5.12, showing every 15'th DTS gather between gathers 400 and 800. The curvatures in these gathers clearly show that the initial operators do not describe the data sufficiently well.



**Fig. 5.10** CMP stack after applying conventional statics. The new datum is marked by the red line. The red dot on the top indicates the location of the shot record in Figures 5.7 and 5.8. (Courtesy of Saudi Aramco)

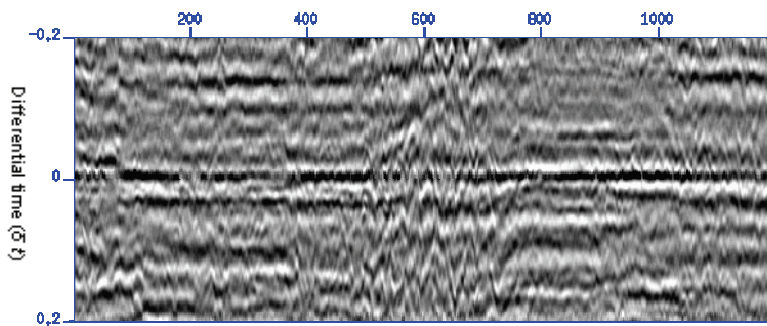


**Fig. 5.11** DTS stack, using focusing operators calculated from the stacking velocities.

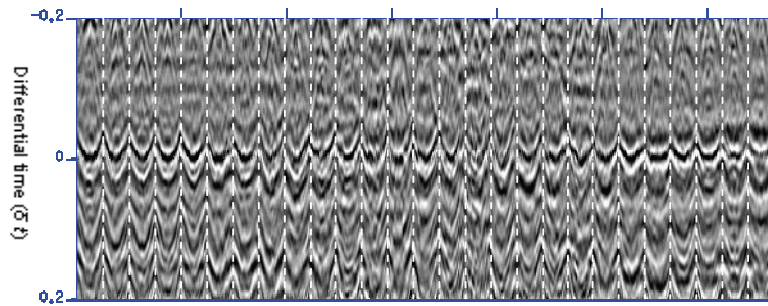


**Fig. 5.12** Every 15<sup>th</sup> DTS gather between datum-locations 400 and 800 as labelled in Figure 5.11. Notice the curvature in the gathers, indicating that the initial operators do not describe the data well.

Tracking the DTS gathers was performed as a 3D volume interpretation task, which is particularly important in low data quality zones to assure the consistency of the tracked reflection events. This task was performed by loading the DTS volumes into a commercial 3D interpretation package (Charisma). Three updating iterations were carried out to the initial operators. Figure 5.13 shows the DTS stack using the final operators. The event of interest is well focused at  $\delta t=0$ . Corresponding unstacked DTS gathers are shown in Figure 5.14 (compare with Figure 5.12). The horizontal alignment of the DTS gathers at  $\delta t=0$  indicates that the estimated operators describe the data very well. Note that at this stage the velocity model of the near-surface is still unknown.

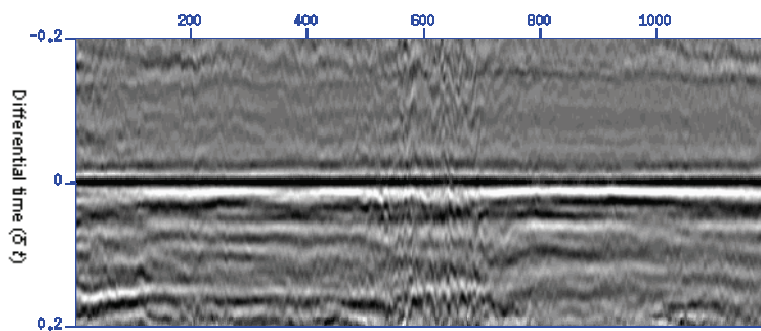


**Fig. 5.13** DTS stack, using focusing operators after three updates. Compare with Figure 5.11.

Subsequently, the final focusing operators were used for redatuming. Figure 5.15 shows a CMP stack of the redatumed source gathers.

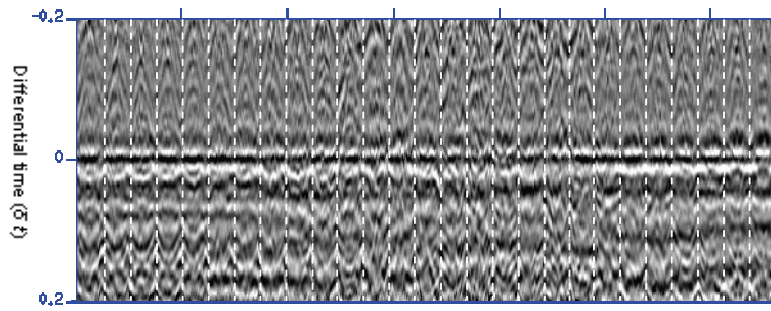


**Fig. 5.14** Every 15<sup>th</sup> DTS gather between gathers 400 and 800 as labelled in Figure 5.13. Compare with Figure 5.12.

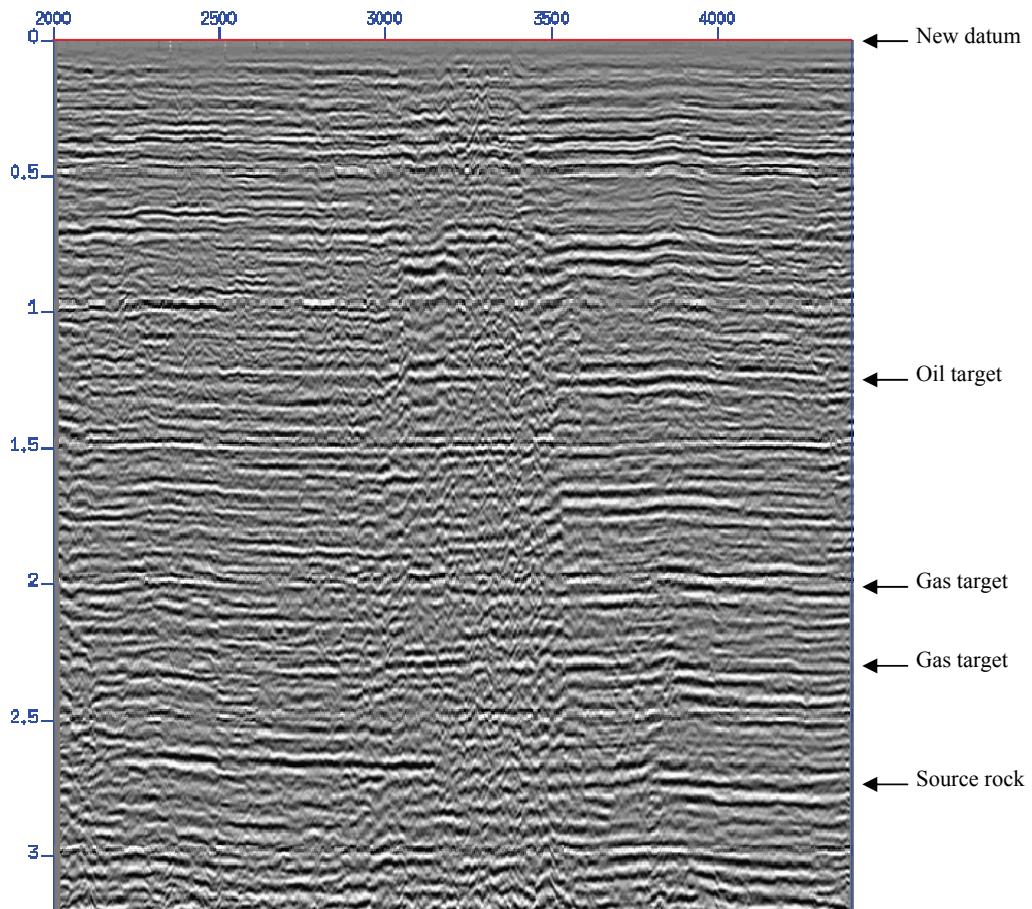


**Fig. 5.15** CMP stack after redatuming using the final operators obtained.

The result of Figure 5.15 shows clear improvements particularly in the middle of the section where the near-surface anomaly is located. This can be best compared to the result of flattening the original CMP stack of Figure 5.10 at the datum reflector, as shown in Figure 5.16. The image of Figure 5.15 can be considered as a prestack wave-equation-based flattened image at the datum reflector.

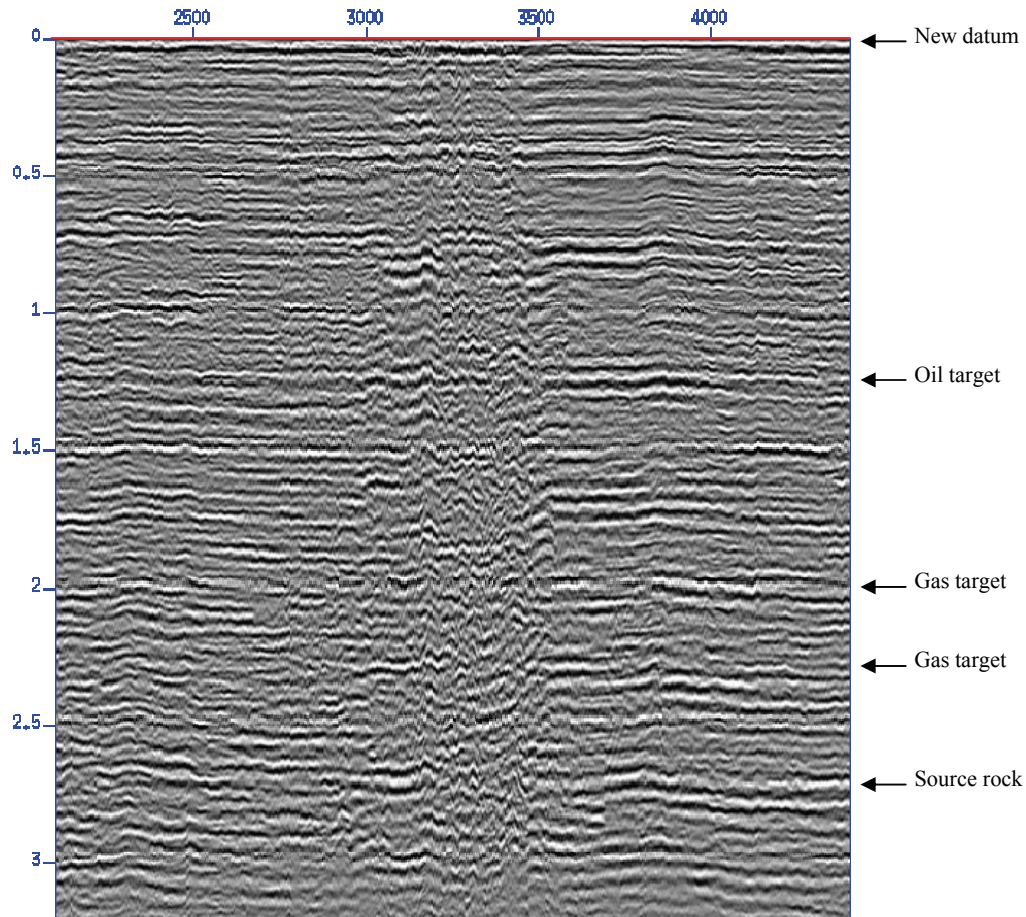


**Fig. 5.16** Flattened stack of Figure 5.10. Compare with Figure 5.15.

In summary, this data example demonstrates the power of the operator-based solution in practice. Although the obtained improvements are significant, they can be increased by estimating the amplitudes of the focusing operators. In addition, removal of surface and interbed multiples should grant more improvements. Appendix B uses the same data set and introduces a new approach for estimating the focusing operators in one-step from tracked reflection two-way-times.

## 5.6 Operators estimation for 3D data

This section describes a method for estimating 3D focusing operators (time-reversed Green's functions) using cross-spread data. Note that a 3D focusing operator contains one-way traveltimes from many points along an areal surface grid towards one subsurface point. An initial operator is updated using the misalignment observed in the DTS gather for the subsurface gridpoint under consideration. However, due to the sparse  $x$ - $y$  geometry an extension of the standard CFP-technology needs to be introduced. The method is demonstrated on synthetic as well as real data.

### 5.6.1 Introduction

CFP imaging technology applies to 2D as well as 3D surface seismic measurements. In the case of 2D, common source gathers are always sampled to meet pre-defined aliasing criteria. This leads to alias-free imaging and, in turn, allows for the creation of an alias-free CFP gather and also an alias-free DTS gather. Note that either the common source or common receiver gathers are required to be adequately sampled so that good quality CFP and DTS gathers can be generated. This also applies to the 3D case where adequately sampled 3D common source or common receiver gathers are needed.

Unfortunately, 3D data are rarely acquired to meet this requirement. One exception may be some cases of ocean-bottom (node-type) surveys where well-sampled 3D common receiver gathers are available. Therefore, data infilling has to be performed before constructing the CFP and DTS gathers. Aliasing in the CFP gathers has been outlined by Thorbecke (1997) and Bolte (2003). Van de Rijzen et al. (2004) discussed a data infilling scheme for sparse (marine type geometry) 3D data that allows the determination and updating of 3D focusing operators in a way similar to the 2D case.

In practice, velocity-driven 3D prestack imaging is often performed using common-offset-azimuth (COA) gathers. Such gathers are single-fold 3D subsets that allow alias-free imaging and they usually extend over the entire survey area. However, exact COA gathers cannot be generated from regularly used land geometries; thus, approximate or regularized COA gathers are used (see for example Cary, 1999, and Vermeer, 2002 and 2005). Vermeer (2002 and 2005) calls these gathers the offset-vector-tiles (OVT). In this chapter, we follow another route by making use of the fact that cross-spreads are also single-fold 3D subsets, which can be generated from regularly acquired 3D orthogonal geometries (land type geometries). Cross-spreads are adequately sampled in two orthogonal directions making them good candidates for 3D prestack migration (Vermeer, 1994). Note that they do not extend over the entire survey area as in the case of COA or OVT gathers.

Note also that neither the COA gathers nor the cross-spreads can be used to generate good-quality CFP gathers. In the following, we use similar arguments as applied in the standard CFP technology, but instead of using common source or receiver gathers, these DTS gathers are constructed using cross-spreads. The proposed method can also be applied to COA gathers.

### 5.6.2 Methodology

A cross-spread combines the densely sampled coordinates of both source and receiver in one single-fold 3D subset e.g.  $(x_s, y_r, t)$  or  $(x_r, y_s, t)$ , where the indices  $s$  and  $r$  represent source and receiver respectively. The main advantage of this combination is that it allows alias-free Fresnel stacking in two directions. The result from this stacking (integration) is a single-fold image of the subsurface gridpoint under consideration where both sources and receivers are focused. This process transforms each cross-spread to one trace of the so-called cross-spread DTS gather. However, without additional information, the DTS gather obtained this way cannot be directly used for focusing operator updating like single-sum DTS gathers. This will be discussed below.

Since the subsurface gridpoint under consideration is normally illuminated by different cross-spreads, we can form a double-sum DTS gather for that gridpoint where each trace in this gather is generated from one cross-spread by double focusing. Note that this DTS gather differs from the original version (i.e. from the standard CFP-technology) which assumes focusing over either the source or the receiver coordinates of the common source or common receiver gathers, respectively, followed by time-shifting. A cross-spread DTS gather is obtained after two focusing steps: a single focusing along one receiver coordinate and a single focusing along the perpendicular source coordinate. Therefore, a trace in this DTS gather cannot be associated with one source location anymore. Nevertheless, if the correct focusing operators per cross-spread are used, then the contributions from all cross-spreads will again align at zero-time in the DTS gather. If an erroneous operator is used, then the DTS gather will not align at the image time but it will have some time-shifts (curvature). In order to correct the focusing operator based on these time-shifts, knowledge of the actual source-receiver pair (stationary point location) that contributed to the result is required for each cross-spread. An automated search method was developed based on coherency that allows determining the contributing source-receiver pair for each cross-spread after having tracked the event of interest. This allows us to iteratively update the erroneous focusing operator towards the correct one using the same flow as used in the standard CFP-technology (see Figure 5.5).

The following steps are involved in the 3D focusing operator determination using cross-spreads:

1. Calculate an 3D initial focusing operator for the subsurface gridpoint under consideration. The CMP stacking velocity can be used for this purpose. For complex near-surface situations, the 3D initial focusing operators can be calculated such that pre-knowledge of the near-surface and surface elevation are incorporated (see Al-Ali and Verschuur, 2006).
2. Apply the focusing operator to the sources and the receivers of each cross-spread within the aperture of this gridpoint. This means applying time shifts to the traces according to the focusing operator times at the source and at the receiver locations.

Next, sum all the traces in a time-corrected cross-spread gather. The resulting trace is assigned to a dummy reference number. We propose this number to be the center position of the cross-spread. This is repeated for all cross-spreads to produce the double-sum DTS gather.

3. If the event of interest is not aligned at  $\delta t=0$ , track the DTS gather and then, for each trace in this gather find the contributing source-receiver pair of the corresponding cross-spread (the method will be discussed in the next section).
4. The differential time ( $\delta t$ ) observed in each trace of the DTS gather is divided by two and assigned equally to the contributing source-receiver pair. The result is used to update the current operator.
5. Iterate steps 2 to 4 until the DTS gather is aligned at  $\delta t=0$ .
6. Result: 3D one-way travel times between the subsurface gridpoint under consideration and the surface gridpoints of the operator (one-way Green's function or focusing operator).

It is important to realize that the single-sum DTS-gather is the result of one focusing step only (along source or receiver coordinates). In the double-sum DTS-gather two focusing steps are used along the source and receiver coordinates of a data subset, thus, it is not linked to the surface anymore but it is assigned to a dummy location which is the center cross-spread coordinate, Figure 5.17. Note that in both DTS-gathers *all* traveltimes (down and up) have been removed and that the imaging principle is *not* applied (all time samples are still available). Note also that each trace of a double-sum DTS-gather represents the DTS-stack of a data subset (here a cross-spread).

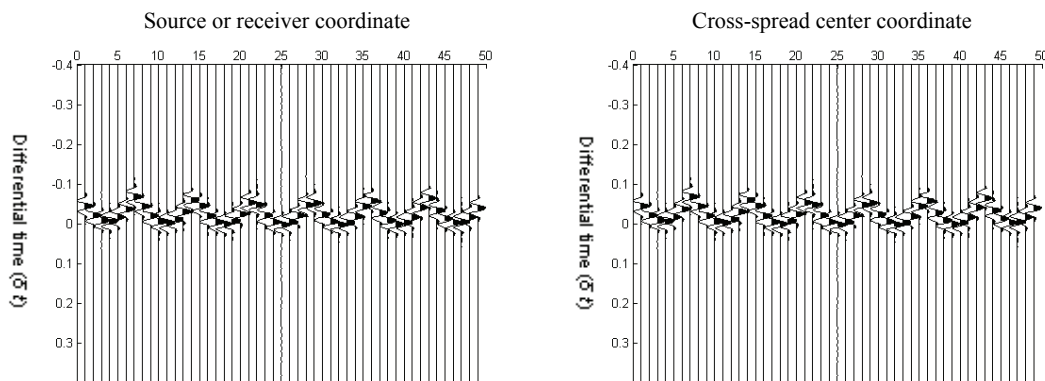


**Fig. 5.17** Single-sum DTS gather referenced to the source or receiver coordinate (left), and double-sum DTS gather referenced to the center cross-spread coordinate which is a dummy number.

### 5.6.3 3D focusing operator updating using cross-spreads

Based on the previous explanation, it is clear that using cross-spreads as basic 3D building blocks and performing a double focusing process will lead to a stacked DTS-gather trace for each cross-spread. If the correct focusing operator per cross-spread is used, then DTS stacks of all cross-spreads will align at zero time. I will demonstrate this in the following numerical example.

The subsurface model used in this example consists of a flat reflector at a depth of 1800 m with a constant velocity of 3000 m/s. The target point is selected to be in the center of the model. The basic acquisition template is shown in Figure 5.18a. The source station interval ( $S_s$ ) is 25 meters and the receiver station interval ( $R_s$ ) is also 25 meters. This template is repeated 12 times in both cross-line and inline directions with an equal distance of 300 meters. This results in 144 cross-spreads (Figure 5.18b). This geometry produces a CMP fold of 36.

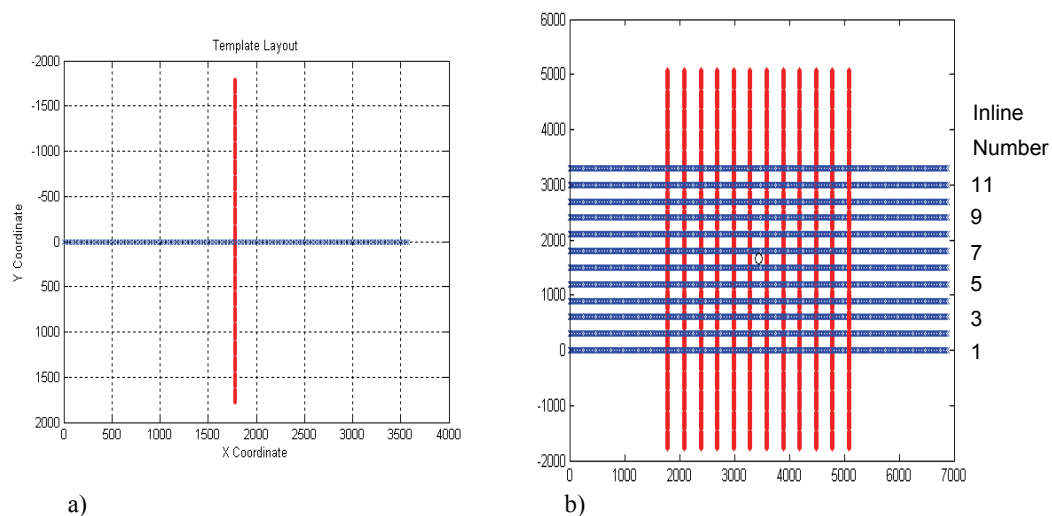


**Fig. 5.18** Cross-spread geometry, a) basic template layout b) complete survey geometry consisting of 144 cross-spreads.

Figure 5.19a shows the DTS-gather obtained from the 144 cross-spreads (each trace of the gather is the DTS stack of one cross-spread), applying a correct focusing operator. Each of the twelve panels in this figure shows the DTS-substacks obtained from the 12 cross-spreads traversing the horizontal direction of the survey (see Figure 5.18 for reference). Together they form the 3D DTS-gather of the cross-spread data. Figure 5.19b shows the same gather obtained using an erroneous operator (calculated by using an erroneous velocity of 2500

m/s). It is clear that in this case the focused gridpoint responses are not aligned at  $\delta t=0$ . The magnitude of the differential times can be obtained from these panels. However, the differential times observed in these panels cannot be directly used to update the one-way-time focusing operator like in the case of DTS-gathers constructed from CFP gathers. This is because we focused both source and receiver coordinates within each cross-spread. The result is not linked anymore to a known source or receiver location, but only to a particular cross-spread. As a consequence, we need to determine the contributing source-receiver pair (specular reflection pair or point of stationary phase) in the corresponding cross-spread for each trace in the DTS-gather prior to updating.

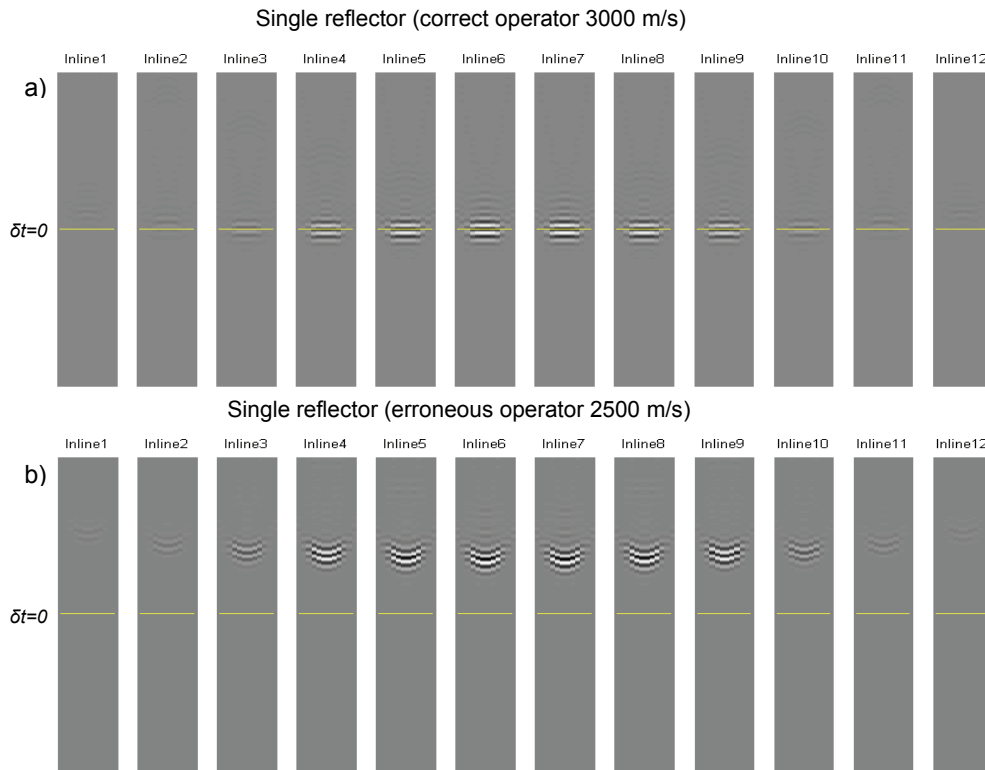


**Fig. 5.19** 3D DTS gather containing 144 traces, one for each cross-spread displayed as successive 2D panels a) correct operator b) erroneous operator.

The current approach for finding this contributing source-receiver pair consists of the following four steps:

1. Apply the focusing operator to each cross-spread *without* stacking. This leads to the so-called CFP data matrix. The zero-time cross section is shown in Figure 5.20a.

2. Stack the CFP data matrix to produce one trace of the DTS-gather (double-sum) for each cross-spread and pick the reflection event of interest (Figure 5.20b). Keep the time pick (i.e. the differential-time-shift) and the trace for the following two steps.
3. Starting with the operator-corrected cross-spread of step 1, perform the summation along the common source gathers, i.e., in the receiver direction only. This will result into a gather along the sources of the cross-spread under consideration. This should allow picking the stationary phase point with respect to the source. Figure 5.20c shows this process. Use coherency (after Neidell and Taner, 1971) or cross correlation between this section and the trace obtained in step number 2 to find the stationary phase point. The coherency or the cross correlation needs only to be performed in a narrow window around the picked differential time for the reflection event of interest.
4. Perform the summation as in 3 but along the common receiver gathers i.e., sum in the source direction only. Now, the stationary phase point with respect to the receiver can be determined in this case as shown in Figure 5.20d.

Thus, having obtained the contributing source-receiver pair, the differential time observed after focusing a cross-spread data can be used to update the focusing operator at the locations of this source-receiver pair. The focusing operator for all the cross-spreads is smooth as it represents an impulse response (one-way Green's function) of the subsurface gridpoint measured at the surface acquisition geometry locations (Figure 5.21). Thus, the number of update points (depending on the number of cross-spreads that illuminated the subsurface gridpoint) is expected to be adequate to converge to an accurate 3D focusing operator.

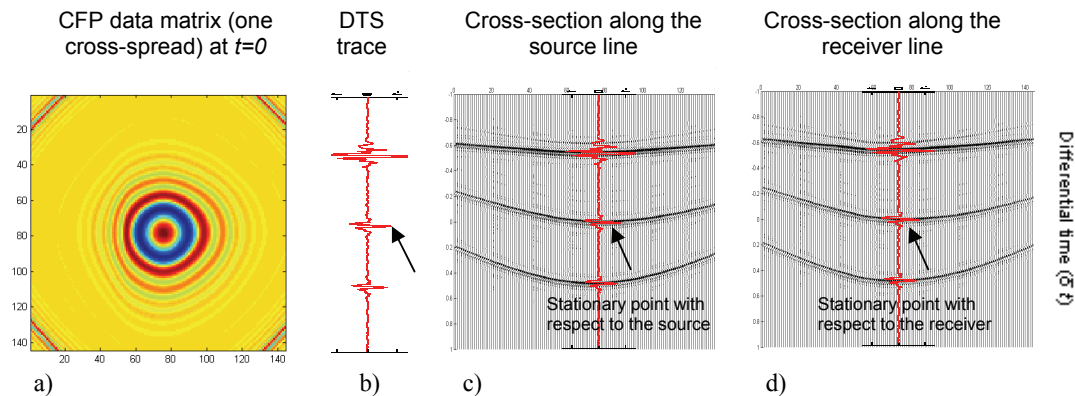


**Fig. 5.20** Stationary point determination per cross-spread, a) cross-spread time slice at zero time; b) DTS trace (double-sum) with the arrow pointing at the target event; c) stationary point with respect to the source (single-sum); d) stationary point with respect to the receiver (single-sum).

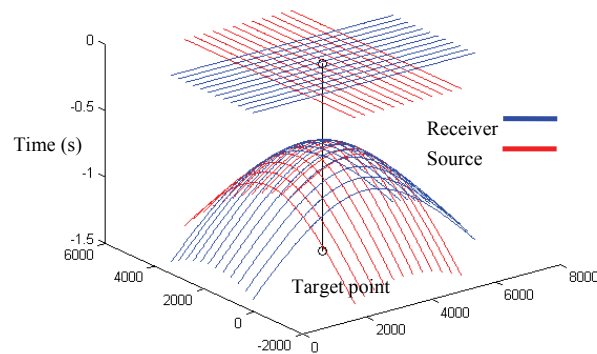


**Fig. 5.21** Travel time surface of a 3D focusing operator for one target point (one-way Green's function).

#### 5.6.4 Synthetic data example (3D)

The following synthetic example illustrates the operator updating approach for cross-spreads. A basic acquisition template of one cross-spread consisting of 144 sources and 144 receivers each spaced at a 25 m interval is used. This template is repeated 12 times along the  $X$ -direction and 12 times along the  $Y$ -direction with a step of 300 m in both directions. This geometry produces a CMP fold of 36 like the geometry used in the previous section. A three layer model was used consisting of two flat layers and one dipping layer in the middle ( $3^\circ$  dip in both  $x$  and  $y$  directions) as shown in Figure 5.22a. The subsurface gridpoint is chosen to be on the second reflector in the center of the survey at a depth of 1800 m. Figure 5.22b shows the DTS gather (double-sum) for the correct focusing operator. Note that only a limited number of cross-spreads out of the 144 cross-spreads have illuminated the target point.

An erroneous initial operator was used with a difference from the correct operator exhibited in a percentage by Figure 5.22c. This figure only extends over the area of the cross-spreads that illuminated the target point. The resulting cross-spread DTS gather is shown in Figure 5.22d. It is clear that the DTS gather for the second reflector is neither at the correct zero time nor flat. After four iterations using the scheme of Figure 5.5, the difference (in percentages) between the estimated operator and the correct operator is shown in Figure 5.22e. The root mean square of the error in the estimated operator is 4.6 ms which is very close to the temporal sampling interval of the synthetic data (4.0 ms). The corresponding DTS gather is shown in Figure 5.22f.

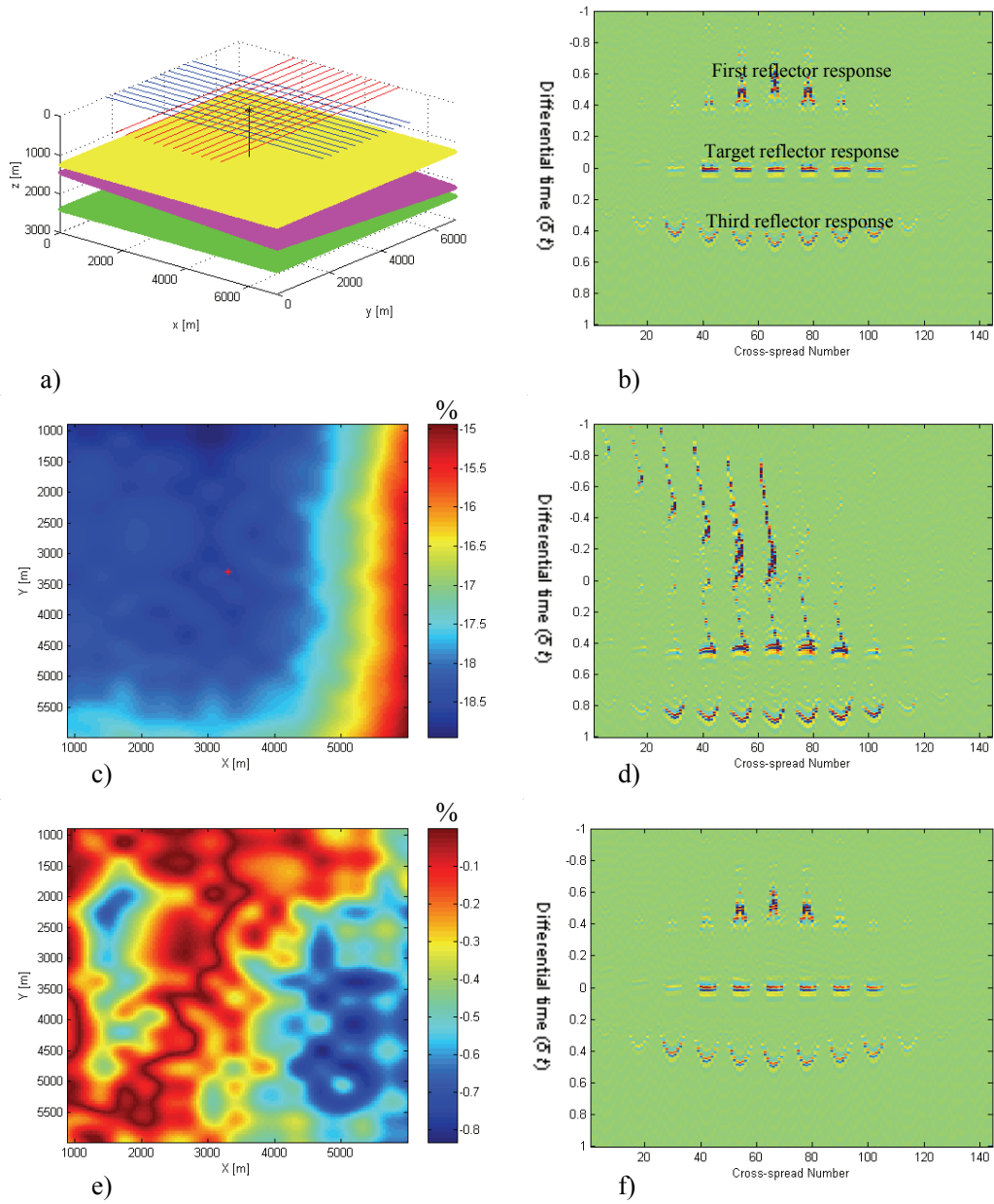


**Fig. 5.22** a) acquisition geometry and model; b) DTS-gather (double-sum) obtained using the correct operator displayed as successive 2D panels; c) difference between erroneous and correct operator; d) DTS-gather (double-sum) obtained using the erroneous operator; e) difference between updated operator and correct operator; f) 3D DTS gather obtained using the updated operator.

### 5.6.5 Field data example (3D)

The example of this section is obtained using a subset of a real 3D field data set acquired in Saudi Arabia. Figure 5.23a shows the geometry of this subset with the background color exhibiting the surface elevation above mean-sea-level (MSL). The data consists of 77 cross-spreads (11 east-west by 7 south-north). Each cross-spread consists of 80 source points and 80 receiver points with equal source and receiver intervals of 30 meters. The source line spacing is 150 meters and the receiver line spacing is 240 meters. This produces a nominal CMP fold of 40, 8 (east-west) by 5 (south-north). Figure 5.23b shows a CMP stack along the middle receiver line with the analysis reflector marked around  $t=0.5$  in red. A target point in the middle of the survey on the analysis reflector was selected. An initial operator was calculated using the stacking velocity (2900 m/s) while also taking into account the surface elevation. This operator was used to calculate an initial DTS-gather (double-sum). Figure 5.24a exhibits the resulting DTS-gather as displayed in 2D panels. This gather contains the DTS traces of 40 contributing cross-spreads. Clearly, the initial operator is incorrect as the event of interest is not aligned at  $\delta t=0$  but at a later time.

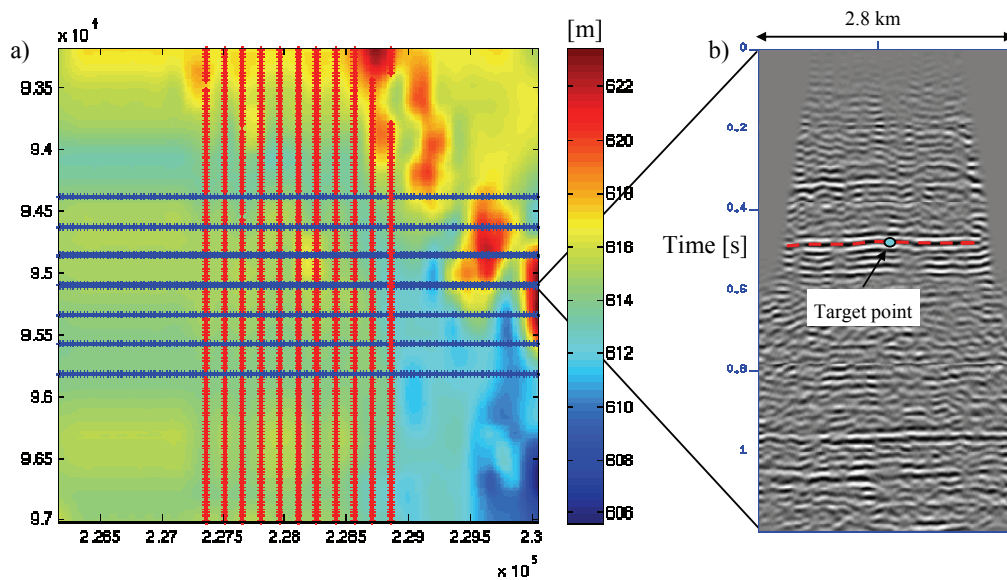


*Fig. 5.23 a) acquisition geometry from a field dataset: sources (red) and receivers (blue) with background color exhibiting the surface elevation above mean-sea-level; b) CMP stack along the middle receiver line. (Courtesy of Saudi Aramco)*

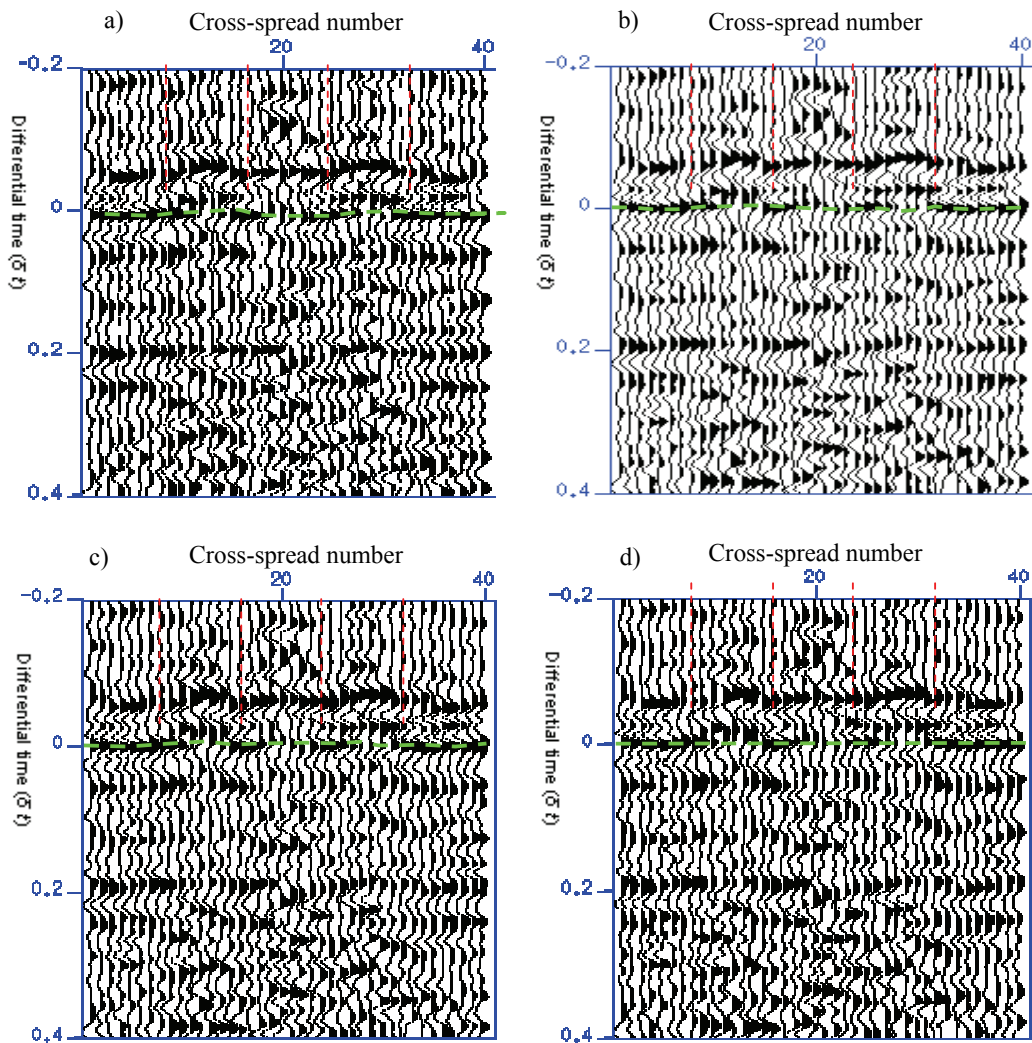


**Fig. 5.24** a) DTS gather generated using the initial operator; b) DTS gather generated after one update; c) DTS gather obtained after two updates; and d) DTS gather obtained after three updates. The dashed vertical red lines indicate the separation between the DTS gather slices since all of these displays are for 3D DTS gathers with 8 traces in east-west direction and 5 traces in the south-north direction.

Three iterations for updating the focusing operator were carried out. Figures 5.24b, 5.24c, and 5.24d show the obtained DTS gathers after each iteration. After the first update the reflection event under consideration is more or less aligned at  $\delta t=0$ . The subsequent two updates show subtle improvements. In practice, this analysis would be performed for a regular grid of target points on the analysis reflector. In that case, the tracked DTS times

have to be contiguous in the entire 5D volume<sup>1</sup> of the DTS gathers. Traversing this 5D volume from different directions will assist in finding the right event particularly in areas with complex near-surface.

Figure 5.25a shows the initial operator and Figure 5.25b shows the operator obtained after three iterative updates with both inline and cross-line maximum offsets of 800 m from the target point. Figure 5.25c shows the difference between the initial operator and the updated operator. This difference is aligned with the orientation of the surface elevation exhibited by Figure 5.23a. Although the surface elevation was taken into consideration when calculating the initial operator using a constant velocity of 2000 m/s, yet the updating revealed that further corrections were required to better align the DTS gather. This indicates that the near-surface velocity is not constant in the data area. Note that a near-surface velocity of 2000 m/s used to account for elevation differences is different from the stacking velocity used to calculate the operator through the more homogenous part (i.e. 2900 m/s) as described in Section 5.3.

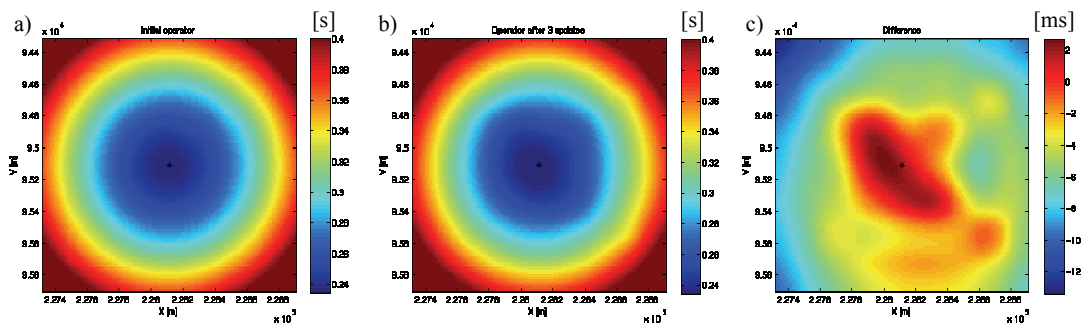


**Fig. 5.25** a) DTS Initial operator in (s); b) Operator after three updates in (s); and c) Difference between a) and b) in (ms).

Finally, similar to the 2D case, once the 3D focusing operators have been determined for a dense grid of point, they can be directly used to redatum to the respective reflector. The redatuming can be performed without a need for data infilling to account for the sparse sampling using the technique developed by Tegtmeier et al. (2004). Furthermore, these operators can also be used to obtain the underlying velocity-depth model using tomographic inversion.

<sup>1</sup> The 5D volume has two surface coordinates  $(x,y)$ , two subsurface coordinates  $(x-cfp,y-cfp)$ , and time.

## 5.7 Concluding remarks

A method for removing the distortion effects of complex near-surface from seismic images has been proposed. The basis of this approach is velocity-independent estimation of the focusing operators (one-way Green's functions). It circumvents the difficulties encountered by equivalent methods that treat the near-surface effects as an imaging problem. The difficulties are attributed to lack of knowing a sufficiently accurate near-surface velocity model. Our approach does not require such a model at forehand. However, *after* the focusing operators have been estimated, the velocity model is obtained via a tomographic inversion process of the operators.

The proposed method stems from the Common Focus Point technology. In addition, it integrates the conventional statics method with the wave-equation datuming approach. This is achieved by using the conventional statics solution in the initial focusing operators. The latter are iteratively updated towards fulfilling the principle of equal travel time without a need for updating the underlying velocity model. The seismic data is preserved with its reference being the actual acquisition surface. It categorizes the method as an uncommitted solution.

The approach shows good results on a complex 2D field dataset from Saudi Arabia with a complex near-surface. This makes this approach a viable alternative to the conventional statics-based processing.

Furthermore, this chapter demonstrated the velocity-independent approach to iteratively estimate 3D one-way focusing operators using cross-spreads without the need for data infill. First results are promising.



## Estimation of one-way focusing operators from two-way traveltimes

*This chapter describes a method for estimating 2D focusing operators (i.e. one-way Green's functions) from tracked two-way reflection traveltimes. This method is introduced to allow estimation of focusing operators in areas characterized by a complex near-surface and a good signal/noise ratio of the datum reflector. It computes the one-way traveltimes from the two-way traveltimes using Fermat's principle (inverse Fermat modeling). The two-way traveltimes are formulated as a function of one-way traveltimes which is minimized using a nonlinear global optimization tool. The objective is to minimize the difference between the input two-way traveltimes and the calculated ones from the one-way traveltimes (forward Fermat modeling). The output one-way traveltimes are used to construct DTS gathers to validate their accuracy. Using the non-zero differential time shifts ( $\delta t$ ), the estimated one-way traveltimes can be updated. The main advantage of the proposed method is to track in the two-way domain and update in the one-way domain by a single-step. The algorithm will be demonstrated on 2D synthetic as well as field data.*

### 6.1 Introduction

The common focus point (CFP) technology (Berkhout, 1997) can be employed to resolve the complex near-surface effects without the knowledge of the underlying velocity model. Focusing operators that describe wave propagation between the surface locations and locations along the datum reflector are estimated from the data by fulfilling the *principle of equal travel time* without updating the underlying velocity model. Subsequently, these operators are used to redatum to the datum reflector. The details of the corresponding theory and examples are shown by Hindriks and Duijndam (1999), Hindriks and Verschuur (2001), Kelamis et al. (2002), Al-Ali and Verschuur (2006), and Chapter 5 of this thesis. The

underlying model between the surface and the datum reflector can be estimated by tomographic inversion of the focusing operators (Cox and Verschuur, 2001; Cox, 2004).

In the CFP technology, the focusing operators are validated or updated using the so called DTS gathers. Operator updating can be performed using an iterative approach (Bolte and Verschuur, 1998) or a one-step approach (van de Rijzen, 2006). The reflection event under consideration has to be tracked at least once in the DTS gathers. In good data areas this is a simple task, but in bad data areas it is not. Bad data areas may result from high noise levels or could result from a complex near-surface. In the latter case, simple initial operators may be quite different from the correct ones.

Verschuur and Hindriks (2004) proposed an automatic approach for estimating the focusing operators for the case of a complex near-surface. This approach is based on describing the focusing operators by a limited number of parameters. These parameters are directly estimated from the seismic data with the constraints being Fermat's principle and the objective function being the stack power. This method is very attractive because of its automatic nature. In addition, it overcomes the implicit uncertainties of the iterative operator updating because the obtained solution in this case is a result of a global optimization procedure that involves all the data. However, in areas with a very complex near-surface, the solution of this automatic method is limited because many parameters will be required to describe the focusing operator and the data quality limits the application of an automatic procedure.

From the above, we can see that focusing operators can be estimated in two domains: the two-way traveltime (TWT) domain of the shot records and the one-way traveltime (OWT) domain of the CFP gather. Figure 6.1 shows the processing flow pertaining to each domain. The first domain is suitable for areas characterized by a good signal-to-noise ratio of the datum reflector. The second domain is better suited for areas with low signal-to-noise ratio because of the involved Fresnel-zone stacking. For the very difficult situation of high complexity combined with low signal-to-noise ratio we recommend the use of shallow borehole measurements of a multi-offset VSP type to enable estimating good initial operators.

## 6.2 Starting with two-way traveltimes

The new approach introduced in this chapter for estimating the focusing operators is based on global non-parametric inversion of two-way traveltimes. This approach is supported by the advantage of tracking two-way data in raw source gathers after noise removal compared to tracking DTS gathers constructed with bad initial operators. Therefore, this approach compliments the other two approaches of estimating the focusing operators mentioned in the previous section. Figure 6.2a shows a traverse through the 3D volume containing the

prestack data of a 2D line data in an area with a near-surface anomaly. Figure 6.2b shows a traverse through the DTS gathers in the same area. Clearly, these two figures show that for this situation tracking the two-way data would be easier and less ambiguous than tracking DTS gathers. This data will be used in the example of Section 6.5.

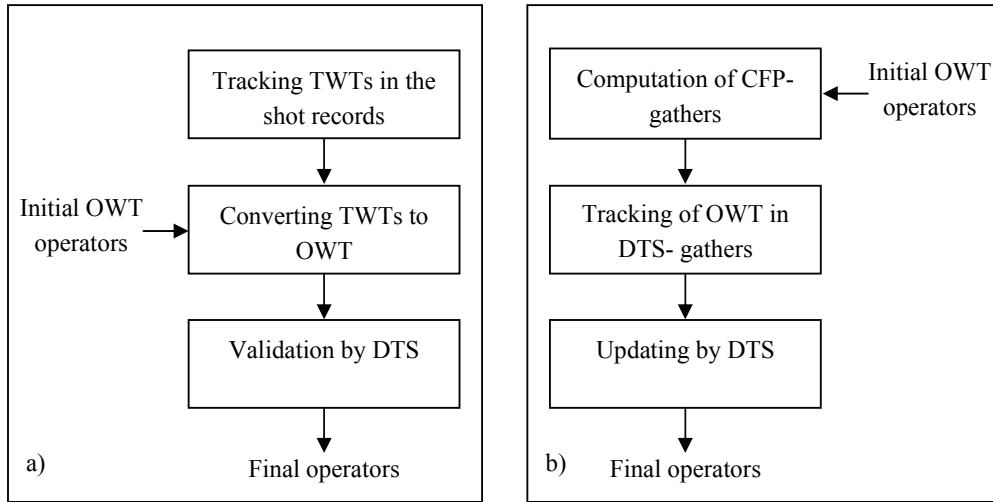


**Fig. 6.1** Two processes of obtaining the one-way focusing operators, a) starting by tracking two-way-times (TWTs) in the shot records; and b) starting by CFP-gathers computation followed by tracking one-way-times (OWT) in the DTS-gathers.

Figure 6.3 shows a block diagram indicating the cases where the new approach (two-way-time tracking) can be applied compared to the other methods mentioned in Section 6.1 (one-way-time tracking). This figure also shows that adequately sampled hard data (i.e. well data) are necessary for resolving the near-surface problems in areas with a complex near-surface and a low signal to noise ratio. Chapter 5, Section 5.3 describes a method of integrating hard data with the focusing operators. Bear in mind that the four situations exhibited by Figure 6.3 may occur along one seismic line or in one 3D area. This means that each portion of the line can be treated with the most suitable method since the final product of each method is a set of one-way focusing operators.

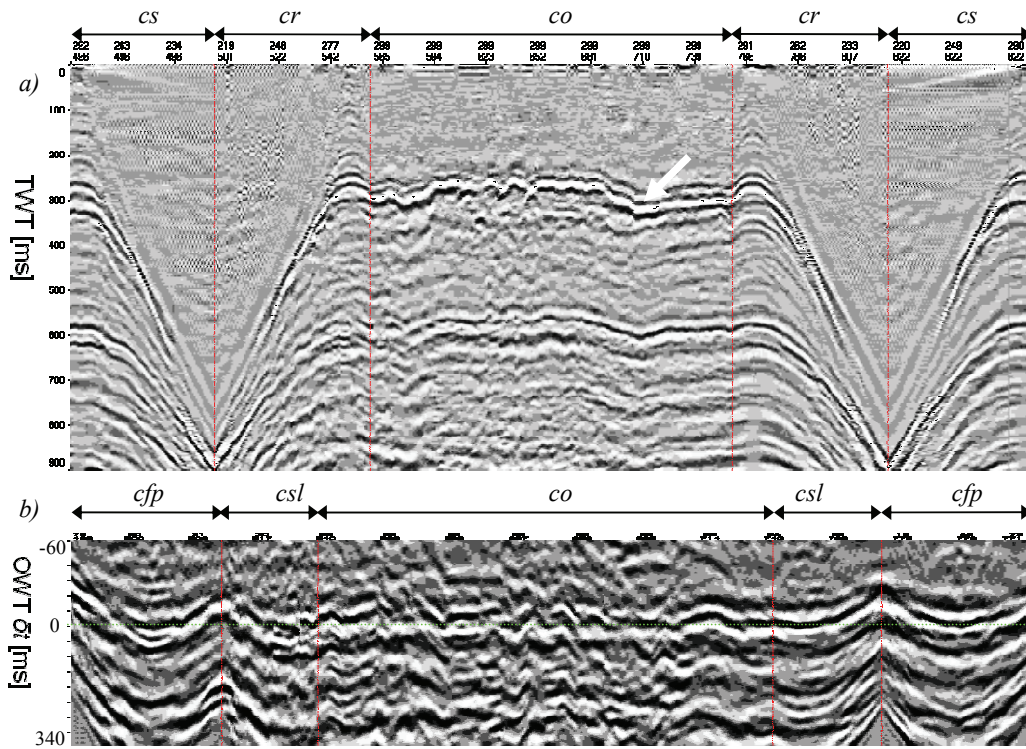


**Fig. 6.2** a) A traverse through 2D data (*cs* is common shot, *cr* is common receiver, and *co* is common offset), b) a traverse through the DTS gathers (*cfp* is common focus point, *csl* is common surface location, and *co* is common offset between *cfp* and *csl*). The reflection event under consideration is marked by a white arrow in both figures. (Courtesy of Saudi Aramco)

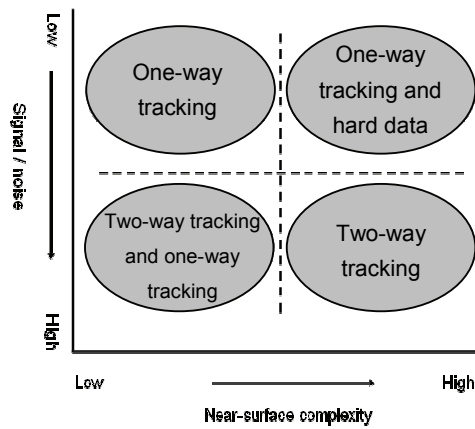


**Fig. 6.3** A block diagram indicating where the different methods of estimating the one-way focusing operators can be employed. Note that in all methods validation and updating occurs in the CFP domain (DTS-gathers).

### 6.3 Theory

Two-way reflection traveltimes can be calculated using one-way traveltime operators while complying with *Fermat's principle*. This principle states that the wave path between two points is the path of stationary time (i.e. the derivative of the traveltime with respect to the reflection location is equal to zero). This is depicted in Figure 6.4 and can be expressed as:

$$t_2(x_r, x_s) = \min \{t_1(x', x_s) + t_1(x', x_r)\}, \quad 6.1$$

where  $t_2(x_r, x_s)$  is the two-way reflection time for source  $x_s$  and receiver  $x_r$ . The  $x'$  refers to the axis along the reflector.  $t_1(x', x_s)$  describes the one-way traveltimes from source  $x_s$  to the reflector gridpoints  $x'$ . Similarly,  $t_1(x', x_r)$  describes the one-way traveltimes from receiver  $x_r$  to the reflector gridpoints  $x'$ .

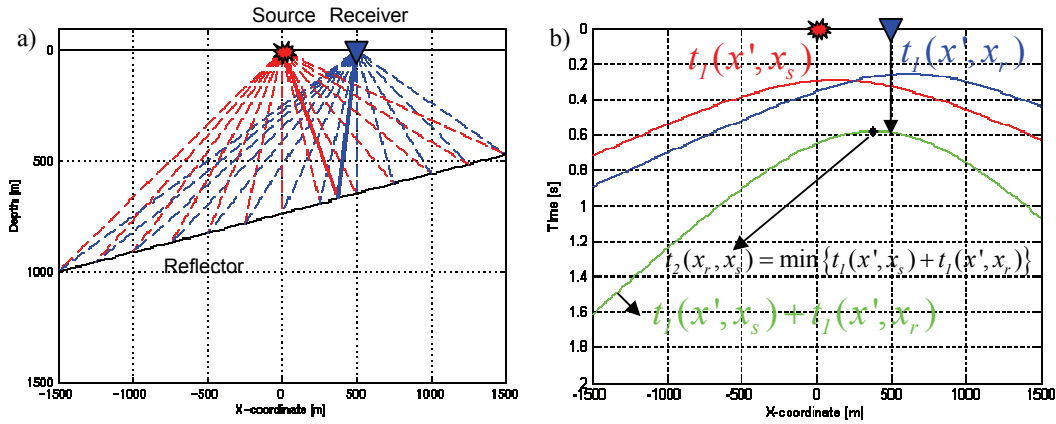


**Fig. 6.4** Schematic representation for calculating two-way reflection times from one-way operators. a) Depth model showing the one-way operators for source (dashed red) and receiver (dashed blue) with solid lines indicating the minimum traveltime path; and b) shows the traveltime curves of the one-way operators for source (red) and receiver (blue) where the TWT at location  $x_r$  is the minimum of the summation of the two involved one-way operators.

Therefore, estimation of the TWT between two points can be written as the minimization of the summation of two estimated one-way operators:

$$\langle t_2(x_r, x_s) \rangle = \min \{ \langle t_1(x', x_s) \rangle + \langle t_1(x', x_r) \rangle \}, \quad 6.2$$

where the reflection point location are represented by the variable  $x'$ . Given the actual TWT tracked from the seismic data, an objective function  $E$  can be written as the difference between equations 6.1 and 6.2:

$$E = \sum_{x_r, x_s} [t_2(x_r, x_s) - \langle t_2(x_r, x_s) \rangle]^2. \quad 6.3$$

Therefore, the goal is to find the one-way operators  $t_1(x', x)$  that minimize the objective function  $E$ . This goal can be achieved by minimizing the objective function using a global inversion technique such as the conjugate gradient. Note that in this minimization process the interaction between all involved ray paths that produce the input data  $t_2(x_r, x_s)$  is taken into consideration. Minimizing the objective function can be optimized in different ways. First, the input data can be formulated in terms of analytical spline functions which will result in a great reduction of the number of parameters to be estimated. Second, weights can be added into the minimization process where high weights can be given to input data points with a high certainty (i.e. in good data zones) and low weights can be assigned to points with a low certainty (i.e. in less good data zones). The details of how to carry out the minimization process are beyond the scope of this discussion.

#### 6.4 Validation and/or refinement of the estimated focusing operators

As mentioned, the output of the global inversion of the TWTs is a set of one-way operators (focusing operators) that describe the input TWTs. The quality of the estimated focusing operators can be assessed by applying them to the seismic data in order to generate DTS gathers as shown in the scheme of Figure 6.5.

DTS gathers allow validation of focusing operators and optionally updating them. If the event of interest is not aligned at  $\delta t=0$ , then the operators are updated using the DTS gathers. It should be noted that the DTS gathers constructed by using the estimated operators from the global inversion of the TWT should be easier to track than those constructed from initial operators that may be far off.

In addition, the estimated one-way focusing operators could also be used to calculate TWT, which in turn, can be compared with the TWT tracked from the seismic data. Discrepancies between the two give indications for areas where the tracked TWT can be revised according to the scheme of Figure 6.6.

Note that this validation and/or refinement procedure is particularly useful if the efficiency of the TWT method has been increased by a spline representation of the operators to reduce the number of parameters.

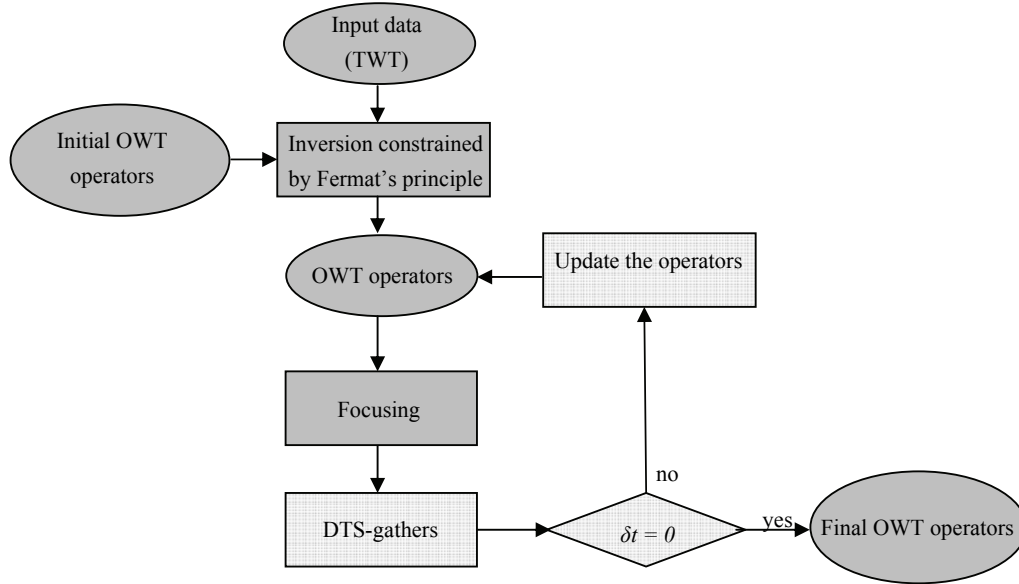


**Fig. 6.5** A scheme for validating and optionally updating the estimated focusing operators from the global inversion of TWTs. Note that the initial operators may include information from a static solution (OWT means one-way traveltimes).

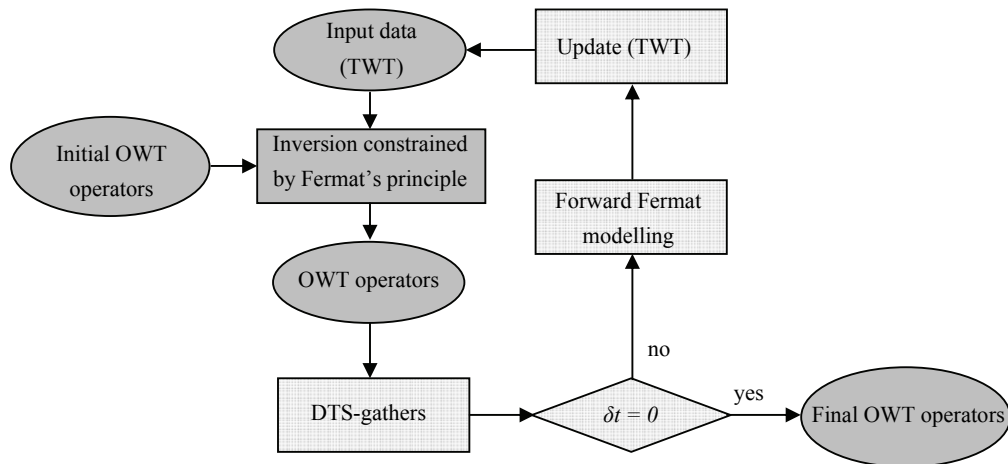


**Fig. 6.6** A scheme for validating and optionally updating the estimated focusing operators from the global inversion of TWT using discrepancies of estimated TWT with tracked TWT.

The scheme of Figure 6.6 may be more accessible to users who are familiar with tracking TWTs. However, the fundamental difference is that in our method OWT validation can be included and TWT-tomography is replaced by the significantly simpler OWT-tomography. In the case where discrepancies of TWTs do not suggest any update to the tracked TWTs, this perhaps means that the reflections are coming from a different plane than the plane of the 2D line. In that situation, updates of the focusing operators using any of the flows of Figure 6.5 or Figure 6.6 will not improve the solution.

## 6.5 Synthetic data example redatuming

The synthetic data used in this section was generated using an acoustic finite difference algorithm. This data was created using the subsurface model displayed in Figure 6.7, which is the same model that has been used by Kelamis et al. (2002) and Hindriks (2007). This model contains most of the features characterizing a land-type near-surface including sand dunes, a valley filled with low velocity sediments, and varying topography. The geometry of the deep parts of this model is simple with a low relief structure. The shot records were modelled with an interval of 20 m assuming a fixed spread of receivers also with a 20 m interval. The complete dataset consists of 363 shots and 363 receivers between positions 11020 m and 18260 m. Figure 6.8a shows the modelled shots between positions 12000 m and 18000 m with a step of 1 km. The distortions caused by the near surface on the reflections from the deeper parts of the model are very clear. Also these shots exhibit some steep events that are caused by energy trapped in the near-surface, particularly in the sand dunes. A dip filter was used to attenuate these steep events as shown in Figure 6.8b.

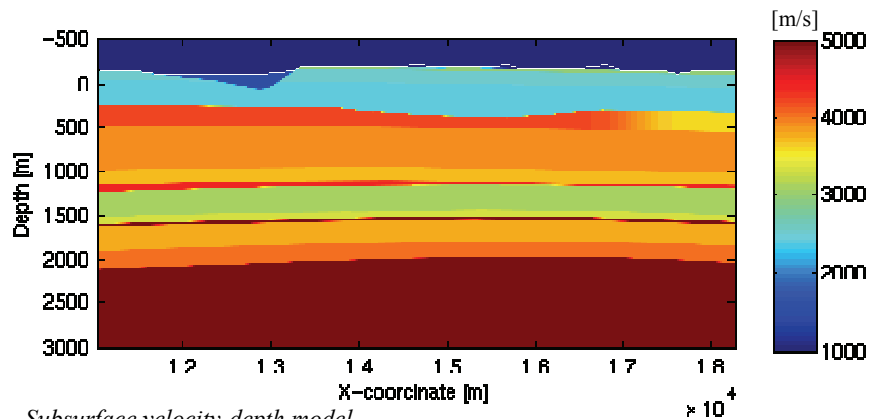
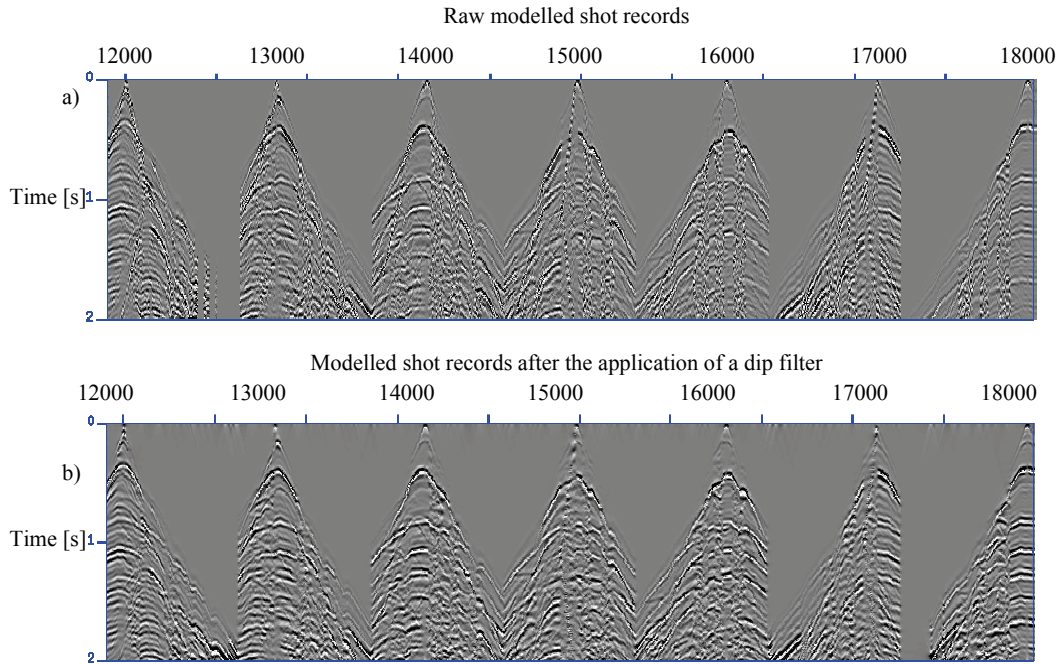


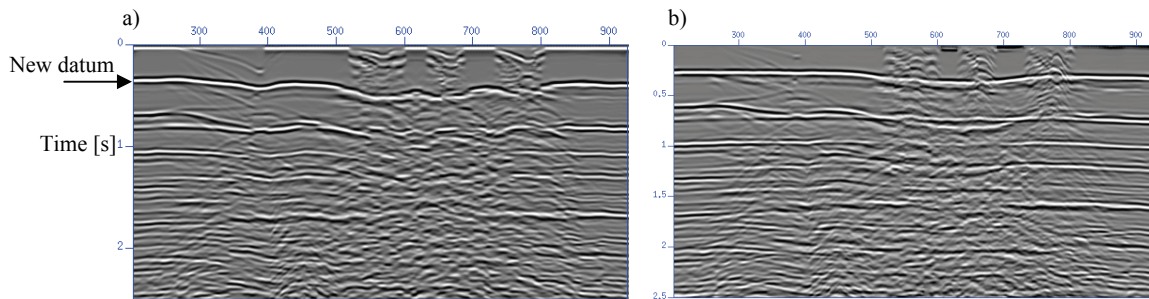
Fig. 6.7 Subsurface velocity-depth model.

Figure 6.9a shows a CMP stack of the modelled data, which clearly shows the distortions caused by the near-surface. Surface consistent statics was calculated to the depth level of -60 m while also using a replacement velocity of 2500 m/s in the interval between -60 m and 60

m. Figure 6.9b shows a CMP stack after applying the statics solution. This figure shows great improvements as compared to Figure 6.9a, but still the continuity of the deeper reflectors is affected by the near-surface. This demonstrates that the statics solution is inadequate to solve the near-surface problems even in the case the near-surface model is perfectly known.



**Fig. 6.8** Shot records between positions 12000 m and 18000 m displayed with a step of 1 km, a) modelled raw shots; and b) the same shots after the application of a dip filter.



**Fig. 6.9** CMP stacks, a) raw shot records; and b) after the application of a statics solution.

Subsequently, the two-way traveltimes of the datum reflector were tracked to a maximum absolute offset of 1200 m. These traveltimes and initial operators calculated using the stacking velocity were input into a global inversion algorithm that uses a pre-conditioned conjugate gradient method. The output from this inversion process are focusing operators.

The operators were used to construct DTS gathers to a maximum absolute offset of 600 m to validate these operators. Figure 6.10a shows a DTS stack around the new datum obtained using the inverted operators. It is used as a quality-control tool. The general flatness of this DTS stack around  $\delta t=0$  indicates that the inverted operators describe the data very well. Figure 6.10b shows every 30<sup>th</sup> DTS gather, which also proves that the inverted operators describe the data very well and the validity of the theory discussed in Section 6.3. To further support the obtained results, an eikonal solver was used to model the focusing operators from the datum reflector to the surface gridpoints. These operators are referred to as the ‘true operators’. These operators were used to construct DTS gathers. Figure 6.10c shows a DTS stack of these gathers while Figure 6.10d shows every 30<sup>th</sup> DTS gather. It is interesting to note that the inverted operators produced flatter DTS gathers than those obtained using the ‘true operators’. This can be attributed on one hand to the limitations of the eikonal method and on the other hand to the fact that the data itself was used for inverting the operators.

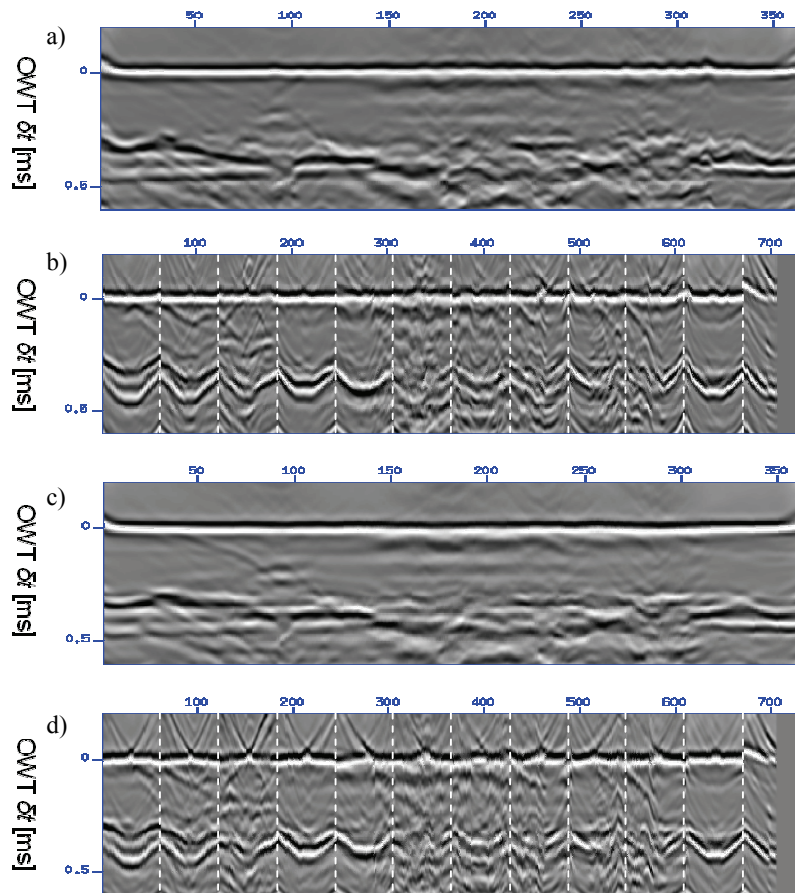


**Fig. 6.10** a) DTS stack using the inverted operators from the TWT's; b) every 30<sup>th</sup> DTS gather using the inverted operators; c) DTS stack using the 'true operators'; d) every 30<sup>th</sup> DTS gather using the 'true operators'.

The inverted operators as well as the ‘true operators’ were used to perform redatuming to the datum reflector. Figure 6.11a shows redatumed shot records between positions 12000 m and 18000 m with a step of 1 km obtained using the inverted operators. Similarly, Figure 6.11b shows the redatumed shot records obtained using the ‘true operators’. These figures clearly show that the complex near-surface distortions have been significantly removed by redatuming to a reflector below the near-surface. Figure 6.12a shows a CMP stack of the redatumed shot records obtained using the inverted operators. Likewise, Figure 6.12b shows a CMP stack of the redatumed shot records using the ‘true operators’. These two figures are very similar indicating the correctness of the inverted operators. Figure 6.12c shows a flattened stack at the datum reflector obtained after the application of a statics solution (Figure 6.9c). It is clear that redatuming has more revealed the continuity and the clearness of the deep reflectors than the statics solution. Remember that in this case we exactly know the near-surface model and so the statics solution. But, the statics solution cannot adequately solve the near-surface problem because of its dynamic nature.

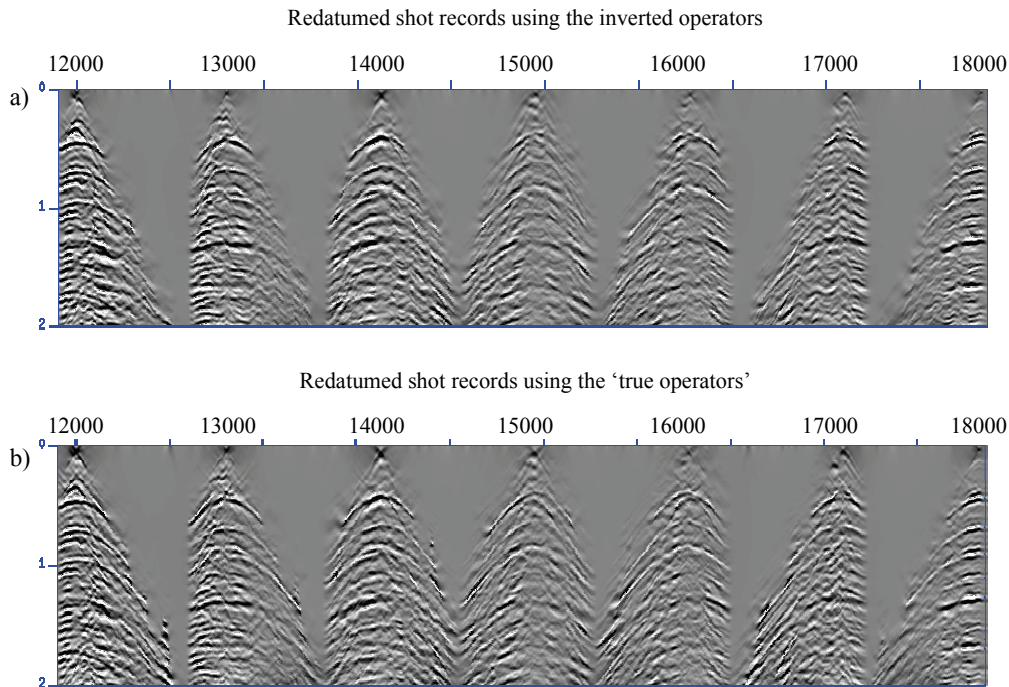


**Fig. 6.11** a) Redatumed shot records using the inverted operators displayed for positions from 12000 m to 18000 m with a step 1 km; and b) redatumed shot records obtained using the ‘true operators’. Compare with Figure 6.8.

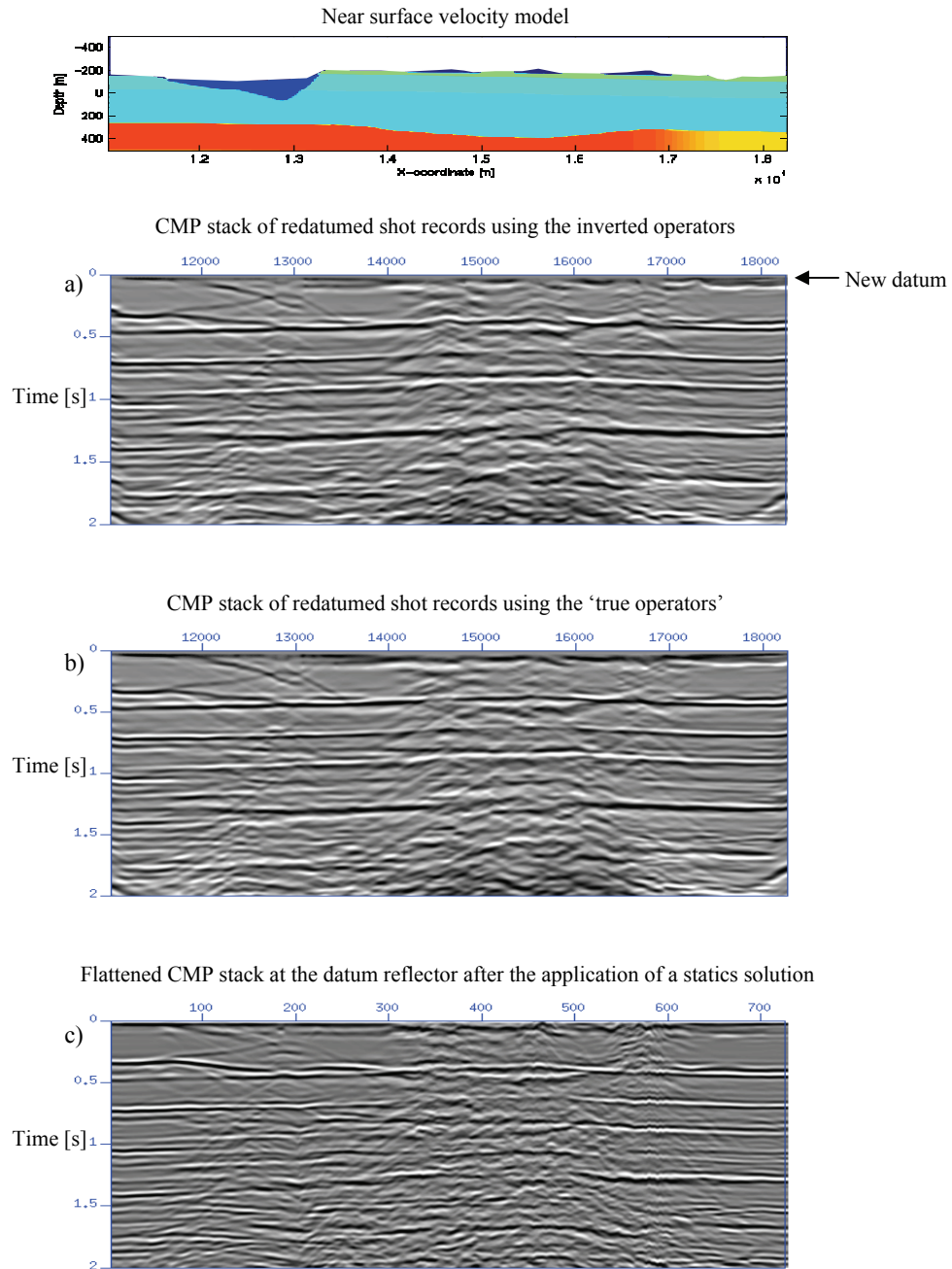


**Fig. 6.12** a) A CMP stack of the redatumed shot records using the inverted operators from the TWT's; b) a CMP stack of the redatumed shot records using the 'true operators'; and c) a flattened stack at the datum reflector of the stack shown in Figure 6.9b, which is obtained after the application of a statics solution. Note that the top figure shows a zoomed display of the near-surface model.

## 6.6 Field data example redatuming

The data set used in this section is the same as the one used in Chapter 5, Section 5.5. Figure 6.13 shows a common-mid-point (CMP) stack of a 30 km long 2D line acquired in Saudi Arabia in an area characterized by complex near-surface geology. Each shot consists of 2880 traces acquired by using symmetric split-spread with a 5 meter group interval for both sources and receivers leading to a maximum offset of about 7200 m. A five to one summation was applied to the data before performing the analysis which results in 576 traces per shot with a group interval of 25 meters for both source and receiver. The stack clearly shows a relatively deep near-surface anomaly around  $t=0.3$  s between CMP's 3000 and 3500 that obscures the deeper reflections. A reflector below the complex near-surface marked by a red line (Figure 6.13) was chosen to be the new datum. TWTs were tracked from pre-processed<sup>1</sup> data using a 3D interpretation package to ensure continuity of the tracked event in all domains (i.e. common shot, common receiver, and common offset) to a maximum offset of 1200 meters (Figure 6.14a). The tracked TWTs were decimated to a group interval of 100 meters for both source and receiver (Figure 6.14b). This is performed for practical reasons only: reduction of the number of parameters to be estimated by the global inversion process.

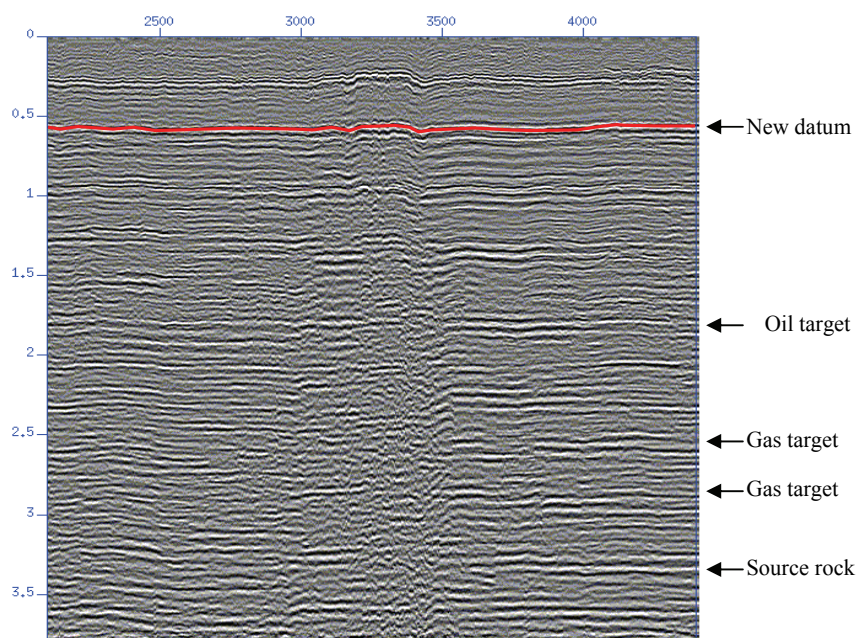


**Fig. 6.13** CMP stack after applying the state-of-the-art statics solution. The new datum is marked by the red line. (Courtesy of Saudi Aramco)

<sup>1</sup> Pre-processing in this case includes only ground roll removal by a proper dip filter.

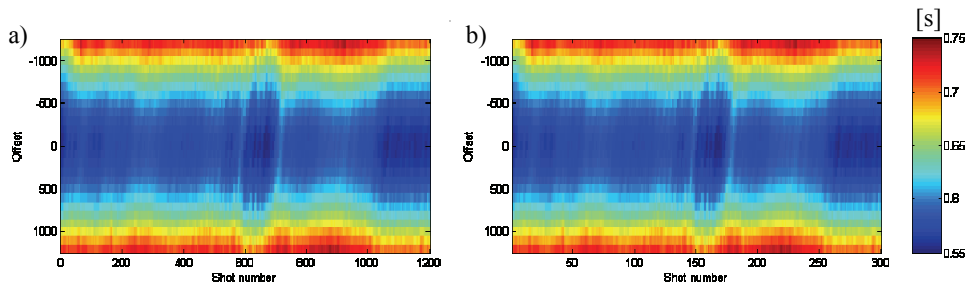


**Fig. 6.14** Color presentation of TWTs of tracked datum reflector, a) Tracked TWTs, and b) Decimated TWTs every 4<sup>th</sup> receiver and every 4<sup>th</sup> source.

Subsequently, the TWTs were globally inverted for one-way-time (OWT) operators using a pre-conditioned conjugate gradient method. The inputs to the inversion process are initial OWT operators (Figure 6.15a), each from a surface gridpoint to varying subsurface gridpoints up to an offset of 1200 meters from both sides of the surface gridpoint, and the tracked TWTs. The output from the global inversion process consists of inverted OWT operators (Figure 6.15b). The difference between the initial OWT operators and the inverted ones is shown in Figure 6.15c. It is clear from this figure that only OWTs with offsets up to 750 meters were updated by the global inversion process because only these offsets are included in the communicating reflection regions of the TWTs with respect to the OWT operators. The term communicating region here refers to the segment of a reflector that is illuminated by a source and detected by many receivers on the surface or visa versa. Note that the length of the communicating region decreases as offset between source and receiver increases. The length of the communicating region also influences the accuracy of the inverted OWT operators.

The TWTs that were estimated from the inverted OWTs can be compared with the input tracked TWTs. Figure 6.15d shows the difference between the input TWTs and the estimated TWTs from the inverted OWTs. The root-mean-square (rms) of the difference in Figure 6.15d is 5.4 ms if all offsets are included (i.e. up to 1200 meters). For offsets up to 600 meters the rms of the difference is 3.79 ms, which is less than the sampling interval of 4.0 ms. The rms of the difference for offsets up to 300 meters is 2.5 ms. Therefore, as the offset increases the rms difference increases.

The obtained operators were used to construct DTS gathers for the validation step. Figure 6.16 shows DTS stack around the new datum obtained using the inverted operators. The general flatness of this DTS stack around  $\delta t=0$  indicates that the inverted operators describe the data very well. Figure 6.17 shows every 15<sup>th</sup> DTS gather between gathers 400 and 800 (i.e. around the near-surface anomaly). These gathers are generally flat at the event of interest. Therefore, the estimated operators are considered to be final.

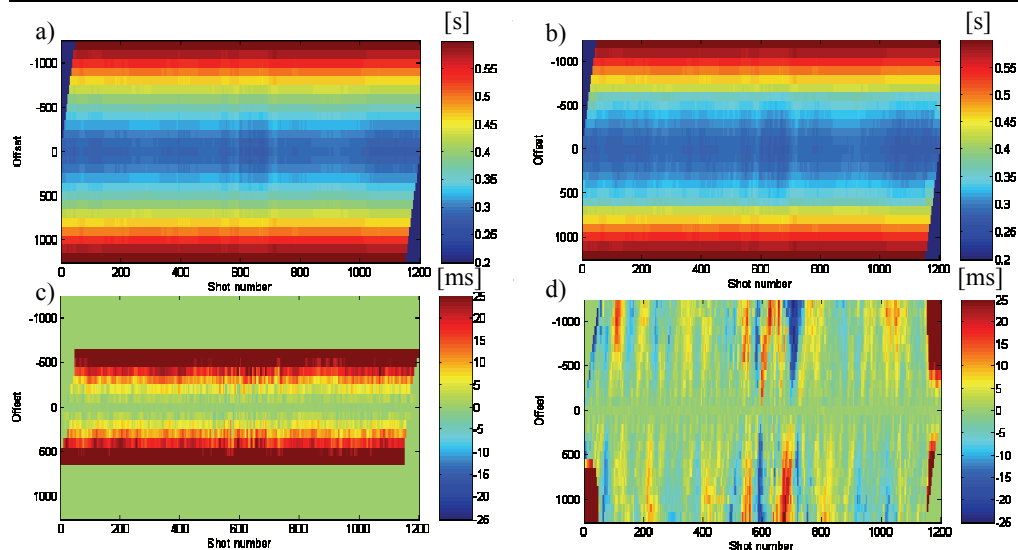


**Fig. 6.15** a) Initial one-way-time (OWT) operators each from a surface gridpoint to varying subsurface grid points up to an offset 1200 meters from both sides of the surface gridpoint; b) Inverted OWT operators; c) Difference between the initial and the inverted OWT operators; and d) Difference between the input TWTs and the estimated TWTs .

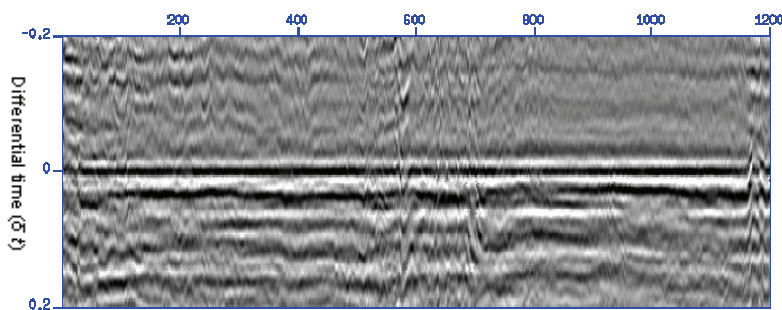


**Fig. 6.16** DTS stack, using the focusing operators obtained from the global inversion of TWTs.

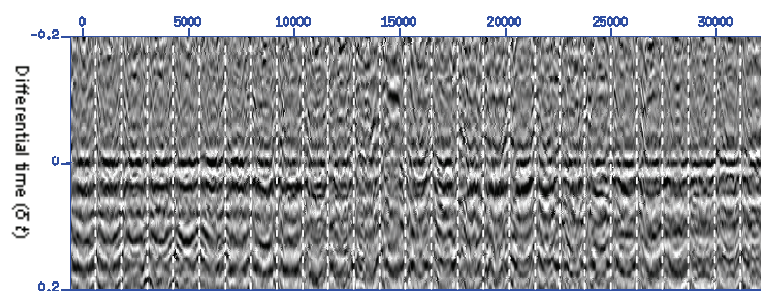


**Fig. 6.17** Every 15<sup>th</sup> DTS gather between datum-locations 400 and 800 as labelled in Figure 6.16.

The OWT operators obtained were used to perform wave-equation redatuming. Figure 6.18a shows a CMP stack of the redatumed source gathers. This result shows clear improvements particularly in the middle of the section where the near-surface anomaly is located. This can be best compared to the result of flattening the original CMP stack of Figure 6.13 at the datum reflector, as shown in Figure 6.18b. The CMP stack in Figure 6.18a can be considered as a time-flattened stack at the datum reflector in a wave-equation based prestack manner.

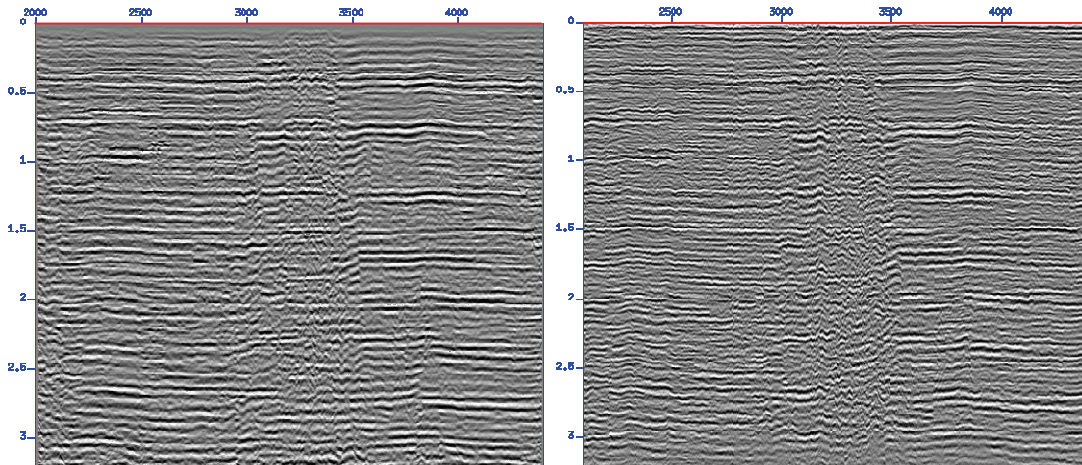


**Fig. 6.18** a) A CMP stack after redatuming to the new datum using the inverted operators from the tracked TWTs. This can be considered as time-flattened stack at the datum reflector in a wave-theory based prestack manner; and b) a flattened stack of Figure 6.13 at the new datum.

## 6.7 Concluding remarks

We have proposed a new velocity-independent approach to estimate 2D one-way-time operators from two-way traveltimes (TWTs). This approach leads to estimating the focusing operators in one step provided that good quality tracked TWTs can be obtained from the source gathers. The new approach is suitable for areas characterized by a good signal-to-noise ratio in the pre-stack data. The new approach can directly be extended to 3D. Bear in mind that this approach works even for sparsely sampled 3D data because there is no data focusing involved. Operators are directly estimated from the observed TWTs in the common source gathers.

## Conclusions and recommendations

### 7.1 Introduction

Acquisition systems have greatly advanced during the last decade. Currently, they are capable of recording the response of one source (array) with more than hundred thousand channels. Optimizing the utilization of such recording capabilities to retrieve high-value information of (potential) reservoirs must be the main goal of the design team. Optimum data acquisition is not the only solution to the problem, it has also to be coupled with preprocessing, imaging and characterization. Therefore, the interaction between acquisition, processing, and characterization has to be considered in the design process. This important aspect is visualized by the seismic value chain as proposed by Berkhout. Efficient and comprehensive tools to perform this optimization do not yet exist. To achieve this ambitious goal, this thesis proposes an integrated scheme for land survey design. The engine behind this scheme explicitly incorporates the geometry (including field arrays) and the preprocessing techniques. Criteria are based on image quality.

The highest priority for better land seismic imaging is attributed to dealing adequately with the complex near-surface. The latter gives rise to two different problems that have to be carefully considered in the survey design process. The first problem refers to the removal of the large amount of near-surface related noise. The second problem refers to removing the near-surface distortion from the signal.

In this thesis, the survey design process is divided into two phases:

- Selection of initial parameters, and
- updating these parameters through the integration with the subsurface model.

The initial survey parameters are selected based on established design rules. The second phase is performed using the focal beam concept which has been extended in this thesis to deal with sparse data and to incorporate noise with signal. The two phases are constrained by the acquisition capabilities, the ability to remove noise from the data, and the ability to remove the near-surface distortions from the signal. Noise can be attenuated in the field using arrays and in preprocessing using multitrace filters. The focal beams provide quantitative measures related to noise removal in these two stages, separately or combined.

During preprocessing the near-surface distortions on the signal are removed, using an *operator-based* approach. This velocity-independent approach is extended from the common source and common receiver gathers to so-called *cross-spread gathers*.

## 7.2 Seismic acquisition

### 7.2.1 Summary of methodology

As already mentioned, the proposed methodology for survey design consists of two phases. In phase one, initial survey parameters are defined based on established rules according to temporal and spatial sampling theory. This initial design includes a macro level and a micro level. The macro level includes the sampling interval, the offset range and the line spacing for both the source and the receiver. The micro level includes the details of the source and receiver field arrays. Phase two involves integrating the initial design with the *subsurface model*. This phase is carried out to validate and update the initial parameters. The actual integration is performed using the concept of focal beams which allows generating image information at selected target points without going into explicit modeling and migration of seismic data. The focal beams take into consideration signal and noise as well as near-surface complexity.

### 7.2.2 Conclusions

*Generic conclusions:*

- The complex near-surface does not cause illumination problems as we observe in the case of complexities that are close to the target. This thesis concludes that the near-surface problem is a *preprocessing* issue provided the data are sampled adequately (phase 1 of the acquisition design).
- The *focal beam* concept provides the necessary tools for comprehensively assessing/optimizing acquisition parameters to any required detail level.
- Single source/receiver acquisition (micro level of the geometry) is the ultimate way of acquiring data, assuming adequate dynamic range of the recording system. However, optimizing the macro level of the geometry design should be achieved before optimizing the micro level. For a certain number of recording channels, the choice of small field arrays, large offsets and small source and receiver line spacing may produce better results than those obtained by a geometry that uses single sources/receivers at the cost of larger source and receiver line intervals.

*Phase one of the geometry design:*

- Initial design rules have been proposed to guide the design team to choose candidate geometries for land seismic acquisition. It is concluded that the crossed-array geometries form an excellent compromise to the full-geometry. In this category, the orthogonal geometry with source lines perpendicular to the receiver lines is preferred over the zigzag and slanted geometries.
- The crossed-array geometry can be constructed from single-fold building blocks called cross-spreads. A cross-spread consists of a source line and a perpendicular receiver line. Hence, designing a land acquisition geometry involves designing the individual cross-spread – sampling intervals, field arrays, and line lengths – and the subsequent spatial distribution of these cross-spreads.
- Alias-free sampling of the signal must be achieved along the two cross-lines of the basic building blocks. Since the sampling requirements for signal are less stringent than those for the noise, this condition requires field arrays to attenuate the noise. These arrays should not affect the signal bandwidth. It is recommended that the sampling of the sources and receivers in the building blocks should be such that the maximum aliased frequency of the noise does not intersect with the signal band at this frequency.
- The lengths of the two cross-lines of the cross-spread determine the maximum inline and cross-line offsets. These are dictated by the maximum reflection angles and their azimuths required to be sampled at the target.
- The spatial distribution of cross-spreads (i.e. the source and receiver line intervals) is determined by the requirements of the shallowest reflector and the near-surface complexities. For retrieving the underlying velocity model, the line intervals should be equal or less than the near-surface anomaly dimensions.
- The aperture of the geometry is dictated by the maximum reflection angles and their azimuths required to be sampled at the target.

*Phase two of the geometry design:*

- The focal detector and focal source beams allow *separate* assessment of the source and receiver geometries of a particular design, including their two design levels: macro and micro. This applies for both signal and noise.
- The scattered Rayleigh waves can be elegantly incorporated into the focal beam analyses. Similar to the signal, this does not require explicit modeling of the scattered Rayleigh waves. The power of using field arrays to attenuate scattered Rayleigh waves is quantified by the focal beams. It is stated that the geometry that is effective for attenuating scattered Rayleigh waves will also be effective for attenuating direct Rayleigh waves. This is because the dominant apparent velocity of the scattered Rayleigh waves is equal to that of the direct Rayleigh waves.

- The effect of the acquisition geometry on the spatial resolution at the target is quantified by the resolution function. The computation of this function involves element-by-element multiplication of the focal beams in the space-frequency domain.
- The imprint of the acquisition geometry on the reflectivity function is quantified by the AVP-imprint function. Computation of this function involves element-by-element multiplication of the focal beams in the Radon domain per frequency component.
- Effects of field arrays on signal bandwidth can be quantified in the resolution function. The computation of the resolution can be carried out while including different coupling conditions and intra-array statics. The effect of positioning errors can also be quantified by the focal beams.
- The differential-time-shift (DTS) gather can be constructed from the resolution function. The DTS-gather provides a measurement of the image-fold at the target point.
- The DTS-gather is also a useful tool for assessing the limitations of near-surface solutions such as statics. This is possible because the imaging process is explicitly formulated in terms of focal beams.
- The DTS-gather allows assessing how well the underlying velocity model can be retrieved by a given acquisition geometry.

### 7.2.3 Recommendations for future research

Figure 7.1 shows the total design scheme that is proposed in this thesis. The parts of this scheme recommended for future research are indicated by the boxes with the white background in Figure 7.1:

- It is advised to incorporate the interaction between the geometry design and the preprocessing techniques into a *focal beam design software package*. The processing techniques should be available as options that the user can choose from.
- Introduce geometry *accept/reject metrics* that can be calculated automatically from focal beam results based on characterization objectives.
- The accept/reject metrics can be used as feedback values in the geometry optimization process, and thus allow updating the geometry parameters if the results of the focal beams are rejected.
- Use of the DTS-gather to assess the possibility of retrieving the underlying velocity model from the acquired data should be explored further (phase 3 of the design package). This can be carried out by linking the DTS analysis with one-way operator tomographic inversion.

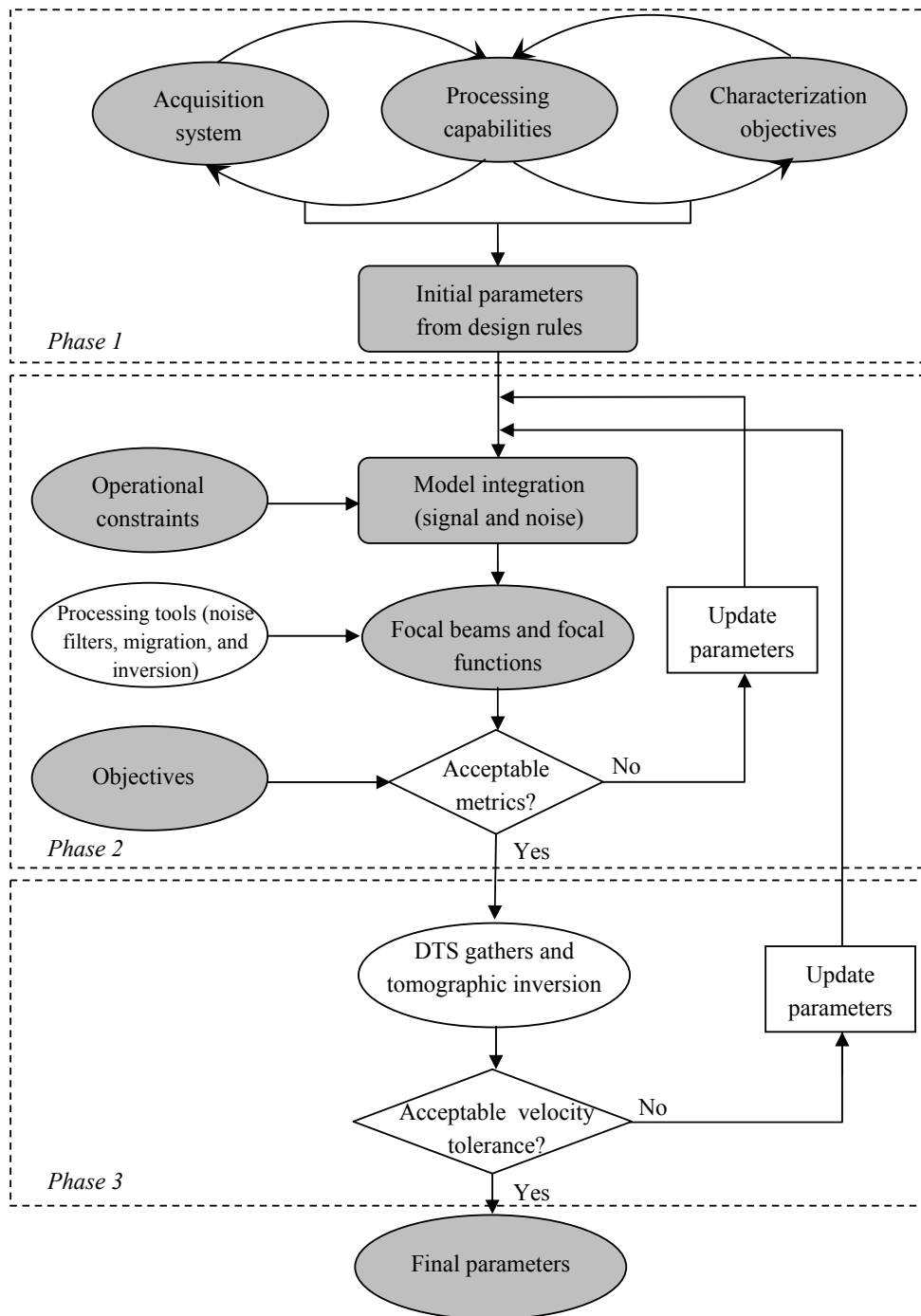


**Fig. 7.1** Survey design as an integrated approach (the phase scheme). Note that the scheme starts with the seismic value chain. Note also that the acquisition system includes instrumentation and geometry. It is advised to use this scheme for an interactive manner.

- It is advantageous to look at the resolution function for a distribution of point diffractor (along one reflector and/or at different reflectors) to show the mutual interaction between them.

### 7.3 Preprocessing

#### 7.3.1 Summary of methodology

The distortions of body-waves (signal) caused by the complex near-surface constitute an imaging problem and cannot be solved during acquisition alone. The solution requires sampling conditions, but the main job is left to *preprocessing*. The conventional way of overcoming this problem – applying surface consistent time-shifts (statics) – should be abandoned. The right approach considers the effects of the near-surface distortion as a dynamic problem. This approach is the subject of this thesis.

To circumvent the requirement for a near-surface macro-model, this thesis has chosen for the velocity-independent approach. The solution is based on wavefield redatuming, where one-way focusing operators are estimated directly from the data. These operators are subsequently used to perform redatuming to the reflector for which the focusing operators are estimated. The underlying velocity model is estimated from the operators by using a one-way tomographic inversion algorithm. In this thesis, priority has been given to the estimation of the focusing operators for 2D and sparse 3D land data.

It is important to realize sparse data can be accurately redatumed by using the technology of Tegtmeier (2007). An advantage of this approach is that the well-known ‘smearing artefacts’ of redatuming are minimized.

#### 7.3.2 Conclusions

*Generic conclusions:*

- The near-surface problem has been worked on for decades. Satisfactory solutions have not been found yet. This thesis shows that the operator-based solution is the way to go.
- The problem of coarse sampling in the land 3D case is solved by extending the operator estimation technique to properly sampled cross-spreads.
- Global updating of focusing operators is crucial for redatuming and tomographic inversion, because the interrelation between these operators need be exploited.

*Data implementation:*

- The operator-based solution shows significant improvements when applied to 2D field data.
- The iterative focusing operator updating scheme, using cross-spread DTS gathers, gives promising results. More experience needs to be gained with this scheme.
- A new global inversion technique for estimating the focusing operators from tracked two-way reflection times is introduced. The approach is demonstrated on 2D field data. The extension of this method to 3D is straightforward.

**7.3.3 Recommendations for future research**

Figure 7.2 shows the preprocessing scheme as introduced in this thesis. The parts of this scheme that are recommended for future research are indicated by the boxes with the white background in Figure 7.2:

- The combination of geometry design and noise removal requires further attention. Data driven filters that are based on the Focal-Transform may offer further improvements.

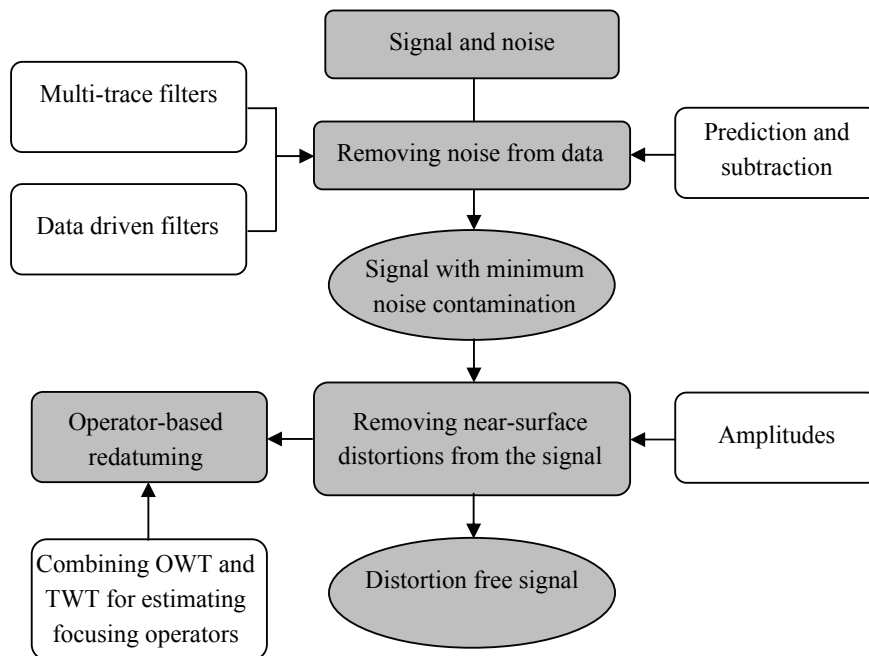


**Fig. 7.2** *Preprocessing scheme. The boxes with the white background include areas for future research.*

- It is advised to develop a prediction and adaptive subtraction method for scattered Rayleigh waves in the cross-spread domain. This is similar to what is currently being done with multiples.
- Combination of one-way-time (OWT) and two-way-time (TWT) in the estimation of focusing operators gives the opportunity to include amplitudes (Hindriks, 2007). The use of TWT traveltimes also overcomes the problem of sparse sampling.

*Data implementation:*

- It is recommended to include in the tomographic inversion the wide-angle information from refraction events. This is considered to be important with respect to low-wavelength structural bias.
- In areas characterized by a very complex near-surface, the use of 3D-VSP like measurements in shallow boreholes need be exploited and integrated with the one-way focusing operator estimation (data acquisition of focusing operators). The measured focusing operators (hard data) and the estimated focusing operators (soft data) shall be used together in the tomographic inversion step while giving the measured focusing operators higher weights.

## Focal source and detector beams

### A.1 Conceptual definitions of focal beams

The concept of focusing (focal beam forming) in seismic migration was introduced by Berkhout in 1982. Seismic migration is described as a double focusing process involving focusing in emission and focusing in detection. The focusing in emission (source beam forming) is performed in such a way that each source at the surface is given a time delay and an optimum weighting factor so that only the subsurface point under consideration is illuminated (Figure A.1a). The actual time delay is performed per frequency component which also takes into account multi-arrivals. Likewise the focusing in detection (receiver beam forming) is obtained by giving each receiver at the surface a time delay and an optimum weighting factor so that only the reception from the respective subsurface point is magnified (Figure A.1b).

According to the description above, the focal source beam can be simulated by having a distribution of sources at the surface so that they emit their energy at different times with different intensities. The time delays and weights are determined based on the subsurface target point. They can be calculated by positioning a point source at the required subsurface point and calculating its response at the surface (i.e. an impulse response of the medium containing the target point or Green's functions). The weights will be the amplitudes while the time delays will be the time reverse of the computed impulse response. In other words, they will be the complex conjugate of the computed response in the Fourier-space domain. If this response is downward propagated to the depth level of the subsurface point of interest, the resulting response will be the focal source beam with a maximum at the subsurface point under consideration (focus point of the source beam).

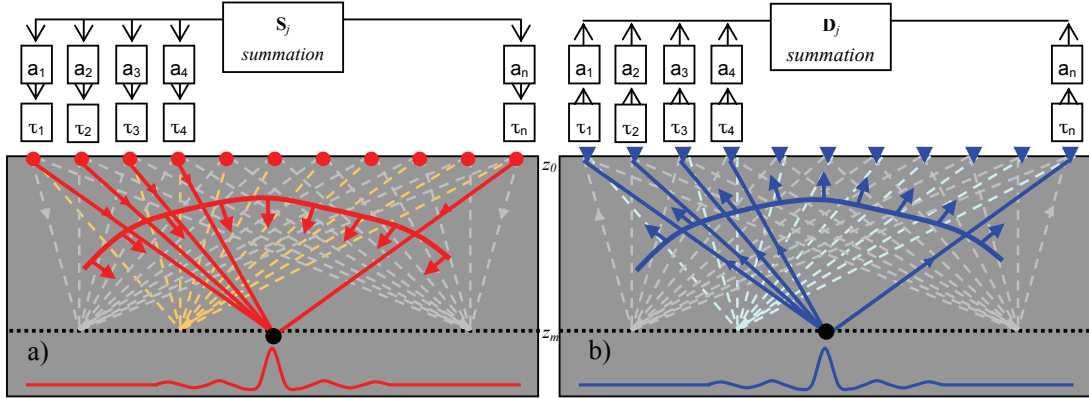


**Fig. A.1** a) focal source beam b) focal detector beam (Berkhout 1982) Dashed lines indicate that weak energy is either being sent to or received from the respective points.

Similarly the focal detector beam can be formed by having a distribution of detectors at the surface where each detector is given a time delay and a weighting factor obtained for the subsurface point of interest. The focal detector beam can then be formed by downward propagation. Its maximum will be situated at the subsurface point under consideration (focus point of the detector beam).

## A.2 Focal source and detector beams computations

The computations of focal source and detector beams were described in Berkhout et al. (2001) and Volker (2002) with some differences in the analytical definitions. Therefore, in the subsequent two subsections we will review these definitions.

### A.2.1 Focal beams computations (Berkhout et al., 2001)

For a stationary geometry (template), meaning that all source generated wavefields are recorded by the same detector distribution, the focal source beam is defined as:

$$\mathbf{S}_{lk}(z_m, z_m) = \mathbf{W}_l^\dagger(z_m, z_0) \mathbf{S}(z_0) \mathbf{F}_k(z_0, z_m) \quad \text{for } l=1:N \quad \text{A.1}$$

$\mathbf{S}(z_0) \mathbf{F}_k(z_0, z_m)$  can be viewed as being a focused source array at the surface with its focus point at the  $k^{\text{th}}$  position in the subsurface  $z_m$ . This array is then downward propagated to the depth level of the focus point in such a way that not only its response at the  $k^{\text{th}}$  position is measured but also at points around the focus point ( $l = 1:N$ ). This response is the focal source beam at depth level  $z_m$  (Figure A.2). Maximum illumination will occur at the  $k^{\text{th}}$  subsurface point (focus point of the source beam).

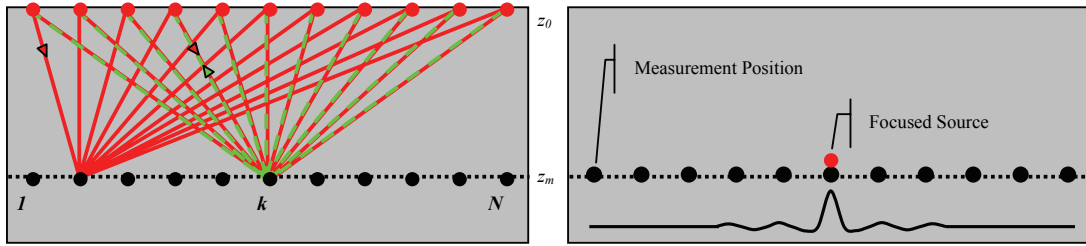


**Fig. A.2** Schematic diagram of the focal source beam according to definition A.1 (left) and measurements reference at depth level  $z_m$  (right).

Similarly, the focal detector beam for a stationary geometry (template) is defined as:

$$\mathbf{D}_{il}^\dagger(z_m, z_m) = \mathbf{F}_i^\dagger(z_m, z_0) \mathbf{D}(z_0) \mathbf{W}_i(z_0, z_m) \quad \text{for } l=1:N \quad \text{A.2}$$

This can be interpreted as having a focused detector array at the surface with its focus point at the  $i^{\text{th}}$  position in the subsurface. This array is listening to waves propagating from not only the  $i^{\text{th}}$  focus point but also from points around it ( $l=1:N$ ). Since this array is focused only for one subsurface point, its maximum detection will be from that point. This response forms the focal detector beam (Figure A.3).

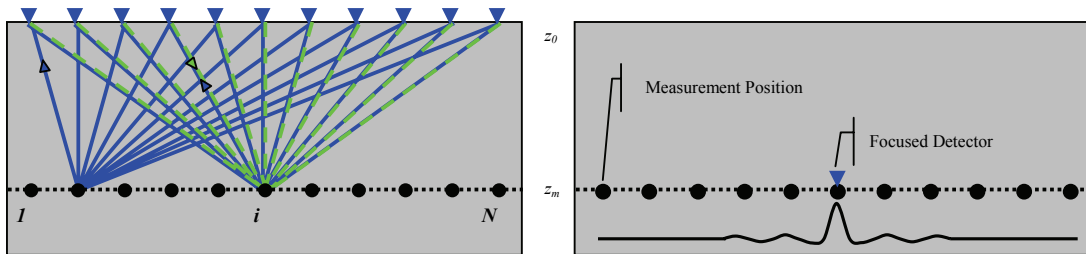


**Fig. A.3** Schematic diagram of the focal detector beam according to definition A.2 (left) and measurements reference at depth level  $z_m$  (right).

For a non-stationary geometry, the total focal beam will be the summation of focal beams computed for each stationary part of the geometry (template). In the extreme situations one template is one shot record or one template is the total survey.

### A.2.2 Focal beams computations (Volker, 2002)

For a stationary geometry (template), the focal source beam is defined as:

$$\mathbf{S}_{lk}(z_m, z_m) = \mathbf{W}_l^\dagger(z_m, z_0) \mathbf{S}(z_0) \mathbf{F}_k(z_0, z_m) \quad \text{for } k=1:N \quad \text{A.3}$$

Note that in this case the index  $k$  is running while  $l$  is fixed. This beam can be viewed as having many focal source arrays at the surface with their focus points at depth level  $z_m$  (for  $k=1:N$ ). These arrays are then downward propagated to the  $l^{\text{th}}$  position at depth level  $z_m$ . The response of each focal source array will be measured at the same  $l^{\text{th}}$  subsurface point of interest. Each measurement is assigned to the focus point of the array under consideration at  $z_m$  (for  $k=1:N$ ). The entire measurements constitute the source beam at depth level  $z_m$  (Figure A.4). Because these arrays are propagating to only the  $l^{\text{th}}$  subsurface point, maximum illumination will be obtained from the focal  $k^{\text{th}}$  source array pertaining to the same  $l^{\text{th}}$  subsurface point.

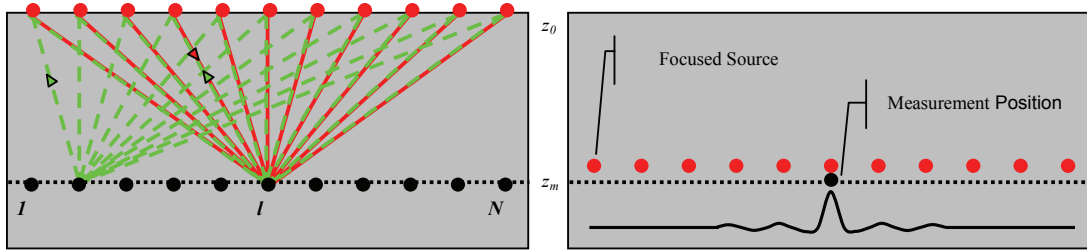


**Fig. A.4** Schematic diagram of the focal source beam according to definition A.3 (left) and measurements reference at depth level  $z_m$  (right).

The focal detector beam for a stationary geometry (template) is given by:

$$\mathbf{D}_{il}(z_m, z_m) = \mathbf{F}_i^\dagger(z_m, z_0) \mathbf{D}(z_0) \mathbf{W}_l(z_0, z_m) \quad \text{for } i=1:N \quad \text{A.4}$$

Note that in this case the index  $i$  is running while  $l$  is fixed. This can be interpreted as having many focal detector arrays at the surface with their focus points at depth level  $z_m$  (for  $i=1:N$ ). Despite their different focus point each array is listening to waves propagating from the same  $l^{\text{th}}$  point at depth level ( $z_m$ ). Each measurement is assigned to the focus point of the array under consideration at  $z_m$  (for  $i=1:N$ ). The entire measurements constitute the focal detector beam at depth level  $z_m$  (Figure A.5). Since these arrays are listening only to the  $l^{\text{th}}$  subsurface point, maximum detection will be by the  $i^{\text{th}}$  focal detector array tuned to the same  $l^{\text{th}}$  subsurface point.

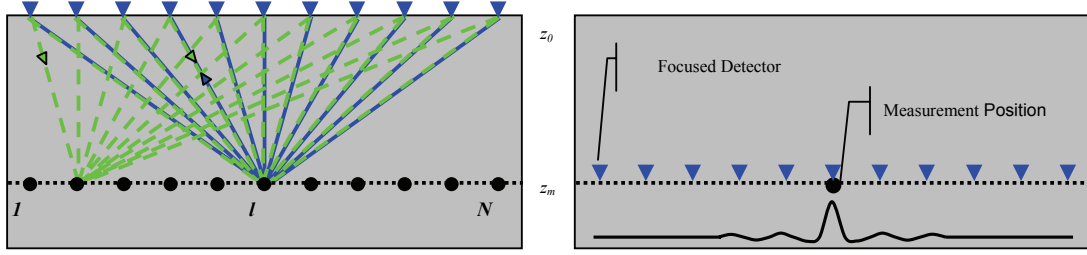


**Fig. A.5** Schematic diagram of the focal detector beam according to definition A.4 (left) and measurements reference at depth level  $z_m$  (right)

Again, for each focal beam in case of a non-stationary geometry, the total focal beam will be the summation of focal beams computed for each stationary part of the geometry (template).

### A.2.3 Concluding remarks

If we define the focal source beam matrix as:

$$\mathbf{S}(z_m, z_m) = \mathbf{W}(z_m, z_0) \mathbf{S}(z_0) \mathbf{F}(z_0, z_m) \quad \text{A.5}$$

and the focal detector beam matrix as:

$$\mathbf{D}(z_m, z_m) = \mathbf{F}(z_m, z_0) \mathbf{D}(z_0) \mathbf{W}(z_0, z_m) \quad \text{A.6}$$

then we see that in the definition of Berkhout et al. (2001), the focal source beams are given by the columns of  $\mathbf{S}(z_m, z_m)$  in equation A.5 and the focal detector beams are given by the rows of  $\mathbf{D}(z_m, z_m)$  in equation A.6. In Volker's (2002) definitions, this is just the other way around: focal source beams are given by the rows of  $\mathbf{S}(z_m, z_m)$  in equation A.5 and the focal detector beams are given by the columns of  $\mathbf{D}(z_m, z_m)$  in equation A.6. By definition, the matched filter approach to inverse wavefield extrapolation (Berkhout, 1982) is given by:

$$\mathbf{F}(z_0, z_m) \hat{=} [\mathbf{W}(z_m, z_0)]^{*T} \quad \text{A.7}$$

where the superscript  $T$  indicates transposition and the asterisk (\*) indicates complex conjugate. Substituting A.7 in A.5 and assuming  $\mathbf{S}(z_0)$  to be a unit matrix gives:

$$\mathbf{S}(z_m, z_m) = \mathbf{W}(z_m, z_0)[\mathbf{W}(z_m, z_0)]^{*T} \quad \text{A.8}$$

For the definitions of the focal source beam in equations A.1 and A.3 to be equivalent, equation A.8 must be equal to its transposed. This condition can be checked as:

$$\begin{aligned} \mathbf{W}(z_m, z_0)[\mathbf{W}(z_m, z_0)]^{*T} &= [\mathbf{W}(z_m, z_0)[\mathbf{W}(z_m, z_0)]^{*T}]^T \\ &= [\mathbf{W}(z_m, z_0)]^* [\mathbf{W}(z_m, z_0)]^T \end{aligned} \quad \text{A.9}$$

Equation A.9 shows that the transposed of equation A.5 is equal to its complex conjugate (i.e. A.9 is Hermitian). Therefore,  $\mathbf{S}_j(z_m, z_m)$  of equation A.1 is complex conjugate transposed of  $\mathbf{S}_j^\dagger(z_m, z_m)$  in equation A.3 and vice versa. This can be proven as follows:

$$\begin{aligned} \mathbf{S}_j^\dagger(z_m, z_m) &= [\mathbf{S}_j(z_m, z_m)]^{*T} \\ \mathbf{W}_j^\dagger(z_m, z_0)\mathbf{S}(z_0)\mathbf{F}(z_0, z_m) &= [\mathbf{W}(z_m, z_0)\mathbf{S}(z_0)\mathbf{F}_j(z_0, z_m)]^{*T} \\ \mathbf{W}_j^\dagger(z_m, z_0)[\mathbf{W}(z_m, z_0)]^{*T} &= [\mathbf{W}(z_m, z_0)[\mathbf{W}_j^\dagger(z_m, z_0)]^{*T}]^T \\ &= [[\mathbf{W}(z_m, z_0)]^* [\mathbf{W}_j^\dagger(z_m, z_0)]^T]^T \\ &= [\mathbf{W}_j^\dagger(z_m, z_0)][\mathbf{W}(z_m, z_0)]^{*T} \end{aligned} \quad \text{A.10}$$

The same conclusions apply for the focal detector beams in equations A.2 and A.4.

In conclusion, the beams according to the two definitions contain the same information, The choice for either of them can be based on which one is most convenient, e.g. from a computational point of view.

## Comparison between TWT and OWT tomography: a case study

*This appendix presents a field data example demonstrating the CFP technology approach to pre-stack depth migration. This approach encapsulates a workflow consisting of three steps. The first step includes direct determination of one-way-time focusing operators from the seismic data. These operators describe the kinematics of wave propagation from the subsurface layers to the surface gridpoints. The second step involves estimation of the subsurface velocity model that describes the operators using tomographic inversion. The third step includes performing pre-stack depth migration using the estimated velocity model. These three steps are performed as a sequence of processes with no iterations between them. In this appendix the one-way-time focusing operators are obtained via a global inversion of the tracked two-way reflection times as described in Chapter 6. These operators are subsequently used to invert for the underlying velocity model. In addition, the tracked two-way times are used to directly invert for the subsurface velocity model using a commercial two-way-time reflection tomography method. Pre-stack depth migration results obtained from these two velocity models are compared.*

### **B.1 Introduction**

This appendix presents a case study for the common focus point (CFP) technology approach to pre-stack depth migration using a real 2D seismic data set. This approach involves three consecutive steps. The first step involves direct estimation of one-way-time (OWT) focusing operators from the subsurface boundaries to the surface gridpoints. This can be seen as conversion of the two-way-time (TWT) seismic data to one-way traveltimes. The second step includes estimation of the underlying velocity model that describes the one-way-time operators using tomographic inversion. The third step includes performing pre-stack depth

migration using the estimated velocity model. There are no iterations between individual steps, but iterations are carried out within each step. This constitutes a primary difference between the CFP technology approach and the conventional way of performing pre-stack depth migration. In the latter, iterations take place between velocity model estimation and pre-stack depth migration. Berkhout (1997) describes the details of the CFP technology and its advantages compared to the conventional method.

## **B.2 Real data description**

Figure B.1 shows a common-mid-point (CMP) stack of a 10.2 km long 2D line acquired in Saudi Arabia. This line was extracted from a 3D data set. Each shot consists of 174 traces acquired using symmetric split-spread with a 30 meter group interval for the receivers and a 150 meter group interval for the sources. This leads to a maximum offset of about 2600 meters. The CMP fold along this line varies between 17 and 18. The stack clearly shows a layer-cake subsurface model with continuous reflectors down to 1.4 s.

## **B.3 Focusing operators estimation**

Nine reflectors marked by black lines in Figure B.1 were chosen to estimate the OWT operators. TWTs were tracked from pre-processed<sup>1</sup> data using a 3D interpretation package (Charisma) to ensure continuity of the tracked event in all domains (i.e. common shot, common receiver and common offset). The maximum offsets of the tracked TWTs for each reflector are stated in Table B.1. The tracked TWTs were decimated to a group interval of 150 meters for both source and receiver. This is performed to reduce the number of parameters to be estimated by the global inversion process. Because our current tomographic inversion software cannot take into account the surface elevation, we applied static shifts to the tracked TWTs before we determined the focusing operators for the nine reflectors. This was applied using a constant velocity of 2500 m/s between the surface elevation and the elevation of 580 meters above mean-sea-level (MSL).

---

<sup>1</sup> Pre-processing in this case includes only ground roll removal by a dip filter.

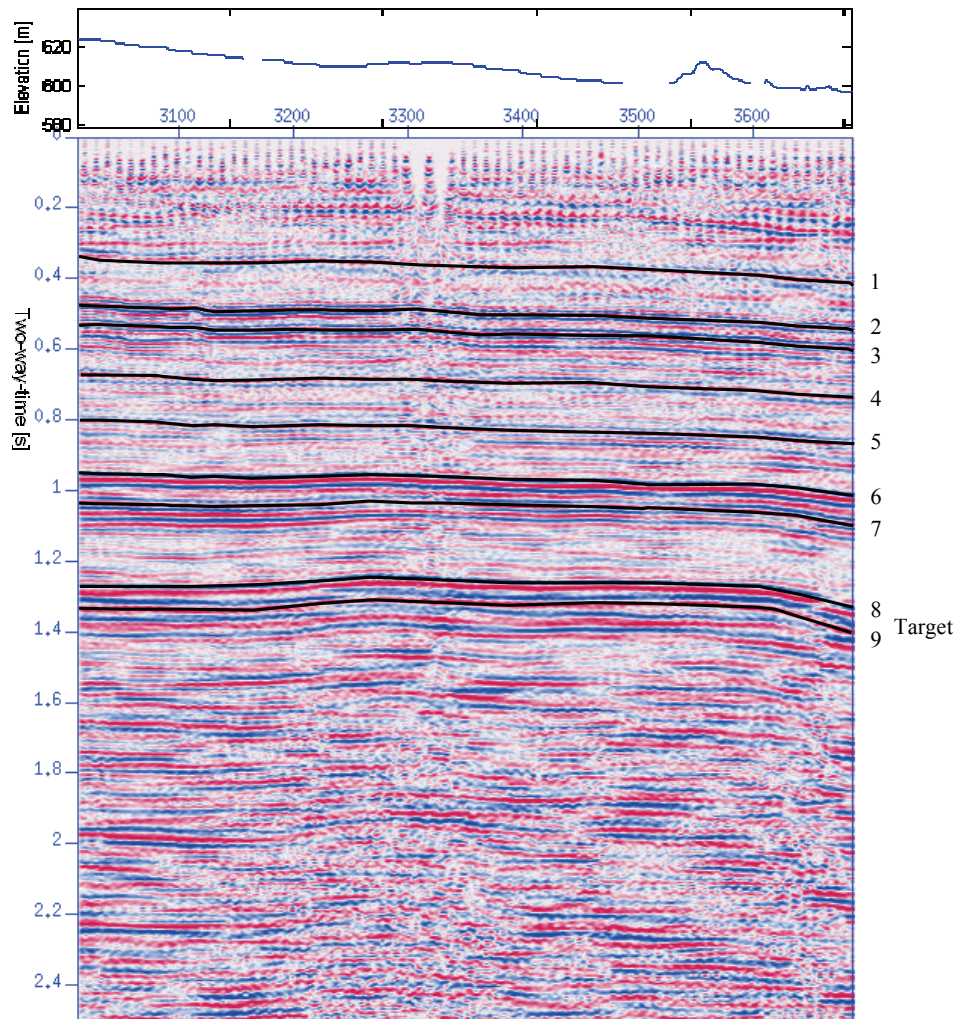


**Fig. B.1** A CMP stack with surface elevation profile at the top. The analysis reflectors are marked by the black lines. (Courtesy of Saudi Aramco)

Subsequently, the tracked TWTs were globally inverted for one-way-time (OWT) operators using a pre-conditioned conjugate gradient method. The inputs to the inversion process are initial OWT operators and the tracked TWTs. The initial operators are determined using the stacking velocity, each from a surface gridpoint to varying subsurface gridpoints with offsets equal to the TWTs offsets from both sides of the surface gridpoint. The output from the global inversion process consists of inverted OWT operators. These operators are only

updated to about half the offsets of the TWTs because these offsets include the communicating reflection regions of the TWTs with respect to the OWT operators (see Table B.1). Note that the length of the communicating region decreases as offset between source and receiver increases. The length of the communicating region also influences the accuracy of the inverted OWT operators.

Reflector	TWT maximum offset [m]	OWT maximum offset [m]
1	500	400
2	1100	500
3	1100	500
4	1600	700
5	2600	1000
6	2600	1100
7	2600	1100
8	2600	1100
9	2600	1100

**Table B.1** Maximum offsets of the tracked TWTs and the inverted OWT operators for each of the analyzed nine reflectors.

The obtained operators from the global inversion process were used to construct DTS gathers for each of the nine reflectors. One iterative-updating step (Bolte and Verschuur, 1998) was carried out to all the corresponding nine reflectors operators to refine their respective inverted operators. The tracking of associated DTS gathers was performed as a 3D interpretation approach. Figures B.2 to B.10 show the zero-offset redatumed image around each reflector obtained using the refined inverted operators. The general horizontal alignment and focusing intensity of these images around  $\delta t=0$  indicate that the used operators describe the data well.

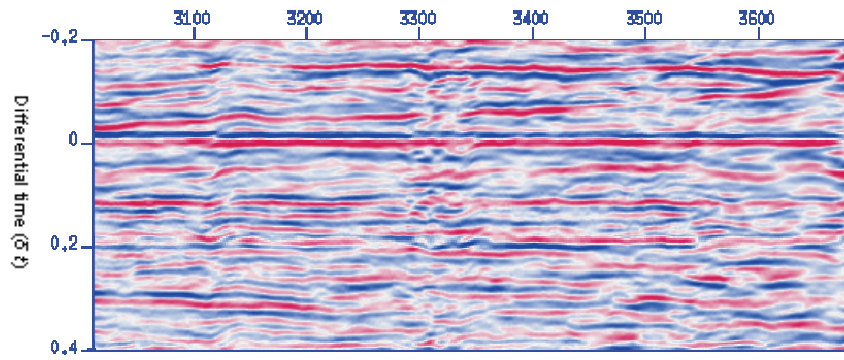


**Fig. B.2** DTS stack, using the final focusing operators for reflector 1.

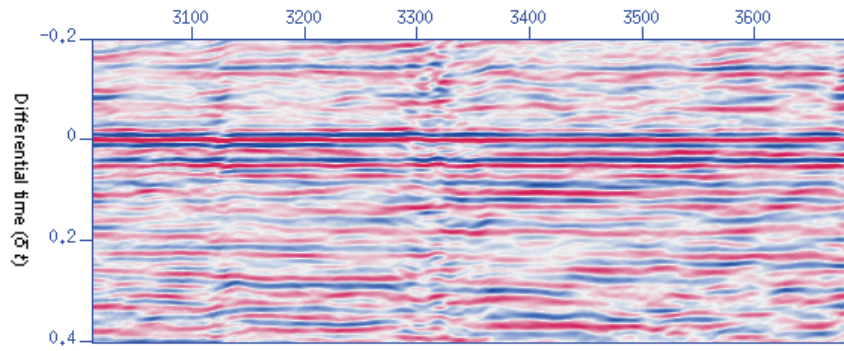


**Fig. B.3** DTS stack, using the final focusing operators for reflector 2.

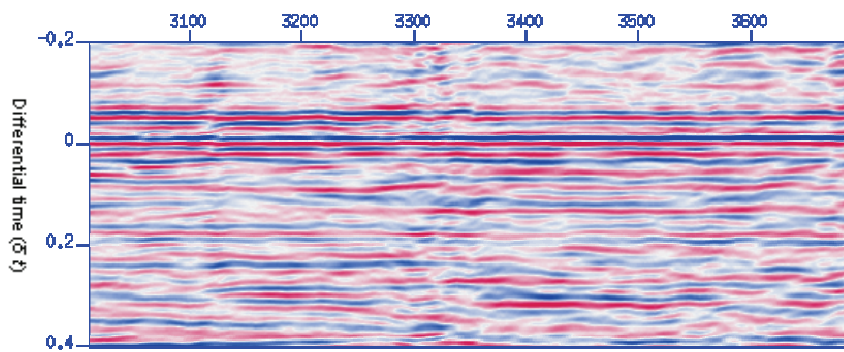


**Fig. B.4** DTS stack, using the final focusing operators for reflector 3.

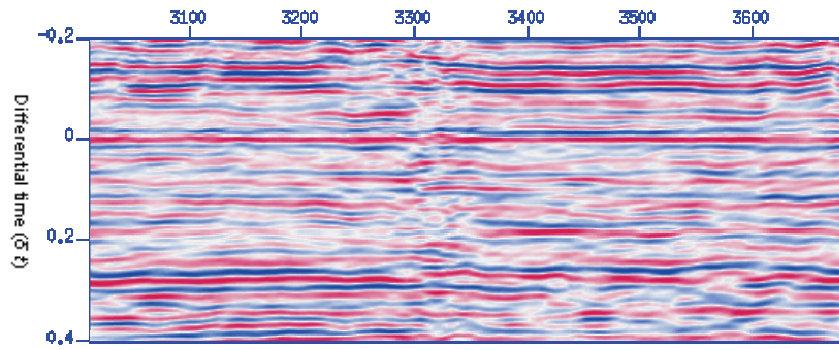


**Fig. B.5** DTS stack, using the final focusing operators for reflector 4.

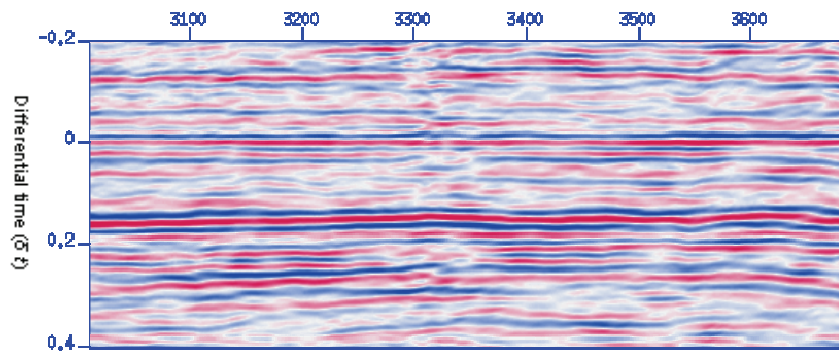


**Fig. B.6** DTS stack, using the final focusing operators for reflector 5.

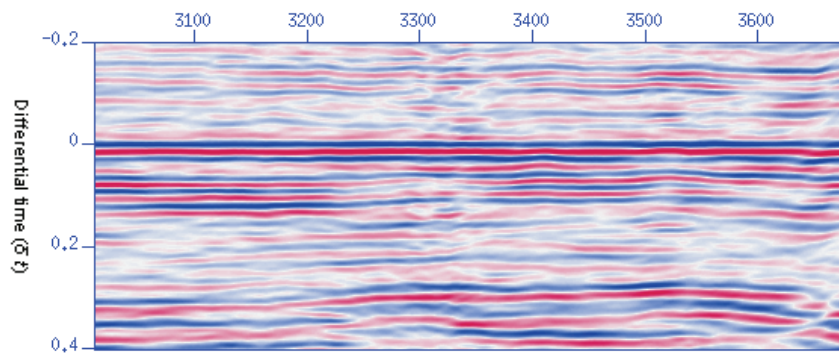


**Fig. B.7** DTS stack, using the final focusing operators for reflector 6.

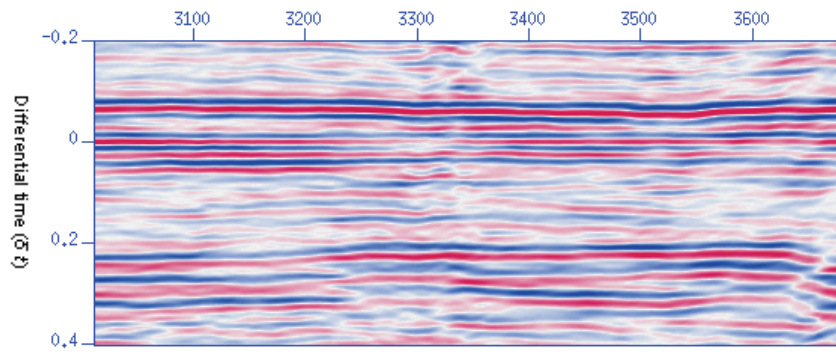


**Fig. B.8** DTS stack, using the final focusing operators for reflector 7.

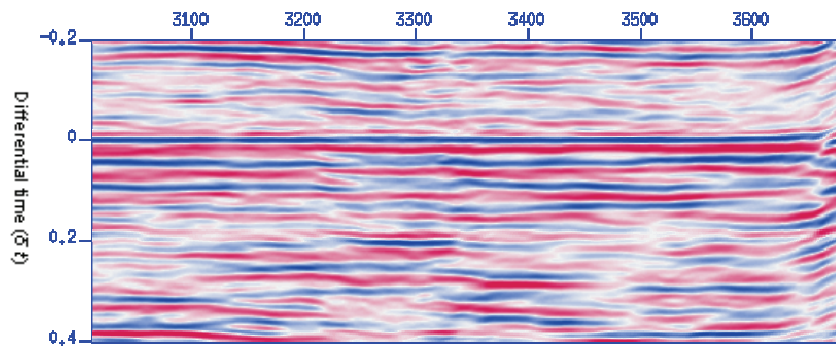


**Fig. B.9** DTS stack, using the final focusing operators for reflector 8.

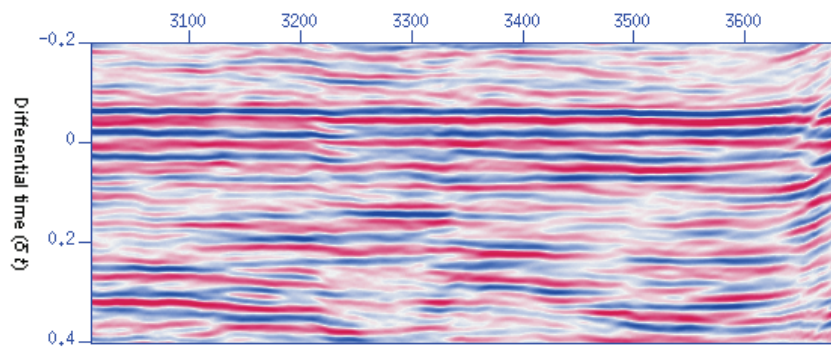


**Fig. B.10** DTS stack, using the final focusing operators for reflector 9.

## B.4 Velocity-depth model inversion

The obtained OWT operators as described in the previous section have been used as input for a tomographic inversion procedure, in which both the velocity distribution and the focal point locations are estimated (Cox and Verschuur, 2001 and Cox, 2004). The maximum offsets of the input OWT operators that are taken into account for the inversion are presented in Table B.1. Figure B.11a shows the output velocity model from this procedure and the estimated focal point depths. This procedure also outputs estimated OWT operators through the inverted velocity model. The root-mean-squared (rms) of the time difference between the input OWT and the estimated OWT is 3.2 ms which is less than the time sample rate of the TWT data that is 4.0 ms. Figure B.12a shows the distribution of this time difference for all operators where about 92 percent of the time differences were within the time sample rate.

It should be noted that tomographic inversion will, in general, generate a lower frequency approximation of the true velocity model. Therefore, we will obtain a smooth version of the true model. Furthermore, usually the bottom of the model and the edges contain a limited number of ray-paths, resulting in fewer grid points, which will finally translate into a less accurate estimation of those regions. Also, as a general rule, the resolution decreases with depth following the decrease in the angle coverage, due to the limited surface recording aperture. However, the final parameterization can help identifying areas where it is necessary to add extra information. In a real data study this might provide very important feedback for acquisition geometry and design.

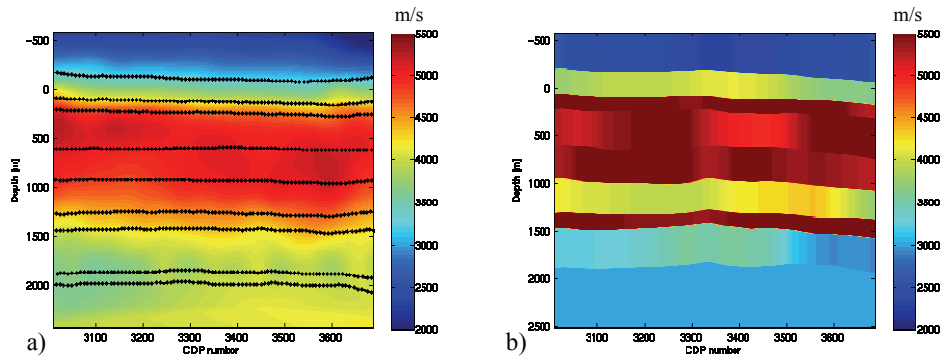


**Fig. B.11** a) The velocity model obtained using tomographic inversion of the OWT operators (the dotted lines indicate the estimated depths of the focal points); and b) The velocity model obtained using TWT reflection tomography. Note that depth is referenced to MSL, positive below MSL and negative above MSL.

For the estimated velocity model in Figure B.11a, we can observe that the velocity varies everywhere in between the nine reflectors, however within the limitations of a smooth velocity model. We expect that further improvement could be obtained by including extra boundaries below the deepest one in the complete inversion process. This will provide a better illumination of the bottom of the model and an improved estimation of the depths and velocities, especially regarding the low velocity area below the seventh interface. However, the maximum offset of the data (2600 meters) is a limiting factor in this case. This maximum offset is barely adequate for the ninth reflector. Yet, in order to estimate a reasonable velocity model down to this reflector, focusing operators for deeper reflectors would be needed. There are hints of a reflector at 2.0 s as shown in Figure B.1, but because of the maximum offset limitation, this reflector is masked by multiples to the extent that it disabled our attempts to estimate OWT operators from it.

To see how our results compare to those from another technology used in the industry, the tracked TWTs for the nine reflectors were given to an independent software provider to estimate the velocity model that describes them. This was done using a commercial layer-based reflection tomography method. The obtained velocity model from this method is shown in Figure B.11b. This model was generated using a layer-stripping approach with straight-rays in the first run. Then, it was updated using bent-rays while fixing the interfaces. The time difference distribution between the input TWTs and the TWTs estimated from this model is shown in Figure B.12b. Most of the errors in this figure fall between -5 to 5 ms. However, the software provider indicated some difficulties in inverting the third reflector which produces the high errors in Figure B.12b. He also indicated that he could not use the TWTs for the ninth reflector because the resulting velocity was less than 1000 m/s between reflector eight and nine. We did not find TWTs pertaining to these two reflectors of a problem when we used them for OWT operators inversion.

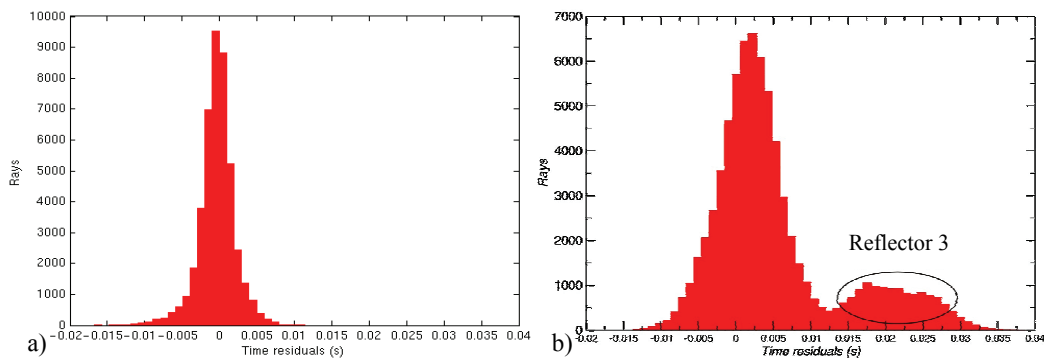


**Fig. B.12** a) Distribution of time difference between input OWT operators and estimated OWT operators through the model of Figure B.11a; and b) Distribution of the time difference between the input TWTs and the TWTs estimated from the model shown in Figure B.11b.

Probably, the problems encountered in the TWT tomography are due to the chosen parameterization. The limited number of parameters of the layered model imposes a constraint on the final results. The OWT tomographic inversion uses a data-driven parameterization. Furthermore, the layer-stripping approach followed by an update while fixing the reflector depths used in the TWT tomography is not as good as the case of inverting all the boundaries together. In the OWT tomography the data pertaining to all the reflectors was used in the inversion process.

### **B.5 Pre-stack depth migration**

The two velocity models shown in the previous section were used to perform pre-stack depth migration (PSDM). The PSDM was performed using a recursive wavefield extrapolation technique in the frequency-space domain (Thorbecke et al., 2004). The resulting depth image obtained using the velocity model of Figure B.11a is shown in Figure B.13. This figure does not show any apparent problems. The PSDM image obtained using the model exhibited by Figure B.11b is shown in Figure B.14. Although the result looks different, this figure does not show any apparent problems either. However, by inspecting the common-image-gathers (CIG's) corresponding to both velocity models in Figures B.15 and B.16 respectively for the images of Figures B.13 and B.14, it is obvious that the velocity model obtained from the OWT operators (Figure B.11a) produced flatter CIG's for the entire depth column. There are some residuals left in the CIG's of Figure B.15 that can be attributed to 3D effects. The flatness of the CIG's can be further improved by possibly one pass of conventional migration velocity analysis, yet this alone provides no guarantee of a better velocity model. Given these results, we can conclude that the image of Figure B.13 is more probable than the image of Figure B.14.

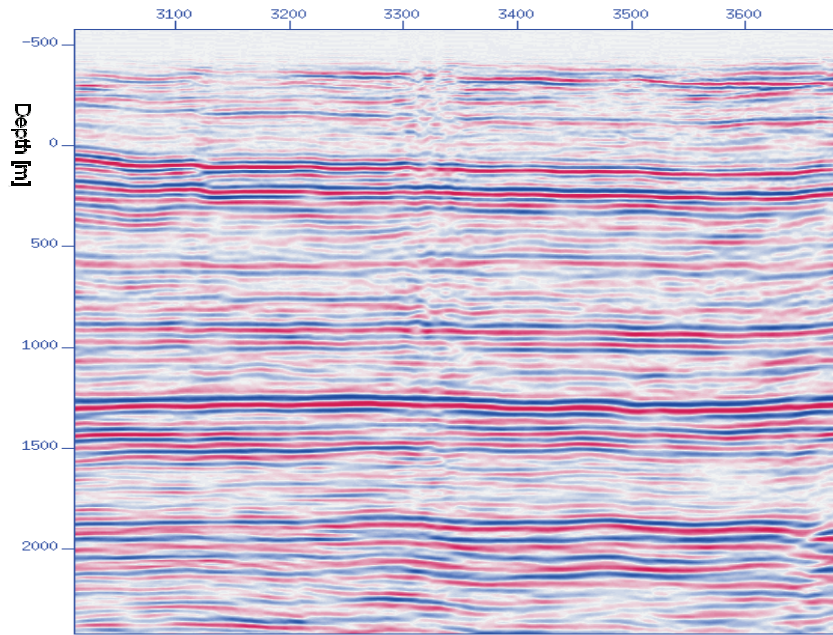


*Fig. B.13* Pre-stack depth migrated image using the velocity model of Figure B.11a. Note that depth is referenced to MSL, positive below MSL and negative above MSL.

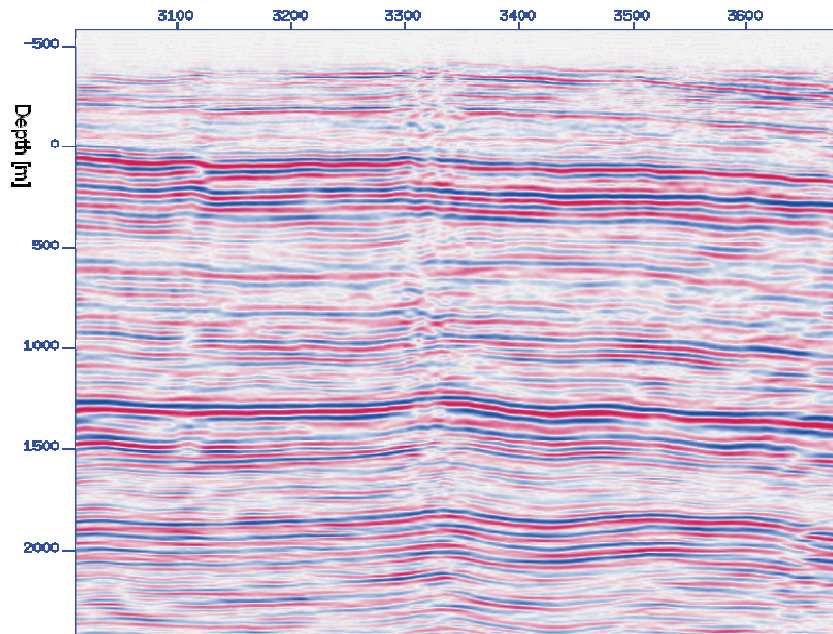


*Fig. B.14* Pre-stack depth migrated image using the velocity model of Figure B.11b.

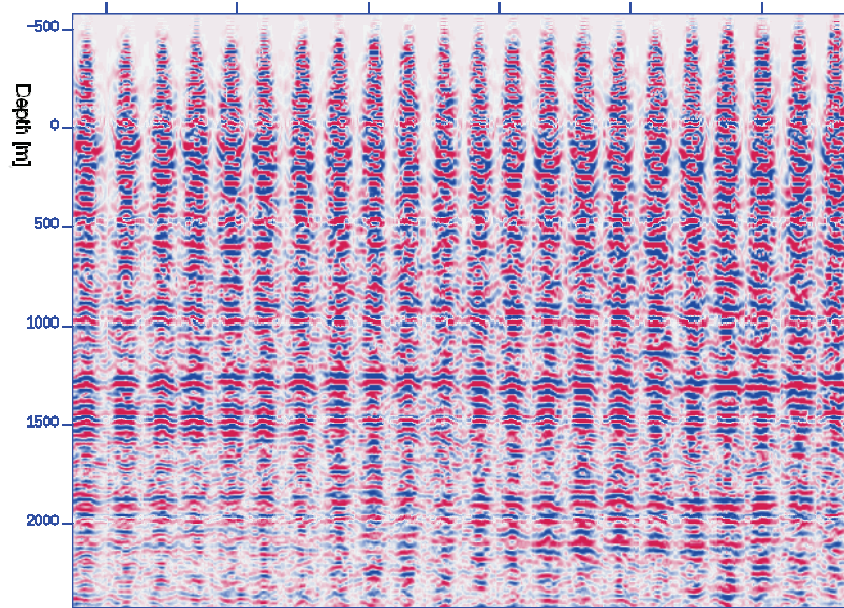


**Fig. B.15** Common image gathers obtained from pre-stack depth migration using the velocity model of Figure B.11a, displayed at every 15<sup>th</sup> CDP point. Note that depth is referenced to MSL, positive below MSL and negative above MSL.

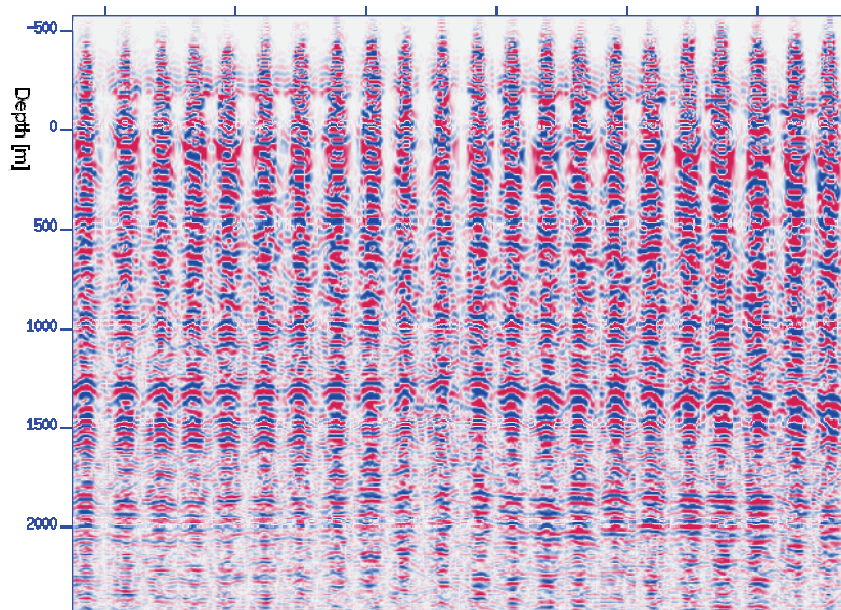


**Fig. B.16** Common image gathers obtained from pre-stack depth migration using the velocity model of Figure B.11b, displayed at every 15<sup>th</sup> CDP point.

---

## **B.6 Concluding remarks**

We have demonstrated in this appendix the CFP technology approach to pre-stack depth migration using a 2D real seismic data set. Our one-way-time tomographic inversion produced a velocity model that is more consistent with the data when compared with results obtained using commercial two-way-time reflection tomographic inversion method. This conclusion is supported by the general horizontal-alignment of the common image gathers. With the absence of well-data, this is the only available fidelity validation mean at our disposal. The velocity model estimation and the imaging results would have tremendously improved, had the seemingly postage-stamp acquisition parameters used a maximum offset of 4000 m instead of 2600 m. This is equally true for both time and depth imaging. It should also be noted that the actual 3D data from which the used 2D data was extracted had a maximum cross-line offset equal to the maximum inline offset, but this alone will not improve the imaging results.



# Bibliography

---

- Aki, K. and Richards, P. G., 2002, Quantitative seismology, second edition: University Science Books.
- Al-Ali, M., Hastings-James, R., Makkawi, M., Korvin, G., 2003, Vibrator attributes leading velocity estimation: *The Leading Edge*, 22, no. 5, 400-405.
- Al-Ali, M.N., and Verschuur, D.J., 2006, An integrated method for resolving the seismic complex near-surface problem: *Geophysical Prospecting* **54**, 739-750.
- Alkhalifah, T., and Bagaini, C., 2006, Straight-rays redatuming: A fast and robust alternative to wave-equation-based datuming: *Geophysics* **71**, U37-U46.
- Anderson, B. et al., 2006, Point-receiver seismic data offers new approach to managing onshore E&P development cycle: *First Break*, 24, 63-69.
- Anstey, N.A., 1986, Whatever happened to ground roll? *The Leading Edge* 5, 40-45.
- Baeten, G.J.M. et al., 2000, Acquisition and processing of point receiver measurements in land seismic: 70<sup>th</sup> Ann. Internat. Mtg., Soc. Expl. Geophys.
- Beasley, C., and Lynn, W., 1992, The zero-velocity layer: Migration from irregular surfaces: *Geophysics* **57**, 1435-1443.
- Berkhout, A.J. and Verschuur, D.J., 2006, Imaging of multiple reflections, *Geophysics*, **71**, SI209-SI220.
- Berkhout, A.J., Ongkiehong, L., Volker, A.W.F., and Blacquiere, G., 2001, Comprehensive assessment of seismic acquisition geometries by focal beams -- Part I: Theoretical considerations, *Geophysics*, **66**, 911-917.
- Berkhout, A.J., 1980, Seismic migration, imaging of acoustic energy by wave field extrapolation, A: Theoretical Aspects: Elsevier.
- Berkhout, A.J., 1982, Seismic migration, imaging of acoustic energy by wave field extrapolation, A: theoretical aspects, second edition, Elsevier.
- Berkhout, A.J., 1984, Seismic migration, imaging of acoustic energy by wave field extrapolation, B: practical aspects: Elsevier.
- Berkhout, A.J., 1984, Seismic Resolution: Elsevier.

- Berkhout, A.J., 1985, Seismic migration: Imaging of acoustic energy by wave-field extrapolation, third edition, Elsevier.
- Berkhout, A.J., 1997, Pushing the limits for seismic imaging, part I and part II: *Geophysics*, **62**, 937-969.
- Berkhout, A.J., 2005, The seismic value chain—providing a new business concept for the seismic industry: *The Leading Edge* 24, 146-149.
- Berkhout, A.J., 2006, Seismic processing the inverse data space, *Geophysics* **71**, A29-A33.
- Berni, A. J. and Roever, W. L., 1989, Field array performance: Theoretical study of spatially correlated variations in amplitude coupling and static shift and case study in the Paris Basin: *Geophysics*, **54**, 451-459.
- Berryhill, J. R., 1979, Wave-equation datuming: *Geophysics*, **44**, 1329-1344.
- Berryhill, J. R., 1984, Wave-equation datuming before stack,: *Geophysics*, **49**, 2064-2066.
- Bevc, D., 1997, Flooding the topography: Wave-equation datuming of land data with rugged acquisition topography: *Geophysics*, **62**, 1558-1569.
- Beylkin, G., 1985, Imaging of discontinuities in the inverse scattering problem by inversion of a causal generalized Radon transform: *J. Math. Phys.*, 26, no. 1, 99-108.
- Biondi, B. L., 2006, 3D seismic imaging: Society of Exploration Geophysicists.
- Blacchiere, G., and Ongkiehong, L., 2000, Single sensor recording: anti-alias filtering, perturbations and dynamic range, 70<sup>th</sup> Ann. Mtg: Soc. Expl. Geophys, 33-36.
- Bleistein, N., 1987, On the imaging of reflectors in the earth: *Geophysics*, **52**, 931-942.
- Bolte, J. F. B., Verschuur, D. J., and Jegge, R. F., 1999, CFP operator estimation and inversion demonstrated on a field data set – Part I: operator updating: 69<sup>st</sup> Ann. Internat. Mtg., Soc.Expl. Geophys., Expanded abstracts.
- Bolte, J.F.B., 2003, Estimation of focusing operators using the common focal point method, Ph.D. thesis Delft University of Technology.
- Bolte, J.F.B., and Verschuur, D.J., 1998, Aspects of focusing operator updating: 68<sup>th</sup> Ann. Internat. Mtg., Soc., Expl. Geophys., Expanded abstracts, 1604-1607.
- Campbell, S., Pramik, W.B., and Cafarelli, B., 2002, Comparative ray-based illumination analysis: 72<sup>nd</sup> Ann. Internat. Mtg., Soc. Expl. Geophys.
- Campman, X. H., 2005, Imaging and suppressing near-receiver scattered seismic waves data: Ph.D. thesis Delft University of Technology.
- Cary, P. W., 1999, Prestack imaging with 3-D common-offset-vector gathers, CREWES Research Report, Vol. 11.

- Chang, T. et al., 2001, Optimization of acquisition design based on common reflection stack: 71<sup>st</sup> Ann. Internat. Mtg., Soc. Expl. Geophys.
- Claerbout, J. F., 1985, *Imaging the earth's interior*: Blackwell Scientific Publications.
- Claerbout, J.F., 1976, *Fundamentals of geophysical data processing*: McGraw-Hill.
- Clark, D., 1987, Near surface effects workshop: *The Leading Edge*, 6, 8–9.
- Cordsen, A., 2000, *Planning land 3-D seismic survey*: Society of Exploration Geophysicists.
- Cox, B.E., 2004, Tomographic inversion of focusing operators, Ph.D. thesis Delft University of Technology.
- Cox, B.E., and Verschuur, D.J., 2001, Data-driven tomographic inversion of focusing operators: 71<sup>st</sup> Ann. Internat. Mtg., Soc., Expl. Geophys., Expanded abstracts, 722-725.
- Cox, E. B., 2004, Tomographic inversion of focusing operators, Ph.D. thesis Delft University of Technology.
- Cox, M., 1999, Static corrections for seismic reflection surveys: *Soc. of Expl. Geophys.*
- Duquet, B., Marfurt, K. J., and Dellinger, J., 1998, Efficient estimates of subsurface illumination for Kirchhoff prestack depth migration: 68<sup>th</sup> Ann. Internat. Mtg., Soc. Expl. Geophys., Expanded Abstracts.
- Galbraith, M., 1994, A Land 3-D survey design by computer: *Austr. Soc. Expl. Geophys.* 25, 71-78.
- Gazdag, J., 1978, Wave-equation migration with the phase shift method: *Geophysics* **43**, 1342-1351.
- Gelius, L.-J., Lecomte, I., and Tabti, H., 2002, Analysis of the resolution function in seismic prestack depth imaging: *Geophysics*, **50**, 505-515.
- Gesbert, S., 2002, From acquisition footprints to true amplitude: *Geophysics*, **67**, 830-839.
- Gibson, R., Tzimeas, C., 2002, Quantitative measures of image resolution for seismic survey design: 72<sup>nd</sup> Ann. Internat. Mtg., Soc. Expl. Geophys.
- Hastings-James, R., Green, P., Al-Saad, R., and Al-Ali, M., 2000, Wide-azimuth 3-D swath acquisition: *GeoArabia*, 5, 103.
- Hindriks, C.O.H. and Duijndam, A.J.W., 1999, Handling near surface effects in imaging by using the common focal point technology: 69<sup>th</sup> Ann. Internat. Mtg., Soc. Expl. Geophys., Expanded abstracts.
- Hindriks, C.O.H. and Verschuur, D.J., 2001, Common Focus Point approach to the complex near surface: 71<sup>st</sup> Ann. Internat. Mtg., Soc. Expl. Geophys., Expanded abstracts, 1863-1866.

- Hindriks, C.O.H., 2007, Estimation and removal of complex near surface effects in seismic measurements, Ph.D. thesis Delft University of Technology.
- Kelamis, P. G., Erickson, K. E., Verschuur, D. J., and Berkhout, A. J., 2002, Velocity independent redatuming: a new approach to the near-surface problem in land seismic data processing: *The Leading Edge*, 21, no. 8, 730-735.
- Krebes, E. S., 2004, Seismic forward modelling, *CSEG Recorder*, April, 29-39.
- Krohn, C. E., and Johnson, M. L., 2006, HFVST<sup>TM</sup>: Enhanced data quality through technology integration: *Geophysics*, **71**, E13-E23.
- Lansley, R. M., 2004, CMP fold: A meaningless number: *The Leading Edge*, 23, 1038-1041.
- Laurain, R., Gelius, L. J., Vinje, V., and Lecomte, I., 2004, A review of 3D illumination studies, *Journal of Seismic Exploration*, No. 13, 17-37.
- Lecomte, I., 2006, Illumination, resolution and incidence-angle in PSDM: a tutorial: 76th Ann. Internat. Mtg., Soc. Expl. Geophys.
- Long, A., 2006, How multi-azimuth and wide-azimuth seismic compare: *First Break*, 24, 55-61.
- Marschall, R., 1997, 3-D Acquisition geometries, review and summary: SEG summer research workshop.
- Meunier, J., 1999, 3D geometry, velocity filtering and scattered noise: 69<sup>th</sup> Ann. Internat. Mtg., Soc. Expl. Geophys., Expanded Abstracts.
- Moldoveanu, N., and Egan, M., 2006, From narrow-azimuth to wide- and rich-azimuth acquisition in the Gulf of Mexico: *First Break*, 24, 69-76.
- Muyzert, E., and Vermeer, P., 2004, The impact of acquisition perturbations on land seismic data, 74<sup>th</sup> Ann. Mtg: Soc. Expl. Geophys.
- Neidell, N. S., Taner, T. M., 1971, Semblance and other coherency measures from multichannel data: *Geophysics*, **36**, 482-497.
- Newman, P. and Mahoney, J. T., 1973, Patterns—with a pinch of salt: *Geophys. Prosp.*, **21**, 197-219.
- Ongkiehong, L., 1988, A changing philosophy in seismic data acquisition: *First Break*, 6, 281-284.
- Ongkiehong, L., and Askin, H.J., 1988, Towards the universal seismic acquisition technique: *First Break*, 6, no 2, 46-63.
- Padhi, T., and Holley, T. K., 1997, Wide azimuths—why not?: *The Leading Edge*, 16, 175-177.

- Quigley, J., 2004, An integrated 3D acquisition and processing technique using point sources and point receivers: 74<sup>th</sup> Ann. Internat. Mtg., Soc. Expl. Geophys., Expanded Abstracts.
- Regone, C.J., 1998, Suppression of coherent noise in 3D seismology, *The Leading Edge*, 17, no 11, 1584-1589.
- Reshef, M., 1991, Depth migration from irregular surfaces with depth extrapolation methods: *Geophysics*, 56, 119-122.
- Robein, E., 2003, *Velocities, Time-Imaging and Depth Imaging in Reflection Seismics*: EAGE Publications.
- Salinas\_Garnica, T., and Larner, K., 1997, Comparison of datuming alternatives in areas of rough terrain: 67<sup>th</sup> Ann. Internat. Mtg., Soc. Expl. Geophys., Expanded abstracts, 1274-1277.
- Sassolas, C., Nicodeme, P., and Lescoffit, G., 1999, The benefits of 3D ray tracing in acquisition feasibility: 69<sup>th</sup> Ann. Internat. Mtg., Soc. Expl. Geophys.
- Schleicher, J. Tygel, M., and Hubral, P., 1993, 3-D true-amplitude finite-offset migration: *Geophysics* **58**, 1112-1126.
- Shtivelman, V., and Canning, A., 1988, Datum correction by wave-equation extrapolation: *Geophysics*, 53, 1311-1322.
- Slawson, S.E., Grove, K. D., and Fischer, G.W., 1994, Model-based 3D seismic acquisition design: 64<sup>th</sup> Ann. Internat. Mtg. Soc. Expl. Geophys., Expanded abstracts, 919-920.
- Tegtmeier, S., Gisolf, A., and Verschuur, D.J., 2004, 3D sparse-data Kirchhoff redatuming: *Geophysical Prospecting* **52**, 509-521.
- Telford, W. M., Geldart, L. P., and Sherif, R. E., 1990, *Applied geophysics*: Cambridge University Press.
- Thorbecke, J. W., 1997, Common focus point technology, Ph.D. thesis Delft University of Technology.
- Torbecke, J.W., Wapenaar, K., and Swinnen, G., 2004, Design of one-way wavefield extrapolation operators, using smooth functions in WLSQ optimization: *Geophysics* **69**, 1037-1045.
- Toxopeus, G., Petersen, S., and Wapenaar, K., 2003, Improved geologic modeling and interpretation by simulated migrated seismics: a tutorial: 73rd Ann. Internat. Mtg., Soc. Expl. Geophys.
- Van de Rijzen, M., 2006, One-step focusing operator updating: *Delphi, The multiple removal and structural imaging project*, Volume XVII, Chapter 8.

- Van de Rijzen, M.J., Gisolf, A., and Verschuur, D.J., 2004, Infilling of sparse 3D data for 3D focusing operator estimation, *Geophysical Prospecting* **52**, 489-507.
- Van Veldhuizen, E., 2006, Integrated approach to 3-D seismic acquisition geometry analysis, Ph.D. thesis Delft University of Technology.
- Van Veldhuizen, E.J. and Blacquiere, G., 2003, Acquisition Geometry Analysis by Focal Beams in 3D Complex Media. Stavanger, EAGE Annual Meeting.
- Vermeer, G. J. O., 1999, Factors affecting spatial resolution: *Geophysics* **64**, 942-953.
- Vermeer, G.J.O., 1994, 3D symmetric sampling: 64<sup>th</sup> Ann. Internat. Mtg., Soc. Expl. Geophys., Expanded Abstracts, 906-909.
- Vermeer, G.J.O., 2002, 3-D seismic survey design: Society of Exploration Geophysicists.
- Vermeer, G.J.O., 2004, An ambitious geometry for 3D land acquisition: *The Leading Edge*, **23**, 1043-1046.
- Vermeer, J. O., 2003, A comparison of two different approaches to 3D seismic survey design: 64<sup>th</sup> Ann. Internat. Mtg. Soc. Expl. Geophys., Expanded abstracts, 919-920.
- Vermeer, J. O., 2005, Processing orthogonal geometry – what is missing?: 66<sup>th</sup> Ann. Internat. Mtg. Soc. Expl. Geophys., Expanded abstracts, 2201-2204.
- Verschuur, D.J. and Hindriks, C.O.H., 2004, Towards automatic estimation of near surface focusing operators: Delphi, The acquisition and preprocessing project, Volume VIII, Chapter 9.
- Volker, A.W.F., Blacquiere, G., Berkhout, A.J., and Ongkiehong, L., 2001, Comprehensive assessment of seismic acquisition geometries by focal beams -- Part II: Practical aspects and examples, *Geophysics*, **66**, 918-931.
- Volker, A.W.F., 2002, Assessment of 3-D seismic acquisition geometries by focal beams analysis, Ph.D. thesis Delft University of Technology.
- von Seggern, D., 1994, Depth-imaging resolution of 3-D seismic recording patterns: *Geophysics* **59**, 564-576.
- Wiggins, J. W., 1984, Kirchhoff integral extrapolation and migration of nonplanar data: *Geophysics*, **49**, 1239-1248.
- Yang, K., Wang, H., and Ma, Z., 1999, Wave equation datuming from irregular surfaces using finite difference scheme: 69<sup>th</sup> Ann. Internat. Mtg., Soc. Expl. Geophys., Expanded abstracts.
- Yilmaz, O., and Lucas, D., 1986, Prestack layer replacement: *Geophysics*, **51**, 1355-1369.

# Summary

---

## **Land seismic data acquisition and preprocessing: An operator solution to the near-surface problem**

The seismic method manifests itself as the most important indirect method for inferring information about the Earth's geophysical layering and physical properties. Seismic data acquisition, being the first step in this method, aims at providing measurements that allow the determination of high-resolution structural images and the estimation of accurate rock properties. Therefore, survey design should be an integrated process that couples acquisition, processing and characterization in a cyclic manner.

Land seismic survey design should aim at maximizing the signal content of the recorded data while minimizing the noise level. Complexities of the near surface and the varying acquisition-surface topography have degrading effects on land seismic images due to two factors. First, the dominance of coherent source-generated noise in terms of waves that are trapped in the near-surface (Rayleigh waves) and scattered Rayleigh waves arising from near-surface heterogeneities. The second effect includes the distortions occurring to the body waves while passing through the complex near-surface. The proposed design should allow for removal of these two unwanted effects during acquisition and preprocessing.

The first phase of the survey design process involves selecting initial parameters based on signal sampling theory. In a second phase of the design process the subsurface model is incorporated. The main objective of this phase is to evaluate and update the initial design parameters. In this thesis the evaluation is based on the quality of pre-stack imaging results. These results are obtained using the concept of focal beams which allows assessing the

effects of an acquisition geometry on the image quality without going into explicit modelling of seismic data. The modelling and imaging of seismic data is carried out by the formation of two focal beams, the focal source beam and the focal detector beam. This is followed by combining these beams in the image space for a specific target point to produce the so called focal functions: resolution function and amplitude-versus-rayparameter (AVP) imprint function. It is shown that the scattered Rayleigh waves can also be incorporated into the focal beam analyses without the need for explicit modelling of such waves. It is advocated that the geometry that is effective in attenuating the scattered Rayleigh waves is also effective in attenuating direct Rayleigh waves. The effects of using field arrays to reduce scattered Rayleigh waves are quantified by the focal beam analyses.

The results obtained in this thesis demonstrate that the complex near-surface causes the seismic wavefronts to be distorted without causing major shadow zones. This is principally different for the situation where the complexities of the underlying macro-model are relatively close to the target.

The distortions caused by the complex near-surface can not be solved during the acquisition phase. However, the acquisition criterion is to provide data that allows removal of these effects during preprocessing. The method of removing these effects is based on wavefield redatuming. This method uses *one-way focusing operators* that are obtained without knowledge of the underlying macro-model. This velocity-independent method is well established for the 2D case using adequately sampled common source or common receiver gathers. However, extension to the 3D case requires either adequately sampled 3D common source or common receiver gathers, which is rarely available by practical 3D acquisition geometries. To circumvent this limitation, this thesis introduces the estimation of the one-way focusing operators using *cross-spreads* without a need for data infill (i.e. trace interpolation).

The estimation of one-way focusing operators using an iterative approach is demonstrated on 2D and 3D field data examples from Saudi Arabia. In addition, a method for estimating 2D focusing operators in one-step is introduced and applied on a complex 2D field data set. This method is based on global non-parametric inversion of tracked *two-way* traveltimes in the common source gathers, using Fermat's principle as a constraint. This method can be directly extended to 3D.

The thesis concludes with recommendations for future research.

Mustafa N. Al-Ali

# Samenvatting

---

## **Seismische data-acquisitie en preprocessing op land: een oplossing voor het probleem van de ondiepe ondergrond gebaseerd op operatoren**

De seismische methode is de meest belangrijke methode om vanaf het aardoppervlak informatie te verkrijgen over de geologische structuur van aardlagen en hun fysische eigenschappen. De eerste stap is de data-acquisitie. Doel daarvan is seismische data in te winnen waarvan de kwaliteit geschikt is om een hoge-resolutie afbeelding van de ondergrond te maken en om de eigenschappen van het gesteente te schatten. Daarom dient het ontwerp van het seismische experiment een geïntegreerd proces te zijn dat acquisitie, dataverwerking en karakterisatie op een cyclische manier koppelt.

Het ontwerp van een seismisch experiment moet gericht zijn op het maximaliseren van de signaal-ruis verhouding. Dit geldt met name voor de situatie op land, waar de aanwezigheid van een complexe ondiepe ondergrond en een variërende topografie een negatief effect hebben op de kwaliteit van de seismische afbeelding. Hiervoor zijn twee redenen aan te wijzen. Ten eerste de dominante aanwezigheid van oppervlaktegolven die als het ware gevangen zijn in de ondiepe ondergrond (Rayleigh golven). Deze worden gegenereerd door de seismische bron zelf. Ook de echo's van deze golven, veroorzaakt door inhomogeniteiten in de ondiepe ondergrond, zijn hierbij inbegrepen. De tweede reden is dat de complexe ondiepe ondergrond de reflectiesignalen (P- en S-golven) afkomstig van de diepe ondergrond verstoort. Het zijn juist deze signalen waarop de het afbeeldingsproces gebaseerd is. Het seismische experiment dient zodanig ontworpen te worden dat de genoemde effecten verwijderd kunnen worden gedurende de data-acquisitie en de preprocessing.

In een tweede fase van het ontwerpproces wordt het model van de ondergrond bij het ontwerpproces betrokken. Voornaamste doel van deze fase is het evalueren en aanpassen van de initiële ontwerpparameters. In dit proefschrift is de evaluatie gebaseerd op de kwaliteit van prestack-migratie resultaten. Deze worden efficiënt verkregen via zogenaamde focale bundels. Zonder een volledige prestack migratie uit te voeren kunnen hiermee de effecten van een bepaald acquisitiegeometrie-ontwerp worden beoordeeld. Het modelleren en afbeelden van de seismische gegevens wordt uitgevoerd via de constructie van twee focale bundels, de focale bronbundel en de focale detectorbundel, gevolgd door het combineren ervan. Dit proces leidt tot twee focale functies, gerelateerd aan een specifieke doellocatie in de ondergrond: de resolutiefunctie en de AVP-functie (AVP staat voor amplitude versus ray-parameter). Gescatterde Rayleigh golven kunnen worden meegenomen in de focale bundels zonder dat het nodig is om deze expliciet te modelleren. De onderdrukking van deze golven door het groeppormingsproces kan door analyse van de focale bundels gekwantificeerd worden. Gesteld wordt dat een acquisitiegeometrie die effectief is voor het onderdrukken van dit type golven ook effectief is voor het onderdrukken van directe Rayleigh golven.

Dit proefschrift laat zien dat de complexe ondiepe ondergrond weliswaar golffronten vervormt, maar geen grote schaduwzones veroorzaakt. Dit verschilt principieel van de situatie waarin de complexiteiten zich relatief dicht bij de (diepe) doellocatie bevinden.

De verstoringen door de complexe ondiepe ondergrond kunnen niet worden opgelost in de acquisitiefase. Criterium voor de acquisitie is echter, dat deze de meetgegevens oplevert waarmee deze effecten kunnen worden verwijderd gedurende de preprocessing. De methode hiervoor is gebaseerd op golfveld redatuming. De methode maakt gebruik van *éénweg focuseringsoperatoren*, die verkregen zijn zonder kennis van het onderliggende macro-model. Deze methode is volledig bekend voor de 2D situatie met een goede bemonstering van bronnen en detectoren. Uitbreiding naar de 3D situatie zou eenvoudig zijn, ware het niet dat ook dan een goede bemonstering van bronnen of detectoren vereist is, ofwel een volledige bedekking. Dit is vrijwel nooit mogelijk in de praktijk. Om deze beperking te omzeilen, is een methode ontwikkeld voor het schatten van éénweg focuseringsoperatoren op basis van acquisitie in zogenaamde *cross-spreads* zonder dat het nodig is om extra meetgegevens te genereren, bijvoorbeeld via interpolatie.

Het schatten van éénweg focuseringsoperatoren met een iteratieve methode wordt met 2D en 3D voorbeelden gedemonstreerd op ‘echte data’ uit Saoedi-Arabië. Daarnaast is ook een éénstap-methode ontwikkeld. Deze is gebaseerd op inversie van *tweeweg* looptijden, die via tracking verkregen worden uit ruwe data, met als randvoorwaarde het principe van Fermat.

Het proefschrift besluit met aanbevelingen voor verder onderzoek.

Mustafa N. Al-Ali

# Curriculum vitae

---

Name: Mustafa Naser Ali Al-Ali  
Born: January 01, 1970, Al-Ahsa, Saudi Arabia  
Nationality: Saudi



## Education

1987-1988 Saudi Aramco College Preparation Center.  
1988-1992 Earth Sciences Department, King Fahad University of Petroleum and Minerals. BSc in Geophysics with honors.  
1999-2002 Earth Sciences Department, King Fahad University of Petroleum and Minerals. MSc in Geology with thesis in computation geology. “Application of vibrator performance control data in improving near-surface velocity determination”.  
2003-2007 Applied Physics, Department of Imaging, Science and Technology (IST), Faculty of Applied Sciences, Delft University of Technology. PhD research, Laboratory of Acoustic Imaging and Sound Control.

## Work

1992-present Saudi Aramco, Dhahran, Saudi Arabia.  
Started with Saudi Aramco’s Geophysical Technology Division in September 1992. In 1993 he went on an eight month training assignment with Halliburton in Houston, USA followed by an assignment in Geophysical Data Processing Division. In January 1996 Mustafa joined the Geophysical Data Acquisition Division, where he was involved in seismic crews supervision, field quality control, contracting, and survey acquisition

design. In July 2001 Mustafa joined the Eastern Area Exploration Division where he worked as an interpreter until January 2003.

**Awards**

- |      |  |
|------|--|
| 1998 | Saudi Aramco Geophysicist of the Year Award.   |
| 2002 | Saudi Aramco Exploration Creativity award as well as the Saudi Aramco Corporate innovation award.                  |
| 2005 | Society of Exploration Geophysicists J. Clarence Karcher Award.  |
| 2006 | Awarded USA patent number (US 6,982,928 B2) titled "Seismic P-wave velocity derived from vibrator control system". |

# Acknowledgments

---

I am indebted to Saudi Aramco for offering me a scholarship to pursue this PhD research. The support of the Exploration Organization management members has been great. I would like to mention in particular Mr. A. Al-Naim, Exploration Vice President, Dr. K. Al-Yahya, Exploration Operations Department Manager, and Mr. A. Al-Hauwaj, Area Exploration Department Manager.

I am eternally grateful to my former mentor Dr. R. Hastings-James for the support he has extended to me during the years we have worked together. Unfortunately, Richard, those good and less good days will never come back in the same form, but I am sure they will continue in other ways.

I would particularly like to record my gratitude to my promoter Prof. Dr. ir. A.J. Berkhout for supervising this thesis and for his invaluable ideas. He has provided me with innumerable and original suggestions that helped improving this thesis. Working with Prof. Berkhout on a scientific matter makes you learn beyond the science. There will be always great management master pieces embedded in the scientific discussions.

I extend my gratitude to Prof. Dr. ir. A. Gisolf for many useful discussions and for providing me with the right atmosphere to conduct my research. Prof. Gisolf has always been there when needed.

Dr. Gerrit Blacquiere has patiently taught me the DELPHI language during my first few months with DELPHI. This has continued to the end. He has always made me feel that he and I work as a team. I express my deep gratitude to you Gerrit for the support you have extended to me during my research. If I am allowed to give Gerrit a nickname, it will be 'never diverge'.

Dr. Eric Verschuur has always been available with answers to all my questions, even if it required somehow deeper thinking. I believe that the DELPHI team is blessed by having Eric. I would like to acknowledge you Eric for your endless support. If I am allowed to give Eric a nickname, it will be the 'geophysical express'.

I am also grateful to the other members of my thesis committee, Prof. D. Simons, Prof. T. Alkhalifa, and Dr. Panos Kelamis. I would like to thank Dr. Kelamis for advising me to pursue my PhD at Delft University of Technology and for his continuing support.

I would like to thank Gijs Vermeer for helping me gain more insight into his work on 3D survey design. His assistance was especially useful in extending the focusing operator determination to cross-spreads. I am also grateful to you Gijs for proofreading of this thesis.

During the biannual DELPHI Sponsors meeting, many fruitful discussions and stimulating ideas arise. I thank all DELPHI sponsors for their comments, numerous discussions and feedback.

I am deeply grateful to colleagues from Saudi Aramco, Abdunnasser Khusheim, Riyadh Al-Saad, Emad Al-Janoubi, and Ameera Al-Mustafa who have assisted me with getting the field data used in this thesis. They have always hosted me during my visits to Saudi Aramco offices in Dhahran.

I would like also to thank my colleagues, former and current, for many useful discussions, in particular, Barbara, Paul, John, Kees, Ayon, Dana, Edith, Justyna, Sandra, Maurice, Niels, Jan, Gert-Jan and Bouchaib. I also thank Arno for explaining his thesis to me at the beginning of my research. Special thanks go to Remco Romijn for getting me started with SU and ProMax. My thanks also go to Margaret, Henry and Edo for their assistance. Thank you Paul for making it possible to run Charisma from my office. Thank you Mohammad for many interesting discussions, I will miss going to Coco Bango with you and Bochaib!

I am also grateful to Abdulrahman Al-Thaqeb and Nabeel Ajaj from Saudi Petroleum Overseas Ltd in UK for their support and cooperation.

During my stay in the Netherlands, I have nurtured many friendships that I value. Among those I would like to acknowledge Firas Al-Abduwani, Abdulwahab Al-Abbas, Fahad Al-Bash, and Omar Al-Amry. Abdulwahab (Abu Khalid), I highly appreciate your support.

I would like to record my deep gratitude to my eight sisters and three brothers and our mother, father, and wife for their endless support. Thank you father and hope everything meets your expectations.

## **Propositions**

accompanying the Ph.D. thesis

“Land seismic acquisition and preprocessing: an operator solution to the near-surface problem”

Mustafa N. Al-Ali

June 18<sup>th</sup>, 2007

1. Current solutions to remove wavefield distortion from seismic land data are still very primitive.
2. In acquisition design, priority should be given to the macro level of the geometry, involving station interval, line spacing and maximum offset. Next, the micro level should be addressed, involving the field arrays.
3. Current directions in marine wide-azimuth acquisition show the importance of establishing a unified framework for designing land and marine acquisition geometries.
4. For land acquisition, model-based design is largely steered by capabilities in pre-processing, while for marine acquisition model-based design is largely steered by illumination.
5. The economic problem of coarse sampling in 3D land acquisition can be best solved by using properly sampled cross-spreads.
6. The CFP solution to the near-surface problem starts where conventional solutions stop.
7. The importance of the cross spread is underestimated by geophysical scientists.  
Reference: Biondo L. Biondi, 3D Seismic Imaging, page 5: “One important template that we will not discuss, despite its having theoretical advantages, is the cross spread template (Vermeer, 1988), which seldom is applied because of its cost”.
8. The majority rule that controls political decision-making must not be transferred to the scientific community.
9. Leading countries, aiming at a radical democratization of our planet, should realize that adaptive democratization might be more effective.
10. Spell checking, available in most of the word processors, does not only decrease someone’s spelling skills, it also decreases someone’s typing skills.

These propositions are considered opposable and defensible and as such have been approved by the supervisor, Prof. Dr. ir. A. J. Berkhout.

## Stellingen

behorende bij het proefschrift

“Land seismic acquisition and preprocessing: an operator solution to the near-surface problem”

Mustafa N. Al-Ali

18 juni 2007

1. De huidige oplossingen om de vervorming van het golfveld te verwijderen uit seismische landacquisitie gegevens zijn nog steeds erg primitief.
2. Bij het ontwerpen van een acquisitiegeometrie dient men prioriteit te geven aan het macroniveau, dat het stationinterval, de lijnafstand en de maximale offset omvat. Vervolgens komt het microniveau aan de orde, dat betrekking heeft op de veldarrays.
3. De huidige trend in mariene ‘wide-azimuth’ acquisitie laat zien dat het belangrijk is dat er een eenduidig raamwerk komt voor het ontwerp van land en mariene acquisitiegeometrieën.
4. Bij landacquisitie wordt het modelgebaseerde ontwerp vooral gestuurd door de mogelijkheden in de ‘preprocessing’, terwijl bij mariene acquisitie het modelgebaseerde ontwerp vooral wordt gestuurd door de belichting.
5. Het economische probleem van de grove bemonstering bij 3D landacquisitie kan het best worden opgelost door goedbemonsterde ‘cross-spreads’ toe te passen.
6. De CFP oplossing voor het probleem van de ondiepe ondergrond begint waar de conventionele oplossingen eindigen.
7. Het belang van de ‘cross-spread’ wordt onderschat door geofysische wetenschappers. Referentie: Biondo L. Biondi, 3D Seismic Imaging, pagina 5: “One important template that we will not discuss, despite its having theoretical advantages, is the cross spread template (Vermeer, 1988), which seldom is applied because of its cost”.
8. Het meerderheidsstandpunt dat het politieke besluitvormingsproces bepaalt dient niet te worden overgebracht op de wetenschappelijke gemeenschap.
9. De leidende landen die een radicale democratisering van onze planeet voorstaan, moeten zich realiseren dat een adaptieve democratisering mogelijk veel effectiever is.
10. Spellingcontrole, beschikbaar in de meeste tekstverwerkers, vermindert niet alleen iemands spellingvaardigheid, maar ook iemands typevaardigheid.

Deze stellingen worden verdedigbaar geacht en zijn als zodanig goedgekeurd door de promotor, prof.dr.ir. A. J. Berkhout.

## **Propositions**

accompanying the Ph.D. thesis

“Land seismic acquisition and preprocessing: an operator solution to the near-surface problem”

Mustafa N. Al-Ali

June 18<sup>th</sup>, 2007

1. Current solutions to remove wavefield distortion from seismic land data are still very primitive.
2. In acquisition design, priority should be given to the macro level of the geometry, involving station interval, line spacing and maximum offset. Next, the micro level should be addressed, involving the field arrays.
3. Current directions in marine wide-azimuth acquisition show the importance of establishing a unified framework for designing land and marine acquisition geometries.
4. For land acquisition, model-based design is largely steered by capabilities in pre-processing, while for marine acquisition model-based design is largely steered by illumination.
5. The economic problem of coarse sampling in 3D land acquisition can be best solved by using properly sampled cross-spreads.
6. The CFP solution to the near-surface problem starts where conventional solutions stop.
7. The importance of the cross spread is underestimated by geophysical scientists.  
Reference: Biondo L. Biondi, 3D Seismic Imaging, page 5: “One important template that we will not discuss, despite its having theoretical advantages, is the cross spread template (Vermeer, 1988), which seldom is applied because of its cost”.
8. The majority rule that controls political decision-making must not be transferred to the scientific community.
9. Leading countries, aiming at a radical democratization of our planet, should realize that adaptive democratization might be more effective.
10. Spell checking, available in most of the word processors, does not only decrease someone’s spelling skills, it also decreases someone’s typing skills.

These propositions are considered opposable and defensible and as such have been approved by the supervisor, Prof. Dr. ir. A. J. Berkhout.

## Stellingen

behorende bij het proefschrift

“Land seismic acquisition and preprocessing: an operator solution to the near-surface problem”

Mustafa N. Al-Ali

18 juni 2007

1. De huidige oplossingen om de vervorming van het golfveld te verwijderen uit seismische landacquisitie gegevens zijn nog steeds erg primitief.
2. Bij het ontwerpen van een acquisitiegeometrie dient men prioriteit te geven aan het macroniveau, dat het stationinterval, de lijnafstand en de maximale offset omvat. Vervolgens komt het microniveau aan de orde, dat betrekking heeft op de veldarrays.
3. De huidige trend in mariene ‘wide-azimuth’ acquisitie laat zien dat het belangrijk is dat er een eenduidig raamwerk komt voor het ontwerp van land en mariene acquisitiegeometrieën.
4. Bij landacquisitie wordt het modelgebaseerde ontwerp vooral gestuurd door de mogelijkheden in de ‘preprocessing’, terwijl bij mariene acquisitie het modelgebaseerde ontwerp vooral wordt gestuurd door de belichting.
5. Het economische probleem van de grove bemonstering bij 3D landacquisitie kan het best worden opgelost door goedbemonsterde ‘cross-spreads’ toe te passen.
6. De CFP oplossing voor het probleem van de ondiepe ondergrond begint waar de conventionele oplossingen eindigen.
7. Het belang van de ‘cross-spread’ wordt onderschat door geofysische wetenschappers. Referentie: Biondo L. Biondi, 3D Seismic Imaging, pagina 5: “One important template that we will not discuss, despite its having theoretical advantages, is the cross spread template (Vermeer, 1988), which seldom is applied because of its cost”.
8. Het meerderheidsstandpunt dat het politieke besluitvormingsproces bepaalt dient niet te worden overgebracht op de wetenschappelijke gemeenschap.
9. De leidende landen die een radicale democratisering van onze planeet voorstaan, moeten zich realiseren dat een adaptieve democratisering mogelijk veel effectiever is.
10. Spellingcontrole, beschikbaar in de meeste tekstverwerkers, vermindert niet alleen iemands spellingvaardigheid, maar ook iemands typevaardigheid.

Deze stellingen worden verdedigbaar geacht en zijn als zodanig goedgekeurd door de promotor, prof.dr.ir. A. J. Berkhout.